

Structure/Function Analysis of Human Integral
Membrane Proteins:
Connexin 26 and the ZnT8 Zinc Transporter

Maciej Jagielnicki

Charlottesville, VA, USA

M.S., Wroclaw University of Technology, 2011

A Dissertation presented to the Graduate Faculty of the University of
Virginia in Candidacy for the Degree of Doctor of Philosophy

Department of Molecular Physiology and Biological Physics

University of Virginia

April, 2018

Abstract

In this dissertation I present a detailed structural and functional characterization of two human membrane proteins – zinc transporter ZnT8 and gap junction channel and hemichannel Connexin26.

The human zinc transporter ZnT8 (SLC30A8), expressed primarily in pancreatic β -cells, plays a key function in maintaining the concentration of blood glucose through its role in insulin storage, maturation and secretion. This transporter is an autoantigen for Type 1 diabetes (T1D) and is associated with Type 2 diabetes (T2D) through its risk allele that encodes a major non-synonymous single nucleotide polymorphism (SNP) at Arg325. Despite its role in diabetes and concomitant potential as a drug target, little is known about the structure or mechanism of ZnT8. To this end, we expressed ZnT8 in *Pichia pastoris* yeast and *Sf9* insect cells. Guided by a rational screen of 96 detergents, we developed a method to solubilize and purify recombinant ZnT8, which is stable in fos-choline 12 for >2 weeks. An *in vivo* transport assay in *Pichia* showed that the protein is functionally active. A fluorescence-based *in vitro* transport assay using proteoliposomes indicated that human ZnT8 functions as a $\text{Zn}^{2+}/\text{H}^{+}$ antiporter in liposomes. We also purified *E. coli*-expressed amino- and carboxy-terminal cytoplasmic domains. Circular dichroism spectrometry showed that the amino-terminal domain contains predominantly β -sheet and turn secondary structure, and the carboxy-terminal domain has a mixed α/β structure. Electron microscopy and single-particle image analysis yielded a density map

of ZnT8B at 20-Å resolution, which revealed that it forms a dimer in detergent micelles. Two prominent lobes are ascribed to the transmembrane domains, which recapitulate the architecture of the bacterial zinc transporter YiiP. These results provide a foundation for higher resolution structural studies and screening experiments to identify compounds that modulate ZnT8 activity.

Connexins (Cx) are a family of integral membrane proteins that assemble as hexameric hemichannels. Hemichannels from adjacent cells dock to form dodecameric gap junction channels (GJCs). GJCs mediate intercellular communication between adjacent cells and exhibit properties of both ligand- and voltage-gated channels, including channel closure at acidic pH. Notably, mutations of the Cx26 gene (GJB2) are the most common cause of sensorineural hearing loss in children. Despite numerous functional studies on gating of connexins, the structural basis for pH-induced gating is not well understood. In order to gain insight into this mechanism, recombinant, human Cx26 was purified as dodecameric GJCs, which remained homogenous and monodisperse when reconstituted in amphipol. To explore pH inhibition, we herein used single-particle, electron cryo-microscopy and mass spectrometry to examine the conformational changes associated with pH-mediated regulation. In pH 7.5, the structure of the Cx26 GJCs reconstituted in amphipol recapitulated the previous GJC crystal structures. Within the transmembrane and extracellular domains, the map resolution was ~ 3.5 Å, whereas the N-terminus showed a conformationally heterogeneous state, which was confirmed by hydrogen deuterium exchange mass spectrometry. Three-dimensional classification of

particles at pH 6.4 yielded two distinct conformations, one resembling the physiological pH structure and another with a pore-occluding density. Modeling of the polypeptide into the cryoEM maps suggests that acidic pH elicits an extension and association of the amino-termini to form the occluding gating particle. Lysine crosslinking with tandem mass spectrometry revealed additional crosslinks at acidic pH between residues K15 and K22 and the cytoplasmic loop, indicative of closer association compared with pH 7.5. Taken together, our results support a 'ball-and-chain' mechanism in which the NTs undergo an extension and associate to occlude the channel pore during pH-mediated gating.

The physiological roles of connexin hemichannels and gap junction channels can be distinguished by their characteristic regulation. GJCs serve as intercellular connections and are in a constitutively open state so that tissues function as syncytia. HCs in the plasma membrane communicate with the extracellular space and by default are in a closed state. As of the time of writing this, no structure of a connexin hemichannel exists and the mechanistic details of their regulation are not well known. To gain insight into the structure of Connexin 26 hemichannel, a mutation in connexin 26 gene was introduced (N176Y) in order to prevent connexin hemichannels from docking and forming GJCs. Electron and cryo-electron microscopy study of the N176Y hexamer in detergent and amphipol has revealed that the protein is conformationally unstable. As a consequence, the protein was reconstituted in lipid nanodiscs. CryoEM analysis of the nanodiscs on C-flat carbon grids resulted in 2D class averages clearly showing *en face* protein views with visible α -helical secondary structure. Unfortunately, particles displayed a preferred

orientation on the grids. To remedy this, pegylated gold grids were prepared in-house, on which the protein adopted a more random orientation which resulted in 2D class averages showing both *en face* views and side views with traces of secondary structure. To conclude, a preparation of connexin 26 hemichannel was optimized for future high-resolution structure determination with cryoEM.

Dedication

To the woman of my life, Iga Kucharska, for her unwavering encouragement and support.

Abbreviations

A₂₈₀, absorbance at 280 nm;

ATP, adenosine triphosphate;

β-ME, β-mercaptoethanol;

BS3, bis(sulfosuccinimidyl)suberate;

C_α, carbon alpha;

cAMP, cyclic adenosine monophosphate;

CH₃CN, acetonitrile;

CL, cytoplasmic loop domain;

CMC, critical micellar concentration;

cv, column volume;

CPM, 7-diethylamino-3-(4'-maleimidylphenyl)-4-methylcoumarin;

cryoEM, cryo-electron microscopy;

CT, cytoplasmic c-terminal domain;

CTF, contrast transfer function;

Cx, connexin;

Cx26, connexin 26;

DFA, differential filtration assay;

DDM, n-dodecyl-β-D-maltopyranoside;

DM, n-decyl-β-D-maltopyranoside;

DTT, dithiothreitol;

E. coli cells, *Escherichia coli* cells;

EM, electron microscopy;

EX1, component of hydrogen-deuterium exchange kinetics;

FA3, façade-EM;

FC-12, fos-choline 12;

FSC, Fourier shell correlation;

GJC, gap junction channel;
HC, hemichannel;
HD, hydrogen-deuterium;
HDX, hydrogen-deuterium exchange;
HEPES, (4-(2-hydroxyethyl)-1-piperazineethanesulfonic acid);
HPLC, high-pressure liquid chromatography;
IMAC, immobilized metal affinity chromatography;
IP3, inositol trisphosphate;
MALDI-MS, matrix-assisted laser desorption ionization mass spectrometry;
MES, 2-(N-morpholino)ethanesulfonic acid;
MOI, multiplicity of infection;
MS, mass spectrometry;
MS/MS, tandem mass spectrometry;
MSP2N2, membrane scaffold protein 2N2;
MWCO, molecular weight cut-off;
NT, cytoplasmic n-terminal domain;
OD, optical density;
OG, n-octyl- β -D-glucopyranoside;
PCR, polymerase chain reaction;
PDB, protein data bank;
PMSF, phenylmethylsulfonyl fluoride;
RMSD, root-mean-square deviation;
SDS-PAGE, sodium dodecylsulfate polyacrylamide gel electrophoresis;
Sf9 cells, *Spodoptera frugiperda* cells;
SNP, single nucleotide polymorphism;
T1D, type 1 diabetes;
T2D, type 2 diabetes;
TBA, tetrabutylammonium;

TBSb, tetrabutylantimony;
TCEP, tris(2-carboxyethyl)phosphine;
TEV, tobacco etch virus;
TFA, Trifluoroacetic acid;
 T_m , melting temperature;
TM, transmembrane;
Tris, tris(hydroxymethyl)aminomethane;
Vj gating, transjunctional voltage gating;
Vm gating, transmembrane voltage gating;
WT, wild-type;
X-ray, x-ray crystallography;
Yeast cells, *Pichia pastoris* cells;
ZnT8A, full-length, 40 kDa ZnT8;
ZnT8B, amino-terminal truncated, 35 kDa ZnT8.

Table of Contents:

Abstract.....	ii
Dedication.....	vi
Abbreviations.....	vii
Chapter 1. Introduction.....	1
1.1 Zinc transporter ZnT8.....	1
1.1.1 Role of zinc.....	1
1.1.2 Zinc transporters.....	3
1.1.3 ZnT8: structure and function.....	10
1.1.4 ZnT8: functional insights from mouse models.....	16
1.1.5 ZnT8: role in disease.....	19
1.2 Gap junction channel Connexin26 and pH.....	24
1.2.1 Connexin topology.....	24
1.2.2 Connexin function.....	26
1.2.3 Connexin regulation.....	29
1.2.4 Connexin26.....	34
1.2.5 Connexin26: regulation by pH.....	39
1.2.6 Connexin26: mechanisms for gating.....	40
1.3 Connexin26 hemichannel and Ca ²⁺	45
1.3.1 Connexin hemichannels and Ca ²⁺	45
1.3.2 Connexin26 hemichannels.....	46
1.3.3 Other connexin hemichannels.....	50

1.4 Accomplishments	53
1.4.1 Zinc transporter ZnT8	53
1.4.2 Gap junction channel Connexin26	55
1.4.3 Connexin26 hemichannel	57
Chapter 2. Structure/Function Analysis of Human ZnT8 (SLC30A8):	
A Diabetes Risk Factor and Zinc Transporter	59
2.1 Introduction	59
2.2 Methods	64
2.3 Results and discussion.....	82
Chapter 3. pH-gating of Gap Junction Channels:	
Visualization of a “ball-and-chain” by cryoEM	102
3.1 Introduction	102
3.2 Methods	104
3.3 Results and discussion.....	115
Chapter 4. Summary	144
4.1 Conclusions	144
4.2 Future directions	148
Appendix 1. Structural investigation of connexin 26 hemichannels	151
2.1 Introduction	151
2.2 Methods	153
2.3 Results and discussion.....	157
References	165

Chapter 1. Introduction

1.1 Zinc transporter ZnT8

1.1.1 Role of zinc. Zinc is the second most abundant trace element in humans, it is thus not surprising that it plays a large role in numerous biological processes including cell division, growth and differentiation. Zinc combines with proteins to act as a structural, catalytic and regulatory component in transcription factors, enzymes, transporters, and receptors [1-3]. It is estimated that about 10 % of the entire human genome encodes zinc proteins with intramolecular zinc-binding sites, with close to 50 % of them being transcription factors and enzymes [2, 4]. Following absorption, zinc is found bound to either albumin or α 2-macroglobulin in the blood and it is subsequently delivered to peripheral tissues [5, 6]. The intracellular distribution of zinc was found to be 50 %, 40 % and 10 % for cytoplasm, nucleus and cell membrane, respectively (12,13) while in the cytosol, the majority of the zinc pool is bound by close to a dozen of different metallothioneins [7]. Zinc has a central role in cellular redox processes (7) and free zinc has a potential to induce oxidative stress leading to metabolic disturbances and possibly cell death (8,9). Zinc homeostasis and intracellular free zinc must therefore be tightly controlled which is achieved by the coordinated regulation of its uptake, efflux, distribution, and storage [3, 8-10].

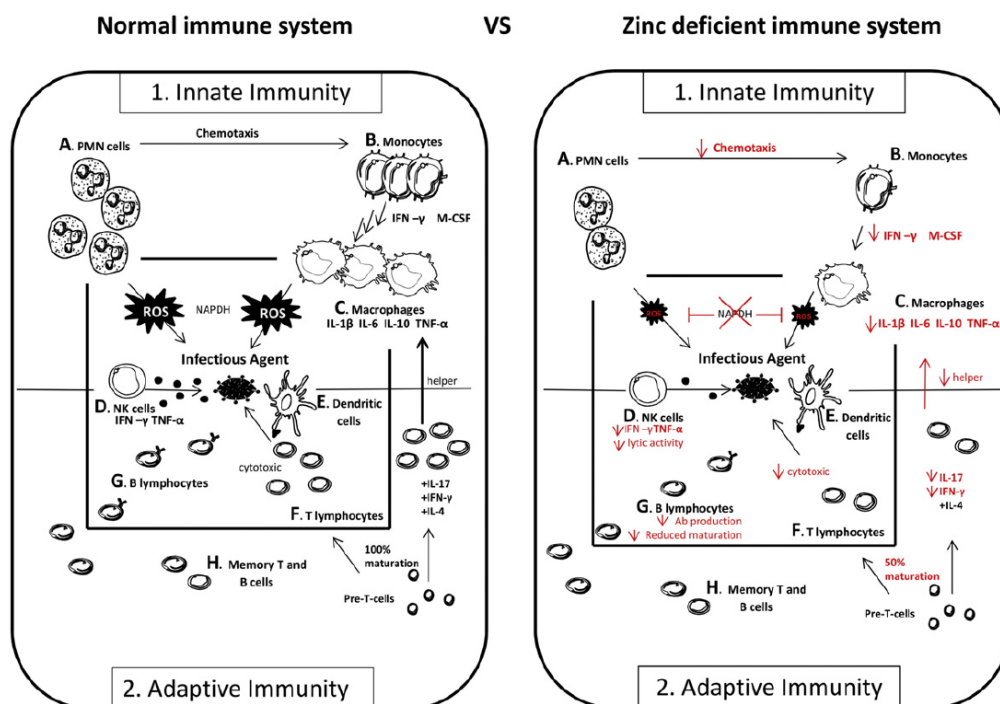


Figure 1.1. Schematic representation of the innate and adaptive immune system acute response in a normal versus Zn-lacking system. Innate immunity: Zn-lacking innate immune system is characterized by reduced polymorphonuclear cell (PMN) chemotaxis and phagocytosis with reduced nicotinamide adenine dinucleotide phosphate (NAPDH) production and consequent reduced production of reactive oxygen species (ROS) for pathogen neutralization (A). Reduced monocyte adhesion and maturation of macrophages (B), as well as reduced natural killer (NK) cell (C) and dendritic cell (DC) maturation (E) are also observed during Zn deprivation. The production of cytokines is also modified by Zn deficiency. Adaptive immunity: Zn deficiency causes thymic atrophy with subsequent T-cell lymphopenia, reduced differentiation of T-cells, increased pre-T-cell death, unpaired balance between Type 1 T helper (Th1) cells (decreased) and Type 2 T helper (Th2) cells, as well as reduced Type helper 17 (Th17) cell subset and subsequent reduced interleukin 17 (IL-17) production (F). B-cell maturation and antibody production are less affected (G). The ratio of memory versus naïve T and B cells is also affected by Zn deprivation (H). Figure from [11].

Alterations in zinc homeostasis, deficiency in particular, have been linked to the development of a number of diseases [12-14] including growth retardation, diarrhea, skin lesions, hypogonadism, immune system dysfunction (commonly found in healthy elderly

patients), and neurological disorders [13-16]. Disturbances in zinc homeostasis may contribute to the pathology of many chronic conditions including Alzheimer's disease, cardiovascular disease, cancer, autoimmunity, and diabetes (Figure 1.1) [17, 18]. Zinc deficiency in developing countries is responsible for 4 % of the global morbidity and mortality of young children, and for over half a million of diarrhea- and pneumonia-related children's deaths [19]. Zinc supplementation has shown to contribute to improved immune functions, decrease the incidence of infections and reduce the incidence of blindness in patients with macular degeneration and vision loss [20].

1.1.2 Zinc transporters. A number of proteins are responsible for the control of systemic and cellular zinc homeostasis including metallothioneins, controlling bioavailability of zinc, and transport membrane proteins. Mammalian membrane zinc transporters can be divided into ZIP proteins (Zrt, Irt-like proteins, Solute Carrier family 39A (SLC39A)) and ZnT proteins (Zn-Cation Diffusion Facilitator (Zn-CDF), Solute Carrier family 30A (SLC30A)). Fourteen ZIP transporters and ten ZnT transporters have been identified (ZnT9 is an exception and has not been shown to participate in zinc transport). The coordination between ZIP and ZnT transporters in maintaining zinc homeostasis is crucial for numerous physiological functions and hence disturbances in it are involved in a wide variety of diseases (Figure 1.2) [1, 21, 22].

The function of ZIP transporters is to uptake zinc into the cytosol from the extracellular space or intracellular compartments. ZIP proteins are predicted to have eight

conserved transmembrane domains (TMDs) and a highly-variable cytoplasmic histidine-rich intracellular loop between TMDs III and IV and an extracellular amino-terminal portion. They are thought to form homodimers to transport zinc across the membrane [23] and contain a zinc-binding motif in TMD V which may determine metal specificity [24].

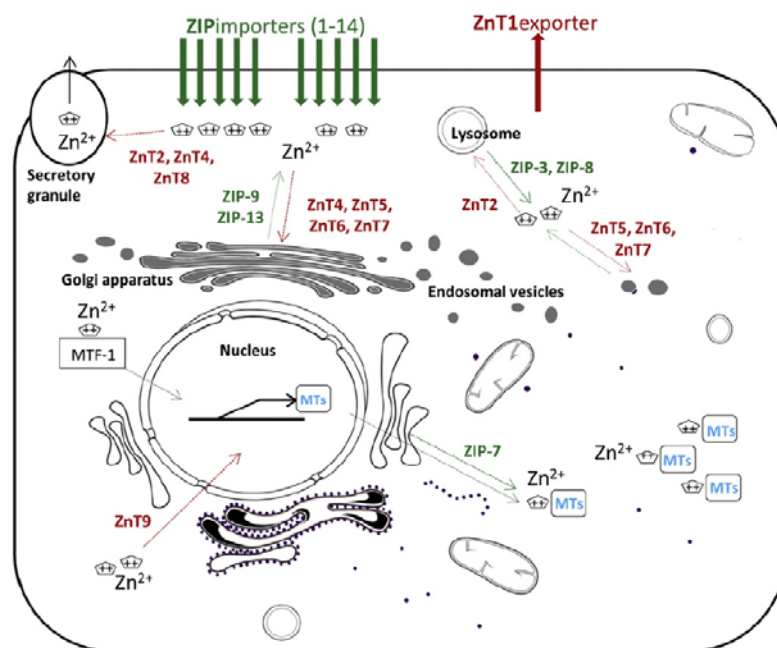


Figure 1.2. Subcellular localization of human ZIP/ZnT Zn transporters and of Zn homeostasis regulators. Directions of Zn transport are indicated with arrows. Green arrows indicate Zn entry in the cytoplasmic space (from extracellular space or from organelles) mediated by ZIP importers (depicted in green) and red arrows indicate Zn exit from the cytoplasmic space (to extracellular space or to organelles) mediated by ZnT exporters (depicted in red). MTF-1 accumulates in the nucleus and binds to DNA for the transcription of MTs (depicted in blue), necessary for Zn homeostasis in the cell. Note that this figure only provides a very simplified view of a general cell type, as expression of some ZIP/ZnT proteins are tissue- or cell type-specific and regulated by Zn and other metal status. Figure from [11].

ZnT transporters are responsible for efflux of zinc from the cytosol to the extracellular space or intracellular compartments. The mammalian ZnT transporters

belong to a superfamily of CDF transporters that also includes transporters of similar topology among bacteria, fungi, nematodes, insects, plants, and other mammals [25]. The CDF transporter proteins can be further classified into three groups based on their phylogenetic relationships (Zn-CDF, Zn/Fe-CDF and Mn-CDF) with ZnT proteins belonging to the Zn-CDF group [26].

The expression of ZnT protein is regulated at the level of transcription and also posttranslationally during differentiation [27], development [28], aging [29] [29], and in various pathological conditions [30, 31]. The regulation occurs in response to numerous stimuli, such as inflammation [32], lipopolysaccharides (LPS) [33], essential nutrients [34], glucose [35], hormones [36] and injury [37]. Zinc concentration can also be regulatory in a cell- or tissue-specific manner [17, 21, 38].

ZnT transporters, with an exception of heterodimeric ZnT5 and ZnT6 [39], form homodimers and are predicted to have six TMDs (except for ZnT5) and the N- and C-terminal domains facing toward the cytosol [40, 41]. This general topology of ZnTs has been suggested based largely on the X-ray crystal structure of a bacterial homolog and CDF transporter YiiP [42, 43].

The crystal structures revealed that YiiP exists as a homodimer in which each monomer binds four zinc ions at three zinc binding sites, A, B, and C [42, 43]. The monomers are noncovalently associated via a charge ring of two Lys-Asp pairs, which are thought to form a pivot for transmitting structural changes from the cytoplasmic to the

transmembrane (TM) domains. The intramembranous zinc-binding site A was found to be the primary zinc transport site and is formed by four conserved hydrophilic residues: three aspartic acid residues and one histidine residue in TMDs II and V. Site B resides at the interface between the TMDs and the C-terminal domain. Site C, capable of binding two zinc ions, is located in the C-terminal domain possessing a metallochaperone-like structure with an $\alpha\beta\alpha$ fold yet lacking sequence similarity to any known metallochaperone (Figure 1.3) [42].

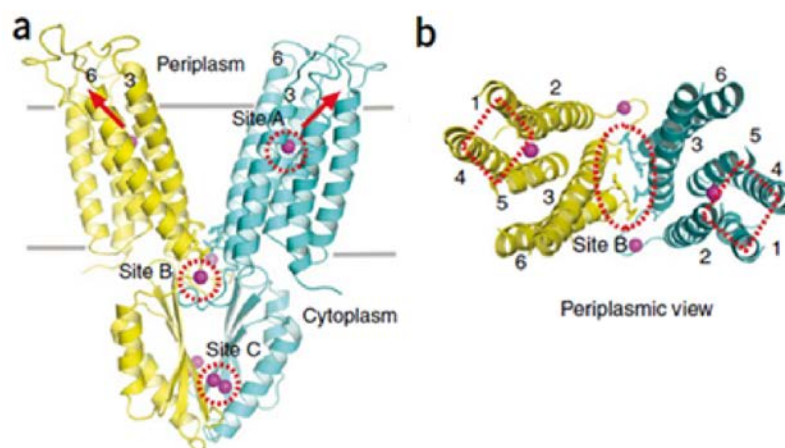


Figure 1.3. YiiP structure and helix packing in the TMD. (A) Ribbon representation of the YiiP homodimer (yellow and cyan for each protomer) viewed from the membrane plane. Magenta spheres represent bound zinc ions in zinc-binding sites, which are marked by red circles. Grey lines indicate the possible membrane boundaries. Red arrows indicate the directions of Zn²⁺ exit from the two active sites. Conserved hydrophobic residues involved in the TMD-TMD contacts are shown as sticks. (B) The YiiP homodimer viewed from the periplasm with the extracellular loops and the CTD removed for clarity. The red oval marks hydrophobic interactions at the TMD-TMD interface, and red diamonds highlight the four-helix bundles. Figure from [42].

ZnT proteins are thus predicted to have an intramembranous zinc-binding site that consists of four highly conserved hydrophilic residues (two histidines and two aspartic acids in most ZnTs) in TMDs II and V. These conserved residues grant ZnTs with high

selectivity for Zn^{2+} ions as opposed to YiiP, which acts as a Cd^{2+}/Zn^{2+} transporter as a result of a different set of amino acids in binding site A [41]. Mutations in the conserved histidine and aspartic acid residues were found to abolish zinc transport activity [44]. Both sites A and C are highly conserved among ZnT transporters. Coordination of zinc ions at the intramembranous zinc-binding site (site A) is thought to be allosterically modulated by binding of zinc to the C-terminal binuclear zinc-binding site (site C) exposed to the cytosol [41-43]. This regulatory role of the C-terminal domain was not supported by the electron crystallography study of YiiP [45].

ZnT proteins usually have long C-terminal domains – the longest belongs to ZnT6 (203 aa) and the shortest to ZnT7 (82 aa) – which are thought to be critical for the regulation of protein dimerization. Supporting evidence comes from the C-terminal deletions of ZnT1 and ZnT5 which result in proteins that are cytotoxic [39, 46], likely due to deposits of nonfunctional protein aggregates. X-ray crystallography analysis of the C-terminal domain from two other bacterial ZnT homologs showed the structure of this domain to be highly conserved, despite a substantial degree of sequence variability, and able to form a stable dimer [47, 48]. The C-terminal region is also important for mediating protein–protein interactions, for example between the ZnT1 and the protein kinase Raf-1 [49].

The length and the sequence of N-terminal domain, which usually contains subcellular targeting signals, differ largely among ZnT proteins. ZnTs also contain a

cytoplasmic histidine-rich loop between TMDs IV and V, not present in the bacterial homolog YiiP. This loop was proposed to function as a determinant of zinc selectivity, a sensor of the cytosolic zinc levels, and a modulator of zinc transport activity [50, 51].

Studies performed on bacterial, yeast, and plant zinc transporters have demonstrated that an electrochemical gradient generated by ATPases is required for $\text{Zn}^{2+}/\text{H}^+$ exchange [52-54] and it seems likely that the mammalian ZnTs use a similar mechanism. It has been shown, using fluorescence-based functional measurements, that the sequestration of cytoplasmic zinc into the Golgi apparatus by ZnT5 is powered by the vesicular electrochemical H^+ gradient generated by V-type ATPases [44].

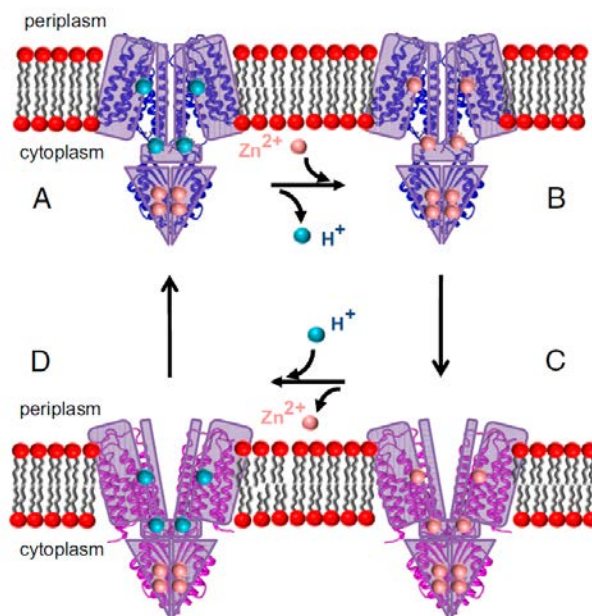


Figure 1.4. Alternating access mechanism for $\text{Zn}^{2+}/\text{H}^+$ antiport by YiiP. This mechanism involves inward-facing (A and B) and outward-facing (C and D) conformations, both of which are able to bind Zn^{2+} or H^+ . The proton motive force provides a driving force for exporting Zn^{2+} from the cytoplasm. The conformation in (A) corresponds to that observed in the helical tubes, whereas the conformation in (C) corresponds to the X-ray structure solved in the presence of Zn^{2+} . Figure from [45].

An alternating access mechanism for $\text{Zn}^{2+}/\text{H}^{+}$ antiport has been proposed based on the available high-resolution 4.1 Å electron crystallography [55] and 2.9 Å X-ray crystallography [42] structures of bacterial YiiP (Figure 1.4). Whereas the X-ray structure represents an outward-facing conformation, a structure determined by electron microscopy (EM) of protein incorporated into helical, lipid nanotubes is consistent with an inward-facing conformation [45]. The stoichiometry of this $\text{Zn}^{2+}/\text{H}^{+}$ exchange was calculated to be 1:1 using proteoliposomes with reconstituted bacterial ZitB [56].

Except for YiiP, only one structure of a zinc transporter has been published. Instead of being a ZnT8 homolog, bacterial ZitB belongs to CorA metal ion transporter (MIT) family. [57]. Structural characterization in a Zn^{2+} -free state via single-particle cryoEM yielded a 4.2 Å map and the resulting structure (pdb:5N9Y) reveals a pentameric transporter, with each 34 kDa monomer consisting of two TM domains and one large cytoplasmic N-terminal domain with $\alpha\beta\alpha$ motif (Figure 1.5) [57]. Both the oligomeric state and the architecture of the domains are thus radically different from those in YiiP [42, 45]. Isothermal titration calorimetry (ITC) experiments coupled with a fluorescent assay in liposomes has shown ZitB to be able to bind Zn^{2+} , Cd^{2+} and Ni^{2+} and transport them across the membrane [57]. A similar metal transport capability has been demonstrated for YiiP which can carry both Zn^{2+} and Cd^{2+} across the membrane [58, 59], with ZnT8 being selective towards Zn^{2+} transport [41]. ZitB-mediated Zn^{2+} transport was found to be stimulated by pH gradient in radioactive and fluorescent transport assays in liposomes. Zn^{2+} uptake into the lumen of liposomes was enhanced by an inward pH gradient,

suggesting that ZitB operates as a co-transporter [57]. In comparison, YiiP utilizes a $\text{Zn}^{2+}/\text{H}^{+}$ antiport alternating access mechanism [45, 60], likely to also operate in ZnT8 [44]. The coupled $\text{Zn}^{2+}/\text{H}^{+}$ co-transport in ZitB is indicative that this protein is an importer of Zn^{2+} rather than an exporter, unlike Zn^{2+} -efflux proteins YiiP and ZnT8 [57].

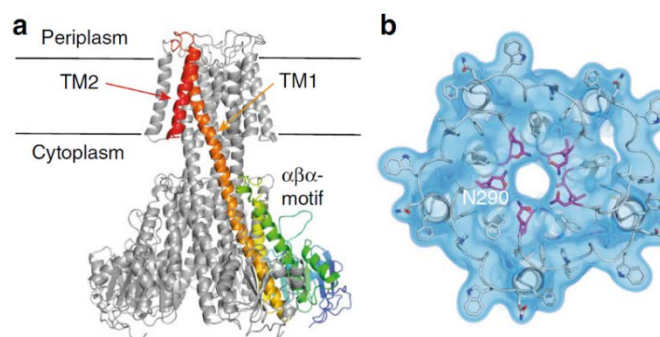


Figure 1.5. The structure of the full-length ZntB. (A) Side view, four subunits of ZntB pentamer are coloured grey, and one is coloured rainbow from blue (N-terminus) to red (C-terminus); the position of the membrane is indicated, trans membrane helices 1 and 2 as well as $\alpha\beta$ -motif are labelled. (B) Top view (from periplasm) onto ZntB—10 trans membrane helices are arranged cylindrically, with TM2 ring at the periphery. Experimental density is contoured in blue. The connecting loops provide residues for the selectivity filter (in magenta). Figure from [57].

1.1.3 ZnT8: structure and function. ZnT8 is a member of ZnT mammalian zinc transporters belonging to a cation diffusion facilitator (CDF) superfamily of heavy metal transporters [26]. ZnTs could be classified into the Zn-CDF subgroup (CDF proteins transporting zinc) and there ZnT8 is clustered together with ZnT2, ZnT3 and ZnT4 based on their sequence similarity [26, 61]. All of these proteins play roles in secretory pathways, providing zinc for lysosomes (ZnT2), synaptic vesicles (ZnT3), endosomes (ZnT4), and secretory granules (ZnT8), respectively [62].

The structure of ZnT8 remains unknown, although the crystallographic analyses of the distantly related bacterial homolog YiiP (17% sequence identity over 290 of 369 aa in ZnT8) belonging to *E. coli* group II transporters FieF (ferrous iron efflux) provided insight into both structure and function of mammalian zinc transporters [42, 43, 45]. Like other ZnTs, ZnT8 is predicted to have six transmembrane helices, an N- and C-terminal domains facing the cytosol [63] and to function as a homodimer of 40 kDa subunits [64, 65]. Key residues regulating metal ion specificity are located in TMDs II and V [66].

ZnT8 has several unique features not present in YiiP, including 49 additional residues in its N-terminal domain and an extended C-tail, as well as a cytoplasmic His-rich loop and pairs of histidine and aspartic residues in TM domains 2 and 5. These two pairs of amino acids form one of the zinc binding sites, mediating Zn²⁺ transport and selecting against Cd²⁺, making it unique in the ZnT family [66]. The His-rich loop is essential for Zn²⁺ transport activity and is proposed to modulate this function by acting as a zinc sensor at the cytoplasmic surface [40, 53] in cooperation with the TM and C-terminal domains [1]. Two groups have developed models of ZnT8 [64, 67] based upon its homology to YiiP which models support the proposed ZnT8 topology. The potential effect of substitutions at position 325, a key ZnT8 residue linked to type 2 diabetes (T2D), was proposed to likely impact key Zn²⁺ binding sites [64], or be unable to influence ZnT8 metal ion-sensing capacity [67].

Up until recently, the functional studies of ZnT8 have been indirect and based on measurements in overexpressing or knockdown cells [63, 64, 66, 68, 69] and could not accurately measure kinetic parameters. They have nonetheless shown that ZnT8 is a zinc transporter with specificity for Zn^{2+} but not Cd^{2+} , unlike its well-known homolog YiiP [66]. The newest 2016 study performed on HEK293 cell-purified, liposome-reconstituted ZnT8 has found the high T2D risk Arg-325 variant to be consistently more active than the Trp-325 variant in a broad range of lipid conditions tested (Figure 1.6) [70]. This finding remains in agreement with the genetic data showing that rare loss-of-function mutations in ZnT8 are associated with reduced T2D risk [71].

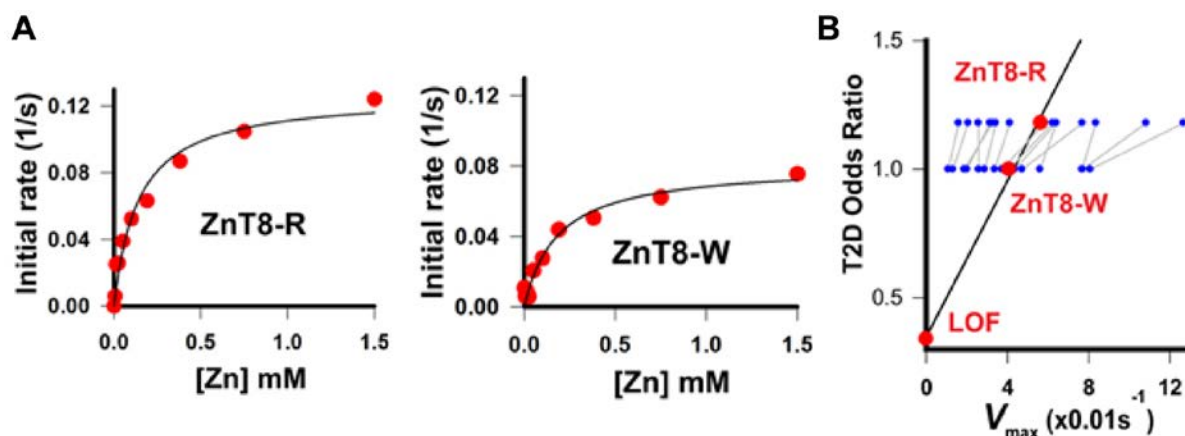


Figure 1.6. Zinc transport activities and their correlations with T2D risk. (A) Steady-state kinetics of ZnT8 variants. The initial rates were calculated using stopped-flow traces obtained from samples with ZnT8 variants in responses to 1:1 mixing with a sequence of zinc concentrations from 0 to 3mM. The solid lines represent least squares fitting of the initial rate as a function of zinc concentration. (B) activity-risk plot reveals a linear relationship between ZnT8 activity and T2D risk. Blue filled circles represent individual V_{max} values measured under different lipid conditions, and gray lines connect pairs of polymorphic ZnT8 variants under identical lipid conditions. Red filled circles represent mean V_{max} versus published T2D odds ratios. Mean V_{max} for ZnT8-R or ZnT8-W is calculated by averaging V_{max} over all tested lipid conditions shown in blue-filled circles. Mean V_{max} for LOF ZnT8 mutants is set to zero. The black line is a linear regression of three red data points. Figure from [70].

ZnT8, the product of the SLC30A8 gene located on chromosome 8 at position 8q24.11, expressed mainly in the endocrine pancreas, is the most abundant ZnT transcript in pancreatic β cells. Both SLC30A8 mRNA and ZnT8 protein levels are highly enriched in β cells and also present in α cells, however at significantly lower levels [72-75]. It has been shown that this specific expression in pancreatic β cells is associated with the expression of a pancreatic β -cell restricted transcription factor Pdx-1 [76, 77]. ZnT8 is also expressed in some extra-pancreatic sites such as retinal pigment epithelium [78] and several layers of the retina [79]. SLC30A8 mRNA has been detected in human adipocytes [80] and lymphocytes [81], evidence of ZnT8 protein expression was not found, however.

The SLC30A8 gene is processed to generate five primary transcripts, at least two of which are co-expressed in β cells and potentially encode different ZnT8 isoforms [74]. The longest open reading frame (ORF), derived from transcript 1, encodes a 369 aa integral membrane protein and transcript 3 generates a truncated product of 320 aa derived from an alternative start site.

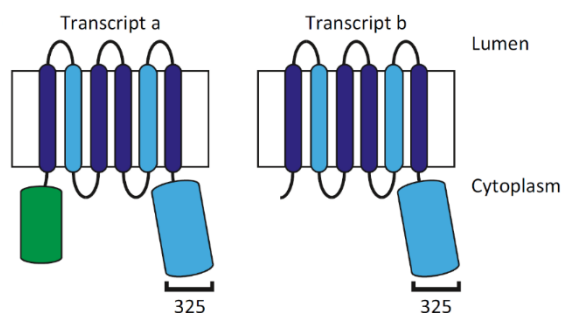


Figure 1.7. The domain structures of the two ZnT8 isoforms. The light-blue shapes indicate domains implicated in Zn^{2+} binding, and the bracket the approximate location of the polymorphic residue 325. Figure from [82].

This truncated ZnT8 isoform lacks most of the N-terminal cytoplasmic domain which domain is lacking in the majority of nonmammalian homologs (Figure 1.7) [26].

Zinc deficiency, glucose and cytokine treatments have all been reported to decrease SLC30A8 gene expression in mouse and rat islet-derived cell lines [35, 83]. These factors might also regulate ZnT8 expression in humans although cytokine treatments had little effect on SLC30A8 transcript levels in cultured human islets [74].

Pancreatic β cells synthesize and secrete insulin, a hormone that regulates glucose homeostasis by promoting glucose uptake from the circulation [84]. Insulin is synthesized as the precursor preproinsulin that is processed to create proinsulin and subsequently insulin. The conversion of proinsulin to insulin starts in the Golgi apparatus and continues after secretory vesicles bud off from it and transport the hormone towards the plasma membrane [85]. One characteristic feature of pancreatic β cells is exceptionally high zinc content [86]. During insulin maturation, both proinsulin and insulin combine with Zn^{2+} in secretory vesicles thus forming crystalline structures for storage and secretion [87]. These crystalline structures are insoluble hexamers in which six insulin molecules are complexed with two Zn^{2+} ions and one Ca^{2+} ion (Figure 1.8A) [87, 88]. The highest levels of zinc in β cells (10 - 20 mM) are found in those insulin secretory vesicles which can store up to 70 % of the total β cell Zn^{2+} [89]. The very high level of zinc accumulation is achieved with ZnT8 which transports zinc from the cytoplasm into insulin-containing vesicles [90] in

exchange for protons translocated by the vesicular proton pump [43, 91], thus providing Zn^{2+} for insulin maturation, storage and subsequent secretion (Figure 1.8B) [63, 92].

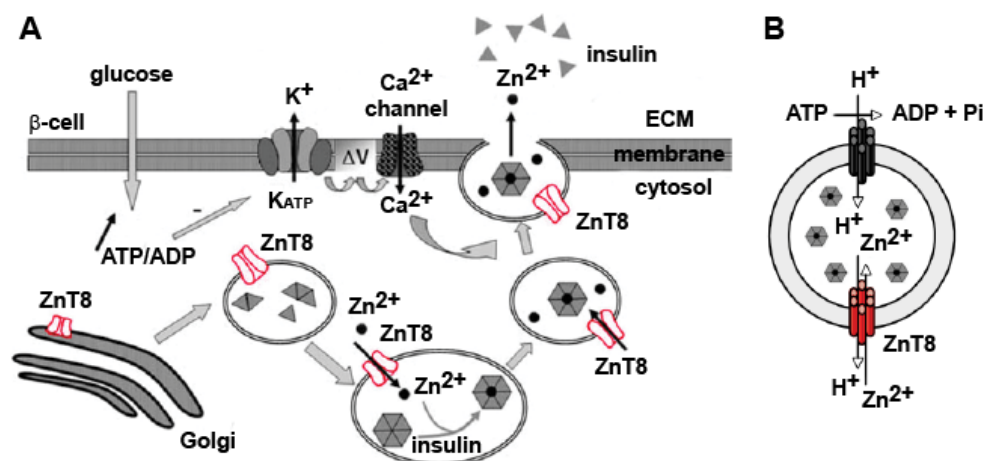


Figure 1.8. Role of ZnT8 (red) in the storage and secretion of insulin. (A) ZnT8 assembles in the ER and traffics to insulin secretory vesicles where it mediates the transport of Zn^{2+} to form stable insulin hexamers. Glucose-induced plasma membrane depolarization opens voltage-sensitive Ca^{2+} channels, which increases cytoplasmic $[Ca^{2+}]$ that triggers fusion of insulin vesicles to the plasma membrane and releases of insulin. Adapted from [92]. (B) Within insulin secretory vesicles, ZnT8 uses the proton gradient generated by the ATPase to exchange two H^{+} ions for a single Zn^{2+} ion. Figure adapted from [93].

At steady-state in human β cells, ZnT8 shows a high degree of colocalization with insulin [64, 94]. This overlap appears incomplete [63], suggesting that ZnT8 may also traffic to other intracellular compartments. At rest, β cell cytoplasmic free Zn^{2+} is estimated to be approximately 400 - 450 pM [95]. Since Zn^{2+} in secretory vesicles exchanges with Zn^{2+} in the cytosol at a slow pace [96], an internal release of Zn^{2+} from the vesicles is not likely to account for the observed increases in cytosolic Zn^{2+} during glucose-stimulated insulin secretion [95, 97]. During exocytosis, the increase in pH from 5.5 in vesicles to 7.4 in blood destabilizes insulin crystals, releasing the hormone, free Zn^{2+} and Ca^{2+} , thus a reuptake of free Zn^{2+} could contribute to the increases in cytosolic Zn^{2+} .

Zn²⁺, co-secreted with insulin during exocytosis, might act in a paracrine manner to regulate glucagon secretion from α cells [98, 99] but may also act in an autocrine fashion to potentiate glucose-stimulated insulin secretion [100]. Fluorescent antibody binding to the extracellular surface of rat insulinoma cells and flow cytometry analysis revealed strong correlation among levels of ZnT8 expression, its display on cell surface and glucose-stimulated insulin secretion (GSIS). Glucose stimulation increased the surface display of endogenous ZnT8, thus providing evidence for a GSIS-dependent exposure of the ZnT8 self-antigen [101].

1.1.4 ZnT8: functional insight from mouse models. The role of ZnT8 in vivo has been investigated by six studies that examined the effect of either global [64, 94, 102, 103] or β cell specific [104, 105] deletion of the SLC30A8 gene in mice (ZnT8 knockout (KO) mice). There were usually no changes in islet insulin content [64, 94, 102-104] or in islet size, numbers, or cell composition [64, 94, 104, 105]. Noticeable changes in the appearance of insulin secretory granules were observed [64, 102, 104, 105] as well as a clear decrease in islet zinc content [64, 94, 103, 105].

There was no agreement in between the studies with respect to the effect of Slc30a8 deletion on glucose-stimulated insulin secretion (GSIS) from isolated islets. Two studies reported no effect of Slc30a8 deletion on GSIS [102, 103], two report impaired GSIS [94, 105], and two reported increased GSIS [64, 104]. It has been proposed that the increase in GSIS in islets could be explained by the reported inhibitory effect of zinc on

insulin secretion [104]. Apart from its role in insulin storage and maturation, Zn^{2+} is an essential cofactor for many components of the proinsulin processing machinery [106] including carboxypeptidase E (CPE) [107] which loss of CPE activity reduces the overall rate of conversion of proinsulin to insulin [108]. Consequently, ZnT8 may play a larger role in sorting proinsulin into the regulated secretory pathway and regulating the activity of enzymes involved in insulin processing such as prohormone convertase (PC)1/3, PC2, or carboxypeptidase E (CPE).

The effect on proinsulin levels and processing has been examined. Two studies reported no effect on proinsulin processing [64, 102], two studies reported a small increase in plasma proinsulin [104, 105] and one group reported a rather unexpected decrease in plasma proinsulin levels [103]. The conclusion is that, at least in mice, the lack of SLC30A8 gene and its product has only a minor effect on proinsulin processing despite profound changes in insulin secretory vesicle morphology [64, 105].

All research groups have found that SLC30A8 deletion does not affect body weight in mice on standard diet with no observed changes in insulin sensitivity [64, 94, 102-105]. Most of the studies reported no change in fasting blood glucose (FBG) [94, 102-105] and some reported no change in fasting insulin [103-105]. An impaired glucose tolerance has been observed by most groups during intraperitoneal glucose tolerance tests (IPGTTs) in young mice, but rarely in older mice [64, 94, 102-104].

Some studies have looked into the effect of high-fat diet (HFD) with an expectation that the additional insulin secretory demand imposed by HFD-induced insulin resistance might unravel a clear phenotype in SLC30A8 knockout mice [109]. Two studies reported no difference in glucose tolerance relative to wild type (WT) mice following HFD in both global and β cell specific KO mice [103, 104]. One study reported little effect in global KO mice on glucose tolerance [102]. Two research groups reported that global KO mice (but not β cell specific KO mice) gained more weight than WT mice on HFD and had higher fasting insulin levels [64, 110]. Interestingly, in humans SLC30A8 is preferentially associated with T2D in lean and not obese individuals [111]. One group reported that the lack of expression of ZnT8 affects insulin clearance by the liver (enhanced insulin clearance). The authors hypothesized that the absence of ZnT8 has a dual effect, promoting GSIS and hepatic insulin clearance, both of which are mediated via the absence of zinc. It was demonstrated that the ZnT8 single nucleotide polymorphism (SNP), encoding a T2D risk-bearing C allele in position 325 aa, is associated with altered insulin clearance in humans [104].

The different results observed between the six KO mouse studies may mean that other factors influence the effect of SLC30A8 gene deletion. Environmental differences are a possibility [112] as well as SLC30A8 expression in tissues other than endocrine pancreas since phenotypes of mice with global and β cell specific deletion differ [103, 104]. In summary, the studies have shown that, at least in mice, the effects of SLC30A8 deletion are modest, especially given the dramatic decrease in free Zn^{2+} levels in KO islets.

The implication is that a) low levels of zinc are sufficient for proper insulin secretion and b) Zn^{2+} accumulation in insulin secretory vesicles is not as important for insulin secretion as had been believed.

1.1.5 ZnT8: role in disease. Diabetes is a chronic disease that damages the heart, blood vessels, eyes, kidneys, and nerves. It is a major cause of mortality and morbidity worldwide, affecting over 340 million people worldwide [113]. In 2012, 29.1 million people had diabetes mellitus, or 9.3 % of the U.S. population [114]. Diabetes greatly increases the incidence of cardiovascular disease [115], including coronary artery disease (CAD), stroke, peripheral arterial disease, cardiomyopathy, and congestive heart failure [116]. Microvascular complications of diabetes also result in end-organ damage such as nephropathy, neuropathy, and retinopathy [117, 118]. Ultimately, this disease doubles an individual's risk of death compared to others in the same age group and is estimated to cost \$245 billion per year for medical care, lost work, and disability [114].

Ninety percent of people with diabetes are diagnosed as T2D, previously referred to as "adult-onset diabetes". It is a progressive disorder characterized by loss of glycemic control and metabolic homeostasis through deterioration of pancreatic β cell function, and insulin resistance. As the disease progresses a lack of insulin may also develop. Hereditary factors and lifestyle (namely, excessive body weight and lack of exercise) play an important role in determining T2D risk.

High interest in ZnT8 as a potential target for drug development and therapeutic interventions began in 2007 when genome wide association studies identified a major nonsynonymous SNP in the SLC30A8/ZnT8 gene as a risk factor for T2D [119-122]. The frequency of this SLC30A8 rs13266634 risk C allele, encoding Arg325, was higher in T2D patients than in healthy controls with an estimated 14 % increased risk [123]. SLC30A8 Exon 13, which encodes the final 52 amino acids was reported to contain 6 SNPs, two of which cause amino acid changes at position 325, from an Arg to a Trp (rs13266634) or Gln (rs16889462) respectively. The predominant residue Arg increases this risk, whereas the less common Trp and Asn residue substitutions lower this risk. The risk allele, encoding R325, is a major allele among most ethnic groups studied. Frequency of this allele in Africans and their descendants is the highest (92 – 99 %) [124] followed by Hispanic Americans at 95 % [125] and European Caucasians and Asians at 80 – 90 % [126]. In addition, the expressivity of the risk of the R325 allele of SLC30A8 for T2D varies among ethnic groups.

The main question was the mechanism responsible for the association of SLC30A8 SNP encoding R325 variant of ZnT8 to T2D and it was assumed that it directly influences ZnT8 ability to transport zinc.

The ZnT8 risk allele R325 variant has shown lower apparent zinc transport activity than the W325 variant [64] and it has been associated with an increase in the ratio of circulating proinsulin-to-insulin [127, 128], a reduced first-phase insulin release [129], a

decrease in the response to insulin [21] and an imbalance of Zn^{2+} between secretory vesicles and the cytosol [17]. It has been shown that zinc co-secreted with insulin from pancreatic β cells can block insulin clearance by hepatocytes and that humans carrying the risk allele R325 exhibit increased insulin clearance [104] which may explain how the ZnT8 R325 relates to the increased risk of T2D.

The potential role of ZnT8 in pathology of T2D became even more complicated as a set of 12 rare loss-of-function ZnT8 mutants has been described that collectively are associated with a 65 % decrease in T2D risk [71]. These frameshift or premature termination mutants actually decrease the risk of diabetes, suggesting that ZnT8 inhibitors could have a therapeutic role in diabetes treatment [71]. The effects of haploinsufficiency associated with marked decreased T2D risk [71] suggested that a more complex mechanism than what had been initially thought may be responsible for the observed SLC30A8/T2D association, e.g. different turnover rates for W325 and R325 variants or different trafficking within the cell. One study has shown that the most dramatic difference between the R325 and W325 variants was seen with respect to cytoplasmic accumulation of zinc suggesting that ZnT8 can operate bidirectionally and mediate uptake across the plasma membrane [64]. The W325 variant might exhibit greater activity at the plasma membrane than the R325 variant, but it was not clear how that could protect against T2D. It might be that the earlier focus on the major (increased T2D risk, R325), rather than the minor (lower T2D risk, W325), rs13266634 allele may have been misleading [71] as extrapolation of the data from genome wide association studies

in humans led to the anticipation that a complete loss of ZnT8 would be deleterious, leading to the development of T2D. Some data from mice models showed decreased GSIS, decreased fasting insulin, and normal glucose tolerance, suggesting improved rather than impaired glucose homeostasis [75], and are thus more consistent with the notion that decreased ZnT8 expression is protective against T2D. It is still unknown how the rare loss-of-function variants and the common rs13266634- encoded Trp variant, which has increased rather than decreased transporter activity [64, 68], can share a common phenotype (reduced risk of T2D) and whether they have distinct mechanisms of action.

Loss of the insulin-producing pancreatic β cells, leading to insulin deficiency is a cause of T1D, previously referred to as “juvenile diabetes”, affecting ten percent of people diagnosed with diabetes in North America and Europe. T1D can be classified as immune-mediated or idiopathic with the majority belonging to the former class where a T cell-mediated autoimmune attack leads to the loss of β cells and, in consequence, insulin.

In addition to its prominent role in T2D, ZnT8 has also received a lot of attention as an autoimmune marker of T1DM. Autoantibodies against ZnT8 are detected in approximately 60 – 80 % of patients at the onset of childhood T1D and adult-onset autoimmune diabetes [130, 131], with a similar prevalence to those against the standard T1D autoantigens such as proinsulin, the 65 kDa form of glutamic acid decarboxylase (GAD65), and insulinoma-associated protein 2 (IA-2) [132]. Being able to measure the autoantibodies against ZnT8 along with other major autoantigens enhances the detection

rate of diabetes-related autoimmunity [132, 133] since autoantibodies against ZnT8 overlap with the other biomarkers, but are independent of them.

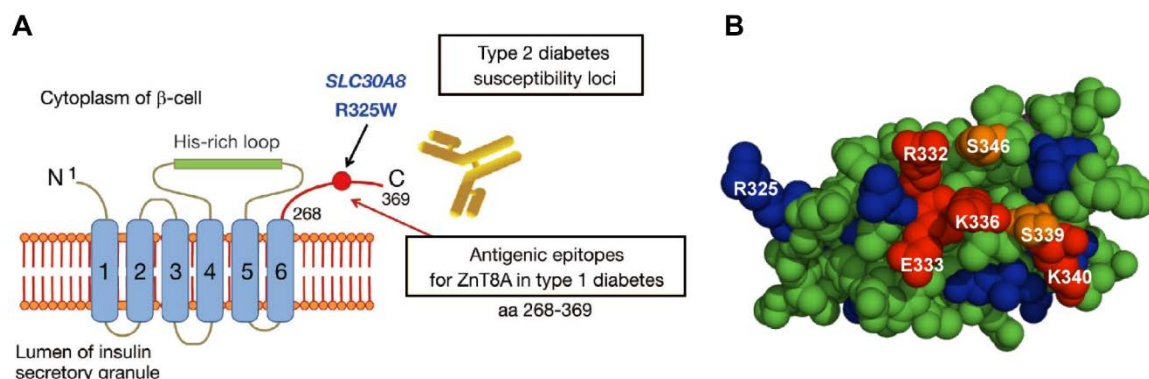


Figure 1.9. Dual role of ZnT8 in diabetes. (A) Recent genome-wide association studies analyzing the susceptible/protective loci for type 2 diabetes revealed that a nonsynonymous single nucleotide polymorphism (SNP) in SLC30A8 (rs13266634 C>T) which changes from arginine (R) to tryptophan (W) at position 325 is associated with type 2 diabetes. Furthermore, major epitope(s) for ZnT8A lie within the cytoplasmic domain of the molecule (aa 268-369) and R325W is a key determinant of humoral autoreactivity to this protein. Figure from [134]. (B) Residues 268–357 of human ZnT8(R325) were modelled based on the X-ray crystal structure of *Escherichia coli* YiiP (PDB:2QFI). Residues that vary between human and mouse are shown in red (contributing) or blue (non-contributing). Two conserved serines that might also contribute to the epitope are shown in orange. Figure from [135].

Approximately 80 % of ZnT8 autoantibodies react with the epitopes that reside in the C-terminal 102 amino acids of the ZnT8 protein [130, 136]. Epitope mapping indicates that more than one epitope in the C-terminal end of ZnT8 is involved in autoimmunity [130]. The nonsynonymous SNP in SLC30A8 gene, described above in its role as a risk allele for T2D, has been shown to also be a key determinant in humoral autoreactivity to ZnT8 [137, 138] with close to two-thirds of ZnT8 antibodies isolated from newly diagnosed T1D patients reacting with the R325 variant of ZnT8 (Figure 1.9) [130]. ZnT8 autoantibodies

that recognize the R325 variant show high specificity and affinity in islet autoimmunity [130]. One study has found that ZnT8 is a T-cell target in T1D [132].

1.2 Gap junction channel Connexin26 and pH

1.2.1 Connexin topology. Connexins (Cx) are a family of integral, vertebrate membrane proteins. There currently are 21 members of this family that can be found in humans, categorized based on their sequence homology into α , β and γ isoforms. All connexin isoforms share a common topology with four α -helical transmembrane (TM) domains (M1-M4), two extracellular loops (E1 and E2), a cytoplasmic (CL) M2–M3 loop and cytoplasmic N- and C-terminal domains (NT and CT) (Figure 1.10A). The membrane-spanning M1-M4 and extracellular E1 and E2 domains are the most conserved among connexins whereas the primary amino acid sequences of cytoplasmic CL, NT and CT are highly variable [139-141]. C-terminal domain varies greatly in length in different Cx isoforms and was shown to regulate Cx function [139, 140, 142-144]. The domains on the cytoplasmic surface are flexible, as assessed by AFM and electron microscopy studies [145-151] and are crucial for proper gating [141].

Connexin monomers form a hexameric connexon (hemichannel) and those in turn can form a dodecameric gap junction channel (GJC) by end-to-end docking of two hemichannels (HCs) from adjacent cells (Figure 1.10B and C). Two extracellular loops E1 and E2, containing intramolecular disulfide bonds, contribute to the formation of the

extracellular domain interface which mediates docking between HCs [152, 153]. Connexins can assemble to form either homomeric or heteromeric HCs and, subsequently, GJCs. GJCs and HCs composed of different connexin isoforms differ in terms of their solute permeabilities, voltage and chemical gating and interaction with regulatory proteins [139, 140, 154-157].

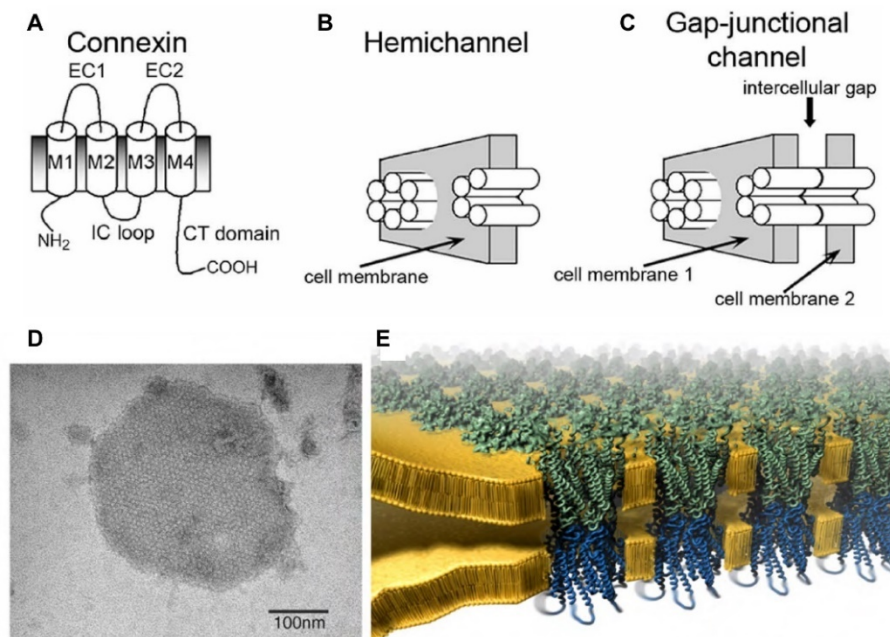


Figure 1.10. Connexin topology. (A) Representation of a connexin subunit, (B) a hexameric hemichannel (HC) and (C) a dodecameric gap junction channel (GJC). M1-M4: trans-membrane helices; EC1 and EC2: extracellular loops; IC loop: intracellular loop. Figure adapted from [158]. (D) Electron micrograph of the Cx26 gap junction prepared from the baculovirus/Sf9 expression system. Each particle is circular and is arranged in a hexagonal lattice with a size of ~ 90 Å. (E) Schematic drawing of the gap junction. The gap junction channels are drawn as a C α trace spanning two adjoining membranes with an inter-membrane space of 40 Å. Figure from [159].

GJCs are aqueous channels which allow a passage of solutes between the cytoplasm of adjacent cells. They can cluster to form quasi-hexagonal arrays of gap junction channel called plaques in the membrane [160] which enabled low-resolution

electron microscopy studies (Figure 1.10D and E) [161]. HCs serve a role in communication between the cytoplasm and the extracellular milieu thus are tightly regulated and may function independently from GJs [162]. Electron cryomicroscopy (cryoEM) studies of two-dimensional crystals of C-terminal truncated Cx43 GJs from cultured mammalian cells [163, 164] revealed that each hemichannel is comprised of 24 TM α -helices thus resulting in a model of hexameric HCs and dodecameric GJs [147, 148].

1.2.2 Connexin function. Gap-junctions are aqueous channels that are responsible for intercellular communication in eukaryotic cells [140, 154, 155]. They enable direct cell-to-cell exchange of small molecules such as hydrated ions (e.g. Ca^{2+}), second messengers (e.g., cAMP, IP3), intracellular metabolites (e.g., glucose, ATP) and small peptides [154, 165-172]. This permeation – diffusion with the concentration gradient - is limited by the construction of the channel pore with a molecular weight (Mw) cutoff at $\sim 1,000$ Da and a size limit of up to ~ 14 Å (Figure 1.11A) [155, 173-175].

GJs and HCs have highly variable selectivities depending on connexin isoforms forming a given channel or hemichannel which accounts for diverse and specialized functions of connexins [154, 172]. GJs and HCs exhibit moderate to substantial charge preferences and display distinct permeabilities to molecules of similar properties such as inositol triphosphate (IP3) isomers and cAMP/cGMP [176-178] which cannot be predicted from the pore size alone (Figure 1.11B).

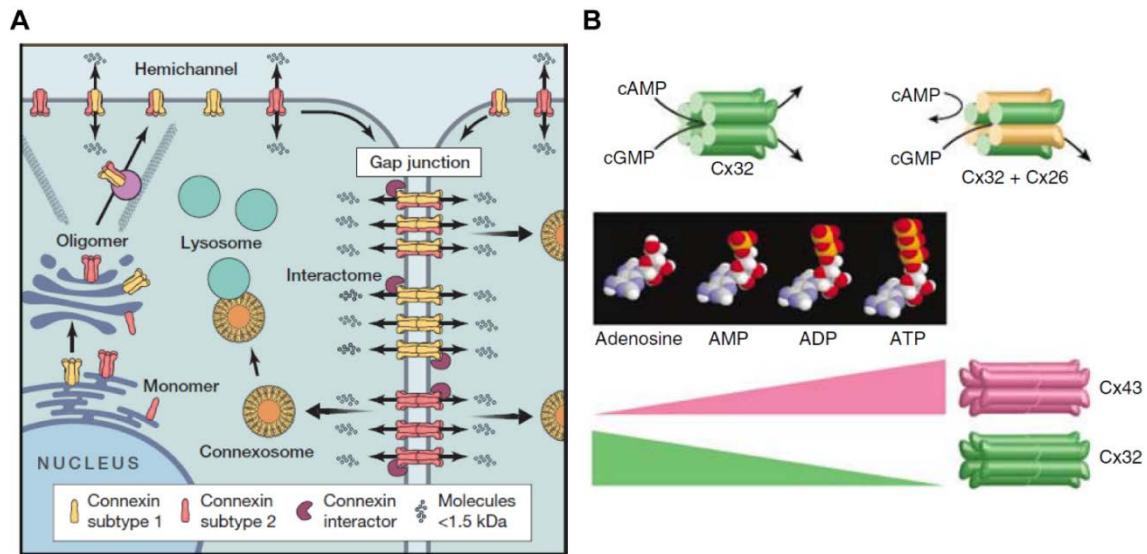


Figure 1.11. Life cycle of connexins in the cell and their selective permeability. (A) Connexins are integral membrane proteins that oligomerize into homomeric or heteromeric hexamers (also called connexons) in the endoplasmic reticulum or Golgi apparatus. Upon microtubule-dependent transport to the cell surface, connexons may function as hemichannels or quickly dock with connexons from an opposing cell to assemble a gap junction channel. Connexons sequester into tightly packed structures termed gap junctions, which may be composed of a single or multiple connexin types. The connexin interactome that consists of dozens of binding proteins has been shown to play critical roles in gap junction assembly, stability, channel regulation, and intracellular signaling pathways. During turnover, one of the two contacting cells sharing a gap junction ingests an entire gap junction or gap junction fragments into a unique structure called a connexosome (or annular junction), where they fuse with lysosomes to be degraded. Figure from [179]. (B) Gap junctions are unique in terms of permeability. Cx32 hemichannels were permeable to both cAMP and cGMP whereas Cx26/Cx32 heteromeric hemichannels showed reduced transfer of cAMP but their permeability to cGMP was comparable to that of Cx32 hemichannels. (C) The addition of extra phosphate groups to adenosine changed its relative permeability through gap junctions. Cx32 intercellular channels were more permeable to adenosine than channels formed by Cx43. However, the Cx43 intercellular channels had progressively higher permeability to AMP, ADP, and ATP than those formed by Cx32. Figure from [155].

Gap junction channels remain mostly open in the plasma membrane, mediating chemical coupling between cells as well as connecting cells electrically by generating high conductance ion pathways [180]. GJs are indispensable to the functioning of many

physiological processes [181] including regulation of the heartbeat and heart muscle contraction [182] and communication in vascular endothelial and smooth muscle cells [183]. Hemichannels are mostly in a closed state as a result of exposure to millimolar extracellular Ca^{2+} and cell-negative membrane voltage [184-187]. HCs are involved in numerous biological functions [188, 189] by mediating fluxes of molecules such as ATP [190], NAD^+ [191], glutamate [192] and glutathione [193].

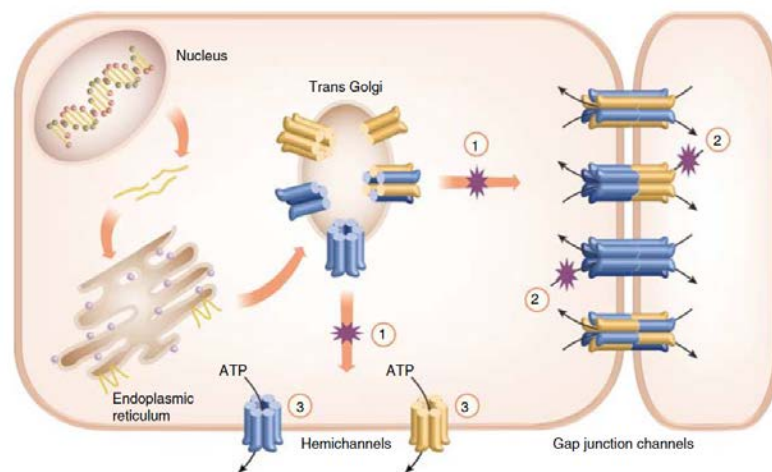


Figure 1.12. Consequences of pathogenic connexin mutations on gap junction biogenesis and function. Pathogenic mutations not only affect gap junction channel formation at different levels from protein translation to assembly of gap junctions but can also alter the channel function. Skin disease-associated connexin mutations have been shown to execute their action through three main mechanisms. They may inhibit protein trafficking to the plasma membrane, thereby impairing connexon/gap junction channel assembly (1). They may exert a dominant-negative action on coexpressed connexins, changing the types of molecules exchanged between the cells (2). Finally, they may result in the production of constitutively active hemichannels (3), leading to the unregulated release of cellular contents into the extracellular space. Figure from [155].

Mutations in connexins have been linked to a wide spectrum of human diseases, including peripheral neuropathies (e.g. Charcot-Marie-Tooth disease) [194], skin disorders [195], syndromic and non-syndromic deafness (e.g. Keratitis-Ichthyosis-

Deafness syndrome) [196, 197], cataracts [198], oculodental dysplasia [199] and developmental abnormalities (Figure 1.12) [156, 200].

1.2.3 Connexin regulation. Gap junction channels and hemichannels require proper and precise regulation as they exert a substantial influence on intracellular communication as well as signaling between the cytoplasm and the cell. One of the main factors influencing channel and hemichannel activity is voltage. Gating by membrane voltage (V_m) was termed V_m gating [201, 202] and gating by transjunctional voltage (V_j), depending on the regulatory mechanism, is referred to as either V_j gating (fast gating) or loop gating (slow gating) [203-206]. A host of other physiological processes and molecules affect GJC and HC activity including pH [154, 207], phosphorylation [183], membrane lipids and membrane-active agents [207], divalent cations such as Ca^{2+} , Zn^{2+} and Mg^{2+} [208-210] and calmodulin [211]. Closure of gap junction channels can be induced by voltage (negative or positive, depending on Cx isoform), lowered pH, elevated intra- and extra-cellular concentration of divalents and protein phosphorylation states [212-216]. Hemichannel activity is known to be decreased by physiological levels of extracellular Ca^{2+} [149, 217, 218]. HCs can however be activated in certain pathological states such as ischemia, inflammation, protein dephosphorylation and extracellular alkalization [219-222].

Early EM analyses of GJCs by negative-stain electron microscopy (EM) [223], low-resolution X-ray scattering [224], and cryo electron microscopy (cryoEM) [161] of rat liver

gap junctions provided a model for channel closure in response to increased Ca^{2+} concentration. The model postulated Ca^{2+} - induced gating that occurs by rotation of all six subunits in a connexon in a manner similar to camera iris shutter [161], later supported by AFM studies (Figure 1.13A) [149]. Alternative hypotheses include intra-connexin interactions leading to the formation of particle-receptor blockage at the cytoplasmic surface (Figure 1.13B, C and D) [225] or a loop gate at the extracellular surface in hemichannels [226]. Research on voltage gating of connexin hemichannels has suggested that cytoplasmic domains CL, CT and NT may be responsible for V_j gating whereas extracellular loop domains E1 and E2 for loop gating [202, 212, 227-230]. Another mechanism could include binding of divalents inside the channel pore resulting in altered electrostatics profile of the pore leading to a block of permeation of positively charged ions (Figure 1.13E and F) [231].

Both connexin GJCs and HCs are voltage-dependent [226][90] in a manner different from other voltage-dependent ion channels in that they sense local voltage inside the channel pore – transjunctional voltage (V_j) [202, 205, 232]. V_j gating, gating by the voltage difference between two cells or transjunctional gating was the first mechanism described [205, 232]. During this type of gating, a transition occurs to a stable subconducting state – the residual conductance state. Polarity of V_j gating can be either negative or positive depending on connexin isoform [212]. It involves movement of NT cytoplasmic domain leading to a partial occlusion of the channel [212, 229, 233, 234] and is referred to as fast gating [202]. The other mechanism of voltage gating – loop gating –

is able to fully close the channel although the gating is characterized by a series of transient subconductance states. The kinetics of these transitions appear as slow in routine electrophysiology measurements [226] hence the use of the term slow-gating [202]. There is evidence that conformational changes in the TM1/E1 interface mediate loop gating which results in narrowing of the aqueous channel pore [226, 227, 230]. In addition, the transient subconductance states resemble transitions associated with docking and opening of gap junction channels [235]. Loop gating is influenced by extracellular, rather than intracellular, Ca^{2+} as well as pH, and together these factors assist in keeping hemichannels closed [226, 236-238]. Extracellular divalents may play a role of gating particles, blocking the pore after membrane hyperpolarization [239, 240]. Various other regulatory factors may also influence loop gating thus making it a potential universal mechanism of channel closure [172, 202, 241].

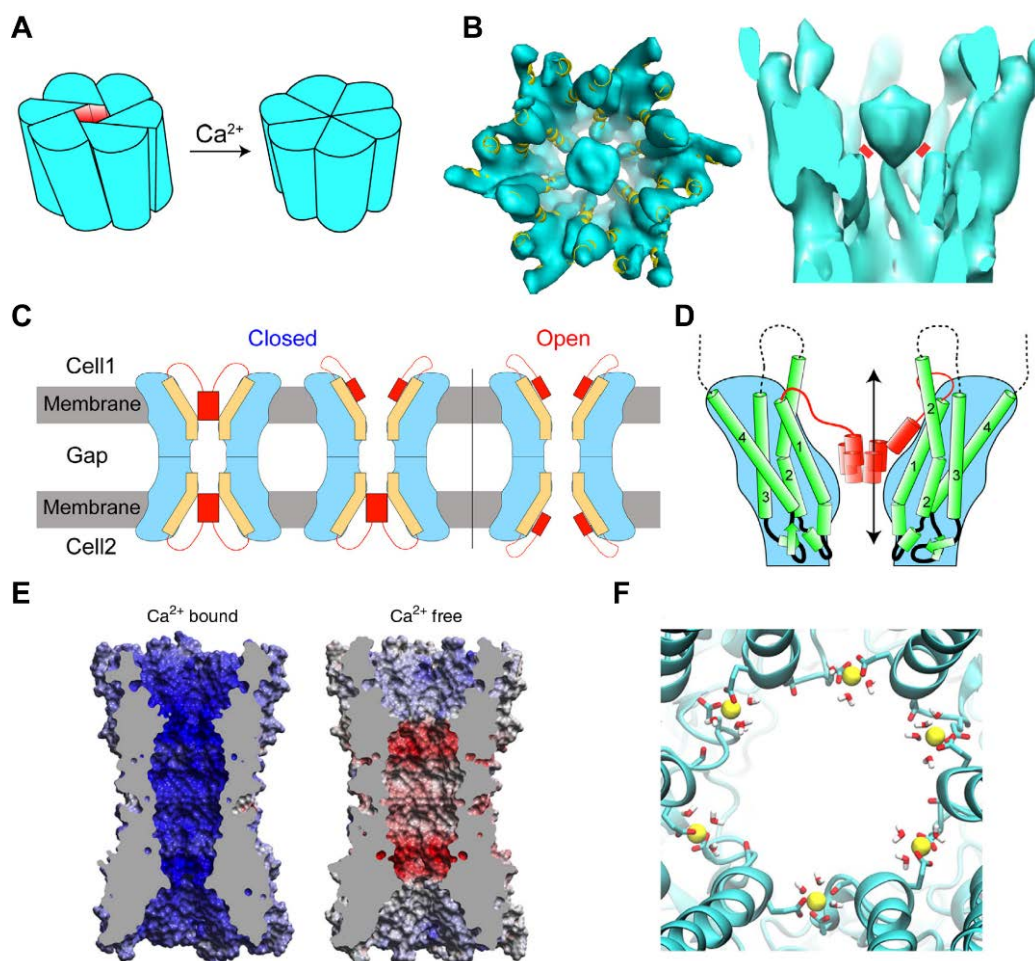


Figure 1.13. Gating models inferred from structural studies of connexin gap junction channels. (A) Camera-iris shutter model for Ca²⁺ - induced gating proposed based on research in [149, 161]. (B) Gating as a result of the formation of a steric block in the channel pore proposed in [145, 146]. (C) Schematic representation of hypothesized plug gating mechanism of gap junctions. Each hemichannel (cyan) has its own plug formed by an assembly of NTs and can regulate its channel activity autonomously. The gap junction is open only when the N-termini (red) in both hemichannels assume an open conformation [242]. (D) For hydrated ion permeation of the plug-gated structure, the movement of one N-terminal helix would be sufficient to create an 8 Å space to pass through. Figure adapted from [242]. (E) An electrostatic barrier model where Ca²⁺ binding functions as an electrostatic switch that dramatically restricts K⁺ permeation. Electrostatic potential surfaces with positive and negative electrostatic potentials shown in blue and red, respectively (color scale is -15 to +15 kTe⁻¹). The protein interior is grey. (F) Hemispheric coordination of Ca²⁺ ions from the structures shown in (E). Figure adapted from [231].

The N-terminus is the most conserved cytoplasmic domain in connexins and although the conformation at the N-terminal end varies between different connexins, its secondary structure is usually helical as assessed by NMR [234, 243, 244]. The importance of N-terminal domain has been demonstrated in mutagenesis studies where mutations in NT led to impaired channel activity and gating in GJCs and HCs [243-245]. The current hypothesis for transjunctional voltage gating, based largely on structural studies, is that the N-terminal domains play a central role [202] and connexin channel is gated by their movement triggered by voltage leading to the formation of a plug along with radial expansion of TM domains [145, 146, 246]. Electrophysiology experiments and mutagenesis studies have shown that the voltage sensor resides on the N-terminus and it involves charged residues in this domain which determine the gating polarity [212, 229, 247]. It was reported that V_j gating can be initiated by a response from just one subunit [228]. N-terminal deletions lead to lack of current in some connexin isoforms [245] and the gating polarity can be reversed by single amino acid mutations in N-terminus [212, 228, 229, 248]. Since connexins are regulated by multiple factors, it is conceivable that this mechanism could be utilized by those other gating factors and that it may involve movement of other connexin domains in addition to N-terminus.

The particle-receptor model for channel closure postulates interaction of CT (particle) with CL (receptor) with CT forming a full or partial pore occlusion [172, 225, 249-254]. This model is mainly supported by the data collected on connexins with long C-terminal domains where lowering of pH is proposed to increase the affinity of CT to CL,

and this interaction resulting in closure of the channel (Figure 1.14) [254-257]. Connexin isoforms with short C-terminal domains are not likely to be regulated in the very same way, although it was hypothesized that interaction of CT and CL is present and can be disrupted by the presence of aminosulfonates leading to channel closure at low pH [258].

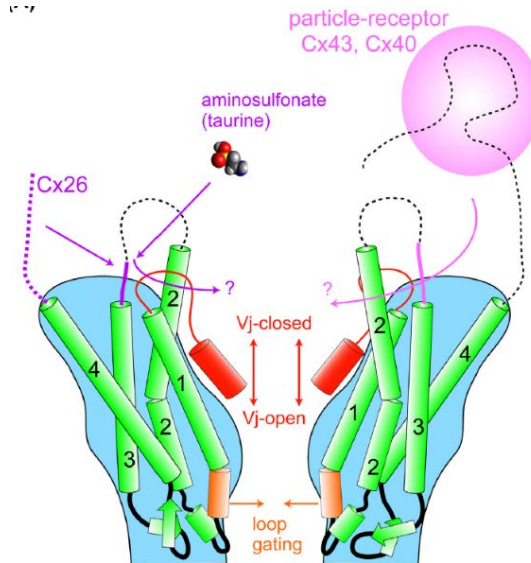


Figure 1.14. Gating properties for connexin gap junction channels demonstrated by functional studies. Several types of hypothesized movements for gap junction gating are represented in a model of a hemichannel. It is proposed that Vj-gating (red) is initiated by the inward translocation of charges in the N-terminus that essentially functions as a Vj-sensor. Loop gating (orange) may involve the TM1/EL1 border as the permeability barrier formed by narrowing the channel pore of the TM1/EL1 domain. Particle-receptor model (pink) proposed for Cx43 and Cx40 junction channels, which involves an interaction between the CT ball and the second half of CL (L2 region) as a receptor. Amino sulfonate, taurine here as a representative, binds to Cx26L2, and the short CT of Cx26 is also involved in the intramolecular gating (purple). Figure from [242].

1.2.4 Connexin 26. Connexin 26 (Cx26) is one of the smallest members of the connexin family of gap junction proteins (26 kDa) with a relatively short C-terminal cytoplasmic domain. Cx26 is capable of forming both homomeric and heteromeric gap junction channels and hemichannels that are permeable to, among others, cAMP, IP3,

glucose and ions while being moderately selective for cations [173, 174, 259]. It is expressed in many crucial organs such as the liver, brain, kidney and skin and involved in hepatic, neural, cutaneous, secretory gland and inner ear systems with mutations often leading to deafness and skins disease [260-264].

Connexin 26 is expressed in the inner ear in the cochlea, in the support cells but not the hair cells of the organ of Corti [261, 263, 265-268], a narrow spiral of epithelial sensory cells responsible for transducing sound waves into electrical impulses. Cx26 gap junctions help form interconnected cellular networks which allow for recycling of potassium ions between perilymph and endolymph [269-272]. Cx26 GJCs contribute to glucose homeostasis [273, 274], mediate the spread of Ca^{2+} waves in support cells [166] and play a role in the early development of the cochlea (Figure 1.15A) [275]. Connexin hemichannel activity in the support cells has been inferred from dye uptake assays and hemichannel function is thought to be mainly involving ATP and IP3 release [165, 167, 276]. HCs are also involved in mediating Ca^{2+} wave propagation in support cells [165].

It is estimated that 1 – 4 % of members of all studied ethnic populations carry disease-causing Cx26 mutations in its encoding GJB2 gene, which account for over 50 % of congenital cases of hearing impairment [175, 196, 197, 264, 277-281]. Over 100, mostly recessive, point mutations have been identified which occur essentially throughout the entire Cx26 sequence and produce loss of function [278, 282-284]. They are the main source of non-syndromic sensorineural deafness [283] and syndromic deafness cases

such as keratitis-ichthyosis-deafness (KID) syndrome [285]. While close to a 100 of non-syndromic Cx26 deafness mutations occur throughout the whole Cx26, ~20 of identified syndromic Cx26 deafness mutants cluster at the M1/E1 boundary and in the NT domain (Figure 1.15B) [284, 286, 287].

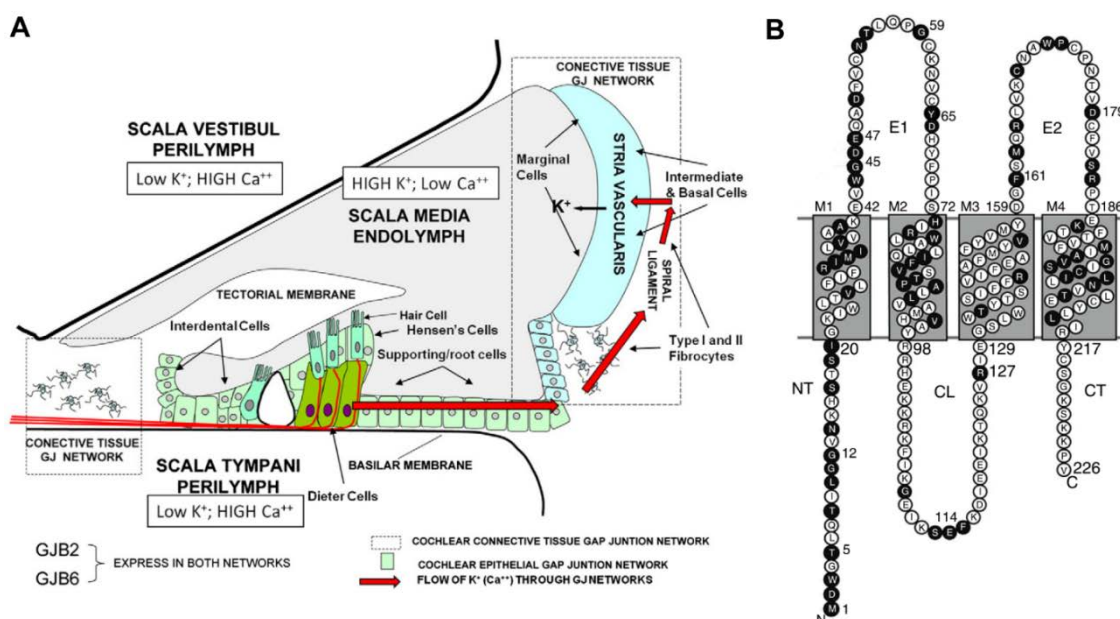


Figure 1.15. The function of connexin 26 in the cochlea and mutations in GJB2 gene leading to deafness. (A) Diagram of the cochlea and its various compartments, showing the proposed return of K⁺ (possibly mediated by a propagated Ca⁺⁺ wave) from the hair cells to the endolymph (red arrows) through the epithelial (green color) and connective tissue (dotted box) gap junction networks. The former is comprised of Dieters' cells and supporting cells, while the latter is comprised of types I and II fibrocytes in the spiral ligament and basal and intermediate cells of the stria vascularis. Ultimately, released K⁺ is taken up by the marginal cells of the stria vascularis and released into the endolymph, thus maintaining the elevated K⁺ levels (and high resting potential of ~+100 mV) in this compartment. This is essential for amplifying the responses of hair cells to sound, by increasing the driving potential for K⁺ flux across the hair cell membrane when it is activated. Figure from [284]. (B) Over 100 point and deletion mutants have been identified in Cx26 that are linked to deafness. Sixty-nine of these mutants have been tested for trafficking and functionality and are mapped onto the Cx26 topology diagram, indicated by circles colored solid black with white lettering. Figure adapted from [231].

Previous experimental studies on multiple isoforms of Cx GJCs and HCs revealed the M1/E1 segment as uniquely important for voltage gating via the loop-gate [227, 230, 288, 289] and regulation by divalent metals [209, 231] and NT domain as a pore-lining voltage sensor essential for gating [212, 229, 246, 247, 290]. Aberrant inhibition of Cx26 deafness mutant hemichannels by extracellular Ca^{2+} as well as Zn^{2+} and pH was shown to contribute to their 'leaky' phenotype [237, 291].

Hair cells in the cochlea require high concentrations of potassium ions in the endolymph and a positive endolymphatic electrical potential [260, 261, 263, 264, 292, 293]. Deafness has been thought to be caused by decreased cochlear potassium recycling leading to apoptosis of the endothelial support cells underlying the hair cells and disruption of the endocochlear potential [293-296]. Majority of syndromic deafness Cx26 mutants possess functional HCs that show aberrant properties and have "leaky" phenotype leading to aberrant signaling across the plasma membrane, cell damage and, ultimately, deafness [297-299]. The mechanisms underlying non-syndromic and syndromic deafness likely differ as loss of function in GJCs does not necessarily lead to skin disorders and syndromic deafness mutants can function as both GJCs and HCs or only as HCs.

The structure of the NT domain has been shown to be critical to connexin function and very sensitive to amino acid substitutions [234, 243, 245, 300]. The first 10 amino acids of NT are located in the pore entrance sensing the voltage field and their movement

has been suggested to initiate voltage dependent gating [212, 228, 229, 248]. The first N-terminal charged amino acid residue, negatively charged aspartic acid Asp2, determines the gating polarity and closes the channel in response to inside positive potential (positive V_j-gating polarity) [212]. Mutations of Asp2 to positively charged amino acids are known to reverse that gating polarity [212]. Those first 10 NT residues form an α -helix that, due to a glycine hinge at residue 12 [234, 300], can fold back toward the pore to form the surface of the funnel-shaped channel entrance [145, 146, 246]. Mutation at G12 to proline that preserves a favorable, kinked NT structure preserves function of Cx26 channels as opposed to mutations to serine, tyrosine or valine [234] with mutation to arginine resulting in more flexible NT structure and 'leaky' channel phenotype [300]. Cx26 N14K mutant was found to undergo no stable closing transitions in response to low extracellular Ca²⁺ and to be insensitive to low pH conditions. The lack of stable closures and slow current kinetics suggested stabilization of open state at the loop gate [301]. Mutations in exposed to the channel pore N14 are likely to alter electrostatic interactions of that residue with M2 domain of the adjacent connexin monomer [301]. Available data supports the hypothesis that the M34 residue in Cx26 is essential for channel function [302-306]. The M34T mutant displays aberrant activity [302, 303, 305] and M34A has decreased permeability and conductivity [307]. Current data suggests that M34 side chains allow for docking of N-termini to the channel pore via interaction of M34/W3 thus stabilizing open state [245, 246]. Whereas G12R and N14K syndromic deafness mutants lead to a development of KID syndrome [286] and M34A/T mutants end in non-syndromic

deafness [302-305], it seems plausible that all of those mutants could disrupt the interaction of NT domain with either M1 or M2 transmembrane domains thus destabilizing channel open state.

1.2.5 Connexin 26: regulation by pH. Changes in intracellular pH affect gap junction conductance and the channel closure brought about by the decrease from physiological pH is a common gating mechanism in connexins [215, 308]. Decrease in pH were shown to cause a decrease in junctional conductance [232, 309, 310] and in permeability as demonstrated in glial, neuronal and lens GJCs [311, 312]. Lowered pH can lead to diminished junctional electrical coupling in cardiomyocytes and in Purkinje fibers [215, 313-315] as well as in teleost and amphibian embryos [232]. Gating of connexin 43 by acidic pH [316] during cardiac ischemia, which causes intracellular pH drop in heart [317], leads to electrical uncoupling and thus triggers channel closure [318] which is likely to contribute to arrhythmogenesis in acute myocardial infarction [319].

The sensitivity to pH varies among the connexin family members, with Cx26 being highly sensitive and Cx43 less sensitive [142, 251, 308], and is hypothesized to be related to the sequence of the regulatory C-terminal domain [140, 142]. A particle-receptor model for pH-induced channel closure was proposed where CT domain forms a gating particle and binds to a part of CL domain in connexins with long CT such as Cx43 and Cx40 [249, 308]. It was not demonstrated for Cx26 with very short CT. The pH effect on Cx26 GJCs and HCs was shown to be either mediated by aminosulfonates acting as a ligand or

modulator [258, 320, 321] or independent of them and thus directly mediated by channel protonation (Figure 1.16) [237]. The prevailing model is that binding of an aminosulfonate to CL domain disrupts the interaction of CL and CT domains which is favored by acidic pH, leading to channel closure [258, 321]. The interactions between CL and CT have been shown to be highly dynamic [149, 151, 322]. In addition, mutations in the NT domain, the domain hosting the voltage sensor with residues located in the channel pore [234, 247] and implicated in the formation of the gating ‘plug’ particle [242], were shown to either remove or diminish the effect of low pH on Cx26 hemichannels [301].

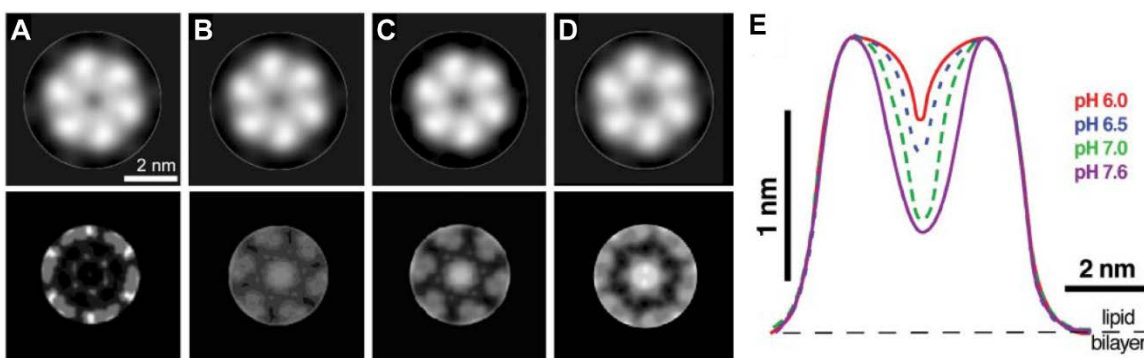


Figure 1.16. pH-dependent conformational changes of extracellular connexon surface. (A-D) Correlation averages (top) and S.D. maps (bottom) were calculated from AFM topographs recorded at pH 6.0 (A), 6.5 (B), 7.0 (C), and 7.6 (D). (E) Two-dimensional profile of the pore channels recorded at different pH values. Figure from [320].

1.2.6 Connexin 26: mechanisms for gating. Two Cx26 structures were published up to date in what is considered to be an open conformation [231, 246]. Both structures showed a gap junction channel formed by two opposed connexons at a resolution of 3.3 – 3.8 Å with a majority of densities corresponding to cytoplasmic domains missing. Whereas one of the structures concentrated on Ca²⁺-binding sites and had no cytoplasmic domains built in (Figure 1.17A and B) [231], the other structure has presented a model

for organization of NT domains (Figure 1.17C and D) [246]. The latter structure reveals six alpha helical NT domains in each connexon, forming a funnel inside the pore, with the domains themselves characterized by a high degree of flexibility [246] in agreement with previous NMR studies [234, 300]. This funnel, restricting the diameter of the channel pore to 14 Å, has a circular girdle at the bottom formed by Asp2 and Thr5 residues interacting on neighboring NT domains. The funnel-forming NTs are locked inside the pore through hydrophobic interaction of Trp3 residues with Met34 residues on neighboring connexin monomer [246].

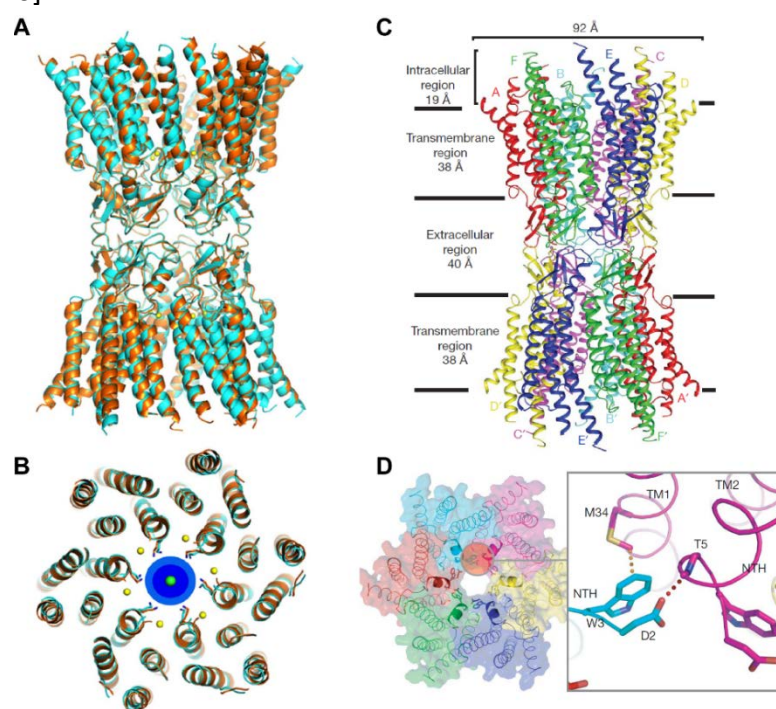


Figure 1.17. X-ray structures of connexin 26 GJC. (A) Side views of superimposed Ca²⁺-bound (cyan) and Ca²⁺-free (orange) GJC structures. (B) Overlay of the Ca²⁺-bound (cyan) and Ca²⁺-free (orange) hemichannels, viewed from the extracellular gap and shown at the level of the minimum pore diameter (~15 Å). Figure from [231]. (C) Side view of the Cx26 GJC. (D) The six NTHs form a funnel structure, which is stabilized by a circular network of hydrogen bonds between Asp 2 and the main chain of Thr 5. Figure from [246].

Electron microscopy (EM) studies of 2-dimensional crystals of Cx26 M34A mutant suggested a sterical pore occlusion via an aggregate density termed the ‘plug’ formed with NT domains as one of the possible ways for gating in connexin channels (Figure 1.18A and B) [145, 146]. Cx26 M34A mutant was shown to have decreased dye coupling [307] and is related to M34T non-syndromic deafness mutant [281] which leads to pore constriction [302]. The pore opening in these closed structures was reduced from 14 Å to as narrow as 6 Å which would not allow for a passage of hydrated ions [323]. The NT was deemed a probable plug-forming domain since the CT in Cx26 is very short and CL would not be able to account for the densities seen in the structures. In addition, the structure of M34A Δ 2-7 mutant showed diminished density inside the pore making NT a likely contributor to the plug density (Figure 1.18C) [145]. It certainly seems plausible given that the NT has been shown multiple times to host a Vj voltage sensor and to be likely located inside the channel pore [212, 228, 229, 247] with movement of charges on NT initiating gating [212, 248].

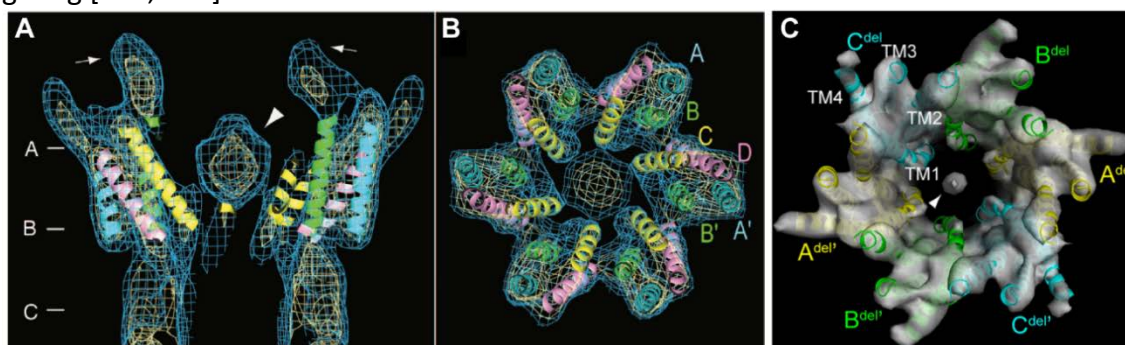


Figure 1.18. Visualization of connexin 26 GJC pore block with electron crystallography. (A) Twenty-angstrom-thick section perpendicular to the membrane plane through the density map of a hemichannel. (B) Thirty-angstrom-thick slab through the density map corresponding to the position of the line B shown in (A). Map resolution is 7 Å. Figure from [146]. (C) Surface representation of the Cx26M34A Δ 2-7 map (10 Å resolution) viewed normal to the membrane plane. Figure from [145].

It is unclear if the structures of a mutant Cx26 represent a functional, closed state of the channel, and if so, what triggered the channel closure, since the structures were obtained in the presence of multiple factors known to close channels through chemical gating (low pH, high Ca^{2+} and Mg^{2+} , carbenoxolone, aminosulfonate) [145, 146]. The M34A mutant is likely to lead to aberrant channel behavior as such a mutation would disrupt the interactions of Met34 with Trp3 necessary for keeping the NT-based funnel attached in the channel and lead to occluded pore [246]. What seems to be clear however, is that conformational changes in NTs are almost certain to play a major role in gating of connexin channels – both chemical gating and voltage gating as well as account for abnormal phenotypes of N-terminal connexin mutants. The flexibility of, mostly disordered, NT domains and its M1-connecting loops as well as low resolution of the plug density indicate that this type of gating could be fast thus corresponding to the proposed fast gating at the cytoplasmic site [226] and that the plug itself would be a relatively mobile component.

The EM structures showed that each hemichannel had its own plug density and that those densities were different [145, 146] which remains with agreement with the notion that hemichannels are capable of regulating their activity independently [205, 212, 324]. Additionally, the NT domains appeared to be arranged asymmetrically inside each hemichannel [145, 146] meaning that the channel regulation occurs on a per-monomer basis as reported previously [228, 325]. The X-ray structure adds more evidence to such a model for channel regulation as the deposited X-ray map (2ZW3) does not have

sufficient densities to build all NTs into them thus forming a complete funnel (poor densities with high B-factor) but rather it supports the notion of NT forming highly dynamic regulatory structures [246]. The asymmetry in the behavior of NTs could mean a different structural response to different gating effectors.

The mechanism for closure of Cx26 GJCs by an insertion of a physical plug formed by NTs supported by the X-ray and EM analyses [145, 146, 246] is different from the mechanism responsible for closing Cx26 HCs in response to Ca^{2+} or low pH/aminosulfonates found via AFM studies. The latter mechanism was proposed to be carried by extracellular loops which are thought to be responsible for the decrease in inner pore diameter, but not outer HC diameter, detected in single hemichannel layers [149, 320]. The change was accompanied by a small 6.5° rotation in connexon lobes in low pH studies [320] but not in the studies on Ca^{2+} effect [149]. This mechanism of closure is likely to be the slow gating (loop gating) utilizing E1 and E2 domains and channel closure with a plug could be the fast gating mechanism with the gate forming closer to the cytoplasmic surface [226]. The V_j gating (fast gating) in Cx26, responding to positive potential inside the pore, would cause disruption of the Asp2 – Thr3 interactions in the funnel formed by NTs therefore causing the assembly of NTs into a plug though a collapse of the circular girdle [246, 326]. It is plausible that the steric occlusion of the pore with a plug density observed in GJCs is also applicable to HCs and that a right experimental method could capture it. Conversely, high Ca^{2+} and low pH also affect GJCs and since

extracellular loops of GJCs may adopt a different conformation than that in HCs [327], gating by Ca^{2+} and pH could use cytoplasmic domains instead.

With NT domains stabilizing the overall structure of the channel and interaction of CT and CL domains implicated in low pH and voltage induced gating, the current model for gating of is that transitions between open and closed states involve structural changes mediated by interaction of M1-M4 transmembrane domains with either NT, CT or both with the NT domains physically closing the channel [328].

1.3 Connexin26 hemichannel and Ca^{2+}

1.3.1 Connexin hemichannels and Ca^{2+} . Connexin hemichannels (HCs) mediate communication between the cytoplasm of the cell and the extracellular milieu. This crucial function requires them to be tightly regulated, not unlike the gap junction channels (GJCs). Opening and closure of HCs is controlled by mostly the same set of ions and molecules as GJCs, with gating by voltage performed via the loop gating (slow gating) mechanism as opposed to fast V_j gating in GJCs [226]. The HC regulation by Ca^{2+} is a universal mechanism in all studied connexins [187]. Variations in external divalent cation concentration regulate currents in HCs, with external Ca^{2+} known to affect voltage gating [238, 240]. An increase in the amplitude of currents follows removal of external Ca^{2+} , with activation shifted towards more negative potential and altered kinetics of both HC activation and deactivation [187].

The unique availability of extracellular domains EL1 and EL2 from the outside of the cell makes these domains a likely place for a location of the putative loop gate, ascribed to the extracellular end of HCs. It is conceivable that such a gate could be modulated by multiple gating factors. It is generally believed that, under physiological conditions, HCs should be in a closed state in the cell membrane in order to prevent leakage of cell contents and ultimately cell death [189, 329]. Unfortunately, there has been no hemichannel structure solved of any of the connexin isoforms thus the molecular basis for HC gating remains shrouded in mystery. The vast majority of studies done on HCs have mainly investigated the functional side of hemichannel regulation with limited structural insight being provided exclusively by atomic force microscopy studies (AFM) in which hemichannel pore narrowing was reported in response to increase in Ca^{2+} or reduction of pH [149, 320, 327].

1.3.2 Connexin26 hemichannels. A number of mutations in Cx26 lead to impaired Ca^{2+} gating and ultimately to disease [286]. Mutations in Cx26 gene can lead to sensorineural hearing loss (~135 mutations identified) or skin diseases (~50 mutations identified). Some of these mutations affect hemichannel, rather than channel, function and can lead to either non-functional 'dead' hemichannels, hemichannels with impaired gating properties characterized by 'leaky' phenotype or hyperactive mixed hemichannels (Figure 1.19). Dysregulation of calcium homeostasis in the epidermis as a result of gain-of-function properties of such 'leaky' hemichannels can lead to KID syndrome (keratitis-ichthyosis with deafness) [179].

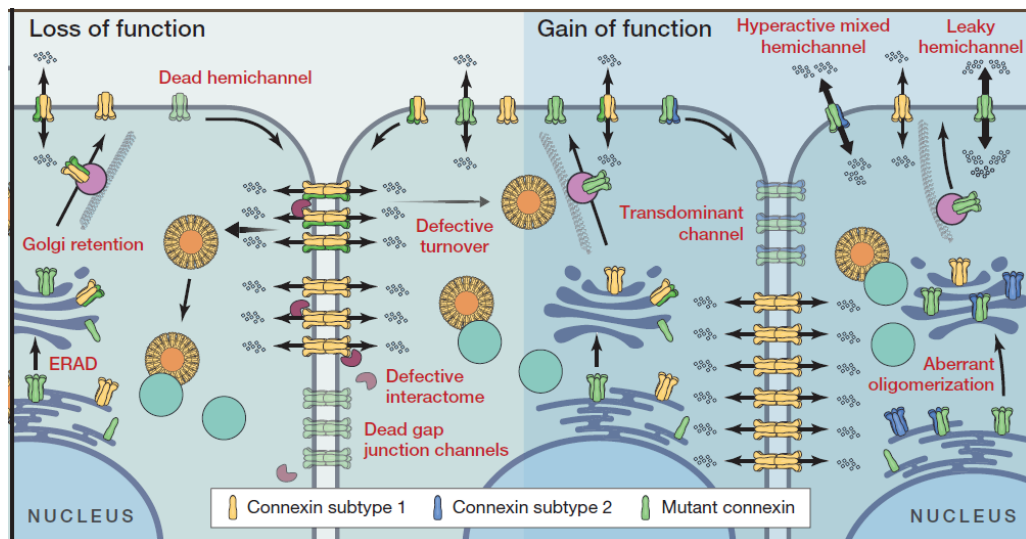


Figure 1.19. Disease-causing mutations in connexin genes have different effects on connexin proteins. In some cases, the mutant connexin fails quality control mechanisms and proceeds to endoplasmic reticulum associated degradation (ERAD) or gets stalled in the Golgi apparatus. Mutant connexins may lose the ability to form functional hemichannels or gap junction channels likely due to aberrant formation of the channel pore. In other cases, connexins acquire an aberrant half-life or lose interactions with the interactome, all of which can contribute to human pathologies. Gain-of-function mechanisms occur when some mutants bind or oligomerize with co-expressed connexins that they would normally not oligomerize with. These aberrant interactions can lead to transdominant effects on wild-type connexins that result in activated hemichannels and/or dead gap junction channels. Other connexin mutants form leaky homomeric hemichannels that may contribute to cellular pathologies. Figure from [179].

One AFM study performed on force-dissected Cx26 GJC plaques reported a reduction of extracellular hemichannel pore diameter from 1.5 to 0.6 nm upon exposure to 0.5 mM Ca^{2+} . This change was reversible and formation of microdomains on the cytoplasmic surface was an additional Ca^{2+} - induced effect (Figure 1.20) [149]. Similar changes in Cx26 hemichannel pore diameter were shown as a response to acidification with diameter changing from ~ 1.7 nm at pH 7.6 to ~ 0.6 nm at pH 6.0. These changes were

aminosulfonate (AS)-dependent [320] although there is contradicting evidence in the literature regarding the pH/AS interplay [237, 258].

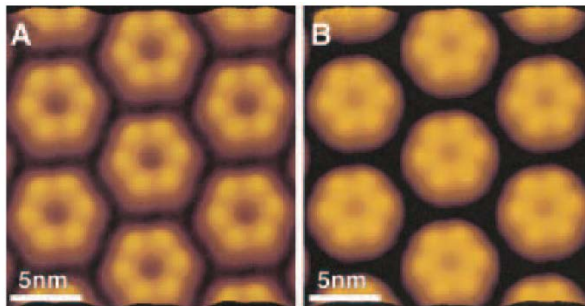


Figure 1.20. Atomic force microscopy (AFM) analysis of connexin 26 plaques from HeLa cell line showing connexon (hemichannel) surface as a function of Ca^{2+} concentration. (A) Images recorded in the absence of Ca^{2+} . (B) Images recorded in the presence of 500 μM Ca^{2+} . Figure from [149].

Cx26 HC currents measured in oocytes were reduced when extracellular Ca^{2+} concentration was raised from 0.1 to 0.7 and then 3.5 mM. In addition, reduction in both extracellular and intracellular pH was reported to suppress currents [330]. Cx26 HCs are Ca^{2+} permeable and therefore could play a role in Ca^{2+} signaling, however Ca^{2+} concentration as high as 1.8 mM was found to be inhibitory to electric currents. Mutant A40V and G45E hemichannels causing KID syndrome displayed altered regulation by Ca^{2+} , with both mutants more refractory to Ca^{2+} -induced HC closure. While A40V was found to require as high as 5 mM Ca^{2+} for closure, G45E was only modestly impaired, required 2 mM and higher Ca^{2+} yet showed more Ca^{2+} permeation activity. The authors concluded that these HC gain-of-function mutants produce similar phenotypes through different mechanisms and their ultimate effects would depend on both Ca^{2+} and voltage regulation [291]. The concentration of Ca^{2+} required to block 50 % of currents, EC_{50} , varies between

low millimolar and high micromolar depending on connexin isoform [187], with Cx26 EC50 measured in oocytes to be ~ 0.7 mM [330] or ~ 0.2 mM [291].

Two detailed functional studies attempted to address the structural basis of Ca^{2+} - gating mechanism in group 1 connexins, one proposing gating with EL1 loop in Cx26 and Cx46 [331] and the other one gating with EL2 loop in Cx32 [217]. The 2016 study examined the role of residues D50 and K61, thought to form electrostatic networks near the extracellular entrance to HC pore (Figure 1.21A). It is worth noting, that only residue D50 is a conserved residue in connexins, with E61 appearing more frequently than K61 [332]. Ca^{2+} was found to disrupt these electrostatic networks thus facilitating HC closure. Point mutants D50N, E47Q and D46C exhibited similar property, reducing barrier to closing by Ca^{2+} . In addition, two negatively charged residues D50 and E47, speculated to form a Ca^{2+} -binding ring, were identified as major contributors to the stability of HC closed state (Figure 1.21B). Point mutants D50N and E47Q were shown to have reduced K_d for Ca^{2+} (1.31 mM and 1.11 mM, respectively, as compared to 0.33 mM for Cx26 WT). Interestingly, binding of Ca^{2+} in that putative gating ring did not prevent ions and small molecules from entering the HC pore suggesting that a physical gate must form during HC closure siting below the Ca^{2+} - gating ring [331].

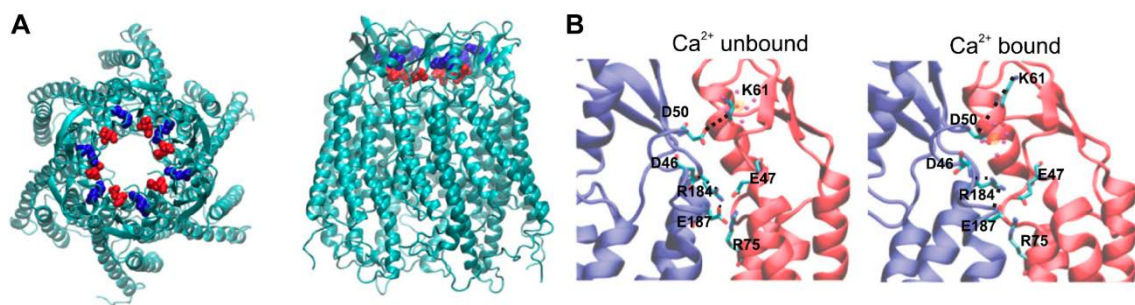


Figure 1.21. Electrostatic network at the entrance of the pore is altered upon the addition of Ca^{2+} . (A) Top (Left) and side views (Right) of the Cx26 hemichannel showing D50 (red) and K61 (blue) at the extracellular entrance of the pore, which form intersubunit salt bridges. (B) Electrostatic network of the Cx26 hemichannel model formed by residues D46, E47, R75, R184, and E187 before (Left) and after (Right) Ca^{2+} is coordinated at position D50, after 50-ns molecular dynamics simulations. Ca^{2+} ions are depicted as small orange spheres. Also note the increased K50–K61 distance with Ca^{2+} bound. Figure from [331].

1.3.3 Other connexin hemichannels. The 2004 study discussed Ca^{2+} -gating in Cx32 as mediated by yet another putative Ca^{2+} binding site, this time localized to residues D169 and D178 in EL2 [217]. As it was the case in the previous publication [331], only one residue under investigation is truly conserved among connexins - residue D178 - which is involved in forming the hydrogen bonding network between opposed hemichannels in GJCs [333]. The authors have found that the currents recorded for point mutants D169N and D178N could no longer be regulated by Ca^{2+} , resulting in favoring of the open conformation by these mutants. At the same time, formation of heteromeric D169N/D178N HCs partially restored the ability of these HCs to regulate voltage gating and ionic conduction with Ca^{2+} . The results suggested that each Ca^{2+} binding site is composed of two Asp residues belonging to adjacent subunits, with a ring of 12 Asp residues binding a total of six Ca^{2+} ions, resulting in HC closure [217].

A study evaluating function of Cx46 and Cx50 HCs expressed in *Xenopus* oocytes has shown that 1.8 mM Ca^{2+} applied from the extracellular side strongly reduced current in Cx50 and changed current magnitude and kinetics of activation in Cx46 [334]. A follow-up study has once again demonstrated the effect of 1.8 mM Ca^{2+} on these connexins. In such conditions, Cx50 showed little evidence of current activation in response to hyperpolarizing or depolarizing voltage steps and Cx46 exhibited a polarity-dependent activation with a slowly rising outward current evident upon depolarization [335]. Ca^{2+} was found to be a modifier of intrinsic voltage gating properties of Cx46. In the absence of Ca^{2+} , large hyperpolarizing voltages were able to close the HCs, although gating was characterized by continuous flickering with brief episodes of quiet closed state. Addition of Ca^{2+} allowed for long-lived quiet closed states. The currents, recorded in oocytes, were largely abolished by addition of Ca^{2+} to 1.8 mM or Mg^{2+} to 20 mM. The research suggests that divalent cations, including Ca^{2+} , stabilize the fully closed conformation of Cx46 HCs, with hyperpolarization triggering channel closure. Moreover, Ca^{2+} was found to only be effective in gating the HCs when applied from the extracellular side, another piece of evidence that Ca^{2+} gating in HCs is likely to require ion binding to EL1/EL2 loops [238]. A study on Cx50 HCs suggested that loop gating involves movement of the TM1/EL1 region, resulting in local narrowing of the hemichannel pore and ultimately leading to closure [227].

A study on Cx37 hemichannels in *Xenopus* oocytes discussed Ca^{2+} and Mg^{2+} gating as a voltage-dependent mechanism of open channel block. The authors proposed that

divalent cations enter and block the channel upon membrane hyperpolarization (Figure 1.22). Ca^{2+} at 1 mM and Mg^{2+} at 20 mM were both found to virtually abolish currents in HCs under investigation when applied from the extracellular side. Since Mg^{2+} is less potent of an inhibitor than Ca^{2+} , higher concentrations of this ion were tested [240]. Interestingly, even though 1 mM Ca^{2+} tested closely matches the ~ 1.4 mM Ca^{2+} concentrations measured in extracellular environment [336], 20 mM Mg^{2+} sits way above the ~ 0.9 mM Mg^{2+} reported for extracellular space [337]. It seems conceivable that cytoplasmic 100 nm Ca^{2+} should not be inhibitory whereas 1-2 mM Mg^{2+} could be, especially given the IC_{50} of 1.3 mM for Cx37 [240]. Calcium was found to induce a reversible change in the extracellular pore diameter of Cx43 HCs.

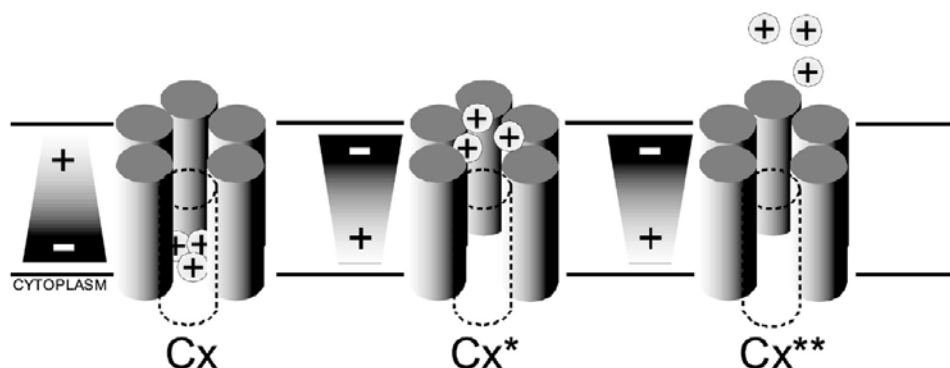


Figure 1.22. Gating model for connexin 37 hemichannels. Illustration of the gating process for hCx37 hemichannels. At negative potentials (left) the channel is occupied with several polyvalent cations. These bind to a site on the cytoplasmic side of the channel, blocking current flow. At positive potentials (center) the koff for the polyvalent cations becomes significant, the ions are ejected from the site of block, and current is allowed to flow. Polyvalent cations remain at a high local concentration. Upon extended depolarization (right), the local concentration is depleted as well. Upon repolarization, the polyvalent cations bind the channel again, inhibiting current flow (left). Figure from [240].

Pore diameter was investigated using AFM. In high calcium conditions, with 1.8 mM Ca^{2+} present, the pore diameter was ~ 1.8 nm, resembling the closed HC conformation. Reduction of Ca^{2+} to 1.4 mM and below yielded a population of HCs with the pore diameter of ~ 2.5 nm, consistent with an open state. Reduction of Ca^{2+} from 1.8 to 1.4, 1 and 0 mM resulted in an increase in the open state HCs population, from 0 to 27, 74 and 100 %, respectively. The conclusion is that open/close probability of Cx43 HCS is Ca^{2+} - dependent (Figure 1.23) [327].

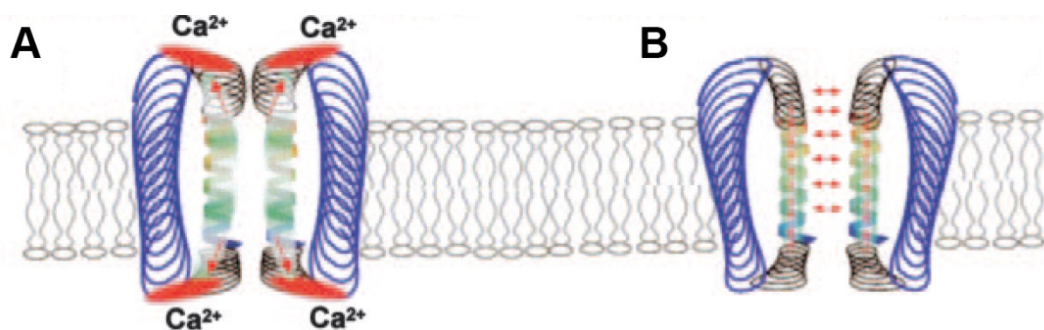


Figure 1.23. A gating model for the mechanism of channel closing in connexin 43 hemichannels. When the tertiary structure of the open connexon (B) is unbalanced by the Ca^{2+} absorbed on the extramembranous surface, the refolding of the E1 and E2 loops hides the hydrophobic domains and at the same time closes the channel (A). Figure from [327].

1.4 Accomplishments

1.4.1 Zinc transporter ZnT8.

Development of protein expression and purification protocols for P.pastoris yeast (ZnT8B protein) and S.frugiperda Sf9 insect cell (ZnT8A and ZnT8B proteins) systems. Protein

purified as a dimer and remained stable in the buffer solution with fos-choline 12 (FC-12) detergent. Protein displayed high melting temperatures indicative of good stability and protein particles had homogenous appearance.

Determination of low-resolution structure of ZnT8B with negative-stain electron microscopy (EM) and single particle image analysis. The map was calculated at 20 Å resolution, with C2 symmetry imposed. The two lobes of density were ascribed to transmembrane domains of ZnT8. The homology model of ZnT8B displayed very good fit to the EM map, especially in the region interpreted as belonging to the cytoplasmic domains.

Design of an assay in liposomes to qualitatively assess ZnT8 activity. Fluorescence signal from proteoliposomes was substantially higher than that coming from control liposomes, indicating that protein was active. The highest fluorescence signal was recorded for conditions with pH gradient favoring Zn²⁺ transport into the vesicles via a H⁺/Zn²⁺ antiport mechanism. Removal or reversal of the pH gradient resulted in reduction of fluorescence signal by ~ 50 %. The behavior of this *in vitro* system mimicked Zn²⁺ transport into insulin secretory vesicles in pancreatic B cells.

These results provide a foundation for higher resolution structural studies and screening experiments to identify compounds that modulate ZnT8 activity.

1.4.2 Gap junction channel Connexin26.

Preparation of connexin26 protein sample for studies in low pH conditions. Thermal stability assay indicated superior protein stability in amphipol A8-35 as opposed to detergent n-Dodecyl β -D-maltoside (DDM). Negative-stain EM single particle analysis revealed prominent densities inside the pore of each hemichannel although the limitations of EM in negative-stain prevented unambiguous interpretation of the map.

Determination of connexin26 structure at pH 7.5 with cryo-electron microscopy (cryoEM).

The 4 Å map, determined with D6 symmetry, revealed well-ordered extracellular gap and transmembrane helix regions. The cytoplasmic domains CT and CL well not resolved however, and the densities interpreted as belonging to the cytoplasmic NT domains were not complete. The map resembled an open channel conformation. The resolution of the map allowed for building of a molecular model and assignment of some bulky side chain densities.

Determination of connexin26 structure at pH 6.4 with cryo-electron microscopy (cryoEM).

The reconstruction has resulted in two maps from one sample grid – a 4.2 Å map resembling an open channel conformation and a 7.6 Å map with a density occluding the channel pore. The resolution of the open conformation map allowed for building of a molecular model and assignment of some bulky side chain densities. The model building process for the closed conformation map was limited to the assignment of the domains. The occluding and connecting densities in the 7.6 Å map were interpreted as belonging

to the N-terminal domain. The participation of six N-terminal domains in formation of the occluding pore density was confirmed by performing control refinement experiments with C6, D2 and D3 symmetries. Mass spectrometry of trypsin-digested protein revealed acetylation on methionine 1, which removes the charge at the N-terminal amine group. This modification was interpreted as crucial to enable N-terminal domains to form the occluding particle. There was a movement of the cytoplasmic portion of M2 helix towards M1 helix within the same connexin26 subunit in pH 6.4 closed structure as compared to the structures in the open conformation.

Investigation of protein dynamics with hydrogen-deuterium exchange (HDX) coupled with tandem mass spectrometry (MS/MS). HDX revealed reduction in deuterium uptake in a few different regions of protein at pH 6, including a reduction in the N-terminal/M1 helix peptide. EX1 kinetics were detected on the N-terminal/M1 helix peptide at pH 7.5 only. These results indicate that N-terminus exhibits conformational flickering at pH 7.5 and reduction of pH shifts the equilibrium towards more static N-terminus. This supports the observations from cryoEM where discontinuous rings of density inside the channel pore were present in the open structures and the densities for N-terminal domains were incomplete.

Protein crosslinking experiments with BS3 amine-to-amine crosslinker coupled with tandem mass spectrometry (MS/MS). Connexin26 was crosslinked to an SDS-resistant hexamer in pH 7.5 and 6. Peptides from trypsin-digested proteins were analyzed and

revealed multiple crosslinks forming between the CT and CL and within CL. No meaningful differences were observed between pH 7.5 and 6 conditions. The crosslinks between NT and CL revealed unique crosslinking of K15 and K22 with lysines on CL under acidic conditions. These results were interpreted as closer interaction of NT and cytoplasmic portion of M1 helix with the CL, in agreement with the observation that M2 helix moves towards M1 helix under acidic conditions as seen in the pH 6.4 closed structure.

These results support the hypothesis that pH-mediated gating of connexin 26 is achieved by a “ball-and-chain” type of mechanism. To my knowledge, this is the first instance in which a complete, oligomeric “ball-and-chain” has been visualized.

1.4.3 Connexin26 hemichannel.

Purification of connexin26 as a hexameric hemichannel. An N176Y docking-impaired mutant of connexin26 was engineered, expressed and purified from Sf9 insect cells. The mutant purified as a hemichannel in façade-EM (FA-3) detergent. Negative-stain EM in amphipol revealed monodisperse population of particles and single particle image analysis resulted in 2D class averages with apparent six-fold symmetry.

Reconstitution of connexin26 N176Y mutant into the lipid bilayer of nanodiscs. N176Y mutant was successfully reconstituted into soybean polar lipid MSP2N2 nanodiscs. EM analysis revealed homogenous and monodisperse nanodiscs of ~ 150 Å in diameter.

Optimization of conditions for cryoEM studies. Multiple freezing conditions and sample grid types were screened to optimize for ice thickness, particle distribution and particle orientational sampling. The best results were achieved on quantifoil gold grids pegylated using a linear, thiol-bearing PEG group. Data collection and subsequent image processing revealed 2D class averages of both top- and side-views of the protein, each displaying secondary structure features.

These results indicate that I have optimized the protein sample and freezing conditions for sub-nanometer structural studies with cryoEM. Future analysis of particles with and without Ca^{2+} could serve as a basis to propose a mechanistic model for Ca^{2+} -gating in connexin hemichannels.

Chapter 2: Structure/Function Analysis of Human ZnT8 (SLC30A8): A Diabetes Risk Factor and Zinc Transporter

Mark J. Daniels*, Maciej Jagielnicki*, and Mark Yeager

* Co-first authors

2.1 Introduction

The human pancreatic β -cell integral membrane protein ZnT8 (also known as SLC30A8) is a major autoantigen for Type I diabetes mellitus (T1D) [93, 338]. ZnT8 autoantibody levels are predictive biomarkers for T1D [130, 135]. The importance of ZnT8 in the etiology of Type II diabetes mellitus (T2D) became clear when the ZnT8 gene *SLC30A8* was first associated with a novel risk locus for T2D, in which the C-allele encodes a major nonsynonymous SNP at Arg325 [119-122]. One study showed a 24% increase in disease frequency with this risk allele [122], which was present at a very high level (55-75%) in the populations studied. The estimated population risk of T2D attributable to this polymorphism is ~9% [123]. In particular, this risk allele is associated with (i) an increase in the ratio of circulating proinsulin-to-insulin, (ii) a decrease in the response to insulin

[21] and (iii) an imbalance of zinc between secretory vesicles and the cytoplasm [17]. Point mutations in the carboxy-terminal domain can increase the risk of T1D and T2D [93]. Paradoxically, frameshift or premature termination mutants actually decrease the risk of diabetes. Taken together, the results suggest that ZnT8 could be an important drug target in the treatment of diabetes [71].

Zinc has a significant role in all processes of insulin trafficking -- synthesis, storage and secretion -- and may also be important in communication between α - and β -cells in the Islets of Langerhans [92, 93]. ZnT8 is expressed almost exclusively in pancreatic islets, mainly restricted to membranes of insulin secretion granules in β cells [65]. ZnT8 regulates transport of Zn^{2+} ions into the lumen of secretory granules in exchange for protons that are translocated by the vesicular ATPase proton pump [339]. Within the lumen of insulin secretory granules, Zn^{2+} ions are chelated by hexamers of insulin to facilitate storage [63, 92]. Recent fluorescent dye transfer in proteoliposomes suggested that the activity of ZnT8 is dependent on the lipid environment [70]. Interestingly, this work also showed that the wild-type Arg325 variant of ZnT8, which confers susceptibility to T2D, displayed higher Zn^{2+} transport activity than the Trp325 isoform.

Studies using transgenic mice have shown that ZnT8 plays a role in β -cell survival and the physiologic response to glucose [340]. As expected, ZnT8 knockout mice do not display zinc-insulin crystals within β -cell secretory granules; however, the animals displayed normal glucose homeostasis [102]. Nevertheless, mice with a specific knock

down of ZnT8 in islet cells display a more drastic phenotype, with abnormal β -cell morphology and impaired glucose homeostasis, which resembles that shown by human carriers of the ZnT8 risk allele [105].

The 40 kDa ZnT8 protein (369 amino acids) has an \sim 8 kDa acidic amino-terminal domain, a putative six-helix transmembrane (TM) bundle core, and a \sim 10 kDa acidic carboxy-terminal domain predicted to have a mixed α - β fold (Figure 2.1) [63, 90]. A truncated isoform of 35 kDa known as ZnT8B has been found *in vivo* and is thought to be the result of translational initiation at a second Met codon at the end of the N-terminal domain [82].

The bacterial homolog, YiiP, has 17% sequence identity over 290 of 369 amino acids in ZnT8, and has provided the only available structures of a zinc transporter [42, 43, 45, 102]. YiiP crystallized as a dimer in a detergent mixture of n-undecyl- β -D-maltoside and fos-choline 12 (FC-12). The monomers are non-covalently associated via a charge ring of two Lys-Asp pairs, which are thought to form a pivot for transmitting structural changes from the cytoplasmic to the TM domains [43]. Whereas the X-ray structure represents an outward-facing conformation [42], the structures determined by electron microscopy (EM) of YiiP incorporated into helical, lipid nanotubes were consistent with an inward-facing conformation [45, 55]. The moderate 13 Å resolution cryoEM structure helped explain the structural foundation for Zn²⁺ transport as occurring by an alternating access mechanism [45]. The follow-up structure at 4.1 Å resolution identified the interface

between membrane domains as a strong determinant of dimerization. This could provide a stable scaffold for “rocking and twisting movements” of the four-helix bundle that is required for alternating access of Zn^{2+} to opposite sides of the membrane. The study also found that the characteristic splaying of transmembrane domains observed in the X-ray structure was not necessary for transport activity, thus questioning the physiological relevance of that structure [55].

It is important to note that ZnT8 has several unique features not present in YiiP:

- (i) An additional 49 N-terminal residues of unknown fold;
- (ii) A C-tail extension of ~12 residues, which contains three cysteines;
- (iii) A cytoplasmic His-rich loop; and
- (iv) A predicted Zn^{2+} binding site composed of two paired His and Asp residues in TM domains 2 and 5. Regarding this last feature, YiiP has an Asp/Asp-Asp/His motif for binding Zn^{2+} ions, whereas the homologous site in ZnT8 bears a His/Asp-His/Asp motif (Figure 2.1). These two pairs of amino acids form one of the zinc binding sites, mediating Zn^{2+} transport and selecting against Cd^{2+} , making it unique in the ZnT family [66]. The His-rich loop is essential for Zn^{2+} transport [40, 53], and a working model suggests that this loop cooperates with the TM and the cytoplasmic C-terminal domains to function as a zinc sensor and regulate Zn^{2+} transport activity [1].

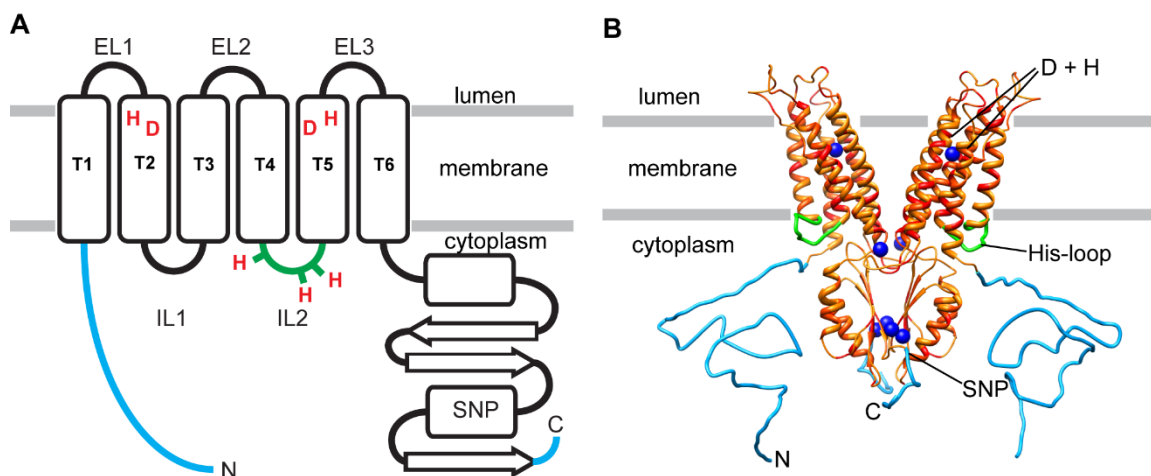


Figure 2.1. ZnT8 topology and structural models based on YiiP, a bacterial homolog. (A) Topology model of ZnT8 indicating positions of the R325W SNP, zinc-sensing His-rich loop (IL2), and pair of His (H) and Asp (D) residues in TM 2 and 5 that are conserved in mammalian ZnT proteins. Also shown are the 49 N-terminal and ~12 C-terminal residues not found in YiiP. (B) Homology model of ZnT8 showing identical residues in YiiP (red), conserved substitutions (dark orange), extended N- and C-termini of ZnT8 (light blue), and zinc atoms observed in YiiP (dark blue spheres).

Except for YiiP, only one structure of a zinc transporter has been published. The bacterial ZitB protein belongs to CorA metal ion transporter (MIT) family and both its oligomeric state and the architecture of the domains are radically different from those in YiiP. ZitB was shown to be able to bind Zn^{2+} , Cd^{2+} and Ni^{2+} and transport them across the membrane in a pH gradient-dependent manner, indicating that this protein is an importer of Zn^{2+} , unlike the Zn^{2+} -efflux proteins YiiP and ZnT8 [57].

To our knowledge, no structure of a human zinc transporter has been determined. We therefore overexpressed and purified recombinant ZnT8 from the yeast *Pichia pastoris* and *Sf9* insect cells, which are cost-efficient alternatives to mammalian expression systems. An *in vivo* assay in yeast cells showed that recombinant ZnT8

enhances zinc efflux from yeast cells. In addition, liposomes reconstituted with purified ZnT8 recapitulated the $\text{Zn}^{2+}/\text{H}^{+}$ antiport activity seen for YiiP and other ZnT proteins [341]. CD spectroscopy suggested that the amino-terminal domain contains β -sheet and turn secondary structure, while the carboxy-terminal domain has a mixed α -helical and β -sheet structure. Biochemical analysis indicated that purified ZnT8 is dimeric when solubilized in detergent micelles, which was confirmed by EM and single particle image analysis. The overall molecular boundary of ZnT8 was similar to that of YiiP.

2.2 Methods

Gene Synthesis and Cloning

Escherichia coli.

The amino- and carboxy-terminal domains of ZnT8A (Uniprot ID Q8IWU4-1) were fused to the carboxy terminus of bacterial thioredoxin (TRX) using the pET32 *Escherichia coli* expression vector (Novagen, Madison, WI). Synthetic genes corresponding to the amino-terminal 73 amino acids or the carboxy-terminal 95 amino acids of full-length ZnT8 were generated (GenScript) and then subcloned into the vector between the NcoI and NotI restriction sites. A construct of TRX alone was generated using QuickChange PCR mutagenesis (Agilent, Santa Clara, CA) to insert a transcriptional stop codon sequence at the NcoI restriction site of pET32. These constructs were then transformed into BL21(DE3) *E. coli* for protein overexpression. All constructs were verified by DNA sequencing (GENEWIZ, Frederick, MD) from both the 5' and 3' ends of the insert.

Pichia pastoris.

ZnT8 gene constructs (Figure 2.2) were synthesized (GenScript) either as the full-length protein ZnT8A or based on the transcriptional variant ZnT8B in which an internal Met codon (Met50) forms the translational start site [82]. *PpZnT8Bopt1* was constructed to have a carboxy-terminal G₃H₆ sequence with a proprietary *Pichia pastoris*-optimized codon bias (GenScript, Piscataway, NJ). *PpZnT8Bopt2* was constructed with a proprietary *P. pastoris*-optimized codon bias (GenScript) and designed to include a carboxy-terminal G₃-tev-G₃-H₁₀-G₃-FLAG sequence adding a tobacco etch virus (tev) protease-cleavable decahistidine and FLAG tag. *PpZnT8Bopt2* was also designed with a membrane protein-optimized *P. pastoris* codon bias [342]. These genes were separately cloned into the pPICZ vector (Invitrogen) and transformed into *P. pastoris* strain KM71H (Invitrogen) by electroporation [343].

Spodoptera frugiperda (Sf9).

A ZnT8A gene construct was designed with a carboxy-terminal G₃-tev-H₁₀ sequence adding a tev protease-cleavable decahistidine tag. A ZnT8B gene construct was designed with a carboxy-terminal G₃-H₆ tag. Both genes were codon-optimized for expression in Sf9 insect cells (GenScript). These genes were cloned separately into pVL1393 donor plasmids (AB Vector), which were then used to generate virus expressing recombinant protein via a commercial baculovirus expression system (BD BaculoGold, BD

Biosciences). Constructs were verified by DNA sequencing from both the 5' and 3' ends of the insert.

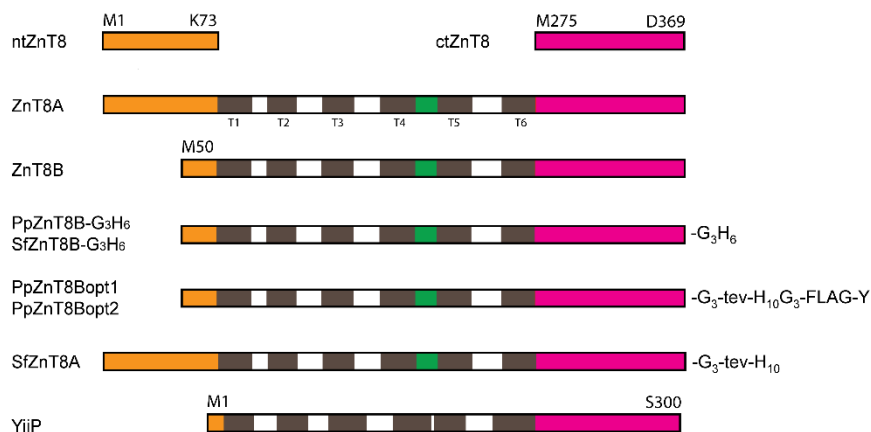


Figure 2.2. Illustration of protein constructs used in this study. Cytoplasmic amino-terminal domains (orange), cytoplasmic carboxy-terminal domains (red), His-rich loop (green), and transmembrane domains of ZnT8 (grey). Amino acid residue and position above construct shows amino acid residue and position of start or end of domain. The letters Pp at start of construct name denotes expression in *P.pastoris*; the letters Sf denote expression in *S.frugiperda* (*Sf9*). Amino acid sequences for PpZnT8Bopt1 and PpZnT8Bopt2 are identical, first construct is codon-optimized using a global *P.pastoris* codon bias, whereas the second is codon-optimized using a *P.pastoris* membrane protein codon bias. FLAG sequence: DYKDDDK, tev sequence: ENLYFQS. Illustration of YiiP shown at bottom for comparison.

Protein expression

Escherichia coli.

Expression of N- and C-terminal domains of ZnT8A in *E. coli* was performed using an auto-induction method [344]. Cells were initially grown in 2x Luria Broth media (2% tryptone, 1% yeast extract, 1% NaCl (pH 7.2)) with shaking at 37 °C to an optical density at 600 nm (OD_{600nm}) of ~2, then diluted 1/100 into 1 L of ZYM-5052 media [344] in 2.8 L baffled Fernbach flasks. The cell culture was shaken continuously, first at 37 °C for 2 hrs

and then at 25 °C for 20-24 hrs. Cells were recovered by centrifugation at 5000 x *g* for 10 min at 4°C. The resulting cell pellet was frozen and stored at -80 °C.

Pichia pastoris.

A fresh culture was started by incubation of an isolated yeast colony in 10 ml of BMGY medium (1% yeast extract, 2% peptone, 1.34% yeast nitrogen base, 100 mM potassium phosphate (pH 6.0), 4×10^{-5} % biotin, and 1% glycerol) overnight at 30 °C with shaking at 275 rpm. A larger volume of BMGY medium (100-200 ml) was inoculated with a 1/100 volume of the starting culture. The second culture was incubated for ~12 h at 30 °C with shaking at 250 rpm. Cells were harvested at an OD_{600nm} of 1-4 and pelleted by centrifugation for 5 min at 1500 x *g*. Induction of protein expression was initiated by resuspending the yeast cells in BMMY medium (1% yeast extract, 2% peptone, 1.34% yeast nitrogen base, 100 mM potassium phosphate (pH 6.0), 4×10^{-5} % biotin, and 1% methanol) to an OD_{600nm} of 1-2 in a volume of 0.1-1.0 l. Incubation was continued at 28 °C with shaking at 175 rpm in baffled culture flasks for 24 hrs. Following induction, cells to be used in assays of protein function were stored at 4 °C and used within four days. Cells for protein purification were pelleted by centrifugation at 4000 x *g* for 15 min at 4 °C. The cell pellet was then frozen and stored at -80 °C.

Spodoptera frugiperda.

Insect cells were infected with baculovirus at a multiplicity of infection (MOI) of 5 and incubated at 27 °C with shaking at 150 rpm. Cells were harvested 48–58 h post

infection and pelleted by centrifugation for 15 min at 4000 x g. The cell pellet was washed with phosphate-buffered saline (PBS) and the washed cells were pelleted by centrifugation at 3000 x g for 10 min. The cell pellet was then frozen and stored at -80 °C.

Protein purification

N- and C-terminal ZnT8 domains from E. coli.

Cells were resuspended in Lysis Buffer E (50 mM HEPES pH 7.5, 250 mM NaCl, 5 mM benzamidine, 20 mM imidazole, 1 mM PMSF) and then disrupted by passage 3-4 times through an 87 μ m interaction chamber at 25,000 PSI using a model M-110P microfluidizer (Microfluidics, Westwood, MA). Cell debris was removed by centrifugation of the lysate at 25,000 x g for 15 min at 4 °C. The clarified solution was mixed with Talon metal affinity resin (Clontech, Mountain View, CA) by gentle stirring for 1-2 h at 4 °C. The resin was pelleted by centrifugation at 500 x g for 10 min at 4 °C and transferred into a chromatography column. The column was washed six times with 10 column volumes (cv) of Lysis Buffer E supplemented with 5 mM β -mercaptoethanol (β -ME) and washed three times with 10 cv of Wash Buffer E (50 mM HEPES pH 7.5, 250 mM NaCl, 20 mM imidazole, 5 mM β -ME). The column was then eluted with four 1-cv aliquots of Elution Buffer E (25 mM HEPES pH 7.2, 100 mM NaCl, 250 mM imidazole, 5 mM β -ME). The eluates were pooled and transferred into a 10,000 MWCO Slide-A-Lyser (ThermoScientific) and dialyzed against Dialysis Buffer E (25 mM Bis-Tris pH 6.5, 100 mM K₂SO₄, 3 mM sodium azide, 10 mM β -ME) overnight at 4 °C. The dialysis buffer was then replaced with the same

volume of fresh buffer, and dialysis was continued for another day. The dialysate was recovered and concentrated to 1 mL using a 10,000 MWCO VivaSpin15R concentrator (Vivaproducts, Littleton, MA) by centrifugation at 1000 x g at 4 °C. This concentrate was applied to a HiLoad 16/600 Superdex 75 chromatography column (GE Healthcare Bio-Sciences, Pittsburg, PA). Following equilibration, chromatography was performed at a flow rate of 1.0 mL/min with Dialysis Buffer at 4 °C, and 2.0 mL fractions were collected. Fractions containing purified protein were identified by SDS-PAGE and stored at 4 °C.

To cleave TRX from the fusion proteins, aliquots of TRX-ntZnT8 or TRX-ctZnT8 were supplemented with CaSO₄ to 2 mM. Recombinant bovine enterokinase (GenScript) was added following the manufacturer's recommendations and incubated for 20 hrs at room temperature. The samples were then applied to a 7.8 x 300 mm Zenix SRT-150 chromatography column (Sepax Technologies, Newark, DE) and equilibrated. Chromatography was performed at 0.5 mL/min with Dialysis Buffer E at 4 °C, and 0.25 mL fractions were collected. Fractions containing purified ntZnT8 or ctZnT8 were concentrated using a 5,000 MWCO VivaSpin500 concentrator (VivaProducts) by centrifugation at 10,000 x g at 4 °C.

ZnT8B from P. pastoris.

Yeast cells were resuspended in Lysis Buffer (50 mM Na-PO₄ pH 7.0, 500 mM NaCl, 10% glycerol (v/v), 1 mM PMSF) and then disrupted by injecting 7-10 times at 30,000 PSI through an 87 µm interaction chamber, using a model M-110P microfluidizer

(Microfluidics). Cell debris was removed by centrifugation of the lysate at 4500 x *g* for 15 min at 4 °C. Membranes were then harvested by centrifugation of the supernatant at 185,000 x *g* for 45 min at 4 °C. The membrane pellet was resuspended in Lysis Buffer using a Dounce homogenizer, and centrifugation was repeated as before. The washed membranes were then resuspended in Extraction Buffer (50 mM Na-PO₄ pH 7.0, 500 mM NaCl, 10% glycerol (v/v), 1 mM PMSF, 20mM imidazole) using 15 pestle strokes in a glass Dounce homogenizer, and Triton X-100 was added to obtain a final detergent concentration of 4%. Four detergents were initially tested for their ability to solubilize yeast membrane proteins (Supplementary Table S1). Triton X-100 was selected based on efficiency of solubilization and cost. The membranes were incubated in Extraction Buffer containing 4% Triton X-100 for 3 h at 4 °C. Insoluble material was then removed by centrifugation at 185,000 x *g* for 45 min at 4 °C. The clarified solution was mixed with Talon IMAC resin (Clontech) by gentle stirring for 3 h at 4 °C. The resin was pelleted by centrifugation at 1000 x *g* for 10 min at 4 °C, and the supernatant was decanted into a chromatography column. The column was washed seven times with 10 column volumes (cv) of Wash Buffer (50 mM Na-PO₄ pH 7.0, 500 mM NaCl, 10% glycerol (v/v), 1 mM PMSF, 20mM imidazole, 0.14% FC-12) followed by elution with three cv of Elution Buffer (50 mM Na-PO₄ pH 7.0, 500 mM NaCl, 10% glycerol (v/v), 1 mM PMSF, 500mM imidazole, 0.14% FC-12). The eluates were pooled and injected into a 10,000 MWCO Slide-A-Lyser (ThermoScientific) for overnight dialysis at 4 °C against SEC/Dialysis Buffer (25 mM triethanolamine (TEA) pH 7.0, 500 mM NaCl, 5% glycerol (v/v), 1mM PMSF, 0.26% FC-12).

The dialysate was recovered and concentrated to ~1 ml by centrifugation at 225 x *g* at 4 °C using a 50,000 MWCO VivaSpin4 concentrator (Vivaproducts). The concentrated solution was pipetted onto a 7.8 x 300 mm SRT-C SEC300 SEC column (Sepax Technologies) that had been equilibrated at 4 °C in SEC/Dialysis Buffer. Chromatography was performed on an AKTA Explorer 10 (GE Healthcare) at 4 °C using a flow rate of 0.3 ml/min. Fractions (0.16 ml) containing purified ZnT8B were identified by SDS-PAGE and Western immunoblot analysis, and pooled fractions were stored at 4 °C. Blue native non-denaturing electrophoresis was performed as previously described [345]. Protein concentrations were determined using the MicroBCA assay (Pierce Biotechnology, Rockford, IL).

Well	Abbreviation	Name	Vendor	Type	MW	CMC (%)	final %
B4	FC-12	fos-choline 12	Anatrace	zwitterionic	351.5	0.047	0.5
D1	TX-100	Triton X-100	Anatrace	nonionic	647	0.010	4.0
G7	DM	n-decyl- β -D-maltopyranoside	Anatrace	nonionic	482.6	0.087	1.0
G12	DDM	n-dodecyl- β -D-maltopyranoside	Anatrace	nonionic	510.6	0.0087	0.5

Table 2.1. Detergents screened for membrane solubilization and extraction of ZnT8B

ZnT8A and ZnT8B from Spodoptera frugiperda.

Cell pellets were resuspended in 100 mL Low-Salt Buffer (50 mM TEA pH 7, 100 mM NaCl, 5 % glycerol (v/v), 1 Complete protease inhibitor cocktail pill w/out EDTA per 50 ml of lysate (Roche)). Cells were disrupted with 20–30 pestle strokes in a glass Dounce homogenizer. Nucleic acids were digested by adding MgCl₂ to 2.5 mM and adding 12.5 units/mL of Benzonase (EMD Millipore), followed by 15 min of gentle stirring at 4 °C. Membranes were then harvested by centrifugation of the supernatant at 125,000 x *g* for

30 min at 4 °C. The membrane pellet was washed twice with High-Salt Buffer (Low-Salt Buffer with NaCl increased to 500 mM). Membrane aliquots were flash frozen in liquid N₂ and stored at -80 °C. When needed, membranes were thawed on ice and resuspended in Extraction Buffer (50 mM TEA pH 7, 500 mM NaCl, 5 % glycerol (v/v), 20 mM imidazole) with 10-15 pestle strokes in a glass Dounce homogenizer. Membranes were solubilized by addition of n-decyl-β-D-maltopyranoside (DM) to a final detergent concentration of 1% (w/v) and gentle stirring for 3 h at 4 °C. Insoluble material was removed by centrifugation at 125,000 x *g* for 45 min at 4 °C. His-tagged ZnT8 was purified from the clarified, solubilized membranes by Talon resin IMAC (Clontech). One ml of affinity resin was added per 50 ml detergent extract, and the suspension was stirred gently for 1 h at 4 °C. The resin was pelleted by centrifugation at 500 x *g* for 5 min at 4 °C, and the supernatant was decanted into a 10 x 100 mm glass chromatography column. DM was exchanged for fos-choline 12 (FC-12) on the column by washing with five column volumes (CVs) of Wash Buffer (50 mM TEA pH 7, 500 mM NaCl, 5 % glycerol (v/v), 20mM imidazole, 0.14% FC-12). During the fourth wash, the column was capped, kept stationary and equilibrated with the new detergent for 15 min at 4 °C. ZnT8 was eluted from the column with 2 CV of Elution buffer (50 mM TEA pH 7, 500 mM NaCl, 5 % glycerol (v/v), 500 mM imidazole, 0.14% FC-12). The eluate was injected into a 10,000 MWCO Slide-A-Lyser (ThermoScientific) for overnight dialysis at 4 °C against SEC/Dialysis Buffer (25 mM TEA pH 7.0, 500 mM NaCl, 5% glycerol (v/v), 2 mM DTT, 0.14% FC-12). The dialysate was collected and concentrated to ~1 ml by centrifugation at 225 x *g* at 4 °C using a 50,000

MWCO VivaSpin4 concentrator (VivaProducts). The concentrate was injected into a 7.8 x 300 mm SRT-C SEC300 SEC column (Sepax Technologies) that had been equilibrated at 4 °C in SEC/Dialysis buffer. Chromatography was performed with SEC/Dialysis Buffer on an AKTA Explorer 10 (GE Healthcare) at 4 °C using a flow rate of 0.3 ml/min. Fractions (0.16 ml) containing purified ZnT8B were identified by SDS-PAGE and Western immunoblot analysis, and pooled fractions were stored at 4 °C. Protein concentrations were determined by their molar absorptivity using a NanoDrop 1000 spectrophotometer (Thermo Scientific), assuming a molar absorption coefficient of 43,000 L/mol-cm for ZnT8A and 40,600 L/mol-cm for ZnT8B.

SDS-PAGE and Western immunoblot analysis.

Protein aliquots were resuspended in SDS sample buffer (2% SDS, 50 mM Tris-HCl [pH 7.5], 10% glycerol, 100 mM dithiothreitol), and incubated at 50 °C for 30 min. SDS-PAGE was performed using a 4-20% acrylamide gradient Tris-glycine gel (Bio-Rad) with Precision Plus (Bio-Rad) prestained protein molecular weight standards. Gel-separated proteins were then electroblotted onto a nitrocellulose membrane. Western immunoblot analysis [346] was performed with ZnT8 polyclonal antibodies diluted 10,000-fold in Blocking Buffer (LI-COR, Lincoln, NE). Donkey anti-rabbit immunoglobulin G antisera coupled to IRDye 800 (LI-COR) was diluted 20,000-fold and used to label the primary antibodies. Detecting the fluorescence of the bound antibodies at a wavelength of 800 nm was accomplished using an Odyssey infrared scanner (LI-COR). Digitized images of the

immunoblot results were corrected for background and contrast using Photoshop (Adobe Systems, San Jose, CA). Densitometry to quantify antibody labeling was performed using NIH-ImageJ [347].

Detergent screening

An array of 96 non- and zwitter-ionic detergents was screened using a differential filtration assay (DFA; Selector Kit, Anatrace, Maumee, OH; Figure S3). The estimated mass of the ZnT8B protein-detergent complex was 100-300 kDa, so that complexes that did not pass through the 300 kDa filter were an indication of protein aggregation. Western immuno-dot-blot analysis, performed as described above, identified 17 detergents in which the ZnT8B protein-detergent complexes passed through the 300 kDa cut-off filter (Table S2).

Solutions of each detergent were prepared in Wash Buffer with detergent concentrations 5-10 x the published critical micellar concentration (CMC) and in Elution Buffer with 1.5-3.0 x the CMC. [348, 349]. ZnT8B was bound to a Talon immobilized metal affinity chromatography (IMAC) column in Wash Buffer with Triton X-100 as described above. The resin was washed with Wash Buffer, and the protein was eluted with Elution Buffer, in which both buffers contained each of the 17 detergents. The eluate was dialyzed as before, but with the new detergent at a concentration of 1.5-3.0 x CMC in SEC/Dialysis Buffer. ZnT8B samples adjusted to the same concentration in each of the 17 detergents were then examined by analytical size exclusion chromatography at 4 °C using a 5 x 150

mm Superdex 200GL chromatography column (GE Healthcare) that had been equilibrated with SEC/Dialysis Buffer containing the same detergent used for elution from the IMAC column. Fractions collected at 0.3 ml/min were examined by Western immunoblot analysis to detect ZnT8B in the chromatogram. FC-12 and APX305 were the optimal detergents for solubilization, on the basis of having the highest OD_{280 nm} ratio of the protein peak to the void peak in the SEC profile (Table S2).

Fluorescent Thermal Stability Assay

Thermal stability of ZnT8 in FC-12 was measured by the fluorescence of the cysteine-reactive dye 7-diethylamino-3-(4'-maleimidylphenyl)-4-methylcoumarin (CPM) over a temperature gradient (10 to 95 °C). The ZnT8B construct has eight potentially free cysteines in the transmembrane domain and five in the soluble domains. (As in the homologous YiiP X-ray structure, our homology model suggests that no cysteines are bonded.) With increasing temperature, ZnT8 unfolds and the dye binds to the thiols and emits fluorescence.

An aliquot of CPM dye (Invitrogen) at 1 mM in dimethylformamide was diluted 1:75 into either a sample of protein at ~50 µg/ml or a buffer-only control. For these experiments, we used was the SEC/Dialysis Buffer (25 mM TEA pH 7.0, 500 mM NaCl, 5% glycerol (v/v), 1mM PMSF, 0.26% FC-12). Following a 15 min incubation on ice, the sample was transferred into a 1.5 mm pathlength quartz spectrofluorometer cuvette (Hellma Analytics, Müllheim, Germany), which was inserted into a FluoroMax-3

spectrofluorometer (Horiba Jobin-Yvon, Edison, NJ) equipped with a thermoelectric, temperature-controlled cuvette holder. The excitation and emission wavelengths were set to 387 nm and 463 nm, respectively. The sample was heated from 5-95 °C at a rate of 2 °C/min, and the fluorescence was recorded every 1 min. The fluorescence versus temperature profile was analyzed by non-linear regression using a Boltzmann sigmoidal equation. The sample melting temperature (T_m) was calculated from the inflection point of the resulting melting curve as previously described [350].

Mass spectrometry

An aliquot of protein was diluted 1:10 with 0.1% trifluoroacetic acid and spotted on a stainless-steel target plate with an equal volume of 15 mg/ml sinapinic acid dissolved in 50% acetonitrile, 0.1% trifluoroacetic acid in water. MALDI-MS was performed using a MicroFlex LT (Bruker, Billerica, MA) calibrated with high molecular weight protein standards. The sample was shot at least 100 times in positive linear mode.

Circular dichroism spectrometry

Samples were prepared in 0.1 and 1.0 mm strain-free quartz cuvettes (New Era, Vineland, NJ) with a buffer of 2.5 mM HEPES- H_2SO_4 pH 6.5, 10 mM K_2SO_4 , 1.0 mM β -me and 0.3 mM sodium azide. Data were recorded at 10 °C on an Model 410 circular dichroism spectrometer (Aviv Biomedical, Lakewood, NJ) using a spectral bandwidth of 1.0 nm, a scanning step of 0.5 nm, and 4-8 sec data averaging per step. Data requiring a photomultiplier voltage greater than 600 VDC was discarded since the signal is typically

poor when collected at high voltages [351]. Three to five scans were averaged to generate the final spectra, after which the buffer-only spectra were subtracted from the protein solution spectra. Protein concentrations were determined by UV-Vis spectrometry, using the predicted molar extinction coefficients [352] of $12950 \text{ M}^{-1}\text{cm}^{-1}$ for ntZnT8, $7155 \text{ M}^{-1}\text{cm}^{-1}$ for ctZnT8, and $13980 \text{ M}^{-1}\text{cm}^{-1}$ for thioredoxin. To compensate for cuvette path-length errors, data collected using a 0.1 mm cuvette was scaled to fit the data collected using a 1.0 mm cuvette. Structural analysis was performed with the online DICHROWEB software suite [353]. Secondary structure was calculated using the CCSSTR algorithm [354]. A solution of holmium perchlorate was used to verify the wavelength accuracy of the spectrometer [355] and camphorsulfonic acid was used to calibrate signal intensity [356].

Electron Microscopy (EM)

For EM of negatively stained samples, a 3.0 μl drop of the FC-12 buffer containing ZnT8 at $\sim 1 \mu\text{g/ml}$ was incubated on a glow-discharged, carbon-coated copper grid for 60 sec. The grid was then washed with three drops of deionized water. The grid was then stained with a drop of freshly prepared 0.75% uranyl formate for 60 sec [357]. Sample, wash drops and the stain were blotted with filter paper. EM was performed using a Tecnai G2 F20 electron microscope (FEI, Hillsboro, OR) equipped with a field-emission electron source, operating at 120 keV. Low electron dose images ($\sim 15 \text{ e}^{-}/\text{\AA}^2$)—were recorded on a 4K x 4K pixel CCD camera (Gatan, Pleasanton, CA) at 62,000 x

magnification (corresponding to 1.8 Å / pixel) with a 1 sec exposure time at an underfocus value of ~1.5 µm.

Single-particle image analysis

The initial steps of image processing were performed using EMAN v2.05 software [358]. To facilitate particle picking, the contrast of the micrographs was enhanced by high- and low-pass Gaussian filtering at 100 and 10 Å, respectively. A total of 3,850 particles were picked manually using a square mask with an edge dimension of 168 Å. The image and particle coordinate files in .mrc and .box format, respectively, were imported into RELION v1.3 [359]. Corrections for effects of the contrast transfer function were performed using CTFFIND4 [360]. All picked particles were screened visually using the Z-score, and 'bad' particles were removed interactively. The remaining particles were then sorted by reference-free 2D classification into 25 classes. We removed particles that belonged to outlier classes with either very few particles per class or signs of protein aggregation, giving a final dataset of ~3,500 particles in 23 classes (Figure 6). EMAN2 was used to derive an initial map using reference-free methods. This map was truncated to 50 Å resolution (Figure S6A), which served as a reference for 3D classification using RELION. The resulting density map (Figure S6B) without applied symmetry (i.e. C1 symmetry) displayed a volume consistent with a ZnT8 dimer, and we therefore applied C2 symmetry and generated a new map (Figure S6C). Given the similarity in size and general appearance of this map to the bacterial homolog YiiP, the X-ray structure of YiiP [102] was

filtered to a resolution of 50 Å in EMAN2 and was used as a new reference for the 3D classification (Figure S7D). Since a map with C1 symmetry displayed dimeric features (Figure S6E), a final map was generated using C2 symmetry (Figure S6F). The resolutions of the maps in (Figure S6B, C, E and F) were calculated using the FSC method in which the data set was divided into two halves and refined independently.

Molecular modeling

To further interpret the 3D map of ZnT8, we generated a homology model of ZnT8 based on the X-ray structure of YiiP [102]. Several excellent applications exist for this purpose as outlined in Dolan *et al.* [361], and in line with their recommendations we chose the Modeller software package [362] for its user-friendliness and low cost. This homology model was then energy minimized and docked into the 3D EM reconstruction using the rigid fit tool in UCSF Chimera [362].

Functional assays

In vivo Zinc Uptake Assay.

P. pastoris transformed with *pPICZ* alone, *ZnT8Bopt1/pPICZ*, or *ZnT8Bopt2/pPICZ* were grown at 30 °C in BMGY media (1% yeast extract, 2% peptone, 100 mM potassium phosphate, pH 6.0, 1.34% yeast nitrogen base without amino acids, 0.4 µg/ml biotin and 1% glycerol) to an OD_{600nm} of 1-2, then diluted 1/100 in BMMY media (1% yeast extract, 2% peptone, 100 mM potassium phosphate, pH 6.0, 1.34% yeast nitrogen base without

amino acids, 0.4 µg/ml biotin and 1% methanol) and grown at 28 °C for 40-42 hrs with vigorous aeration in baffled flasks. An aliquot of each culture was then diluted to give an OD_{600nm} of 10 in 25 ml BMMY media and transferred into 250 ml baffled flasks, which were then incubated either on ice or at 23 °C with gentle shaking. $^{65}ZnCl_2$ (PerkinElmer, Boston, MA) was added to a concentration of 10 µM, after which 1.0 ml aliquots were collected at 15-30 min intervals. For each aliquot, cells were pelleted by centrifugation at 2700 x *g*, and the supernatant was discarded. Each cell pellet was washed with 1.0 ml BMMY media and re-pelleted as above. Each cell pellet was then resuspended in 150 µL BMMY media and transferred into a 25 mL glass scintillation vial. A 20 ml aliquot of Ultima Gold liquid scintillation cocktail (PerkinElmer) was added to each vial, and ^{65}Zn decay was measured using a model LS 6000SC scintillation counter (Beckman Instruments, Fullerton, CA). The experiments were replicated four times from three unique preparations of cells. The counting results for the four replicates were averaged and scaled so that the maximum signal from *pPICZ*-only control cells at the final time point was equal in each experiment.

In vitro liposome-based transport assay.

The lipid for protein reconstitution was prepared by mixing chloroform stocks of phosphatidylcholine (POPC) and phosphatidylserine (POPS) at a 2:1 mass ratio (Avanti Polar Lipids, Alabaster, AL). The lipid solutions were lyophilized for 2 hrs using a stream of dry argon gas followed by vacuum desiccation for 2 hrs. The dried lipids were rehydrated

at room temperature in Lipid Buffer (25 mM HEPES pH 7.5, 100 mM KCl and 2.3 % (w/v) n-octyl- β -D-glucopyranoside (OG)) to a final concentration of 10 mg/ml.

Aliquots of detergent-solubilized lipid were mixed with detergent-solubilized, IMAC-purified protein in a 1:3000 protein:lipid molar ratio, and the fluorescent Zn²⁺ indicator dye fluozin-1 (Life Technologies, Grand Island, NY) was added to a final concentration of 20 μ M. The sample was incubated in the dark for 1 h at room temperature. Control, protein-free liposomes were prepared using the same procedure. An Econo-Pac 10DG desalting column (Bio-Rad) was equilibrated with Sample Buffer containing either 25 mM HEPES pH 7.5 and 100 mM KCl or 25 mM MES pH 6.0 and 100 mM KCl. Shortly before purification on the column, the liposome sample was diluted with Sample Buffer sufficient to produce an OG concentration of 0.4%, thus bringing the detergent concentration below its critical micellar concentration (0.53%). A 200 μ l aliquot of 20 μ M Fluozin-1 in Sample Buffer was applied to the desalting column, followed by 1 ml of liposome sample and 2 ml of Sample Buffer. Elution of the resulting liposomes was performed by applying an additional 1.5 ml of Sample Buffer to the column and collecting 500 μ l fractions. The first fraction was discarded, and the two subsequent fractions were pooled and stored in the dark at room temperature.

Purified liposomes were mixed with 3 volumes of Sample Buffer at either pH 7.5 or 6.0. The sample was transferred into a quartz cuvette (Hellma Analytics, Mullheim, Germany), which was then inserted into the temperature-controlled holder of a

spectrofluorometer (Fluorolog-3, Horiba Scientific, Edison, NJ), with excitation and emission wavelengths set to 480 nm and 520 nm, respectively. The sample was constantly mixed using a magnetic stir bar, and after 1 min the extra-liposomal concentration of free Zn^{2+} was increased to 100 μ M by the addition of $ZnCl_2$. After 5 min the liposomes were solubilized by the addition of OG to 0.5 % (w/v). Spectra were recorded and analyzed using the DataMax software package. All experiments were performed at 22 °C.

2.3 Results and discussion

Despite its role in diabetes and cardiovascular disease and its concomitant potential as a drug target, little is known about the structure or transport mechanism of ZnT8.

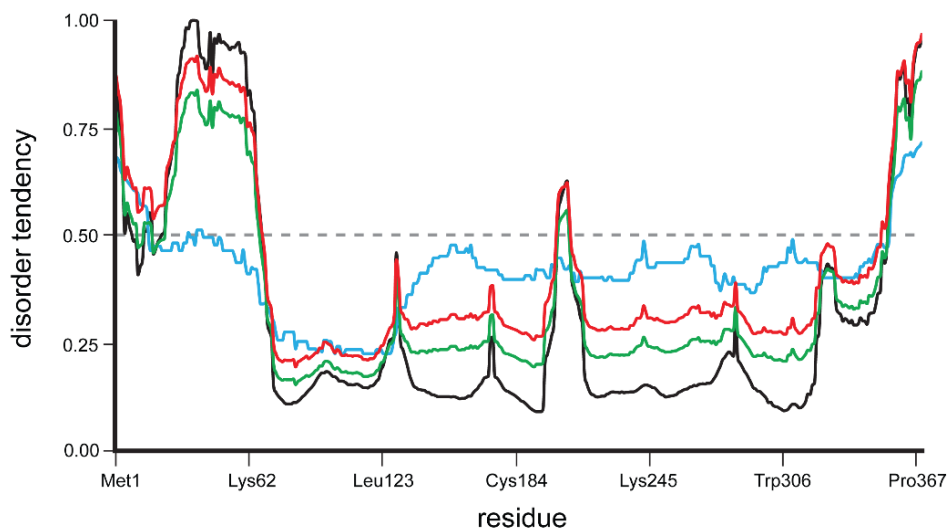


Figure 2.3. Predictions of disordered residues in ZnT8A. Plot shows disorder index values corresponding to the protein amino acid residues. MetaDisorder [363] calculations shown in black, with results from the 3D method in blue, MD method in green, and MD2 method in red. Residues with a score greater than 0.5 (dashed grey line) are predicted as likely being disordered. Note that the amino-terminal domain of ZnT8A (AA 1-73) is predicted to be mostly disordered.

To this end, we developed two *in vivo* transport assays, performed physicochemical studies and determined a low-resolution EM structure that provide a foundation for higher-resolution structural studies and potential drug discovery efforts. We initially focused our efforts on the amino-terminal truncated isoform ZnT8B since the amino-terminal domain was predicted to be disordered (Figure 2.3).

Recombinant human ZnT8 functions as a zinc antiporter

In vivo transport and viability assays show that ZnT8 is functionally active

A zinc uptake assay in *P. pastoris* showed that yeast overexpressing ZnT8B constructs with different codon bias (designated PpZnT8Bopt1 and PpZnT8Bopt2) exhibited a significant reduction in zinc uptake compared with control yeast (Figure 2.4A). The cell line producing the most ZnT8 (PpZnT8Bopt1) almost completely excluded labeled zinc (Figure 2.4A, dashed line), while the cell line producing ~40% less ZnT8 (PpZnT8Bopt2) (Figure 2.4C) accumulated half as much $^{65}\text{Zn}^{2+}$ as mock-transformed control yeast (Figure 2.4A, dotted line versus solid line). Although the opt2 construct was generated with a membrane protein-optimized *P. pastoris* codon bias [342], it showed no significant improvement on protein expression levels.

Zinc uptake was unidirectional: once accumulated, cell-associated $^{65}\text{Zn}^{2+}$ was not observed to decrease following incubation in media lacking Zn^{2+} . Since *Pichia stipitis* and *Saccharomyces cerevisiae* yeast generally have a cytoplasmic pH that is one pH unit higher than the media [364], the resulting proton gradient would greatly favor zinc export from

cells overexpressing a Zn^{2+}/H^{+} antiporter such as ZnT8. Supporting this idea, zinc uptake decreased in more acidic media, as the proton gradient disfavored zinc uptake (Table 2.2). We also noted that cadmium competed with zinc for uptake through the ZnT8 transporter (Table 2.2). Yeast expressing PpZnT8Bopt1 showed less zinc uptake than yeast expressing PpZnT8Bopt2, which is likely because of a ~40% reduction in ZnT8 accumulation by PpZnT8Bopt2-expressing cells (Figure 2.2 C). Cell densities of the three cultures remained comparable during the experiment, with the difference less than 20% at the end of the 2-hr assay period.

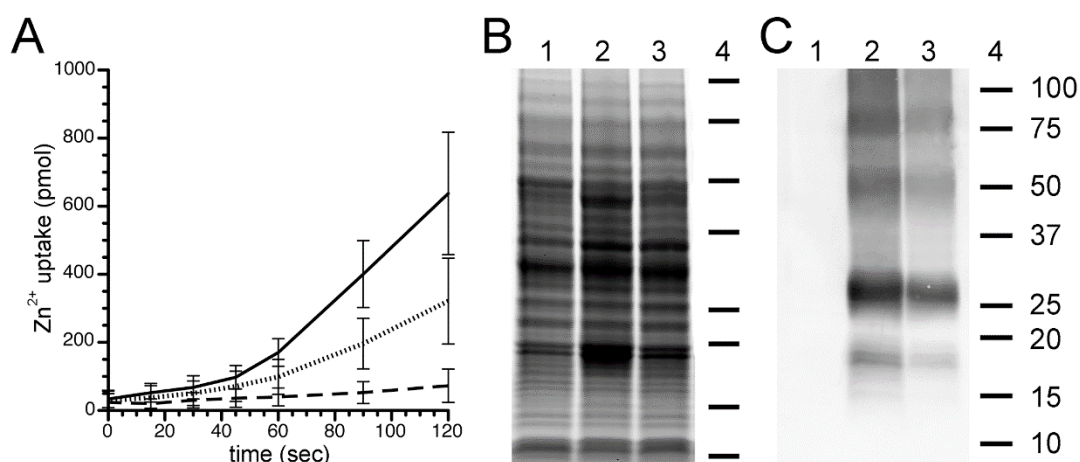


Figure 2.4. *P. pastoris* expressing ZnT8B exclude extracellular Zn^{2+} . (A) Yeast overexpressing either PpZnT8Bopt1 (dashed line), PpZnT8Bopt2 (dotted line), or expression vector alone (solid line) were supplemented with $10\ \mu M$ $^{65}ZnCl_2$ and aliquots were taken at time points thereafter. Uptake of $^{65}Zn^{2+}$ into the cells was measured using a scintillation counter. Results show the average of seven replicates, and error bars indicate ± 1 SD. SDS-PAGE of membrane-enriched protein fractions shown as a Coomassie stained gel (B) or Western immunoblot using ZnT8 antibodies (C). Extracts are from yeast expressing expression vector alone (lane 1), PpZnT8Bopt1 (lane 2), or PpZnT8Bopt2 (lane 3). Similarity in protein staining profiles (B) indicates comparable loading of protein, while the corresponding immunoblot (C) shows a 40% reduction of ZnT8B in PpZnT8Bopt1 compared to PpZnT8Bopt2. Molecular weight markers indicated in lane 4, with weight in kiloDaltons (kDa) shown to the right of lane 4 in panel C. Assay performed by Dr. Mark Daniels, University of Virginia.

	MMY (unbuffered)				BMMY pH 6.0
	pH 4.0	pH 5.0	pH 6.0	pH 6.0 + Cd ²⁺	
vector only	3.1 pmol/min	7.3 pmol/min	6.7 pmol/min	2.8 pmol/min	7.8 pmol/min
PpZnT8Bopt1	0.1	0.3	0.7	0.1	0.5
PpZnT8Bopt2	1.7	4.9	4.8	1.1	3.7

Table 2.2. Rates of zinc ion uptake in transformed *P. pastoris* cell cultures. Values shown are the average of at least three replicates. Assay performed by Dr. Mark Daniels, University of Virginia.

The yeast cell wall can adsorb zinc [365], which could result in spuriously elevated levels of zinc uptake. To address this, we repeated our Zn²⁺ uptake assay with yeast cultures incubated on ice. A slight amount of zinc immediately became associated with the cells, but this amount did not change over time and was similar for the three cell lines tested (Figure 2.5). Since this background signal did not change over time, its effect on our assay results is negligible. Taken together, these results suggest that any growth-related increase in the amount of zinc-adsorbing cell wall was insignificant compared to the effects of ZnT8 expression.

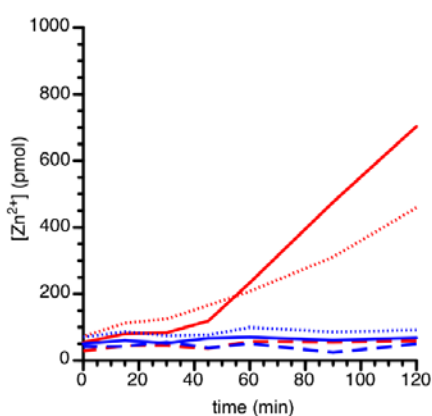


Figure 2.5. Temperature-dependent ⁶⁵Zn²⁺ uptake indicates that activity is protein-dependent. Yeast overexpressing PpZnT8Bopt1 (dashed line), PpZnT8Bopt2 (dotted line), or expression vector alone (solid line) were incubated at either 23 (red) or 0 °C (blue), the extracellular media was supplemented with 10 μM ⁶⁵ZnCl₂, and aliquots were taken at time points thereafter. Uptake of ⁶⁵Zn²⁺ into the cells was measured using a scintillation counter. Assay performed by Dr. Mark Daniels, University of Virginia.

In vitro transport assay shows that ZnT8 from P.pastoris is functionally active.

Proteoliposomes were formed by using size-exclusion chromatography to rapidly remove the solubilizing detergent from a ZnT8-lipid-detergent solution. The chromatography buffer included the zinc fluorophore fluozin-1, which was captured in the proteoliposome lumen as it formed (Figure 2.6A). Electron microscopy showed that negatively-stained proteoliposomes were primarily unilamellar and uniform in appearance with a diameter of 70 – 120 nm (Figure 2.6B). To determine zinc uptake, the liposomes were prepared with a proton gradient in which the internal pH was 6.0 and the external buffer pH was 7.5. ZnCl₂ was added to 100 μM, and the change in fluozin-1 fluorescence over time was measured. At the conclusion of the assay β-octylglucoside was added to a final concentration of 1%, which solubilized the liposomes and exposed the fluozin-1 dye to the zinc in solution, from which a reference maximum fluorescence was determined. Compared with control liposomes, ZnT8-containing liposomes displayed a significant increase in fluorescence in the presence of Zn²⁺ (Figure 2.6C). When the pH gradient was eliminated, the fluorescence change was reduced (Figure 2.6D), which was also observed when the pH gradient was reversed (Figure 2.6E), supporting our observation that Zn²⁺ uptake via ZnT8 was driven by H⁺ efflux resulting from the pH gradient across the liposome membrane. Since ionic metals do not have a membrane-permeable neutral form, any increase in liposome fluorescence results from ZnT8-mediated zinc transport. The increase in fluorescence observed for control, protein-free

liposomes is possibly due to either adsorption of fluozin-1 to the lipid layer or residual dye in the buffer.

These *in vitro* results are in agreement with the prevailing notion that ZnT8 operates as a $\text{Zn}^{2+}/\text{H}^+$ antiporter, similar to the bacterial homolog YiiP. In addition, the results are consistent with the inward proton gradient between the insulin secretory vesicle lumen and the β -cell cytoplasm, which is a necessary component for ZnT8-mediated zinc loading of these vesicles [339].

Implications for the zinc transport mechanism

A necessary component for zinc/proton antiport is a proton gradient across the cell membrane. We have not characterized the driving force for zinc ion export from the cell cytoplasm by ZnT8 in the *P. pastoris* plasma membrane, but we hypothesize that this yeast has the requisite proton gradient. Aerobically cultured yeast have a cytoplasmic pH of ~ 7 when grown in media buffered to pH 6 [364, 366], which would suggest that a favorable proton gradient is present. Rapid zinc uptake by *P. pastoris* is likely since *Saccharomyces cerevisiae* and other yeast have a zinc import system comprised primarily of the Zrt1 high-affinity and the Zrt2 low-affinity zinc transporters [367], which are both members of the taxonomically widespread ZIP protein family [61]. The mechanism of Zn^{2+} transport in this family is unknown, but may be via HCO_3^- symport as described for human ZIP2 [368].

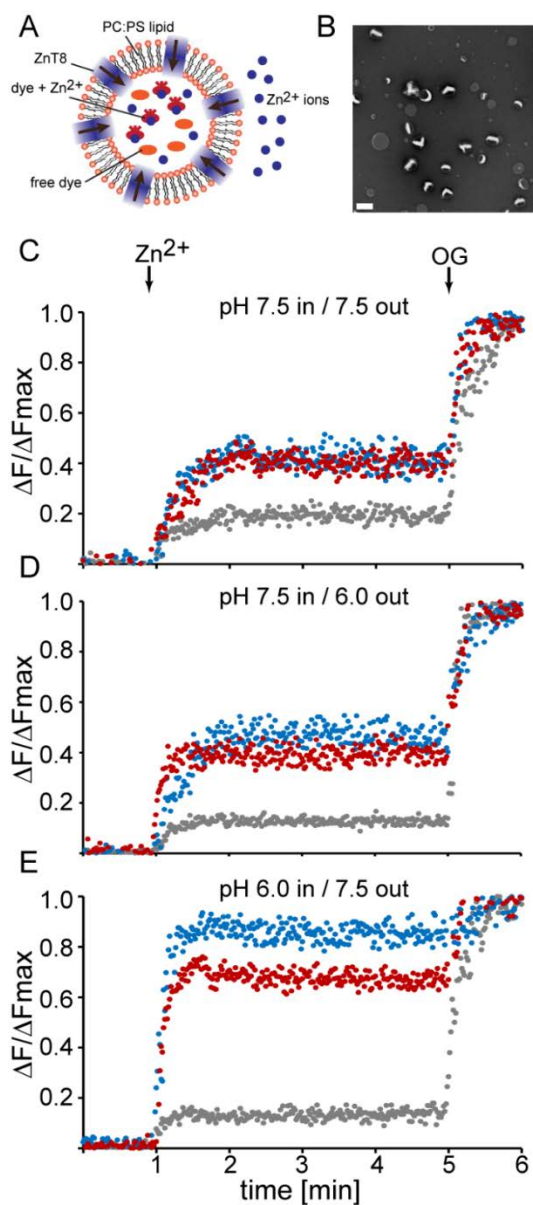


Figure 2.6. In vitro liposome assay indicates that both purified ZnT8 isoforms A and B are functional. (A) A cartoon model representing the principle of the assay. (B) An electron micrograph of negatively-stained ZnT8 proteoliposomes; white bar denotes 200 nm. (C) Transport of Zn²⁺ by reconstituted ZnT8 with both liposomal and external pH of 7.5, (D) Transport with an internal liposome pH of 7.5 and an external buffer pH of 6.0, and (E) transport with an internal liposome pH of 6.0 and an external buffer pH of 7.5. Changes in fluozin-1 fluorescence upon Zn²⁺ and subsequent β -octyl glucoside (OG) addition (arrows), using either ZnT8A (blue trace) or ZnT8B proteoliposomes (red trace) or protein-free liposomes (grey trace). $\Delta F/\Delta F_{max}$ is the relative change in fluorescence normalized to the maximum fluorescence following proteoliposome dissolution by OG.

Structural analyses reveal that the transmembrane and carboxy-terminal domains of ZnT8 recapitulate that of the bacterial homolog YiiP

ZnT8B forms a stable dimer when purified in fos-choline 12

Full-length ZnT8A was expressed in *P. pastoris*, but this isoform expressed poorly and so we did not continue its study. In contrast, an amino-terminal truncated form of recombinant ZnT8, designated ZnT8B, expressed well in *P. pastoris* (Figure 2.7) and the protein was amenable to purification. In a parallel experiment we expressed full-length ZnT8A in *P. pastoris*, but this isoform expressed poorly and so we did not continue its study.

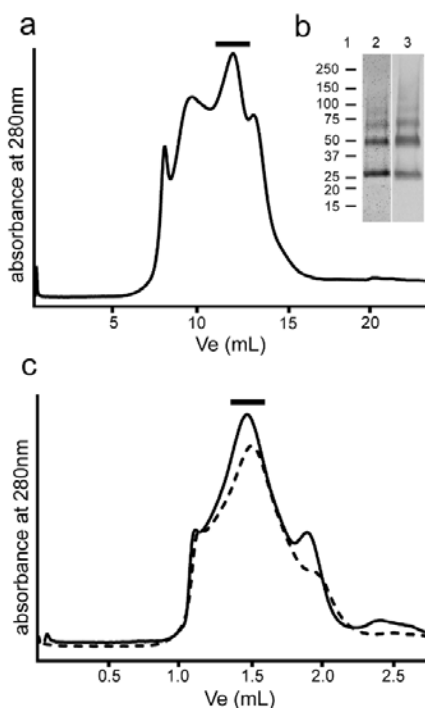


Figure 2.7. SEC purification of ZnT8B-G₃H₆ from *P.pastoris*. (A) SEC elution profile, indicating pooled peak fractions of apparent mass ~150 kDa (black bar). (B) Peak fractions contain ZnT8 as indicated by SDS-PAGE (lane 2) and Western immunoblot analysis (lane 3). Position of molecular weight markers in kDa are indicated. (C) Stability of ZnT8 shown by SEC elution profiles performed after 5 d (dashed line) and 10 d (solid line) incubation at 4 °C.

Guided by previous protocols for transporter solubilization from *P pastoris* and cost effectiveness [369, 370], membranes were solubilized in Triton X-100. Since ZnT8B was unstable in this detergent, we used a differential filtration assay (DFA) of 96 detergents (Figure 2.8) [371] to determine that ZnT8B displayed minimal aggregation when solubilized in the zwitterionic detergent fos-choline 12 (FC-12; Table 2.3). Triton X-100 was therefore exchanged to FC-12 during immobilized metal-affinity chromatography (IMAC). The protein was then purified to homogeneity by size-exclusion chromatography (SEC) (Figure 2.5).

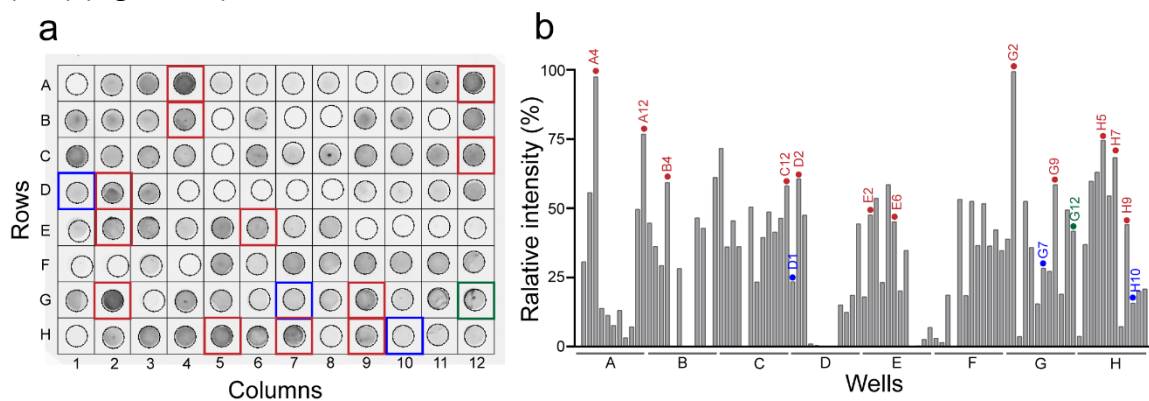


Figure 2.8. Differential filtration assay (DFA) used to guide detergent selection for protein solubilization. (A) Image of ZnT8 immunoblot showing minimally aggregated, detergent-solubilized protein able to pass through a nitrocellulose membrane with a 300 kDa molecular weight cutoff. (B) Densitometry of immunoblot shown in (A). Detergents selected for further analysis by IMAC and SEC were chosen based upon DFA performance (red), success in solubilizing the bacterial homolog YiiP (green), or previous experience in our laboratory (blue). Well detergents are as described in the Selector Kit method (Anatrace).

A thermal denaturation assay measuring the accessibility of a thiol-reactive fluorescent dye to free cysteine residues showed that the melting temperature of the ZnT8B/FC-12 complex is $\sim 57^\circ\text{C}$ (Figure 2.6A), which is within the range observed for stably folded membrane proteins [350].

Well	Abbreviation	Name	Vendor	Type	MW	CMC (%)	final %	DFA	SEC
A4	ZC-14	Anzergent 3-14	Anatrace	zwitterionic	363	0.007	0.021	+	-
A12	CF-6	Cyclofos-6	Anatrace	zwitterionic	349	0.094	0.188	+	-
B4	FC-12 *	fos-choline 12	Anatrace	zwitterionic	352	0.047	0.094	+	+
C12	APB035	Anapoe 35	Anatrace	nonionic	1198	0.011	0.028	+	-
D1	TX-100	Triton X-100	Anatrace	nonionic	647	0.010	0.040	-	-
D2	APX305 **	Anapoe X305	Anatrace	nonionic	1526	0.099	0.248	+	+
E2	APO109	Anapoe C10E9	Anatrace	nonionic	555	0.072	0.18	+	-
E6	APO138	Anapoe C13E8	Anatrace	nonionic	553	0.0055	0.0138	+	-
G2	CYMAL-7	CYMAL-7	Anatrace	nonionic	523	0.01	0.03	+	-
G7	DM	n-decyl- β -D-maltopyranoside	Anatrace	nonionic	483	0.087	0.174	-	-
G9	UDM	n-undecyl- β -D-maltopyranoside	Anatrace	nonionic	497	0.029	0.087	+	-
G12	DDM	n-dodecyl- β -D-maltopyranoside	Anatrace	nonionic	511	0.0087	0.026	-	-
H5	UDTM	n-undecyl- β -D-thiomaltopyranoside	Anatrace	nonionic	513	0.011	0.033	+	-
H7	FA-231	Façade-EM	Avanti	nonionic	1115	0.02	0.040	+	-
H9	DMNG	decyl maltose neopentyl glycol	Anatrace	nonionic	950	0.0034	0.0068	+	-
H10	LMNG	lauryl maltose neopentyl glycol	Anatrace	nonionic	1005	0.001	0.002	-	-
	TFA-1	Façade-TFA1	Avanti	nonionic	2148	0.0028	0.0056	n/d	-

Well coordinates as shown in Figure 2.8.

* Best detergent selected based on DFA screen and IMAC/SEC screening

**Detergent promoted high protein solubility, not used for purification due to its chain length

Table 2.3. Detergents screened for ZnT8B solubility.

Native gel electrophoresis suggested an apparent molecular mass of 140 kDa (Figure 2.9B), which when the added mass of the Coomassie blue dye is accounted for [345] suggests a protein component of 70-80 kDa size. Matrix-assisted laser desorption ionization mass spectrometry (MALDI-MS) of the purified ZnT8B in FC-12 showed a monomeric species of 36.1 kDa, as well as a dimer of 72.0 kDa (Figure 2.9C), which corresponds to the predicted 36.05 kDa size of ZnT8B-G₃H₆.

Purification of both ZnT8A and ZnT8B from *S.frugiperda* showed high protein purity, lower levels of protein aggregation as compared with protein purified from *P.pastoris* and good long-term stability (Figure 2.10).

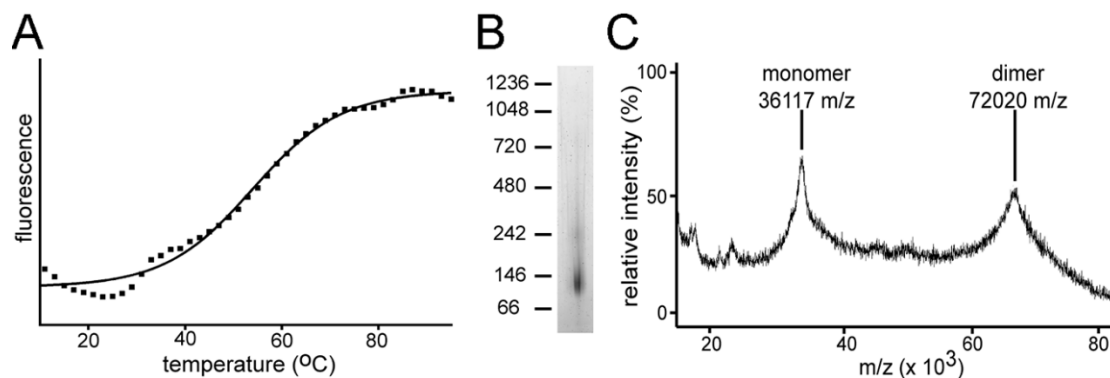


Figure 2.9. Purified ZnT8B forms a highly stable dimer. (A) Fluorescent thermal stability assay. Plot shows dye fluorescence per °C increase in temperature from which the calculated T_m of ZnT8B is 57 °C. (B) Non-denaturing PAGE of ZnT8B-G₃H₆, showing the protein-detergent micelle complex with an apparent molecular weight of ~140 kDa, which corresponds to an actual molecular weight of ~80 kDa. Positions of molecular weight markers in kDa (left). (C) MALDI-MS of purified ZnT8B-G₃H₆ showing number of sample ions detected and their corresponding mass-to-charge (m/z) ratio. The ZnT8B construct appears as both a monomer of 36.117 kDa and a dimer of 72.020 kDa.

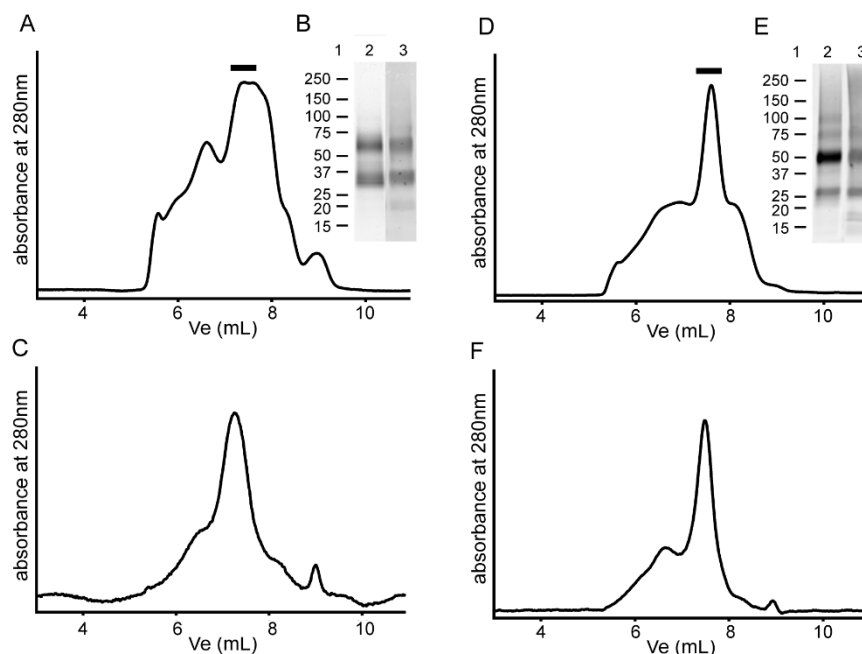


Figure 2.10. SEC purification of ZnT8A and ZnT8B from *S.frugiperda* (*Sf9*). SEC elution profile, indicating pooled peak fractions of apparent mass ~150 kDa indicated (black bar) corresponding to ZnT8A (A-C) and ZnT8B (D-E). SDS-PAGE gel stained with Colloidal Blue (lane 2) and ZnT8 immunoblot (lane 3) of SEC eluate of ZnT8A (B) and ZnT8B (E). Position of molecular weight markers in kDa are indicated. Stability of ZnT8 shown by SEC elution profiles of purified ZnT8A (C) and ZnT8B (F) after one-week incubation at 4 °C.

The ZnT8A amino- and carboxy-terminal ectodomains display ordered secondary structure

The amino-terminal domain of ZnT8 is extremely interesting since this 73-residue domain shows little similarity to any other protein sequence and its function is unknown. The putative cytoplasmic amino- and carboxy-terminal domains of ZnT8 were expressed in *E. coli* as fusions with bacterial thioredoxin. Following proteolytic digestion with enterokinase the fragments were purified by SEC. MALDI-MS verified that the purified fragments showed the expected mass. Following dilution into low-salt buffer, circular dichroism (CD) spectrometry showed that these two protein domains exhibited distinctive secondary structures (Figure 2.11). The secondary structure content was deconvoluted using the DICHROWEB CD analysis server [372] (Table 2.4).

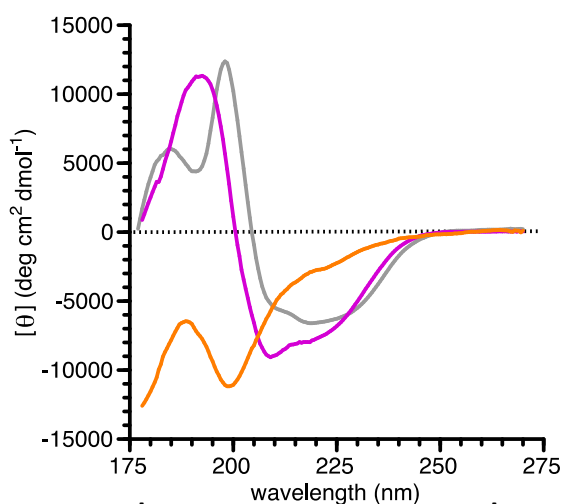


Figure 2.11. CD spectroscopy shows that the amino-terminal domain of ZnT8 contains significant β structure, whereas the carboxy-terminal domain has a mixed α - β fold. Far-ultraviolet circular dichroism spectrometry of ZnT8 and thioredoxin (TRX) constructs, showing molar ellipticity per residue by wavelength of ntZnT8 (orange line), ctZnT8 (violet line), and TRX (grey line). Spectra shown are from data collected using sample path lengths of 1.0 and 0.1mm that were scaled and merged together. Experiment performed by Dr. Mark Daniels, University of Virginia.

	ntZnT8 (CD) ¹	ctZnT8 (CD) ²	ctYiiP (X-ray) ³	Thioredoxin (CD) ²	Thioredoxin (X-ray) ³
α -helix	2%	26%	33%	32%	39%
β -sheet	42%	21%	29%	13%	30%
β -turn	28%	19%	14%	19%	15%
other	28%	13%	13%	17%	16%
disordered	-	19%	11%	20%	0%

Table 2.4. Secondary structure composition of ZnT8 constructs and thioredoxin determined by deconvolution of circular dichroism (CD) spectra. ¹Deconvolution using the VARSLC algorithm. ² Deconvolution using the CDSSTR algorithm. ³ Secondary structure assignments using DSSP. Experiment performed by Dr. Mark Daniels, University of Virginia.

Sequence analysis suggested that the 73 amino-acid amino-terminus is primarily disordered (Figure 2.3). However, the CD spectrum of the amino terminus displayed a negative CD peak of $-11200 \text{ deg}\cdot\text{cm}^2\cdot\text{dmol}^{-1}$ at 199 nm (Figure 2.11), indicative of significant β -sheet and β -turn content (Table 2.4). By use of the VARSLC algorithm [354] the quantitative estimates of structure were 2% α -helical, 42% β -sheet, 28% β -turn, and 28% other.

Our homology model of ZnT8 shows the cytoplasmic carboxy-terminal domain to have a mixed α 1- β 1- β 2- α 2- β 3 fold, as does an earlier model [67]. Correspondingly, our CD spectra of this 85 amino-acid domain showed a strong α -helical signal (Figure 2.11), with a negative CD peak of $-9100 \text{ deg}\cdot\text{cm}^2\cdot\text{dmol}^{-1}$ at 209 nm and a positive CD peak of $11300 \text{ deg}\cdot\text{cm}^2\cdot\text{dmol}^{-1}$ at 193 nm. By use of the CDSSTR algorithm [354] the quantitative estimates suggested a mixed α - β fold (26% α -helical, 21% β -sheet, 19% β -turn, 13% other, and 19% disordered). This agrees well with the X-ray structure of the *E. coli* homolog YiiP, in which the carboxy-terminal domain displays 33% α -helical,

29% β -strand, 14% β -turn and 13% unassigned content, as determined by DSSP [373]. Another 11% appears to be disordered, as 10 of the 95 residues of the carboxy-terminus were not resolved in the initial structure [43] and were removed in crystallographic studies.

As a control for correct folding of overexpressed protein and our circular dichroism methods, we also characterized bacterial thioredoxin (TRX) (Figure 2.11). Previous CD spectra of TRX showed a broad negative CD signal with a peak of $-6800 \text{ deg}\cdot\text{cm}^2\cdot\text{dmol}^{-1}$ at 219 nm and a sharp positive CD signal with a peak of $17300 \text{ deg}\cdot\text{cm}^2\cdot\text{dmol}^{-1}$ at 196 nm [374]. Our results with TRX are similar, with a broad negative CD signal with a peak of $-6800 \text{ deg}\cdot\text{cm}^2\cdot\text{dmol}^{-1}$ at 219 nm, a sharp positive CD signal with a peak of $11000 \text{ deg}\cdot\text{cm}^2\cdot\text{dmol}^{-1}$ at 198 nm, and an additional peak of $5100 \text{ deg}\cdot\text{cm}^2\cdot\text{dmol}^{-1}$ at 185 nm with a trough at 191 nm between the two positive peaks. As a control experiment, our CD spectrum of bacterial thioredoxin alone (Figure 2.11) appears similar to previous results [374], supporting the fidelity of our protein overexpression and purification method and our CD spectrometry results.

The molecular boundary of the ZnT8B dimer recapitulates that of YiiP, a bacterial homolog

EM images of negatively stained ZnT8B expressed in *P. pastoris* displayed a field of discrete particles showing minimal aggregation (Figure 2.12) and are thus suitable for single-particle image analysis. Individual complexes were masked using the EMAN2 [358] software package.

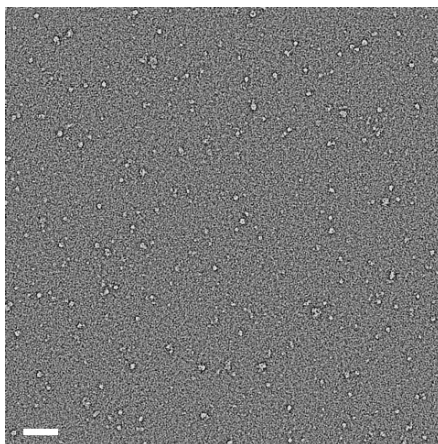


Figure 2.12. Electron micrograph of ZnT8 purified from *P.pastoris*. Particles stained with uranyl formate. The contrast of the micrograph was enhanced by high- and low-pass Gaussian filtering at 100 and 15 Å, respectively. Magnification = 62,000x. Scale bar denotes 50 nm.

By use of the RELION software package [359], 23 2D class averages were derived for ~3,500 particles (Figure 2.16). A 3D map without applied symmetry was derived by reference-free methods using EMAN2. The map was truncated at 50 Å resolution (Figure 2.13A), which served as a starting model for further refinement using RELION. The resulting non-symmetrized map (Figure 2.13B) displayed two elongated lobes of density with apparent two-fold symmetry, consistent with our biochemical results that ZnT8B is a dimer in FC-12. We therefore applied C2 symmetry, and the resulting map had a calculated resolution of 20 Å using a conservative Fourier shell correlation (FSC) cut-off value of 0.5 (Figure 2.14). Interpretation of the low-resolution map was aided by docking of a homology model using the structure of the bacterial YiiP homolog as a template, which displays a good fit to the 105 Å x 70 Å x 55 Å molecular boundary and suggests an assignment of the transmembrane and cytoplasmic domains (Figure 2.13C). To extend the analysis, we used a 50-Å resolution map of YiiP as a reference (Figure 2.13D) for

refinement by RELION. The resulting non-symmetrized map of ZnT8 again demonstrated a bilobed appearance (Figure 2.13E) and consequently we applied C2 symmetry during refinement of the final map (Figure 2.17, Figure 2.13F), which had a calculated resolution of 20 Å using a conservative FSC cut-off value of 0.5 (Figure 2.15). As expected, the subunits within the ZnT8 dimer have improved definition compared with the initial, reference-free map and slightly more compact dimensions of 90 Å x 70 Å x 50 Å.

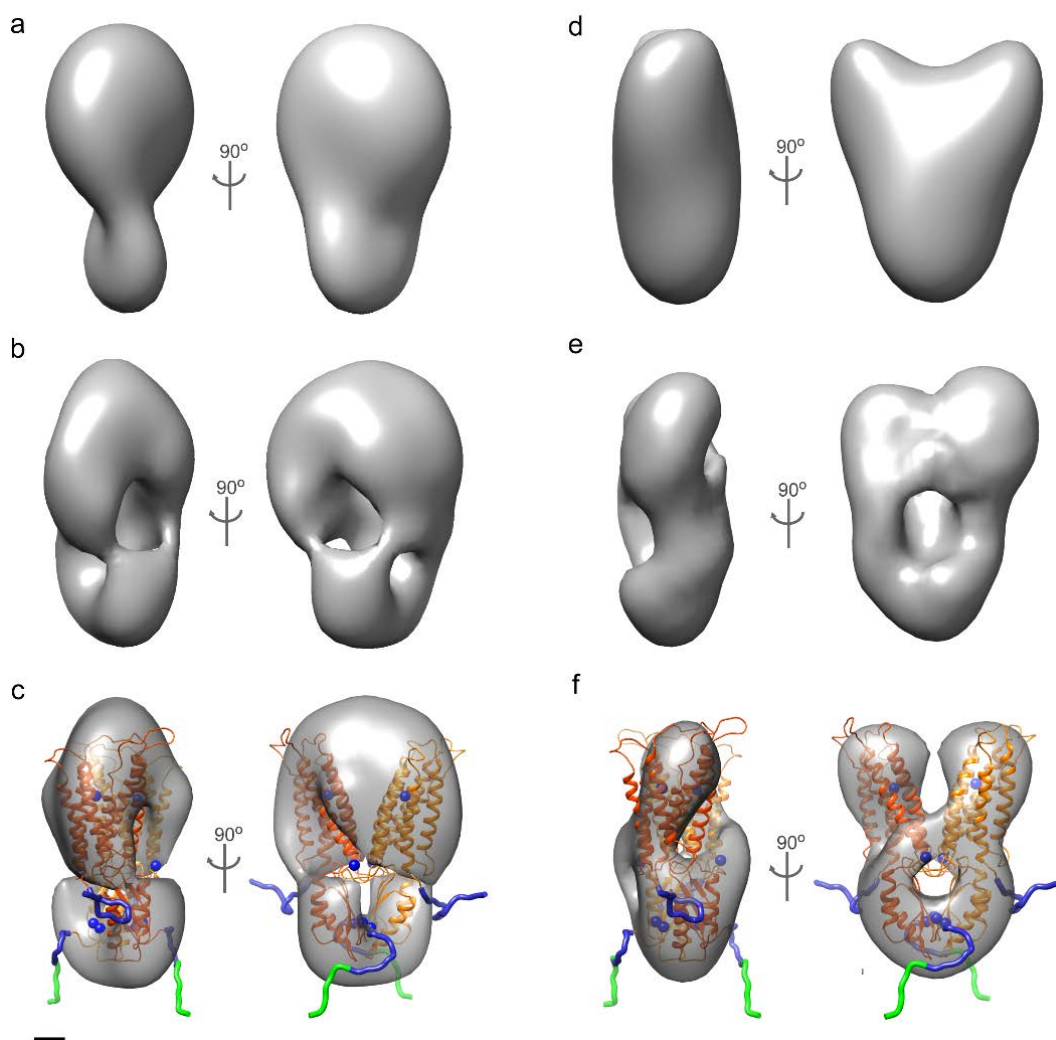


Figure 2.13. Steps in the determination of the 3D structure of ZnT8. (A) Reference-free EMAN2 reconstruction of ZnT8, without symmetry, at 50 Å resolution. (B) Reconstruction of ZnT8, without symmetry, at 20 Å resolution, generated by RELION using the map of panel (A) as a reference. (C) Reconstruction of ZnT8, with C2 symmetry applied, at 20 Å resolution, generated by RELION using map of panel (A) as a reference. (D) Map of YiiP derived from the X-ray structure (PDB ID 3H90) filtered to 50 Å resolution. (E) Reconstruction of ZnT8, without symmetry, at 20 Å resolution, generated by RELION using the map of YiiP in panel (D) as a reference. (F) Final reconstruction of ZnT8, with C2 symmetry applied, at 20 Å resolution, generated by RELION using YiiP map of panel (D) as a reference. The isosurface was set at a volume of a ZnT8 dimer, based on a protein partial specific volume of 0.74 cm³/g. For the single-particle analyses shown in panels (B, C, E and F), 23 2D class averages were derived from ~3,500 particles. A homology model of ZnT8 based on the X-ray structure of YiiP is docked within the molecular boundary of ZnT8 in panels (C) and (F). Subunits (orange and yellow), zinc ions (blue spheres), amino-terminal fragment (blue), His₆ tag (green). Scale bar denotes 10 Å

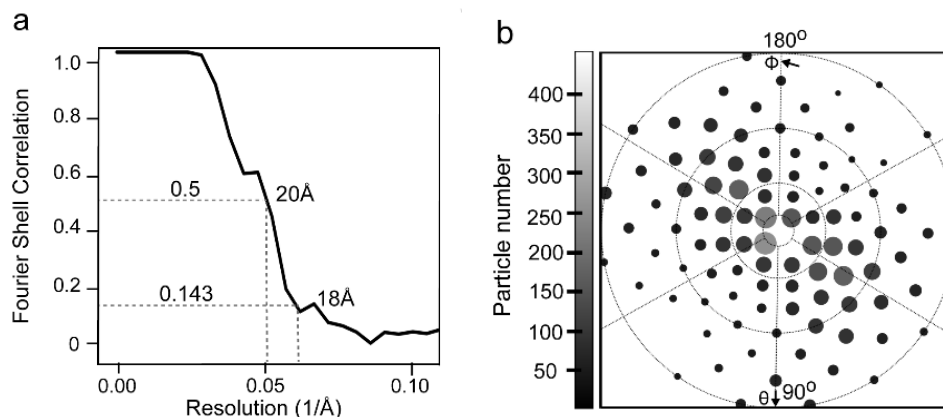


Figure 2.14. ZnT8B EM reconstruction statistics using a reference-free model. (A) Fourier shell correlation (FSC) between two EM density maps (solid line), each calculated from half of the data. The FSC drops below 0.5 at ~ 20 Å resolution. (B) Euler angle plot showing angular distribution of particle orientations. Each spot represents a particular orientation of the two Euler angles ϕ (phi) and Θ (theta) and is assigned a size and greyscale value corresponding to the number of particles with that orientation.

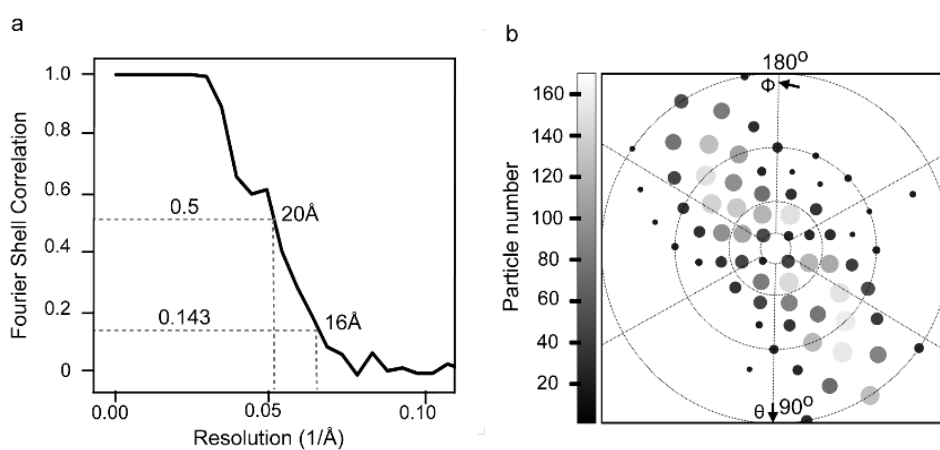
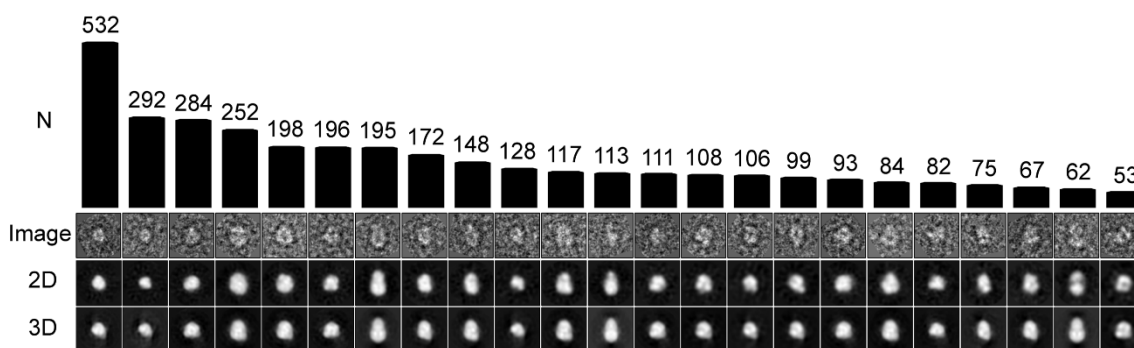


Figure 2.15. ZnT8B EM reconstruction statistics, YiiP starting model. (A) Fourier shell correlation (FSC) between two EM density maps (solid line), each calculated from half of the data. The FSC drops below 0.5 at ~ 20 Å resolution. (B) Euler angle plot showing angular distribution of particle orientations. Each spot represents a particular orientation of the two Euler angles ϕ (phi) and Θ (theta), and is assigned a size and greyscale value corresponding to the number of particles with that orientation.



2.16. EM and single particle analysis using RELION. Shown are the 23 final particle classes used in determining the ZnT8B structure. Top row indicates number of particles in each class average (N), second row shows image of a representative raw particle belonging to class, third row shows 2D class average, bottom row displays back projections of 3D particle with view corresponding to class average shown in third row. Note the close correspondence of the back projections of the 3D map having C2 symmetry to the 2D class averages in which symmetry was not applied.

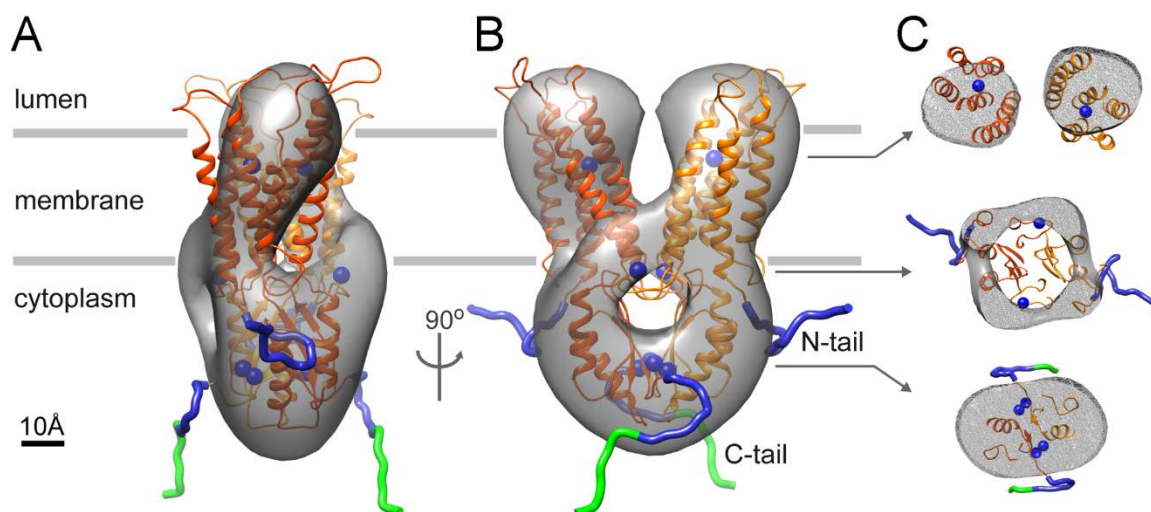


Figure 2.17. ZnT8 map and homology model. Front (A) and side (B) views of the ZnT8 homology model fitted into the EM density map calculated at 20 Å resolution. The complex has a height of 90 Å and a girth of 70 Å x 50 Å. Axial sections (C) of density map corresponding to transverse planes in B as indicated. Subunits (orange and yellow), zinc ions (blue spheres), amino-terminal fragment (blue), His₆ tag (green).

Given the relatively low expression of ZnT8 in *P. pastoris*, the current protocol would require substantial scale-up to yield the milligram quantities required for X-ray crystallography. The ~72 kDa ZnT8B dimer is one of the smallest studied by EM and single-particle analysis [375]. Consequently, near-atomic resolution structure analysis will require the use of the most contemporary EM technologies such as a direct electron detector [376] and a phase plate [377]. Furthermore, addition of fusion proteins [378] and/or Fab fragments [375, 379, 380] will not only aid the identification of domains within the complex but will also add mass and identifiable structural features to facilitate the determination of particle orientations.

Chapter 3: pH-gating of Gap Junction Channels: Visualization of a “ball-and-chain” by cryoEM

Ali Khan*, Maciej Jagielnicki*, William E. McIntire, Michael D. Purdy, Venkat Dharmarajan, Patrick R. Griffin and Mark Yeager

* Co-first authors

3. 1 Introduction

Connexins (Cx) are a family of integral membrane proteins found in all vertebrate organisms. All connexin isoforms share a common topology with four α -helical transmembrane (TM) domains (M1-M4), two extracellular loops (E1 and E2), a cytoplasmic (CL) M2–M3 loop and cytoplasmic N- and C-terminal domains (NT and CT). The M1-M4 and E1-E2 domains are the most conserved among connexins whereas the sequences of flexible CL, NT and CT domains[145-149] are highly variable[140, 141]. Connexins assemble to form hexameric connexons or hemichannels (HC), and HCs from adjacent cells can form dodecameric gap junction channels (GJCs) by end-to-end docking. The E1 and E2 loops form the extracellular domain that mediates docking between HCs[152, 153]. Gap junction channels have an aqueous pore that enables the intercellular

communication between cells[140, 154] that is indispensable to the functioning of many physiological processes[181]. GJCs enable direct cell-to-cell exchange of small molecules such as hydrated ions (e.g., Ca^{2+}), second messengers (e.g., cAMP, IP3), intracellular metabolites (e.g., glucose, ATP) and small peptides[154, 167-169, 171, 172]. In addition to mediating chemical coupling, GJCs connect cells electrically by functioning as high conductance ion channels[180]. Gap junction channels are regulated by transmembrane potential (V_m gating)[202], transjunctional voltage (V_j gating)[202], pH[154], phosphorylation[183], membrane lipids and membrane-active agents[207] and divalent cations such as Ca^{2+} , Zn^{2+} and Mg^{2+} [208-210].

The Yeager laboratory has had a keen interest in the mechanistic aspects of pH gating in GJCs, which result in myriad physiologic and pathologic consequences. For example, decreases in pH were shown to cause a decrease in junctional conductance[232, 309, 310] and in permeability as demonstrated in glial, neuronal and lens GJCs[311, 312]. Lowered pH can also lead to diminished junctional electrical coupling in cardiomyocytes and in Purkinje fibers[215, 313-315] as well as in teleost and amphibian embryos[232]. Since Cx26 is highly sensitive[142, 251, 308] to pH, and has been extensively studied by us and others, we chose this isoform as our model system to study the molecular determinants of pH regulation in GJCs. Using cryoEM and mass spectrometry, we have data that support a ball-and-chain mechanism for pH regulation in the Cx26 GJC.

3.2 Methods

Protein expression and purification.

Protein expression and purification were performed as described in [231]. For MS/MS and HDX experiments, the final buffer was 50 mM HEPES pH 7.5, 500 mM NaCl, 0.025 % n-Dodecyl- β -D-Maltopyranoside (DDM; Anatrace). Samples for EM experiments and the thermal stability assay were purified into buffer with 50 mM HEPES pH 7.5, 1 M NaCl, 2.5 % glycerol (v/v), 0.025% DDM. The final eluate from the desalting column was concentrated to 4 – 5.5mg/ml (150–210 μ M) using a 0.5 ml or 4 ml concentrator (100 kDa MWCO; Millipore). In order to increase protein stability and contrast for cryoEM, detergent was exchanged to amphipathic surfactant Amphipol A8-35. Protein sample at 5 mg/ml was mixed with amphipol (10 mg/ml stock in protein buffer) at a ratio of 1:3 (w/w), diluting protein to \sim 2 mg/ml. The sample was incubated for 4 h at 4°C with gentle mixing. Detergent was removed with Bio-Beads SM-2 (BioRad) by addition of beads to 30mg/ml to protein/detergent/amphipol mixture and ON incubation at 4°C with gentle mixing. Bio-beads were then removed over a 0.5 ml disposable column, eluent spun down for 10min at 16, 000 x g at 4°C and purified further on a Superdex 200 10/300 column in buffer composed of 50 mM HEPES pH 7.5, 1 M NaCl. The peak corresponding to dodecameric Cx26 channels was collected and concentrated to 2 mg/ml in 4 ml concentrator (100 kDa MWCO; Millipore).

Negative stain EM analysis.

For EM of negatively stained samples, a protein sample was applied on a glow-discharged, carbon-coated copper grid which was next stained with 2 % uranyl acetate pH 4.5. EM was performed using a Tecnai G2 F20 electron microscope (FEI, Hillsboro, OR) equipped with a field-emission electron source, operating at 120 keV. Low electron dose images ($\sim 15 \text{ e}^-/\text{\AA}^2$) were recorded on a 4K x 4K pixel CCD camera (Gatan, Pleasanton, CA) at 62,000 x magnification (corresponding to $1.8 \text{ \AA} / \text{pixel}$) with a 1 sec exposure time at an underfocus value of $\sim 1.5 \mu\text{m}$. The image processing was performed using EMAN v2.05 software [358]. A dataset of $\sim 3,000$ particles yielded a set of initial three-dimensional maps. The best map, as judged by the presence of continuous densities and partial specific volume corresponding to a Cx26 GJC, was subsequently refined with D6 symmetry.

CryoEM Sample Preparation.

Purified Cx26 ($\sim 2 \text{ mg/mL}$ in 50 mM HEPES pH 7.5, 1 M NaCl, amphipol (A8-35)) was diluted to 0.4 mg/mL with a final buffer concentration of 50 mM HEPES pH 7.5, 200 mM NaCl. $3.5 \mu\text{L}$ of sample was then immediately applied to a glow-discharged (with amylamine) C-flat holey carbon grid (copper, $2 \mu\text{M}/2 \mu\text{M}$ hole size/hole space), manually blotted with Whatman no. 1 filter paper for $\sim 3\text{-}5 \text{ s}$, and plunge-frozen in liquid ethane cooled by liquid nitrogen. For the low pH sample, purified Cx26 (2.5 mg/mL) was diluted 1:3 (v/v) with a 50 mM MES pH 6 solution to make a 0.63 mg/mL Cx26 protein solution in 12.5 mM HEPES, 37.5 mM MES pH 6.4, 125 mM NaCl. After a brief incubation ($\sim 2\text{-}5$

minutes) on ice, 3 μL of sample was applied to a glow-discharged C-flat holey carbon grid, blotted with Whatman no. 1 filterpaper using a Vitrobot (FEI company) using 4 s blotting time, blot force of 3, and 100 % humidity at 22°C, and then plunge-frozen in liquid ethane cooled by liquid nitrogen.

CryoEM Data Acquisition.

Data sets were collected at the Electron Bio-Imaging Centre (eBIC) at the Diamond Light Source (Didcot, United Kingdom) on a Titan Krios cryo-electron microscope, operated at 300 kV, equipped with GIF Quantum Energy Filter operated in zero-energy-loss mode with a slit-width of 20 eV and a K2 Summit direct electron detector (Gatan, Inc.). Images were collected using the automated procedure in EPU (FEI) at a 130,000 X nominal magnification corresponding to a 1.06 Å physical pixel size. Images for pH 7.5 sample were recorded in counting mode as a 20-frame movie with an exposure time of 8 s and dose rate of 5.625 $\text{e} \text{Å}^{-1} \text{s}^{-1}$ (total dose 45 $\text{e} \text{Å}^{-1}$). Low pH images were recorded in super resolution mode (0.53 Å super resolution pixel size) as a 25-frame movie with an exposure time and dose rate of 10 s and 4.5 $\text{e} \text{Å}^{-1} \text{s}^{-1}$ (total dose 45 $\text{e} \text{Å}^{-1}$), respectively.

CryoEM Data Processing.

For neutral pH, all movie frames were motion-corrected and integrated using MOTIONCORR [381] while applying a b-factor of 150 pixel^2 and frame offset of 5. On the first 94 images collected from the microscope, the contrast transfer function (CTF) was estimated on each integrated image using CTFIND4 [382]. In RELION [359, 383, 384],

two-dimensional (2D) class averages calculated from 745 manually picked particles were used as an input for template-based auto picking. 2D class averages of the auto-picked particles were calculated and used to generate a *de novo* D6 symmetric initial model in EMAN2 [358]. On the full dataset, the contrast transfer function (CTF) of each integrated micrograph was estimated using Gctf [385]. 2D class averages generated from the previous auto-picked particles were used as templates for automated picking on the full dataset using Kai Zhang's Gautomatch software. Using the resolution limit value output by Gctf, all micrographs worse than 3.3 Å were discarded, and the remainder of the processing was performed in RELION v2. 2D class averages were calculated, and particles from class averages containing helical features (Extended Data Fig. 3b) were subjected to 3D classification (with D6 symmetry) using the EMAN2-generated initial model. All initial models used in 3D class averaging and refinement mentioned herein were lowpass filtered to 50 Å resolution. Approximately 60% of the particles were assigned to a 3D class containing apparent secondary structure and were used for subsequent 3D auto-refinement (with D6 symmetry), that resulted in a gold-standard FSC resolution of 4.5 Å. Beam-induced motion correction and radiation-damage weighting implemented in the RELION particle polishing procedure was used to improve the signal-to-noise ratio of individual particles [386]. Refinement with the "polished" particles improved the resolution to 4.4 Å (Extended Data Fig. 3c, d, and g). In the RELION post-processing procedure, applying a soft mask that excludes the low-resolution signal from the

amphipol and cytoplasmic domains and performing automated B-factor sharpening [387] improved the resolution to 4.0 Å (Extended Data Fig. 3e-g).

For acidic pH, all super-resolution movie frames were motion-corrected and integrated using MOTIONCORR while applying a b-factor of 150 pixel² and frame offset of 6. CTF estimation was performed with Gctf, and summed micrographs with a resolution limit worse than 3.75 Å were discarded. To generate an initial model, in RELION, 2D class averages generated from 1008 manually picked particles were used as templates for auto-picking on all micrographs. Secondary structure containing 2D class averages calculated from 2x down-scaled particles from 234 micrographs were used to sort particles from all the micrographs based on the difference between the particle and its aligned reference. The top ~50% of particles were subjected to two consecutive rounds of 2D classification, selecting particles in secondary structure-containing 2D class averages after each round. In EMAN2, 2D class averages of the remaining particles were then calculated and used to generate a *de novo* D6-symmetric initial model. Particles were then subjected to two rounds of 3D class averaging with C1 symmetry and one round of 3D class averaging with D6 symmetry to remove bad particles and further improve the initial model. Between each 3D class averaging round, particles and density from a secondary structure containing 3D class was chosen as inputs for the next round. After the initial model generation, we performed image processing on summed micrographs with a resolution limit better than 3.75 Å. 2D class averaging was performed on 4x down-scaled particles, and particles in secondary structure containing class averages were subject to two rounds

of 3D class averaging with C1 symmetry. Particles were then used to generate a *de novo* D6 symmetric initial model in cryoSPARC and subjected to a round of 3D classification with D6 symmetry. Particles from the best 3D class average were re-extracted from the micrographs, down-scaled 2x, and subjected to another round of 3D classification with D6 symmetry. Subsequent 3D auto-refinement with D6 symmetry resulted in a 6.1 Å model, which improved to 4.7 Å (gold-standard FSC) with particle polishing (Extended Data Fig. 5a). 3D classification was then performed on the “polished” particles increasing the angular sampling incrementally from 7.5° to 0.9°. From the resulting three 3D classes (Extended Data Fig. 5b-d), particles in two of the classes were subjected to 3D refinement, resulting in a 7.5-Å map of the Cx26 GJC in the occluded state (Extended Data Fig. 5e). Refinement of the remaining class resulted in a 4.5-Å map of the Cx26 GJC open state, that improved to 4.2 Å resolution (Extended Data Fig. 4h) with post-processing (Extended Data Fig. 5f).

Model Building.

Both pH 7.5 and pH 6.4 open models were built following the same procedure. The X-ray structure of Cx26 (PDB code: 5ERA) [231] was used as a starting model. The real space refinement tool in Phenix [388] was used to refine the model to the B-factor sharpened cryoEM map with ‘secondary structure restraints’, ‘reference model restraints’, and electron scattering table options selected [389]. WinCoot [390] was then used to perform local real-space refinement on selected fragments of the structure, as

well as to improve the fit of bulky side chains to the density. Residues 214 and 215 were deleted from the cytoplasmic end of the M4 due to insufficient density and amino acids 17 and 134 were added to the cytoplasmic ends of M1 and M3 based on unaccounted for densities. The unsharpened cryoEM map was used to dock the N-terminal domain from another X-ray structure (PDB code: 2ZW3) [246] into a stretch of density lying inside the channel pore, proximal to M1 helix. Residues Met 1 and His 16 were added, and the N-terminal fragment was connected to M1 helix. The model was analyzed for rotamer outliers and clashes using validation tools in WinCoot, and problematic areas were manually refined. The model was then subjected to two cycles of refinement in Phenix and manual adjustment in WinCoot. The structures were validated using MolProbity [391] as a part of Phenix and EMRinger [392].

The acidic pH 'plug' model was based on the same starting structure as the other two models. After real-space refinement in Phenix, the backbone of M1-M4 helices was adjusted in WinCoot. The building process was limited to manipulations of C α and main chain atoms. Next, N-terminal residues 1 – 17 were added, rigid docked into the density, and refined. At the end of the process the model was subjected to another round of refinement in Phenix. The model was validated as described above.

Fluorescent Thermal Stability Assay.

Thermal stability of Cx26 in DDM and in amphipol A8-35 across a range of pH values was measured by the fluorescence of the cysteine-reactive dye 7-diethylamino-3-

(4'-maleimidylphenyl)-4-methylcoumarin (CPM) over a temperature gradient. The Cx26 construct used for cryoEM has only one free cysteine at position 202, in the middle of M4 (the other 2 free cysteines, at 211 and 218, were mutated to serine). Upon increasing temperature, Cx26 unfolds and the dye binds to the C202 thiol and emits fluorescence at 463 nm. For experiments on Cx26 in DDM at pH 7.5 the buffer used consisted of 50 mM Hepes pH 7.5, 500 mM NaCl, 2.5 % glycerol (v/v), 0.025% DDM. Experiments at lower pH were performed in MES-based buffer at pH of 6.5 or 6.0. For Cx26 samples in amphipol A8-35, no detergent was added to the buffers. An aliquot of CPM dye (Invitrogen) at 10 mM in dimethylformamide was diluted 1:150 into either a sample of protein at ~300 µg/ml or a buffer-only control. Following a 15-min incubation on ice, the sample was transferred into a 1.5 mm path-length quartz spectrofluorometer cuvette (Hellma Analytics, Müllheim, Germany), which was inserted into a FluoroMax-3 spectrofluorometer (Horiba Jobin-Yvon, Edison, NJ). The excitation and emission wavelengths were set to 387 nm and 463 nm, respectively. The sample was heated from 6-96 °C at a rate of 2 °C/min, and the fluorescence was recorded every 1 min. The fluorescence versus temperature profile was analyzed as described in[350].

Hydrogen Deuterium Exchange and Data Analysis.

Protein sample in HDX buffer (50 mM Hepes pH 7.5, 500 mM NaCl, 0.025% DDM) was concentrated to ~5.2 mg/ml (200 µM), frozen in liquid nitrogen and stored at -80°C. Initially, tandem mass spectrometry (MS/MS) was used to optimize protein

concentration, protease digestion times and quench conditions for maximum protein sequence coverage with recovered peptides. MS/MS data were acquired separately from HDX data, in experiments with a 60 min gradient column. Data-dependent MS/MS was performed in the absence of exposure to deuterium and the amino acid sequence of each peptide used in the HDX peptide set were confirmed if they had a MASCOT score of 20 or greater and had no ambiguous hits using a decoy (reverse) database. A post-translational modification (PTM) of the methionine 1 residue with an acetyl cap (Ac-Met) of the 1 – 7 peptide was included in MASCOT search. The best condition identified yielded a 74 % peptide recovery. Shortly before HDX experiments, sample was thawed on ice and diluted 1:3 (v/v) to ~50 μ M protein in either HDX buffer pH 7.5 (50 mM Hepes pH 7.5, 500 mM NaCl, 0.025% DDM) or pH 6 (50 mM MES pH 6, 500 mM NaCl, 0.025% DDM). Solution-phase amide HDX was carried out with a fully automated system as described previously [393] with slight modifications. The automation system (CTC HTS PAL, LEAP Technologies, Carrboro, NC, USA) was housed inside a chromatography cabinet held at 4 °C. For each HDX reaction, 5 μ L of 50 μ M Cx26 at pH 7.5 or 6 was diluted to 25 μ L with D₂O-containing HDX buffer (either pH 7.5 or pH 6) and incubated at 4 °C for 10, 30, 60, 900, or 3600 s. Following exchange, unwanted forward or back exchange was minimized and the protein was denatured by dilution to 50 μ L with 0.1 % (vol/vol) TFA in 3 M urea and 20 mM TCEP, 0.025 % DDM. Samples were then passed over an immobilized pepsin column (prepared in house; [394]) at 50 μ L/min (0.1 % vol/vol TFA, 15 °C); the resulting peptides were trapped on a C8 trap cartridge (Hypersil Gold, Thermo Fisher). Peptides were then

gradient-eluted (4 % (w/v) CH₃CN to 40 % (w/v) CH₃CN, 0.3 % (wt/vol) formic acid over 5 min, at 4 °C) across a 1 mm×50 mm C18 HPLC column with a 8 min gradient (Hypersil Gold, Thermo Fisher) and subjected to electrospray ionization directly coupled to a high resolution (60,000) Orbitrap mass spectrometer (LTQ Orbitrap XL with ETD, Thermo Fisher). For on-exchange experiments, the intensity-weighted average m/z value (centroid) of each peptide's isotopic envelope was calculated using software developed in-house [395]. For back exchange correction, full deuterium control was run as reported previously [396], and 59% peptide recovery was calculated. The temperature was constant at 4 °C in all HDX experiments. To measure the difference in exchange rates between experiments conducted at pH 7.5 and 6, we calculated the average percent deuterium uptake for peptides from both samples following 10, 30, 60, 900, and 3600 s of on-exchange. Intrinsic exchange rate (K_{ch}) at pH 6.0 was converted to pH 7.5 using an equation describing the temperature and pH dependence of amide hydrogen exchange rate [397]. After normalization, a time point of ~10 and ~30 seconds was used to calculate the average percent HD exchange in Cx26 at pH 7.5 and pH 6.0).

Protein crosslinking and MS/MS analysis.

We performed lysine proximity crosslinking with bis(sulfosuccinimidyl)suberate (BS3) amine-to-amine at either pH 7.5 or 6 and confirmed the presence of crosslinks by SDS-PAGE gel analysis, in which BS3-crosslinked Cx26 migrated as a hexamer. The conditions sufficient for efficient crosslinking were 1mM BS3 (diluted from freshly made

100mM ddH₂O stock) and incubation with protein for 1 h at 4 °C. In order to ensure proper pH for crosslinking, protein samples were diluted 1:3 to ~1.2mg/ml with either pH 7.5 or 6.0 buffer. The compositions of these buffers were 50 mM HEPES pH 7.5, 500 mM NaCl, 0.025 % DDM and 50 mM MES pH 6.0, 500 mM NaCl, 0.025 % DDM, respectively. At the end of the reaction time, quenching of excess BS3 reagent was done with 1M Tris pH 7.5 to a final concentration of 50mM. Protein samples were then exchanged into pH 7.5 buffer in preparation for trypsin digestion. A desalting column (GE Healthcare, G-25) was equilibrated with 4 x 1 ml of ice-cold pH 7.5 buffer, sample volume was increased to 0.5 ml and loaded onto the column. After flow through was collected, protein was eluted with 1 ml of ice-cold pH 7.5 buffer. The collected eluate from the desalting column was concentrated to ~2 mg/ml (~80 uM) using a 0.5 ml or 4 ml concentrator (100 kDa MWCO; Millipore) at a speed of ~1000 x rcf at 4°C. Using mass spectrometry (MS), we confirmed the presence of the acetylated N-terminal peptide of Cx26 (residues 1 – 150) in the trypsin digest. The samples were flash-frozen in liquid N₂ and sent to The Scripps Research Institute, Jupiter, FL, USA. Trypsin digestion was performed at 37 °C, for 12 hrs. Next, tandem mass spectrometry (MS/MS) was used to separate resulting peptides and crosslinked peptide pairs. MS/MS analysis was performed as described in [398]. MassMatrix software [399] was used to identify detected peptides. All detected lysine crosslinks were organized on separate heat maps for either pH 7.5 or pH 6 condition, with color intensity indicating crosslinking efficiency. The crosslinks were then evaluated based on their PP and PPTag scores (both statistical) and color tag number, which are indicative

of the quality of a peptide match, with higher values determining higher confidence in the match. Low-confidence crosslinks were not analyzed further and neither were the low-scored crosslinks with lysine 168, interpreted as occurring in between different Cx26 gap junction proteins. The remaining crosslinks could be assigned into three groups, based on where in the cytoplasmic domains the crosslinking reaction occurred: NT-CL, CL-CL and CL-CT.

3.3 Results and discussion

Acidic pH stabilizes a conformation of the Cx26 GJC with a pore occlusion

Using single-particle cryoEM (Table 3.1) we reconstructed the Cx26 channel reconstituted in amphipol 8-35 at physiological pH level of 7.5 with D6 symmetry applied (Figure 3.1A and B). The channel recapitulated the authentic Cx43 channel from native lipid bilayers [147, 148] and previous Cx26 X-ray structures (Figure 3.2 and 3.3) [231, 246]. While the resolution was calculated to 4 Å using the gold-standard Fourier Shell Correlation (FSC) (Figure 3.4G), local resolution calculation with Resmap revealed that the map resolution was quite heterogeneous (Figure 3.4E and F). Within the transmembrane and extracellular domains, the map resolution was ~3.5 Å, whereas the cytoplasmic loop and cytoplasmic tail were not resolved, likely due to conformational flexibility.

Summary of CryoEM Data Collection and Processing			
	pH 7.5	pH 6.4 (Open)	pH 6.4 (Closed)
Voltage (kV)	300	300	300
Magnification	130,000	130,000	130,000
Camera	Gatan K2 Summit	Gatan K2 Summit	Gatan K2 Summit
Camera Mode	Counting	Super-resolution	Super-resolution
GIF slit-width (eV)	20	20	20
Defocus	-2.0 to -3.5	-1.2 to -3.5	-1.2 to -3.5
Pixel Size (Å)	1.06	0.53	0.53
Total Electron Dose (e⁻/Å²)	45	45	45
Exposure Time (s)	8	10	10
Initial Number of Images	2,401*	1,547**	1,547**
Number of Frames per Image	20	25	25
Initial Particle Number	64,087	449,556	449,556
Final Particle Number	10,345	25,236	22,805
Resolution (unmaksed, Å)	4.4	4.5	7.5
Resolution (maksed, Å)	4.0	4.2	

*After removal of micrographs with estimated resolution limits worse than 3.3 Å

**After removal of micrographs with estimated resolution limits worse than 3.75 Å

Table 3.1. Summary of CryoEM Data Collection and Processing.

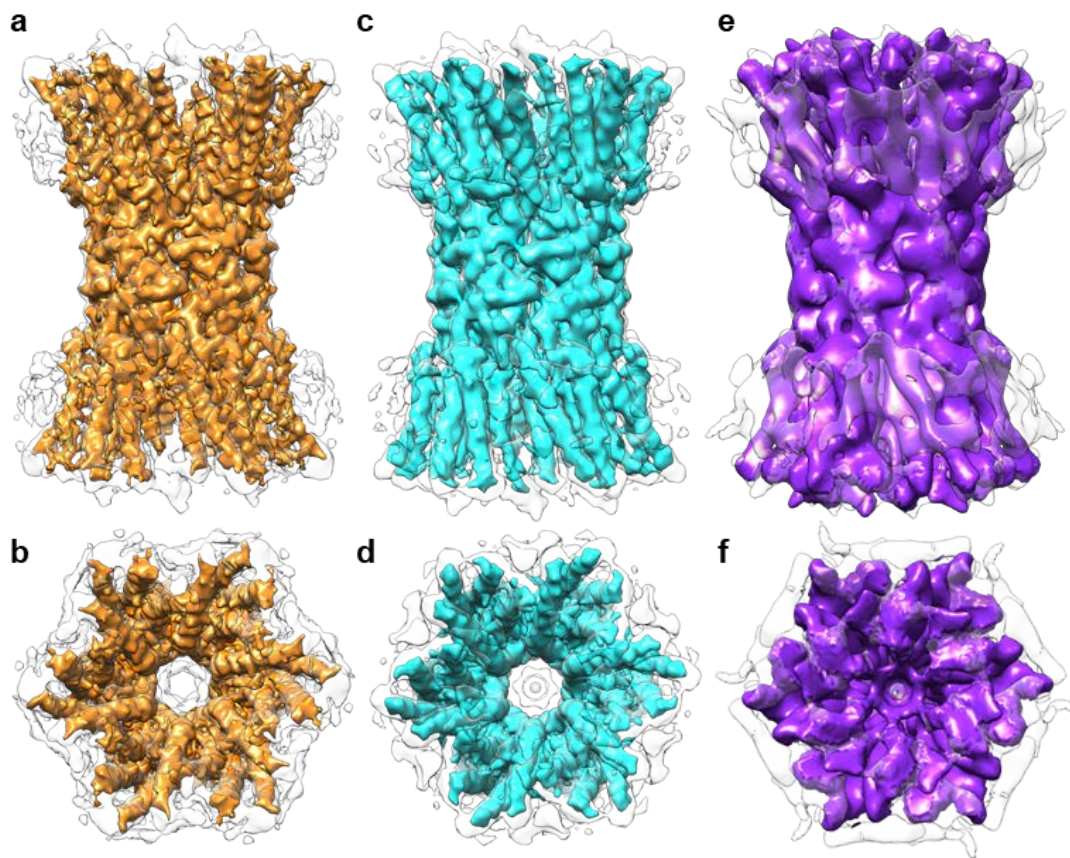


Figure 3.1. CryoEM structures of the human recombinant Cx26 GJC in amphipol A8-35. Side view (parallel to the membrane) and cytoplasmic view of the open physiologic pH (A and B), open acidic pH (C and D), and occluded acidic pH (E and F) Cx26 cryoEM maps. Colored maps (A – D) represent sharpened densities while colored maps (E and F) were not subjected to sharpening. Amphipol densities were removed from all colored maps. Volumes reconstructed by Ali Khan, University of Virginia.

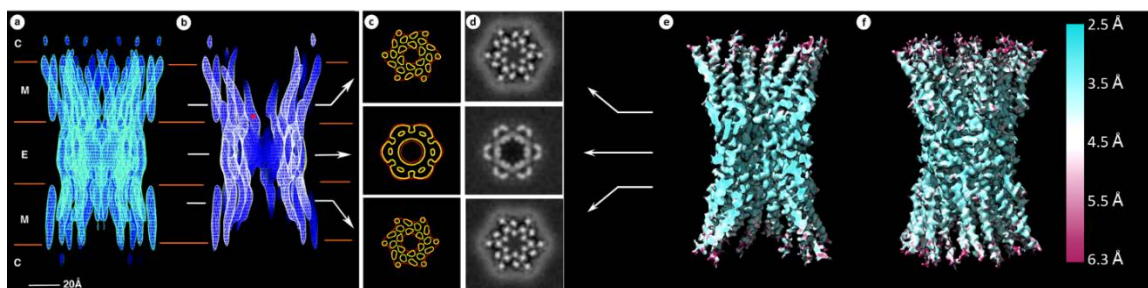


Figure 3.2. Comparison of Cx43 electron crystallography structure with Cx26 single particle cryoEM structure. (A) Side view, (B) side view with cropped density to show channel interior, and (C) cross sections parallel to membrane bilayer of recombinant Cx43 channel solved to 7.5 Å in the membrane plane and 21 Å in the vertical direction. The approximate boundaries for membrane bilayer (M), extracellular gap (E), and cytoplasmic side (C) are indicated. Images (A), (B), and (C) are from [147]. (D) Slice views of 3D density map of Cx26 single particle cryoEM structure shown as side view (F) and side view with cropped density (E). (E) and (F) are colored by local resolution calculated by ResMap [400] with color bar shown.

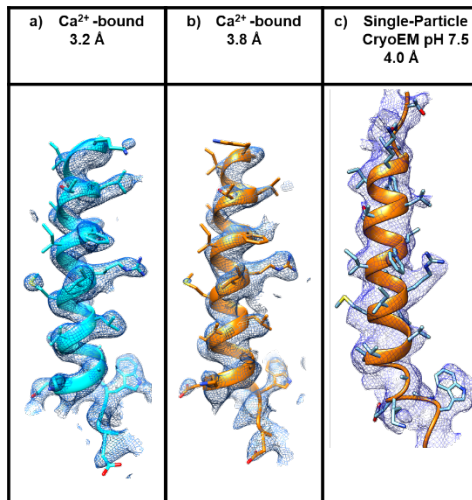


Figure 3.3. Cx26 M1 Helix (residues 17-46). Comparison between the M1 helix calculated by X-ray crystallography with calcium (A), without calcium (B), and by single-particle cryoEM at pH 7.5 (C).

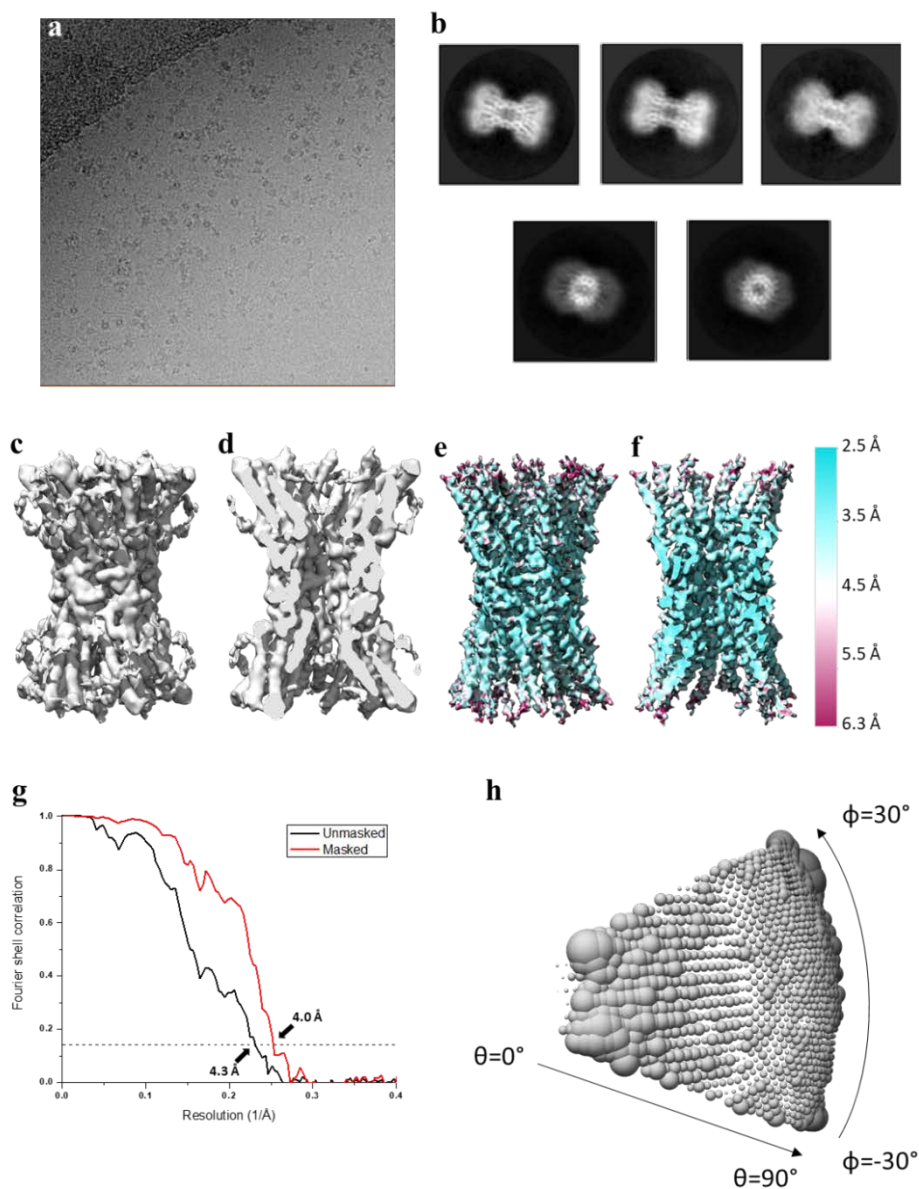


Figure 3.4. Single-particle image processing of the Cx26 GJC at physiological pH. (A) Representative raw micrograph and (B) 2D class averages. (C) Density after refinement is shown with cropped-view (D) to display the interior of the pore. (E-F) Post-processed map colored by local resolution calculation by Resmap reveals that resolution is highest in the transmembrane and extracellular domains and lowest in the cytoplasmic domains. (G) Gold-standard Fourier Shell Correlation (FSC) shows the global resolution of the map before and after masking performed in post-processing to be 4.3 Å and 4.0 Å, respectively. (H) Euler angle distribution of particles depicted as relative size of grey spheres. Analysis performed by Ali Khan, University of Virginia.

We then proceeded to image the channel in acidic conditions (pH 6.4), which is below what was reported to be required for a pH-induced Cx26 channel closure[237, 258]. Using negative stain EM, we discovered a persistent density inside the pore of each hemichannel (Figure 3.5) in a similar position in the channel as observed in a previous study[146].

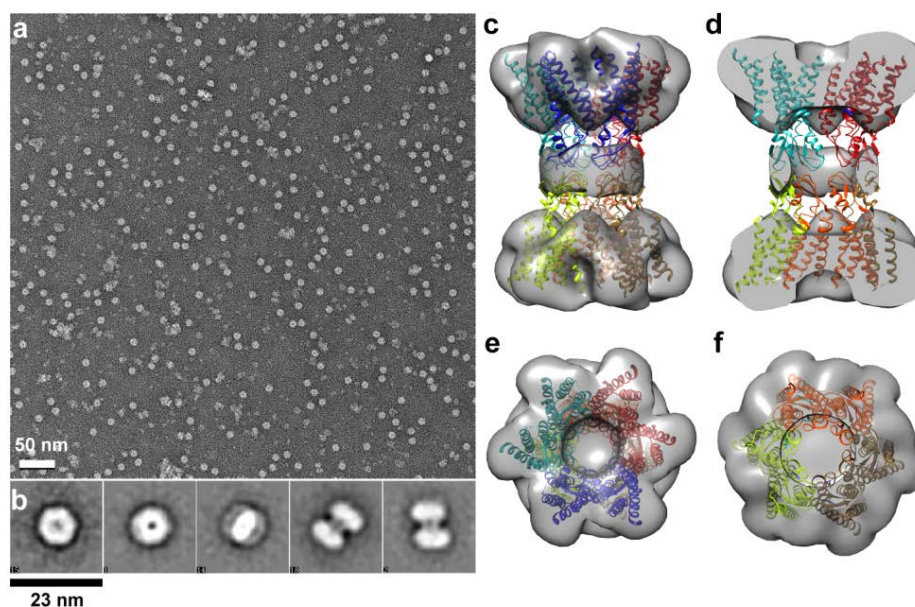


Figure 3.5. Negative-stain EM and single particle analysis. (A) A representative image of Cx26 GJC in amphipol, stained with uranyl acetate. (B) Select 2D class averages showing the particle top view, side view and in-between tilted view. A side view (C) and a top view (E) of the EM density map calculated at 29 Å resolution with Cx26 GJC X-ray structure (pdb: 5ERA) rigid-docked. (D) and (F) are the cutaways of the views shown in (C) and (E), respectively. Map volume adjusted based on Cx26 partial specific volume (for 0.74 cm³/g)

Three-dimensional classification of cryoEM images recorded from particles at pH 6.4 yielded both open and closed states (Figure 3.1C, D, E and F) in equally populated conformations (Figure 3.6, Figure 3.7G). The open conformation refined to 4.2 Å resolution (Figure 3.7 E and H) and resembled the physiological pH structure (Figure .3.1A

and B), but with a less pronounced ring of density in the pore. The closed conformation refined to a resolution of 7.6 Å (Figure 3.7 F and H) but revealed a larger occluding density in the pore of both hemichannels with a connecting density to the M1 helix of each Cx26 protomer (Figure 3.1A and B).

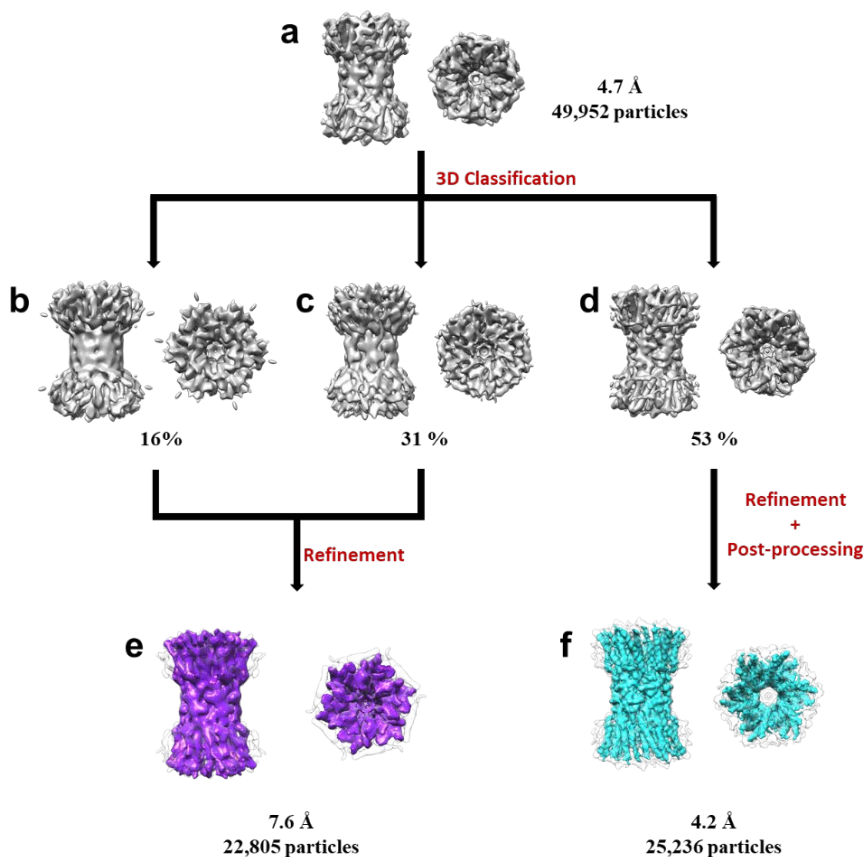


Figure 3.6. 3D Classification and refinement of the Cx26 GJC at acidic pH. Initial refinement and particle polishing resulted in a 4.7 Å resolution model (A) which was subjected to 3D classification while increasing the angular sampling incrementally from 7.5° to 0.9°. From the resulting three classes (B-D shown with relative particle distribution), particles in two classes underwent 3D refinement to create the channel in the occluded state at 7.6 Å (purple) (E) shown with amphipol density in white. Refinement of the remaining class reconstructed the open state of the channel at 4.5 Å resolution (white) and improved to 4.2 Å resolution with post-processing (cyan). All maps are contoured at 4 sigma (σ) with the exception of (F), which is contoured at 4.5 sigma (σ). Analysis performed by Ali Khan, University of Virginia.

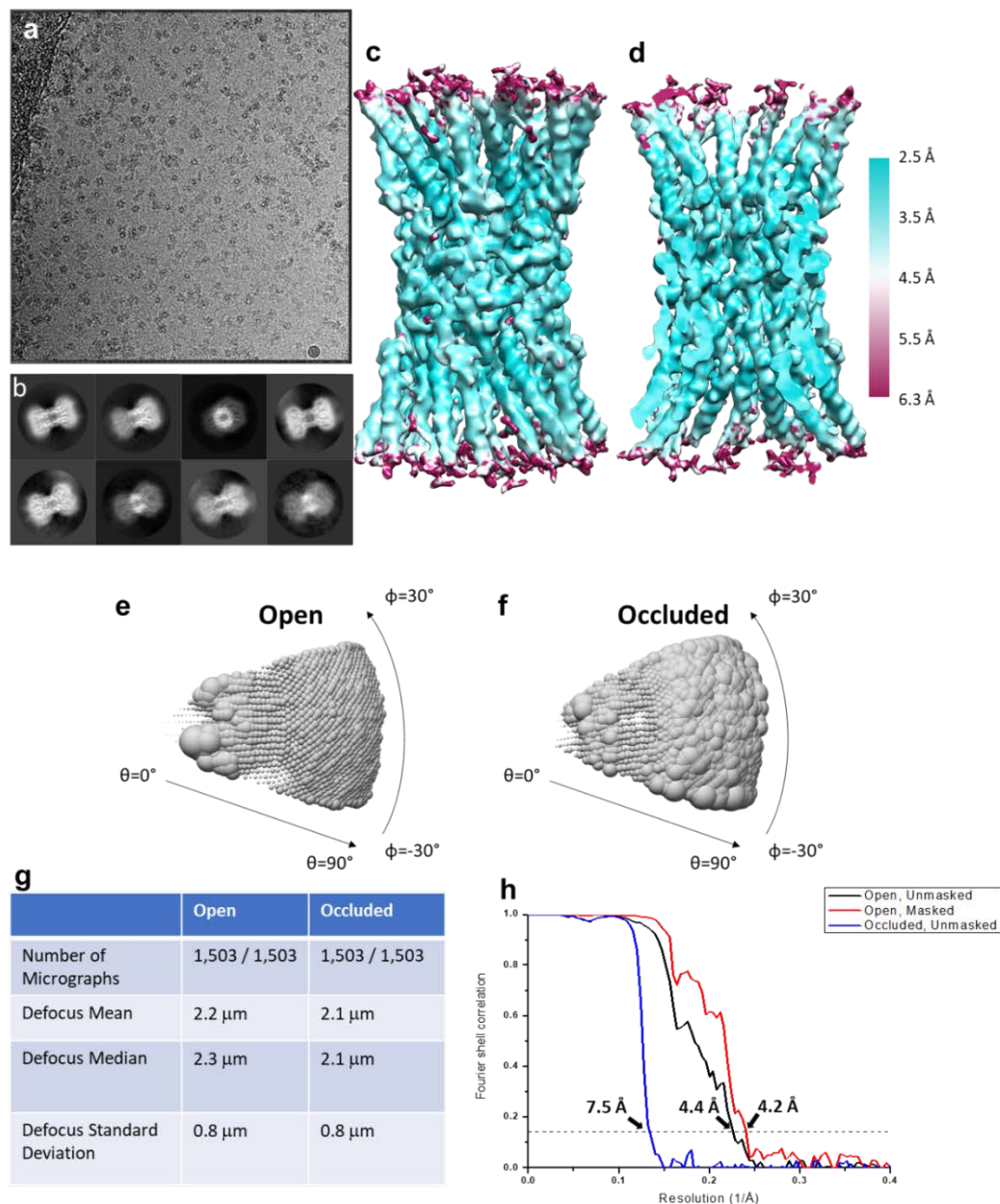


Figure 3.7. Single-particle image processing of the Cx26 GJC at pH 6.4. (A) Representative raw micrograph and (B) 2D class averages. (C) Post-processed map of open structure is shown with cropped-view (D) colored by local resolution calculation by Resmap. Euler angle distribution of open state (E) and occluded state (F) particles depicted as relative size of grey spheres. (G) Both open and occluded maps were calculated from the same final 1503 micrographs and have similar defocus values. (H) Gold-standard Fourier Shell Correlation (FSC) shows the global resolution of the map before and after masking performed in post-processing to be 4.4 Å and 4.2 Å, respectively. The resolution for the unmasked occluded structure is 7.5 Å. Analysis performed by Ali Khan, University of Virginia.

Our models display a good fit into their corresponding densities in the regions covering helices M1 through M4 and extracellular loops E1 and E2 (Table 3.2). These regions are the best resolved in all three maps (Figure 3.8). In the case of unoccluded physiological pH and low pH structures, some bulky side chains were resolved (Figure 3.8A–D, E – H), whereas the occluded low pH structure building was limited to an assignment of C α through the whole model (Figure 3.8I–L). The resolution of the maps drops towards the cytoplasmic ends of the gap-junction channel, with the last few residues of M1-M4 helices in that regions largely missing side chain densities, regardless of the overall resolution of the maps. The densities are missing for both CL and CT domains, and the densities for NT domains are incomplete and of lowest resolution in the unoccluded maps.

Refinement and Validation						
	pH 7.5		pH 6.4 (Open)		pH 6.4 (Closed)	
	NTs	no NTs	NTs	no NTs	NTs	no NTs
Start model RMSD (Å)	1.170	1.170	1.254	1.254	2.246	2.246
Ramachandran						
Favored (%)	88.37	91.03	84.30	84.62	84.30	85.26
Allowed (%)	11.05	8.33	15.70	15.38	15.70	14.74
Outlier (%)	0.58	0.64	0.00	0.00	0.00	0.00
RMSD						
Bond length (Å)	0.010	0.010	0.008	0.009	0.008	0.008
Bond angles (°)	1.190	1.176	1.137	1.155	1.283	1.319
Rotamer outliers (%)	0	0	0	0	0	0
Clashscore (Molprobit)	9.57	10.75	4.45	3.32	5.57	5.26
Molprobit score	2.10	2.07	1.89	1.79	1.97	1.94
EMRinger score	2.71	2.83	1.55	1.57	-0.60	-0.63
Map cross correlation	0.748	0.767	0.740	0.748	0.784	0.755

Table 3.2. Statistics of atomic model refinement. Start model RMSD was calculated in Chimera between a model built to cryoEM density and starting X-ray structure (pdb: 5ERA). Map cross correlation (CC) was obtained in real-space refinement tool in Phenix. The remaining parameters were calculated in either EMRinger (EMRinger score) or MolProbit, both distributed with Phenix package.

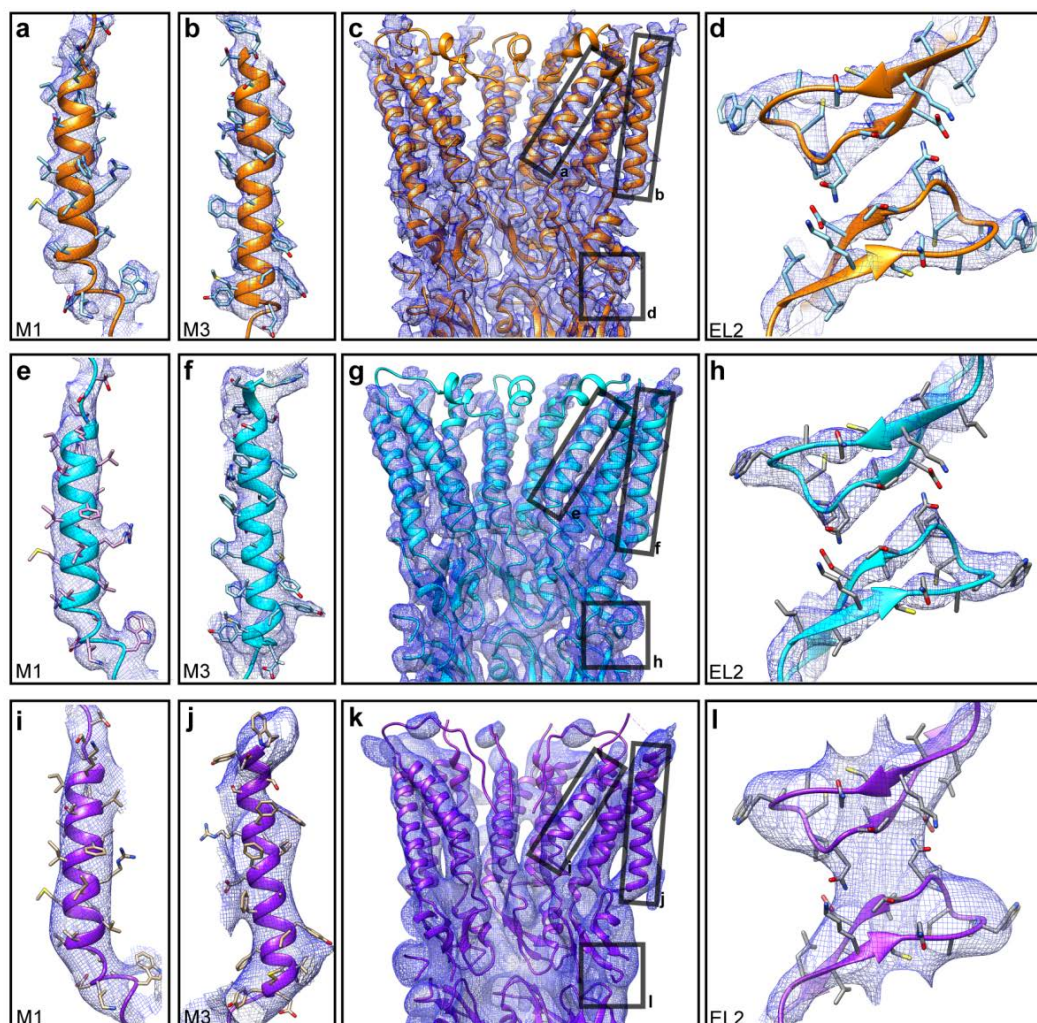


Figure 3.8. Analysis of Cx26 cryoEM maps and atomic models at neutral and acidic pH. (A-D) Analysis of neutral pH open GJC structure at 4 Å resolution. Cross-sectional view (C); a subsection of the extracellular gap region, showing E2 domains from two monomers from two opposed hemichannels (D); a close-up of M1 helix (A) and M3 helix (B). (E-H) An analogous analysis of low pH open GJC structure at 4.2 Å resolution and (I-L) low pH closed GJC structure at 7.6 Å resolution. Contour levels adjusted individually on a per-image basis. Masking and sharpening procedures were applied to neutral pH and low pH open maps.

As noted, we observe a discontinuous ring of density in the unoccluded state of the channel at both physiological (Figure 3.9 and 3.10 A, D) and acidic pH (Figure 3.9 and 3.10 B, E) with roughly the same diameter and in the same location as the terminal end of the pore occluding density seen in pH 6.4 closed map. It is unlikely that this occlusion represents an experimental artifact. At a contour level of 4σ , the occlusion and six connecting densities have a volume of $\sim 8.4 \times 10^3 \text{ \AA}^3$, which is too high to represent the amphipol membrane mimetic (9 kDa) or any buffer components.

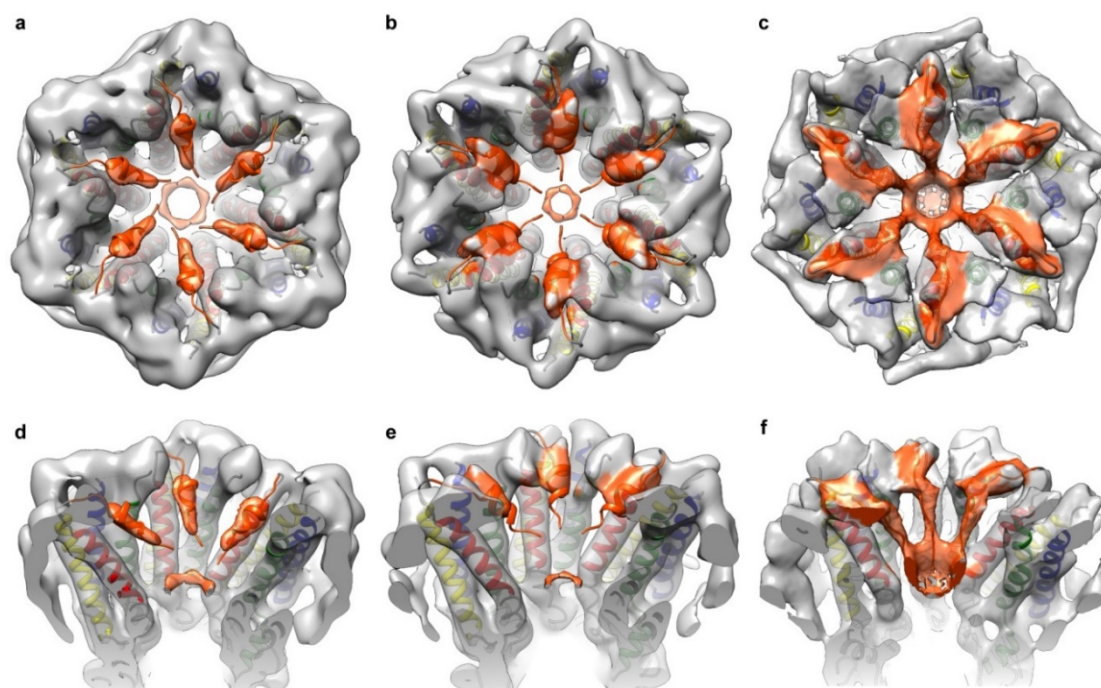


Figure 3.9. Analysis of cryoEM maps and models showing pH-gating in Cx26 mediated by NT domains. End-on views of Cx26 hemichannel from the cytoplasmic side extending to the end of transmembrane helices at the extracellular gap; pH 7.5 structure (A), pH 6.4 structure (B) and pH 6.4 'plug' structure (C). Tilted cross-sectional views of Cx26 hemichannel showing the organization of three monomers; pH 7.5 structure (D), pH 6.4 structure (E) and pH 6.4 'plug' structure (F). M1 helix (red), M2 helix (green), M3 helix (blue), M4 helix (yellow), NT domain 1-15 aa (orange), cryoEM densities (transparent light grey) and NT densities (transparent orange). Helices M1 and M4 of the central monomer in panel (F) were not colored (white). All the maps shown are at a resolution of 7.6 \AA and displayed at 4.1σ contour level. No masking or sharpening procedures were applied.

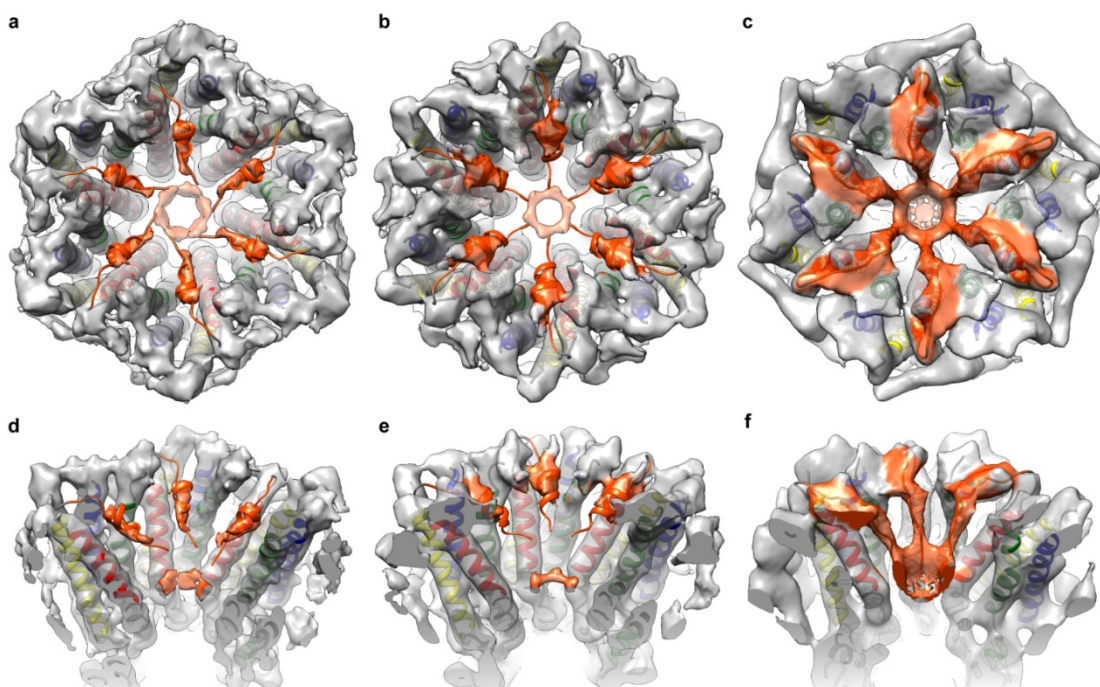


Figure 3.10. Analysis of cryoEM maps and models showing pH-gating in Cx26 mediated by NT domains. End-on views of Cx26 hemichannel from the cytoplasmic side extending to the end of transmembrane helices at the extracellular gap; pH 7.5 structure (A), pH 6.4 structure (B) and pH 6.4 'plug' structure (C). Tilted cross-sectional views of Cx26 hemichannel showing the organization of three monomers; pH 7.5 structure (D), pH 6.4 structure (E) and pH 6.4 'plug' structure (F). M1 helix (red), M2 helix (green), M3 helix (blue), M4 helix (yellow), NT domain 1-15 aa (orange), cryoEM densities (transparent light grey) and NT densities (transparent orange). To aid in interpretation, helices M1 and M4 of the central monomer in panel (F) were not colored (white). Maps displayed at 4 sigma (σ). Maps shown are without masking or sharpening procedures applied, at a resolution of 4.4 Å (pH 7.5), 4.5 Å (pH 6.4) and 7.6 Å (pH 6.4 closed).

It is also unlikely that this obstruction is an artifact of the applied D6 symmetry. Using the same particle set, we refined the occluded structure using no symmetry and C6, D2, and D3 symmetry. The no-symmetry refinement yielded an uninterpretable map (>10-Å resolution). Refinement with C6 symmetry, in which the two-fold symmetry axis parallel to the membrane is removed, revealed occlusion in both connexons indicating

that the pore is blocked on both sides (Figure 3.11A). Though at lower resolution than the D6 map, the D2- and D3-symmetric reconstructions each revealed six connecting densities to each hemichannel occlusion (Figure 3.11B and C, respectively), demonstrating that the occluding density is not an artifact of applying 6-fold symmetry and suggesting a model in which all promoters of each hemichannel contribute to the occluding density. We believe that the ring of density at physiological pH is a result of the NT equilibrating between unoccluding and occluding conformations. This hypothesis is supported by EX1 kinetics observed in the NT during HDX experiments at physiological pH (Figure 3.14B) as opposed to pH 6 which displayed no EX1 kinetics.

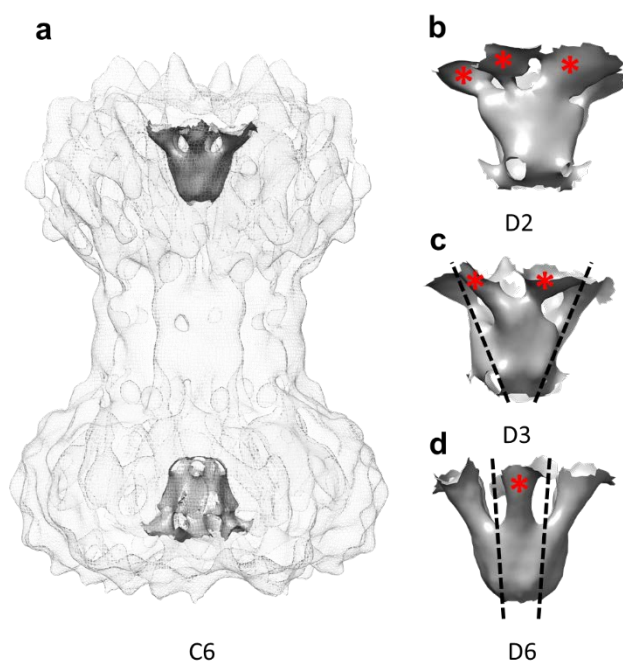


Figure 3.11. “Ball” and “chains” are conserved when cryoEM density is refined at lower symmetry values. (A) C6 symmetry refinement shows the “ball-and-chain” densities (grey) in both hemichannels. D2 (B), D3 (C), and D6 (D) refinements show six chains attached to the ball. Dotted lines roughly demarcate the symmetry axis and the red asterisk (*) specify each chain density within a single asymmetric unit of the plug. The D2 symmetry axis is parallel with the page.

While the resolution of the occluded model (7.6 Å) prohibits unambiguous assignment of amino acid residues, it is sufficient to exclude both the cytoplasmic loop and tail. The cytoplasmic tail with poly-histidine tag in our Cx26 construct is too short to occupy the connecting density and gating particle. In addition, we anticipate that the poly-histidine tag would repulse other C-tails, preventing association to form the occlusion. The cytoplasmic loop is long enough to accommodate the occlusion, but in such a scenario we would anticipate to observe twelve connecting densities, while our model only shows six that are too slim to accommodate more than one polypeptide chain (Figure 3.9 and 3.10 C and F). Another possibility is that only 3 CLs participate in gating, but the application of D6 symmetry to the map would weaken the signal from the “chain” rather than strengthen them as we observe. The occluding and connecting density in the closed state is thus most likely composed of the amino terminus. In this scenario, the acetylated N-termini (Figure 3.12) extend and accurately conforms to the complete volume of the occluding and connecting densities (Figure 3.9 and 3.10 C and F). Furthermore, the partial specific volume corresponding to all six acetylated N-termini (residue 1-14) is $\sim 10.9 \times 10^3 \text{ \AA}^3$, which closely matches the volume of the occlusion and six connecting densities ($\sim 8.4 \times 10^3 \text{ \AA}^3$).

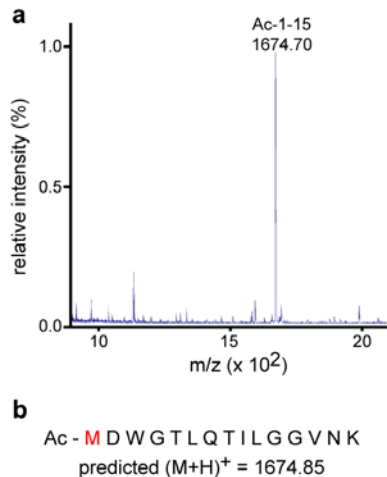


Figure 3.12. Mass spectrometry analysis of trypsin-digested Cx26 GJC. (A) Peak corresponding to the mass of Ac-1-15 amino acid peptide. (B) Sequence of the peptide detected in (A).

Hydrogen deuterium exchange reveals dynamic N-terminus at physiological pH

Hydrogen deuterium exchange (HDX) coupled with mass spectrometry was used to evaluate solvent accessibility (Figure 3.13). Several regions of Cx26 exhibited decreased deuterium exchange at lower pH: the parahelix (residues 37-50), the TM3/CL region (residues 121-132) and the NT domain (residues 7-28) (Figure 3.14A). However, differences were subtle and difficult to interpret owing to the overlap of regions of the GJC analyzed in the experiment. Additional data for the first half of NT (residues 1-7) would provide great aid in investigating the dynamics of NT region. Unfortunately, the detection rate for the 1-7 peptide during HDX experiments was unsatisfactory and HD exchange changes for that peptide could not be interpreted unambiguously.

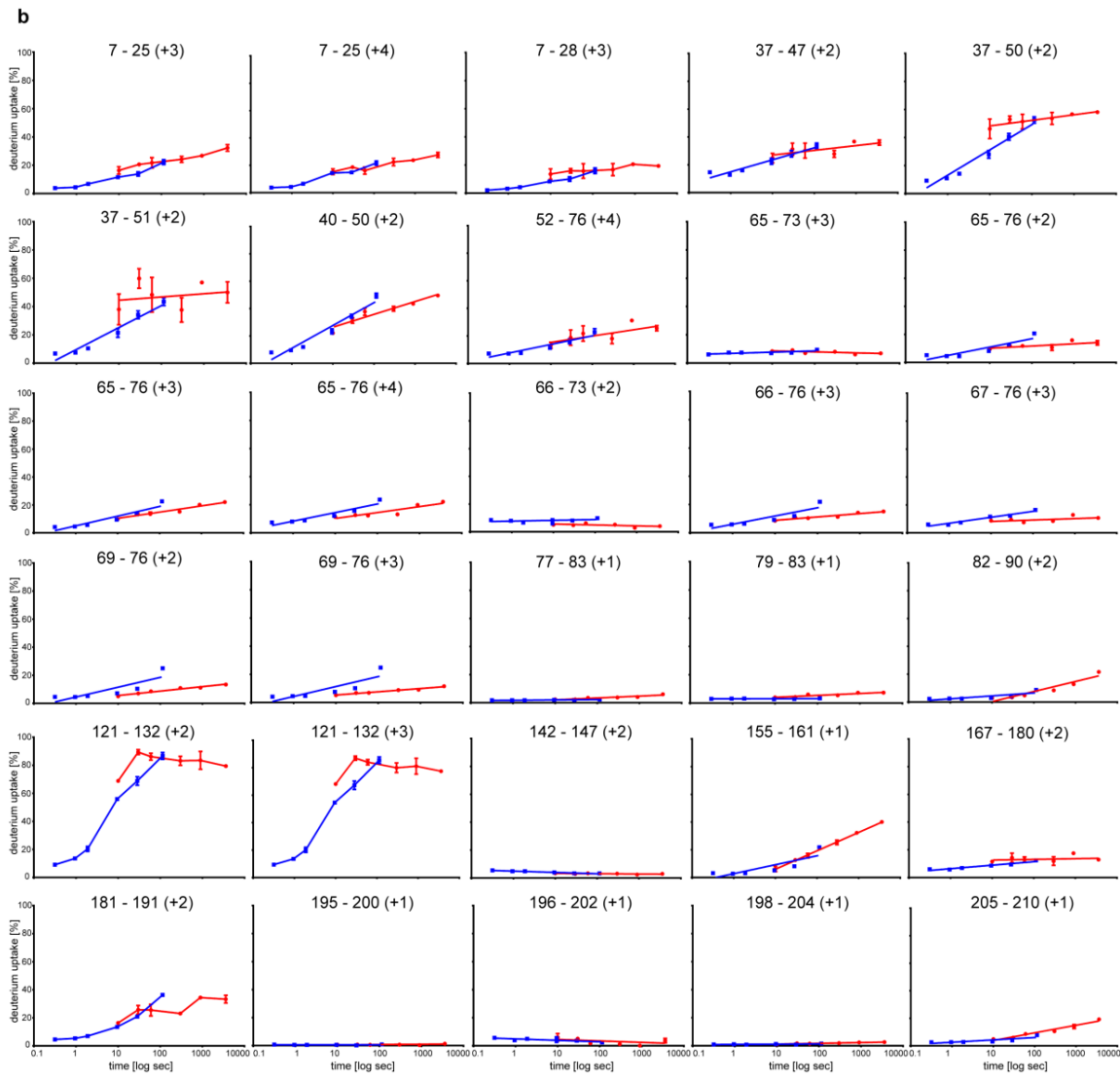
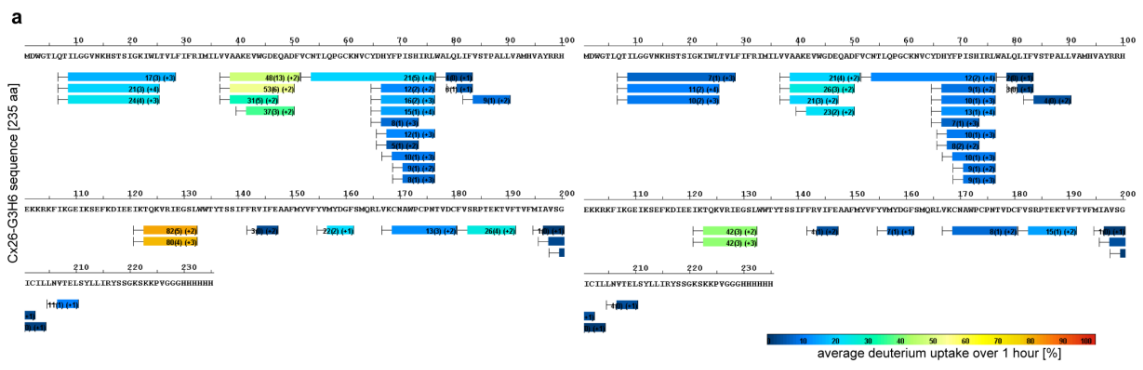


Figure 3.13. Dynamics of Cx26 GJC as revealed by hydrogen-deuterium exchange (HDX). (A) HDX results obtained at physiological pH 7.5 (left) and acidic pH 6.0 (right), mapped onto Cx26 sequence. The bars below the sequence represent the peptide fragments resolved by mass spectrometry and the bar color represents the relative deuterium/hydrogen exchange (color code on the bottom). Number within each bar is the average % of deuterium incorporated over six time points (10, 30, 60, 300, 900, and 3600 s). (B) Deuterium build-up curves of all detected peptides. Curves for pH 7.5 peptides (red) and pH 6.0 peptides (blue). The pH 6.0 curves were translated in time due to slower exchange rate of amide hydrogen. HDX experiment and mass spectrometry analysis performed by Venkat Dharmarajan, The Scripps Research Institute in Florida.

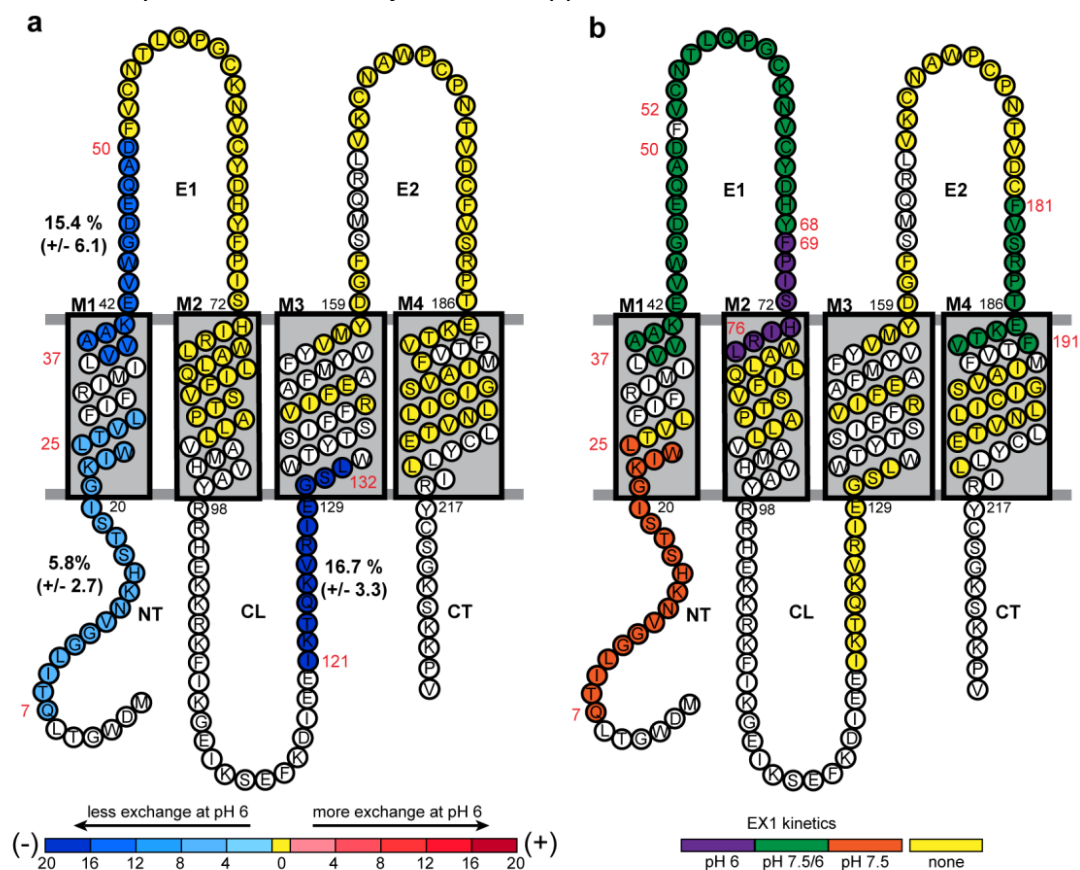


Figure 3.14. Comparison of the dynamics of Cx26 GJC between pH 7.5 and 6.0 using HDX mass spectrometry. (A) Change in deuterium uptake at pH 6.0 compared to pH 7.5. The topology model shows the localization of three regions with reduced deuterium uptake at pH 6.0. The numbers next to each of these peptides show % deuterium uptake change, along with their associated SD. (B) A topology model illustrating detected EX1 kinetics of deuterium exchange which arise from transient, large-scale unfolding events, interpreted as multiple conformational states of a given peptide. HDX experiment and mass spectrometry analysis performed by Venkat Dharmarajan, The Scripps Research Institute in Florida.

However, important information on the dynamic nature of the regions of the Cx26 GJC were obtained by HDX. EX1 kinetics which are indicative of transient conformational transitions, were observed at the N-terminus at physiological pH, but not acidic pH (Figure 3.14B). This suggests that the N-terminus may exist at more static lower energy states at acidic pH. These results indicate that the NT takes multiple conformations at physiological pH, but at acidic pH, the interconversion between states has become slower than the timescale of the HDX experiment. Taken in conjunction with the cryoEM results, we believe at physiological pH the NT is freely able to adopt multiple conformations, and acidic pH shifts the equilibrium towards the formation of occluding pore density.

Acidic pH induces movement of M2 helix

We observe no additional pore constriction due to the positioning of M1-M4 helices in our low pH closed structure which argues against the 'camera-iris'-type of mechanism for low pH gating[161]. We observe, however, RMSD values of ~ 1.5 Å for M2 helix in gated structure compared to the other structures indicative of a change in the position of that helix (Table 3.3). Indeed, while M1 helix remains largely stationary throughout our structures, M2 helix exhibits movement in the direction of M1 (Figure 3.15A–C). Our measurements indicate that high RMSD of M2 translates into the movement of C α atom of A92 on M2 helix by ~ 5 Å toward the C α atom of K22 on M1 (Figure 3.15D–E). This movement of the helix is reflected in the unoccluded cryoEM maps, where the density of the cytoplasmic end of M2 is weakest of all 4 TM domains, indicating

that this portion is likely more flexible than the others. It is worth mentioning that the density of the cytoplasmic end of M2 is weakest of all 4 TM domains, indicating that this portion is likely more flexible than the others. This behavior is observed in all the cryoEM maps. We interpret this movement as a potential part of low-pH gating mechanism where the more distant, cytoplasmic portion of M2 or even the M2-proximal part of CL interact with NTs or cytoplasmic portion of M1 within the same subunit. This interaction could be viewed as both promoting and stabilizing the occluded state visualized by cryoEM and it is also reflected in our lysine-lysine BS3 crosslinking experiment describing NT – CL interactions. (Figure 3.17).

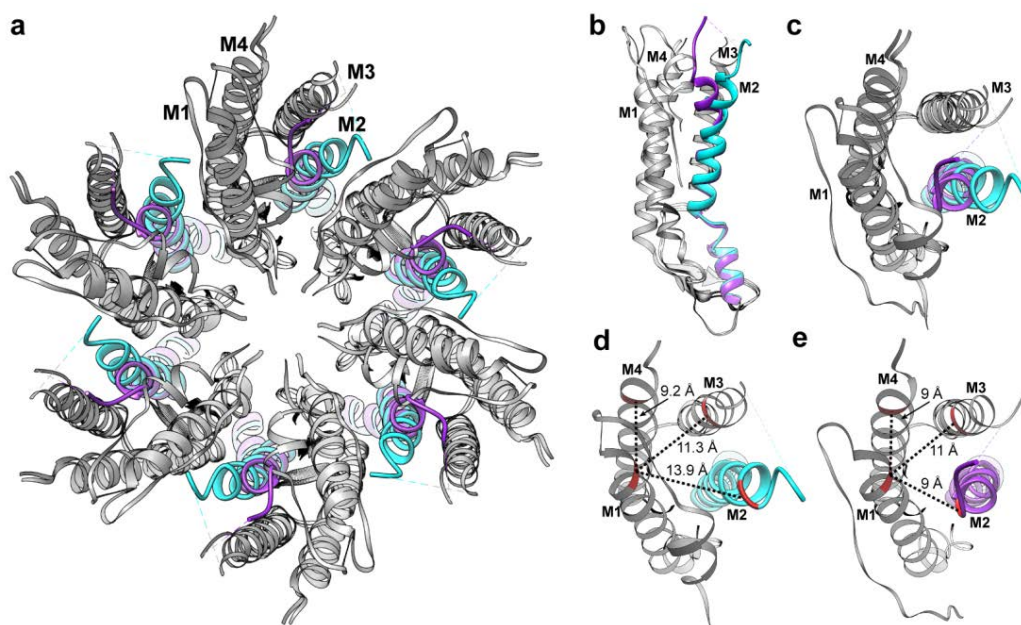


Figure 3.15. Visualization of M2 helix movement during pH-induced gating. (A) A top view of a Cx26 GJCs from pH 6.4 open and closed structures. (B) A side view of superposed Cx26 monomers from pH 6.4 open and closed structures. (C) An end-on view of superposed Cx26 monomers from pH 6.4 open and closed structures. (D) An end-on view of a Cx26 monomer from the cytoplasmic side showing distances between C α atoms of Lys22 (M1) and Ala92 (M2), Ile140 (M3) and Glu209 (M4) in the pH 6.4 open structure. (E) The same view of a Cx26 monomer but shown for the pH 6.4 closed structure. Ribbon coloring: pH 6.4 open structure (cyan), pH 6.4 closed structure (violet).

RMSD (C α)				
Region	Residue range	pH 7.5 vs pH 6.4 open	pH 7.5 vs pH 6.4 closed	pH 6.4 vs pH 6.4 closed
M1 helix	20 - 38	0.16	0.31	0.29
M2 helix	73 - 92	0.26	1.47	1.53
M3 helix	137 - 157	0.36	0.31	0.50
M4 helix	185 - 210	0.21	0.42	0.47
EL1 domain	158 - 184	0.45	0.58	0.79
EL2 domain	39 - 72	0.31	0.60	0.62

Table 3.3. RMSD values for C α atoms between neutral pH open, low pH open and low pH closed structures. RMSD calculations were performed in Chimera

Increased NT-CL association at acidic pH

The CL and CT domains were not visualized in our cryoEM experiments at either pH. In order to elucidate the conformational relationships between cytoplasmic domains, we generated lysine crosslinks of Cx26 using the bis(sulfosuccinimidyl)suberate (BS3) amine-to-amine crosslinker, with a flexible spacer arm 11.4 Å in length (Figure 3.16) and characterized each crosslink using tandem mass spectrometry (Table 3.4 and 3.5) [398, 401-403]. This approach takes advantage of the abundant lysine residues in the NT, CL and CT (2, 8, and 3 residues, respectively), but has the disadvantage of not being able to distinguish between intermolecular versus intramolecular crosslinks.

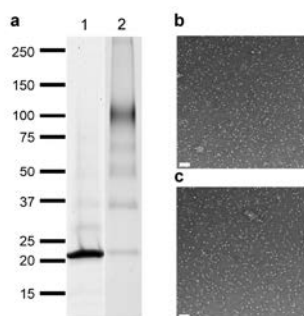


Figure 3.16. Lysine crosslinking with BS3. (A) SDS-PAGE shown as a Coomassie stained gel; lane 1: Cx26, lane 2: Cx26 treated with BS3 at 1mM for 1h at 4°C. (B-C) Negative-stain EM electron micrograph of Cx26 (B) and of Cx26 treated with BS3 (C). White bars on the EM micrographs denote 50 nm.

Crosslinks pH 7.5								
crosslink	region 1	peptide 1	region 2	peptide 2	Crosslink score	PP score	PP2 score	PPTag score
N-terminal crosslinks								
15-103	1:22	MDWGTLQTLGGVNK(\$1)HSTSIGK	103:105	K(\$1)RK	30.25	10.4	6.4	2.9
15-122	2:22	DWGTLQTLGGVNK(\$1)HSTSIGK	117:125	DIEEK(\$1)TQK	11.86	8.9	6.7	1.4
15-125	2:22	DWGTLQTLGGVNK(\$1)HSTSIGK	123:127	TQK(\$1)VR	10.28	7.4	4.2	2.1
22-116	16:32	HSTSIGK(\$1)IWLTVLFIFR	113:122	SEFK(\$1)DIEEK	16.72	8.0	9.1	1.7
22-122	16:32	HSTSIGK(\$1)IWLTVLFIFR	117:127	DIEEK(\$1)TQKVR	19.56	6.6	8.9	2.1
C-loop crosslinks								
102-105	100:103	HEK(\$1)K	105:108	K(\$1)FIK	99.58	20.7	15.8	8.2
105-103	105:108	K(\$1)FIK	103:104	K(\$1)R	42.30	6.0	9.5	3.6
108-102	106:112	FIK(\$1)GEIK	100:103	HEK(\$1)K	101.94	10.1	6.7	11.4
108-103	106:112	FIK(\$1)GEIK	103:104	K(\$1)R	144.58	21.4	7.3	11.2
108-125	106:112	FIK(\$1)GEIK	123:127	TQK(\$1)VR	108.84	22.0	6.6	14.9
112-102	109:116	GEIK(\$1)SEFK	100:103	HEK(\$1)K	75.52	22.0	9.7	9.9
112-103	109:116	GEIK(\$1)SEFK	103:104	K(\$1)R	92.74	12.0	6.6	11.6
112-105	109:116	GEIK(\$1)SEFK	105:108	K(\$1)FIK	80.93	15.6	7.9	13.9
112-125	109:116	GEIK(\$1)SEFK	123:127	TQK(\$1)VR	128.98	27.7	6.3	13.6
116-102	113:122	SEFK(\$1)DIEEK	100:103	HEK(\$1)K	91.12	28.1	9.1	16.0
116-103	113:122	SEFK(\$1)DIEEK	103:104	K(\$1)R	114.00	21.6	7.0	15.2
116-105	113:122	SEFK(\$1)DIEEK	105:108	K(\$1)FIK	206.92	18.9	8.3	20.3
116-108	113:122	SEFK(\$1)DIEEK	106:112	FIK(\$1)GEIK	130.42	21.4	5.8	18.6
116-125	113:122	SEFK(\$1)DIEEK	123:127	TQK(\$1)VR	124.38	26.3	6.2	16.4
122-102	117:125	DIEEK(\$1)TQK	100:103	HEK(\$1)K	135.41	27.3	9.7	14.2
122-103	117:125	DIEEK(\$1)TQK	103:104	K(\$1)R	235.09	25.1	7.6	18.3
122-105	117:125	DIEEK(\$1)TQK	105:108	K(\$1)FIK	211.04	26.6	9.1	20.2
122-108	117:125	DIEEK(\$1)TQK	105:112	KFIK(\$1)GEIK	132.58	15.1	8.4	8.3
122-112	117:125	DIEEK(\$1)TQK	109:116	GEIK(\$1)SEFK	115.47	22.5	6.0	15.8
125-102	123:127	TQK(\$1)VR	100:103	HEK(\$1)K	94.90	24.1	9.3	11.0
125-103	123:127	TQK(\$1)VR	103:104	K(\$1)R	65.46	13.9	6.8	5.2
125-105	123:127	TQK(\$1)VR	105:108	K(\$1)FIK	108.56	19.7	8.0	7.8
C-terminal crosslinks								
105-223	105:108	K(\$1)FIK	222:224	SK(\$1)K	84.47	6.1	6.1	3.8
108-221	106:112	FIK(\$1)GEIK	217:223	YSSGK(\$1)SK	77.71	17.2	6.6	11.9
108-223	106:112	FIK(\$1)GEIK	222:224	SK(\$1)K	100.40	14.6	9.0	7.8
112-221	109:116	GEIK(\$1)SEFK	217:223	YSSGK(\$1)SK	61.70	12.0	6.6	11.6
112-223	106:116	FIKGEIK(\$1)SEFK	222:224	SK(\$1)K	42.02	7.0	4.8	3.1
116-221	113:122	SEFK(\$1)DIEEK	217:223	YSSGK(\$1)SK	103.22	27.2	7.0	17.0
116-223	113:122	SEFK(\$1)DIEEK	222:224	SK(\$1)K	91.40	17.5	4.9	11.9
116-224	109:122	GEIKSEFK(\$1)DIEEK	222:235	SKK(\$1)PVGGGHHHHHH	31.17	7.2	6.6	3.0
122-221	117:125	DIEEK(\$1)TQK	217:223	YSSGK(\$1)SK	143.25	12.2	8.5	5.3
122-223	117:125	DIEEK(\$1)TQK	222:224	SK(\$1)K	103.09	22.9	9.4	15.8
221-102	217:223	YSSGK(\$1)SK	100:103	HEK(\$1)K	71.88	18.5	8.5	5.8
221-103	217:223	YSSGK(\$1)SK	103:104	K(\$1)R	69.58	13.2	11.4	6.1
221-105	217:223	YSSGK(\$1)SK	105:108	K(\$1)FIK	88.20	19.0	8.9	11.2
221-125	217:223	YSSGK(\$1)SK	123:127	TQK(\$1)VR	77.61	12.1	11.0	5.1
223-102	217:224	YSSGKSK(\$1)K	99:103	RHEK(\$1)K	58.38	16.4	11.1	4.6
223-103	222:235	SK(\$1)KPVGGGHHHHHH	103:105	K(\$1)RK	5.65	2.1	5.2	2.0
223-125	217:224	YSSGKSK(\$1)K	123:127	TQK(\$1)VR	27.65	5.6	8.4	1.9
224-102	224:235	K(\$1)PVGGGHHHHHH	100:103	HEK(\$1)K	11.42	7.7	5.4	2.5
224-103	224:235	K(\$1)PVGGGHHHHHH	103:105	K(\$1)RK	32.41	10.9	7.2	2.8
224-105	224:235	K(\$1)PVGGGHHHHHH	105:108	K(\$1)FIK	45.39	13.7	8.9	4.3
224-108	222:235	SKK(\$1)PVGGGHHHHHH	106:112	FIK(\$1)GEIK	38.16	4.4	6.5	8.1
224-122	222:235	SKK(\$1)PVGGGHHHHHH	117:125	DIEEK(\$1)TQK	39.18	6.3	4.6	2.5
224-125	222:235	SKK(\$1)PVGGGHHHHHH	123:127	TQK(\$1)VR	20.24	10.8	4.9	2.8
224-221	224:235	K(\$1)PVGGGHHHHHH	217:223	YSSGK(\$1)SK	53.83	7.3	7.7	1.4

Crosslinks pH 6.0								
crosslink	region 1	peptide 1	region 2	peptide 2	Crosslink score	PP score	PP2 score	PPtag score
N-terminal crosslinks								
15-105	2:22	DWGLTQLTILGGVVK(\$1)HSTSIGK	104:108	RK(\$1)FIK	19.65	5.1	2.4	3.2
15-108	2:22	DWGLTQLTILGGVVK(\$1)HSTSIGK	105:112	KFK(\$1)GEIK	7.20	5.1	4.5	2.4
15-112	1:22	MDWGLTQLTILGGVVK(\$1)HSTSIGK	106:116	FIKGEIK(\$1)SEFK	6.35	3.9	5.8	1.5
15-122	2:22	DWGLTQLTILGGVVK(\$1)HSTSIGK	117:125	DIEIK(\$1)TQK	13.11	8.5	5.6	1.9
15-125	2:22	DWGLTQLTILGGVVK(\$1)HSTSIGK	123:127	TQK(\$1)VR	15.23	7.4	4.3	1.9
22-102	16:32	HSTSIGK(\$1)IWLTVLFIFR	100:103	HEK(\$1)K	6.75	5.3	4.4	1.9
22-105	16:32	HSTSIGK(\$1)IWLTVLFIFR	105:108	K(\$1)FIK	7.45	4.7	5.2	2.5
22-116	16:32	HSTSIGK(\$1)IWLTVLFIFR	113:122	SEFK(\$1)DIEIK	9.34	4.5	6.7	1.8
22-122	16:32	HSTSIGK(\$1)IWLTVLFIFR	117:127	DIEIK(\$1)TQKVR	17.53	6.6	4.2	2.4
C-loop crosslinks								
102-105	100:103	HEK(\$1)K	105:108	K(\$1)FIK	124.07	7.2	10.7	3.6
105-103	105:108	K(\$1)FIK	103:104	K(\$1)R	67.06	14.7	13	8.4
108-102	106:112	FIK(\$1)GEIK	100:103	HEK(\$1)K	121.25	17.5	9.8	10.8
108-103	105:112	KFK(\$1)GEIK	103:104	K(\$1)R	181.01	11.8	8.0	7.5
108-125	106:112	FIK(\$1)GEIK	123:127	TQK(\$1)VR	100.19	19.3	6.4	15.3
112-102	109:116	GEIK(\$1)SEFK	100:103	HEK(\$1)K	60.15	19.8	9.7	8.9
112-103	109:116	GEIK(\$1)SEFK	103:104	K(\$1)R	87.97	12.0	5.8	11.6
112-105	109:116	GEIK(\$1)SEFK	105:108	K(\$1)FIK	105.79	20.0	8.0	16.7
112-125	109:116	GEIK(\$1)SEFK	123:127	TQK(\$1)VR	105.46	19.5	6.2	12.8
116-102	113:122	SEFK(\$1)DIEIK	100:103	HEK(\$1)K	75.08	28.1	9.3	16.0
116-103	113:122	SEFK(\$1)DIEIK	103:104	K(\$1)R	109.75	23.2	7.8	12.6
116-105	113:122	SEFK(\$1)DIEIK	105:108	K(\$1)FIK	165.88	21.1	7.9	17.7
116-108	113:122	SEFK(\$1)DIEIK	106:112	FIK(\$1)GEIK	158.92	20.6	7.4	19.9
116-125	113:122	SEFK(\$1)DIEIK	123:127	TQK(\$1)VR	120.10	25.5	6.2	17.9
122-102	117:125	DIEIK(\$1)TQK	100:103	HEK(\$1)K	138.15	29.9	9.4	14.2
122-103	117:125	DIEIK(\$1)TQK	103:104	K(\$1)R	217.43	27.7	7.8	18.7
122-105	117:125	DIEIK(\$1)TQK	105:108	K(\$1)FIK	176.43	22.4	8.6	16.3
122-108	117:125	DIEIK(\$1)TQK	105:112	KFK(\$1)GEIK	187.48	16.3	8.2	8.4
122-112	117:125	DIEIK(\$1)TQK	109:116	GEIK(\$1)SEFK	95.38	17.6	7.0	11.3
125-102	123:127	TQK(\$1)VR	100:103	HEK(\$1)K	72.20	19.7	8.9	5.2
125-103	123:127	TQK(\$1)VR	103:105	K(\$1)RK	59.61	10.0	7.7	2.8
125-105	123:127	TQK(\$1)VR	105:108	K(\$1)FIK	99.57	15.0	7.5	7.0
C-terminal crosslinks								
102-223	100:103	HEK(\$1)K	222:224	SK(\$1)K	49.91	4.5	7.2	3.8
103-223	100:104	HEK(\$1)R	222:224	SK(\$1)K	33.66	6.1	8.3	2.4
105-223	104:108	RK(\$1)FIK	222:224	SK(\$1)K	126.10	7.1	7.0	3.3
108-221	106:112	FIK(\$1)GEIK	217-223	YSSGK(\$1)SK	93.07	17.9	6.1	11.9
108-223	106:112	FIK(\$1)GEIK	222-224	SK(\$1)K	104.52	12.4	11.6	7.8
112-221	109:116	GEIK(\$1)SEFK	217-223	YSSGK(\$1)SK	81.15	26.5	7.0	16.1
112-223	106:116	FIKGEIK(\$1)SEFK	222:224	SK(\$1)K	46.72	4.4	7.3	2.4
116-221	109:122	GEIKSEFK(\$1)DIEIK	217-223	YSSGK(\$1)SK	111.14	13.8	12.1	3.0
116-223	113:122	SEFK(\$1)DIEIK	222:224	SK(\$1)K	84.33	11.5	7.1	10.7
116-224	109:122	GEIKSEFK(\$1)DIEIK	222:235	SKK(\$1)PVGGGHHHHH	38.72	4.9	5.3	3.9
122-221	117:125	DIEIK(\$1)TQK	217-223	YSSGK(\$1)SK	138.51	27.4	6.1	16.1
122-223	117:125	DIEIK(\$1)TQK	222:224	SK(\$1)K	100.99	29.0	9.6	18.0
125-223	123:127	TQK(\$1)VR	222:224	SK(\$1)K	47.77	11.3	8.2	1.9
221-102	217:224	YSSGK(\$1)SKK	99:103	RHEK(\$1)K	57.61	15.8	12.4	2
221-103	217:223	YSSGK(\$1)SK	103:104	K(\$1)R	82.04	13.2	7.4	6.5
221-105	217:223	YSSGK(\$1)SK	105:108	K(\$1)FIK	88.68	14.3	7.6	7.1
221-125	217:223	YSSGK(\$1)SK	123:127	TQK(\$1)VR	98.14	26.9	7.0	11.9
224-103	224:235	K(\$1)PVGGGHHHHH	103:105	K(\$1)RK	27.56	13.1	8.2	2.5
224-108	224:235	K(\$1)PVGGGHHHHH	106:112	FIK(\$1)GEIK	25.71	3.3	8.4	3.2
224-112	224:235	K(\$1)PVGGGHHHHH	106:116	FIKGEIK(\$1)SEFK	13.60	5.6	5.3	1.9
224-122	224:235	K(\$1)PVGGGHHHHH	117:127	DIEIK(\$1)TQKVR	14.72	10.3	5.6	1.9
224-125	224:235	K(\$1)PVGGGHHHHH	123-127	TQK(\$1)VR	8.33	1.5	5.1	2.4
224-221	224:235	K(\$1)PVGGGHHHHH	217:223	YSSGK(\$1)SK	55.07	5.0	6.9	2.1

Table 3.4 and 3.5. Mass spectrometry analysis of BS3 crosslinking experiment at pH 7.5 (top) and 6 (bottom). High-confidence crosslinked peptide pairs selected based on the PP and PPTag scores as well as the number of color tags. Higher PP and PPTag scores indicate better peptide match quality. The cut-off criterion for 'real' matches was set to 2.4 for PP score and 1.3 for PPTag score. Color tags on protein sequence indicate an amino acid residue with a pair of consecutive y ions (green), a pair of consecutive b ions (blue) or with both pairs of consecutive b and y ions (red). Tags provide a direct visual indication of match quality and the higher the number of color tags of a peptide match the better the match. Crosslinked lysines are labeled with a (\$) symbol. For some crosslinks identified in multiple peptide pairs, only the best pair was included in the table. Mass spectrometry experiment performed by Venkat Dharmarajan, The Scripps Research Institute in Florida.

The most populated group includes crosslinks between the cytoplasmic C-terminal (217-235 aa) and C-loop (98-129 aa) domains with lysines 221, 223 and 224 crosslinked with every lysine in the C-loop (Figure 3.17E). While the CT is too short to form the gating particle, CT-CL interactions have been previously reported to be pH-dependent [258]. The observed pH-dependent changes concern only K224, which forms unique crosslinks with K102 and K105 at pH 7.5 and with K112 at pH 6. The rest of K224 crosslinks was detected in both pH conditions. Given the proximity of K223 and K221 to K224 and their unchanged crosslinking pattern, the subtle changes in K224 crosslinking do not appear meaningful enough to allow for a clear interpretation of the pH effect on CL-CT interaction.

The second most numerous group of crosslinks consists of those located within the CL domain (98-129 aa), which is not surprising given the proximity of M2 and M3 helices in Cx26 structure restricting the spread of CL lysines (Figure 3.17D). Almost every lysine in this lysine-rich domain (8 residues out of 15 in total in Cx26) was crosslinked with every other lysine in that region. No difference was detected between samples from pH 7.5 and pH 6 though. There is no evidence that the CL domain participates in pH-gating in

Cx26. It was, however, shown to be dynamic[149], which could help explain the abundance of crosslinks in CL. This notion was further fortified by the lack of C-loop densities in existing structural X-ray and cryoEM data.

Crosslinks between N-terminal (1-15 aa) and C-loop (98-129 aa) domains are characterized by lower overall crosslinking efficiency scores with a number of crosslinks obtained from pH 7.5 sample assigned poor confidence rating (Figure 3.17C). Despite that, 10 peptide pairs have been identified with confidence. Under acidic conditions, K22 (M1) uniquely crosslinked with K102 and K105, and K15 (NT) crosslinks with K105, K108, and K112. The only unique crosslink in physiological pH was K15 to K103. It was suggested that residues N14 and H100 interact electrostatically what contributes to the ability of Cx26 to close in response to lowered pH, which can be abolished by substituting a positively charged amino acid in position 14 and rescued by mutating residue 100 to one without charge[301]. Our observations from cryoEM and crosslinking experiments are consistent with this previous work because we see crosslinking of nearby residues and a shift of M2 towards NT of the same protomer which would bring these residues closer together in the occluded structure (Figure 3.15A). This hypothesis is further strengthened by the lack of observing any intermediate “ball-and-chain” structures that involved fewer than six “chains.”

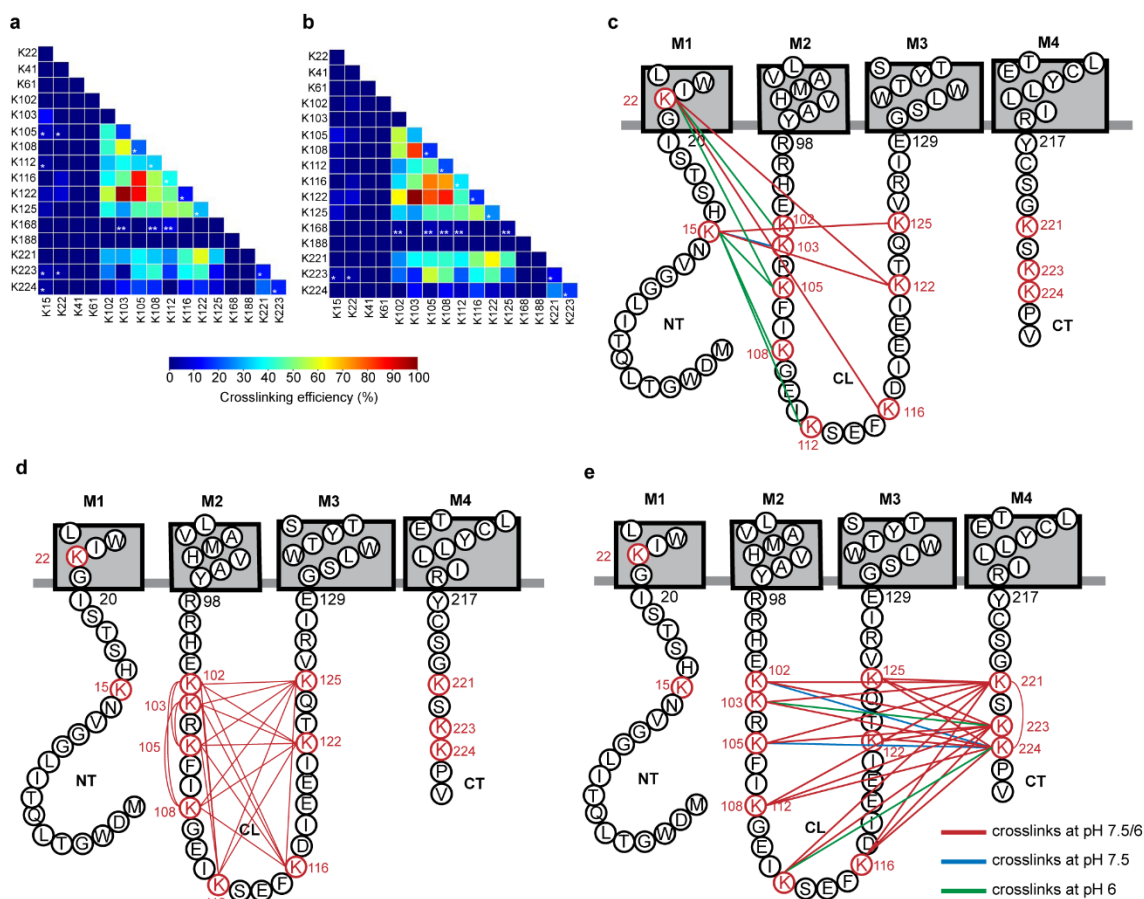


Figure 3.17. Mapping of lysine-lysine crosslinks. The heat maps showing crosslinks detected at pH 7.5 (A) and pH 6.0 (B). The square color represents crosslinking efficiency (color code on the bottom). Squares denoted with (*) are low-confidence crosslinks, not included in the analysis. Squares denoted with (**) are low-scored crosslinks with lysine 168 and are not analyzed. (C) Crosslinks between NT and CL domains. (D) Crosslinks within CL domain. (E) Crosslinks between CL and CT domains. Mass spectrometry experiment performed by Venkat Dharmarajan, The Scripps Research Institute in Florida.

Concluding Remarks

GICs are believed follow a “ball-and-chain” mechanism of closure similar to that of the voltage-gating of sodium and potassium channels [404, 405]. This hypothesis was first established in studies of Cx43 where acidification-induced uncoupling was abolished

with a C-terminal truncation at residue 257[251] and could be restored if the truncated CT portion was co-expressed as a separate peptide [225]. While most connexins show pH gating in this manner, truncation of the CT does not affect pH gating of Cx26 [reference]. Evidence of the particle receptor model of pH closure in Cx26 first came from 2D crystallographic studies, where a low-resolution model of Cx26 M34A at pH 5.8 with several other GJC inhibitors (calcium, magnesium, carbenoxolone, and aminosulfonates) displayed an occluding density in the channel pore [146]. The identity of the occluding particle was unclear from these studies since the resolution was too low for unambiguous assignment and since there was no visible density connecting the occlusion to the rest of the channel, though it should be noted that follow-on studies with an N-terminal deletion (residue 2- 7) revealed a less prominent occluding density [145]. Supporting the notion of the the N-terminal domain playing the role of a physical plug, mutations in the NT domain were shown to either remove or diminish the effect of low pH on Cx26 hemichannels[301].

Our observations support the hypothesis that pH-mediated gating of Cx26 is achieved by a “ball-and-chain” mechanism. We conclude that acidic pH shifts the equilibrium of a highly flexible NT towards an extended state which then associates with other NTs to form the gating particle or “ball” (Figure 3.18). This association is accompanied by translocation of M2 towards M1, and increased proximity of CL with NT. Formation of the “ball” appears to be required for inhibition. The pore diameter with the connecting densities or “chains” alone is measured to be roughly ~ 16 Å in the pH 6.4

closed structure, which would allow passage of a potassium ion with at least 2 shells of hydration (12 Å in diameter). The movement of the M2 helix may be correlated to an interaction between residues N14 and H100, which previous studies have shown to be essential for pH regulation [301], but the resolution of the closed structure and incomplete visualization of the cytoplasmic domains precludes analysis of these amino acids. Future structures with N-terminal deletion mutants would certainly help validate the identity of the gating particle but attempts to delete N-terminal residues thus far have resulted in constructs with severe expression defects.

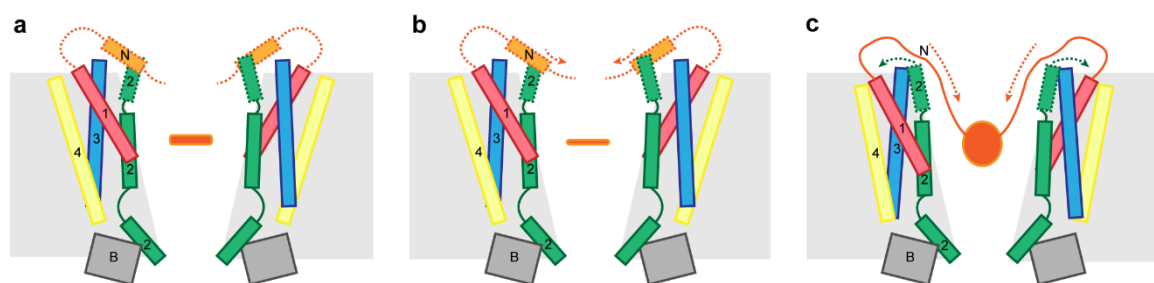


Figure 3.18. Low pH – induced gating model. (A) Neutral pH open structure. (B) Low pH open structure. (C) Low pH occluded structure. M1 helix (red), M2 helix (green), M3 helix (blue), M4 helix (yellow), NT domain 1-15 aa (orange), β -sheet EL1 and EL2 domains (dark grey).

Our gated cryoEM structure clearly shows occlusion in both hemichannel pores, and we were not able to individually classify any 3D classes with ball-and-chains formation on only a single hemichannel. However, it should be noted that the protein preparations for both cryoEM and mass spectrometry studies lack any chemical gradient across the junction. In the presence of a pH gradient, it is plausible that the channel can be gated on only one side. Our structure also shows the “ball” made up of six “chains.” Previous studies on concatemer pannexin channel have revealed that C-terminal gating does not

require participation from all protomers. It is easy to envision a similar phenomenon in Cx26, where the “ball” can be formed by fewer NTs, which would still successfully halt or greatly dampen conductance. Indeed, traces of asymmetry in the “ball” closing the channel in pH-gating can be found in electron crystallographic studies of Cx26 M34A mutant [145]. Moreover, analysis of the pH sensitivity of heteromeric Cx32 GICs demonstrated that connexin subunits act independently of each other [325].

To our knowledge, this is the first instance in which a complete, oligomeric “ball-and-chain” has been visualized. While not exactly like fast inactivation of sodium and potassium channels, we observe several properties consistent with these “ball-and-chain” mechanisms. First, in shaker K⁺ channels, the ball-and-chain are formed by the terminal end of the N-terminus. Based on X-ray crystal structures of KcsA K⁺ channel in the presence of tetrabutylammonium (TBA) and tetrabutylantimony (TBSb), Zhou *et al.* proposed that gating requires extending of the N-terminus so that may enter and gate the pore[406]. Our structure is consistent with this finding because the N-terminus appears to be fully extended all the way to the acylated cap of NT to fit the ball-and-chain density. Second, sodium and potassium channels only receive the “ball-and-chain” in the open state. The gating particle of Cx26 also seems to occlude an open pore conformation which could easily accommodate hydrated potassium ions. It is unclear currently what drives the formation of the ball, but it maybe that a conformational change such as the camera-iris model[161] proposed by Unwin and Ennis would preclude formation of the pH gate. Lastly, ball-and-chains are believed to be inherently disordered structures, which

has precluded their visualization thus far. At physiological pH, both HDX EX1 kinetic measurement and cryoEM reveal inherent conformational heterogeneity in the gating particle (NT), and our occluded structure is significantly lower resolution than the open state, though the imaging conditions are identical to the ungated acidic pH map. This moderate resolution maybe a result of the heterogeneity that arises from this relatively disordered state. Fortunately, the ability of single-particle cryoEM to resolve heterogenous particle states and refine moderate resolution structures has given us the ability to visualize the pH induced “ball-and chain.”

Chapter 4. Summary

4.1 Conclusions

To develop a purification protocol and characterize zinc transporter ZnT8, I have utilized microbiological, biochemical, spectroscopic and electron microscopy techniques. Initial protein expression and two-step purification from yeast cells resulted in recovery of small amounts of ZnT8B. Higher protein expression levels and protein purity were achieved when I transitioned to an insect cell expression system. This system has resulted in purification of both ZnT8B and ZnT8A isoforms, although the latter with a lower yield. Extensive detergent screenings have revealed FC-12 as the only detergent able to keep the target protein stable in solution, with melting temperatures recorded of around 57°C. MALDI-MS analysis of purified protein showed a monomeric as well as dimeric species which masses corresponded to that of ZnT8. Native gel electrophoresis has suggested that the mass of the protein was ~ 70 – 80 kDa. Taken together with SEC purification profiles, these results indicated that purified ZnT8 is indeed a dimeric protein. I have then performed several single particle analyses of negative stained ZnT8B particles. These analyses have resulted in a low-resolution structure of ZnT8, with molecular boundary clearly recapitulating that of bacterial homolog YiiP, thus suggesting a dimeric architecture for ZnT8. The *in vivo* transport assay in yeast with radioactive Zn²⁺ has shown that yeast overexpressing ZnT8 gained the ability to exclude labeled Zn²⁺, interpreted as the result of the proton gradient present, driving Zn²⁺ efflux from yeast cells. An *in vitro*

transport assay was developed in which ZnT8A and ZnT8B were reconstituted into unilamellar liposomes loaded with a fluorescent Zn²⁺ indicator dye. We observed that Zn²⁺ uptake via ZnT8 was driven by H⁺ efflux resulting from the pH gradient across the liposome membrane. The results from both functional assays are in agreement with the prevailing notion that ZnT8 operates as a Zn²⁺/H⁺ antiporter, similar to the bacterial homolog YiiP. In order to structurally investigate the novel N-terminal domain of ZnT8 as well as its C-terminal domain, both were produced in *E. coli* as fusion proteins. Circular dichroism (CD) spectrometry showed that these two protein domains exhibited distinctive secondary structures. The structure of C-terminal domain resembled that of the characterized bacterial homolog, whereas the unique N-terminal domain was found to have significant β -sheet and β -turn content, contrary to it being predicted disordered. In conclusion, we have been able to obtain a stable and homogenous preparation of ZnT8, that displayed a predicted dimeric architecture with a structured N-terminus and functioned as a proton gradient-driven Zn²⁺ transporter.

To investigate pH regulation of gap junction channel Connexin 26, I have utilized biochemical, mass spectrometry and cryo-electron microscopy techniques. I have purified Cx26 GJC and transferred the protein into amphipol. Thermal stability assay has reported high melting temperatures in pH range 6.0 – 7.5, indicating good protein stability. I reconstructed the volume of the protein using negative stained particles and single particle analysis. The low-resolution map has closely resembled the existing X-ray structures of Cx26 and there were unidentified densities inside the channel pore. Cryo-

electron microscopy was used to determine the structure of Cx26 at pH 7.5. This high-resolution structure represented an open state of the channel, with traces of density inside the channel pore forming a flat ring, however. From all three cytoplasmic domains, only the N-terminal domain was assigned to resolved densities. Then, cryoEM single-particle analysis of protein sample at pH 6.4 has yielded two maps. Whereas the higher-resolution map has largely resembled the map calculated at pH 7.5 and thus recapitulated the previous GJC crystal structures, the lower-resolution map has revealed pore-occluding densities. After verifying that the occluding density is not an artifact of applying 6-fold symmetry during map refinement and that it could not represent any of the buffer components, it was interpreted as N-terminal domains associating inside the channel pore and forming a physical blockage. The position of M2 helix in this map was found to be different than those in the other two maps, with the C-loop proximal part of M2 helix leaning closer to M1 helix in the same subunit. This finding was further strengthened by the findings from lysine crosslinking with tandem mass spectrometry experiments. They revealed closer association between the N-terminal domains and the cytoplasmic loops at acidic pH relative to neutral pH. To evaluate protein dynamics, we resorted to hydrogen deuterium exchange (HDX) coupled with mass spectrometry. Although several regions of Cx26 exhibited decreased deuterium exchange at lower pH, differences were subtle and difficult to interpret. However, EX1 kinetics were observed at the N-terminus at physiological pH, but not acidic pH, indicating that the N-terminus takes multiple conformations at physiological pH only. Taken together, we proposed a 'ball-and-chain'

mechanism in which the N-terminal domains associate to form a gating particle and occlude the channel pore during pH-mediated gating.

To gain insight into the structure of Connexin 26 hemichannel, I have tested various membrane mimetics and utilized electron and cryo-electron microscopy techniques. A mutation in connexin 26 gene was introduced (N176Y) in order to prevent connexin hemichannels from docking and forming GJCs. This mutant was then purified as a hexameric hemichannel. Electron and cryo-electron microscopy study of the N176Y hexamer in detergent and amphipol has revealed that although protein particles appear homogenous shortly after purification, the protein is conformationally unstable. This instability is pronounced after prolonged protein incubation, where the presence of small molecular weight debris indicates that N176Y hexamers collapse. As a result, I have decided to reconstitute the protein in lipid nanodiscs. CryoEM analysis of the nanodiscs on C-flat carbon grids resulted in 2D class averages clearly showing *en face* protein views with visible α -helical secondary structure. Unfortunately, particles displayed a preferred orientation on the grids. To remedy this, I prepared pegylated gold grids, on which the protein adopted a more random orientation which resulted in 2D class averages showing both *en face* views and side views with traces of secondary structure. To conclude, I have obtained a sample of connexin 26 in its hemichannel form and optimized protein sample, EM grid type and freezing conditions for future high-resolution structure determination.

4.2 Future Directions

The low-resolution structure of ZnT8B in detergent is but the first step in its structure determination. With the recent advances in cryo-electron microscopy of small proteins, including the development of Volta phase plate, imaging of proteins under 100 kDa and their structure determination now became feasible. Single particle analysis of ZnT8 which is, depending on the isoform, a 70 – 80 kDa protein, would also benefit from its C2 symmetry. If need arises, ZnT8 could be attached to a fusion protein partner for increased mass and number of structural features thus facilitating particle picking and alignment – both crucial steps in structural work with small proteins. Potential issues with protein flexibility or instability in the membrane region could be remedied by reconstituting it in nanodiscs. Addition of Zn²⁺ to stabilize its bound state should also be considered.

The pH-gating mechanism of connexin 26 could be further explored by cryoEM studies in nanodiscs where protein would be allowed to adopt conformations even closer to their physiological state than in amphipol. Apart from lipids having a potential beneficial stabilizing effect on connexins, if sufficiently high resolution of cryoEM maps is achieved, lipid binding sites could be unraveled. This might be particularly interesting since lipid and lipid-active compounds were found to modulate connexin activity. Additionally, structure determination in amphipol or nanodiscs without any symmetry enforced (C1 symmetry) would help to capture any asymmetry in GJCs, although this would require very large particle datasets. Another possibility for shedding more light at

the pH-gating mechanism would be to use the cryoEM maps and the crosslinking results as restraints for MD simulations to further discern the conformational changes associated with this type of gating. The existing crosslinking results could be supplemented by results obtained using a lysine crosslinker with a shorter linker arm length than BS3, for example DST. Results obtained using such a crosslinker could in principle help to reduce the number of restraints for analyses with MD, as a shorter linker arm would further limit the number of lysines close to each other to undergo the crosslinking reaction. It might be helpful to devote experimental time to finding crosslinking conditions that would not result in the formation of SDS-resistant hexamer but rather which would favor formation of only intramolecular crosslinks within a single subunit. If successful, results obtained from such samples would only include intramolecular crosslinks, and comparison of such results with results that contain both inter- and intramolecular crosslinks would greatly aid in both designing MD simulations as well as interpreting other structural data.

Structural studies of connexin hemichannels would be of extreme value to the connexin field, since as of the time of writing this no such studies have been published. Hemichannels are thought to be in a default closed state in the cell membrane, kept in it largely due to extracellular Ca^{2+} concentration. A structure of hemichannel in a Ca^{2+} -free environment and in the presence of Ca^{2+} could shed light on the mechanism of Ca^{2+} regulation of hemichannels and be contrasted with the existing data on analogous regulation of GJCs. Also, successful cryoEM studies of this relatively small connexin hexamer would demonstrate methodology that could be used on different connexin

types leading to an avalanche of much needed structural data complimenting the abundance of functional studies.

Appendix 1. Structural Investigation of Connexin 26 Hemichannels

A1.1 Introduction

Gap junction channels (GJCs) mediate intercellular communication between adjacent cells and are formed by the end-to-end docking of two hexameric hemichannels comprised of connexin (Cx) subunits. The axial pore enables the exchange of hydrated ions, second messengers and metabolites up to ~ 15 Å in diameter. A variety of physiological processes and pathological states affect channel activity, including intracellular Ca^{2+} [208], pH [154], membrane potential [201], and trans-junctional voltage (V_J) [205].

Connexins expressed in cells are thought to assemble as hemichannels (HCs) that are transported to the plasma membrane. The hemichannels travel to sites of gap junction plaques and dock with hemichannels in the apposed membrane to form a complete dodecameric channel [407]. Numerous functional studies have shown that connexins can operate as both HCs and GJCs [237, 408, 409], and that they exhibit properties of both ligand and voltage-gated channels [172]. The physiological roles of hemichannels and gap junction channels can be distinguished by their characteristic regulation. GJCs serve as intercellular connections and are in a constitutively open state

so that tissues function as syncytia. HCs in the plasma membrane communicate with the extracellular space and by default are in a closed state.

A 2002 study using atomic force microscopy (AFM) revealed conformational changes on the extracellular surfaces of Cx26 HCs plaques upon addition of Ca^{2+} that were consistent with the steric model of gating [149]. The limited resolution of the surface topography did not identify which regions of the protein were undergoing conformational changes (e.g., transmembrane helices and/or extracellular loops). Although our analysis of intact GJCs suggested an electrostatic mechanism for Ca^{2+} -mediated regulation [231], it may still be the case that hemichannels are regulated by a steric mechanism. Consequently, it would be valuable to compare the structures of dodecameric GJCs and HCs.

The X-ray structures of Cx26 [231, 246] revealed that the docking interface between the hexamers is stabilized by hydrogen bonds between the extracellular loops. This observation served as a basis for the analysis of docking in Cx32-Cx32 homotypic and Cx26-Cx32 heterotypic channels [410]. The analysis showed that the Cx32 N175Y mutant, which was predicted to remove three hydrogen bonds from the docking interface, failed to form functional gap junction channels [333]. The insight from these studies allowed us to introduce the equivalent mutation into the second extracellular loop of Cx26 (N176Y).

The expressed and purified mutant assembles as hexamers that can be reconstituted into nanodiscs for improved stability. Subsequent EM and cryoEM analyses

revealed monodisperse and evenly distributed particles. The use of PEG-ylated UltrAuFoil holey gold grids [411] has rectified the problem of preferential particle orientation thus making our protein sample amenable to high-resolution cryoEM and image analysis. Detailed structural studies of a connexin in its hexameric form will be invaluable to gain deeper insight about the mechanisms of regulation of hemichannels and GJs and the conformational changes associated with docking.

A1.2 Methods

Protein expression and purification.

Protein expression and purification were performed as described in [231]. Samples for EM experiments were purified into buffer with 25 mM Tris pH 7.5, 500 mM NaCl, 2.5 % glycerol (v/v), 0.025% façade-EM (FA3). The final eluate from the SEC column was concentrated to ~ 2 – 4 mg/ml using a 0.5 ml or 4 ml concentrator (100 kDa MWCO; Millipore). If protein was not used for experiments shortly after the purification, it was aliquoted into 0.6 ml tubes, flash-frozen and stored at -80°C. In order to increase protein stability and contrast for cryoEM, detergent was exchanged to amphipathic surfactant Amphipol A8-35. Protein sample at 4 mg/ml was mixed with amphipol (10 mg/ml stock in 25 mM Tris pH 7.5, 500 mM NaCl, 0.025% façade-EM (FA3)) at a ratio of 1:3 (w/w), diluting protein to ~1.8 mg/ml. The sample was incubated for 4 h at 4°C with gentle mixing. Detergent was removed with Bio-Beads SM-2 (BioRad) by addition of beads to 30mg/ml to protein/detergent/amphipol mixture and ON incubation at 4°C with gentle mixing. Bio-

beads were then removed over a 0.5 ml disposable column and eluent spun down for 10 min at 16,000 x g at 4°C.

MSP2N2 expression and purification.

The plasmid for the membrane scaffold protein construct was obtained from Addgene, Cambridge, MA. *E. coli* strain BL21(DE3) competent cells were transformed with the MSP2N2 plasmid and protein expressed and purified as described in [412]. Since the protein was only found in the soluble fraction after cell lysis (no inclusion bodies have formed), only the part of the purification protocol describing purification of soluble protein was followed. At the end of the purification, TEV-cleaved (protease purified in-house) MSP2N2 protein was concentrated to ~ 2 mg/ml, aliquoted into 100 µl portions in 0.6 ml tubes, flash frozen in liquid N₂ and stored at -80°C.

Nanodisc reconstitution.

An aliquot of stock MSP2N2 scaffold protein at ~ 2 mg/ml was thawed on ice. Freshly-prepared N176Y protein at ~ 2 mg/ml was used or alternatively a flash-frozen aliquot was thawed on ice prior to reconstitution. Lipid stock at 7.5 mg/ml (~10 mM) was prepared (Soybean polar lipids, Avanti, Miami, FL). An aliquot of lipid at 25 mg/ml in CHCl₃ was transferred into a brown glass vial, dried under an inert gas and solubilized in buffer (25 mM Tris pH 7.5, 150 mM NaCl, 2% n-Octyl-β-D-Glucopyranoside (OG) (w/v)) by vigorous mixing. Next, N176Y protein, MSP2N2 and lipid were combined in a 1.5ml tube at a 1:1.5:112 molar ratio. If needed, connexin SEC purification buffer (25 mM Tris pH 7.5,

500 mM NaCl, 2.5 % glycerol (v/v), 0.025% FA3) was used to adjust the volume of the mixture. The mixture was incubated on ice for 1h, after which Bio-beads SM2 (Sigma-Aldrich, St. Louis, MO) were added to the tube to 10 mg/ml. After another 1h incubation at 4°C on a rotating or nutating mixer, another batch of Bio-beads was added to bring their concentration up to 30 mg/ml. The sample was then gently mixed ON at 4°C. Bio-beads were removed by decanting the mixture over a 0.5 ml disposable column and eluent was spun down for 10 min at 10, 000 x g at 4°C. Purification of nanodiscs was carried out on a Superdex 200 10/300 SEC column (GE Healthcare Bio-Science, Pittsburgh, PA) in a buffer composed of 25 mM Tris pH 7.5 and 150 mM NaCl. Fractions corresponding to the SEC peak identified as carrying N176Y reconstituted in nanodiscs were pooled and concentrated to ~ 0.4 – 0.5 mg/ml using a 0.5 ml or 4 ml concentrator (100 kDa MWCO; Millipore).

Preparation of pegylated UltrAuFoil grids.

A linear, thiol-bearing PEG compound SPT-0011P6 (SensoPath Technologies, Pray, MT) was solubilized in EtOH to 50 mM, flushed with an inert gas to protect thiol -SH groups from oxidizing, and stored at -20°C. The whole procedure of applying the reagent onto grids was carried out in a chamber filled with an inert gas. A 100 ul aliquot of the reagent at 5 mM concentration (dilution in EtOH) was prepared in a 0.6 ml tube per each UltrAuFoil gold grid (EMS, Hatfield, PA) that was to be coated. Gold grids were first glow-discharged for 60 sec at 20 mAmp and then transferred into 0.6 ml tubes with the reagent,

one grid per tube, making sure that the entire area of the grid was submerged in the reagent. Tubes were capped, lids secured with parafilm, and stored protected from light for 24 – 48 hours at RT. After the reaction has finished, the grids were carefully removed from the tubes with tweezers. Each grid was washed with 3 drops of EtOH and liquid was blotted away with filter paper. Dry grids were placed in a storage box and used within a few days since the preparation.

Negative stain EM analysis.

For EM of negatively stained samples, a protein sample was applied on a glow-discharged, carbon-coated copper grid which was next stained with 2 % uranyl acetate. EM was performed using a Tecnai G2 F20 electron microscope (FEI, Hillsboro, OR) equipped with a field-emission electron source, operating at 120 keV. Low electron dose images ($\sim 15 \text{ e}^-/\text{\AA}^2$) were recorded on a 4K x 4K pixel CCD camera (Gatan, Pleasanton, CA) at 62,000 x magnification (corresponding to $1.8 \text{ \AA} / \text{pixel}$) with a 1 sec exposure time at an underfocus value of $\sim 1.5 \text{ \mu m}$. Image processing was performed using EMAN v2.05 software [358].

CryoEM sample preparation.

For protein samples in amphipol, purified Cx26 N176Y ($\sim 2 \text{ mg/mL}$ in 25 mM Tris pH 7.5, 500 mM NaCl, amphipol (A8-35)) was diluted to 0.4 mg/mL with a final buffer concentration of 25 mM Tris pH 7.5, 200 mM NaCl. 3.5 \mu L of sample was then immediately applied to a glow-discharged (with amylamine) C-flat holey carbon grid ($1.2 \text{ \mu M}/1.3 \text{ \mu M}$

or 2 μM /2 μM hole size/hole space), blotted with Whatman no. 1 filter paper using a Vitrobot (FEI company) using 4 s blotting time, blot force of 3, and 100 % humidity at 22°C, and then plunge-frozen in liquid ethane cooled by liquid nitrogen. For protein samples in nanodiscs, 3.5 μl of reconstituted Cx26 N176Y (\sim 0.4 – 0.5 mg/mL in 25 mM Tris pH 7.5, 150 mM NaCl) was applied to a glow-discharged (with amylamine) C-flat holey carbon grid (1.2 μM /1.3 μM or 2 μM /2 μM hole size/hole space) or a pegylated UltrAuFoil holey gold grid (1.2 μM /1.3 μM hole size/hole space) and then blotted and plunge-frozen using a Vitrobot as described above. The grids were purchased from Electron Microscopy Sciences, Hatfield, PA.

CryoEM data acquisition and analysis.

Data sets were collected at either UVa Molecular Electron Microscopy Core (MEMC) on an FEI Titan Krios cryo-electron microscope, operated at 300 kV, with FEI Falcon 2 or Falcon 3ec detector or at Baylor College of Medicine National Center for Macromolecular Imaging (NCMI) on a JEOL3200FSC cryo-electron microscope, operated at 300 kV, with Gatan K2 Summit detector. Images were collected using the automated procedure in EPU (FEI) at UVa MEMC or using SerialEM at Baylor College of Medicine NCMI. Image processing was performed using Relion 2.0 software [383].

A1.3 Results and discussion

Electron microscopy of Cx26 hemichannels in amphipol.

Connexin 26 N176Y docking-impaired mutant was expressed in and purified from Sf9 insect cells. A two-step purification protocol consisting of IMAC and SEC yielded a preparation of highly pure protein in FA3 detergent (Figure A1B). The SEC purification profile suggests that the N176Y mutant in detergent has an apparent molecular weight (Mw) of ~230 kDa, or half that of the wild-type (WT) protein (Figure A1A). Indeed, N176Y mutant seems to migrate as a smaller oligomeric species than the WT as judged from the overlay of their respective SEC profiles (Figure A1C), indicating that it is a ~160 kDa hexamer (hemichannel) rather than a ~320 kDa dodecamer (GJC). An SEC analysis of purified and concentrated to ~2-3 mg/ml N176Y mutant shows minimal aggregation (Figure A1C). The same protein sample appears monodisperse and homogenous on a negative stained electron microscopy (EM) grid (Figure A1D).

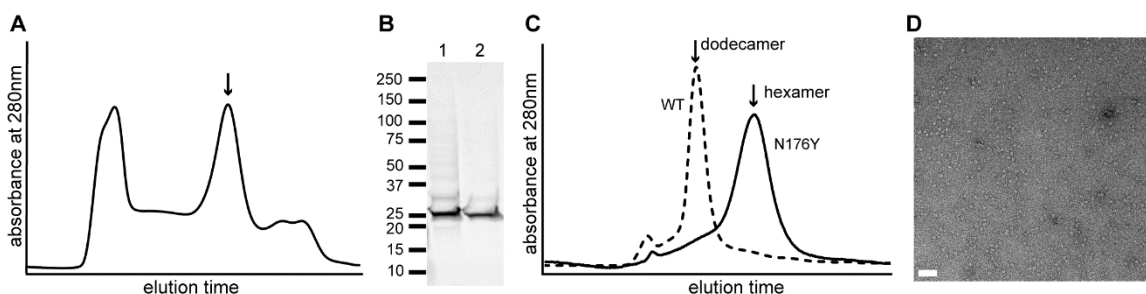


Figure A1. Purification of Cx26 N176Y. (A) SEC profile from the purification on Superdex 200 10/300 column. The arrow indicates the peak corresponding to the Cx26 hemichannel. (B) Coomassie-stained SDS PAGE gel showing (1) IMAC-purified protein (2) SEC-purified protein (fractions corresponding to the peak labeled in (A)). (C) SEC profiles comparing SEC-purified wild type, dodecameric Cx26 channels and N176Y hemichannels, which migrate at a position corresponding to a hexamer. (D) Electron micrograph of SEC-purified, negatively-stained Cx26 N176Y. Magnification = 62,000x. Scale bar denotes 50 nm.

The nonionic detergent FA3, used in the final stage of protein purification, was exchanged for the amphipathic surfactant amphipol A8-35, known to provide protein

particles with superior contrast on cryoEM grids. Then N176Y mutant was imaged on negative stained copper EM grids to verify sample stability. The particles had a uniform appearance and good distribution (Figure A2A). A small set of images was collected and the particles 2D classified, yielding class averages showing predominantly the *en face* views of the protein particles (Figure A2B). Although the classes displayed expected 6-fold symmetry, the sheer size of particles (~ 180 Å in diameter as opposed to ~ 100 Å) was seen as indicative of potential issues with sample preparation.

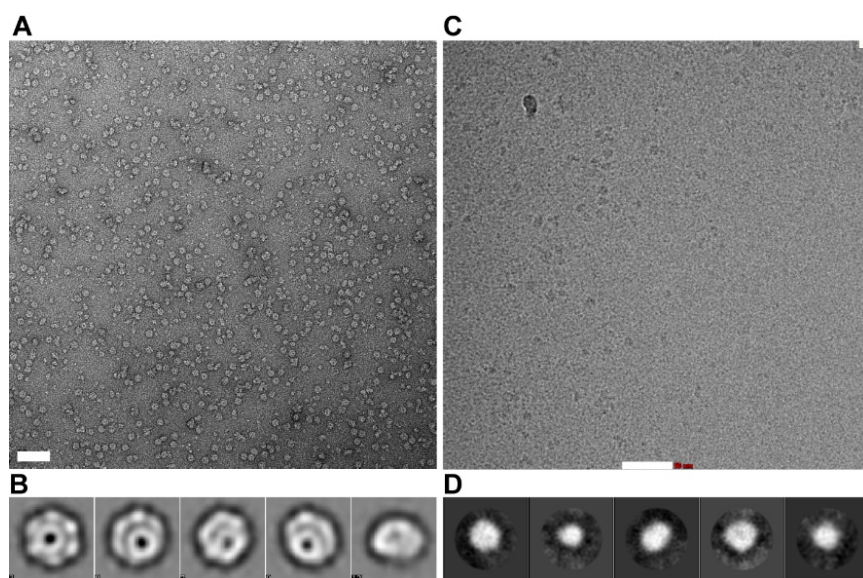


Figure A2. Electron microscopy of Cx26 N176Y hemichannel in amphipol. (A) Electron micrograph of negative stained Cx26 N176Y particles on a copper grid. (B) 2D class averages of *en face* and tilted views from particles shown in (A). (C) Electron cryomicrograph of Cx26 N176Y particles on C-flat holey carbon grids recorded on Titan Krios with a Falcon 2 detector. (D) 2D class averages obtained from particles shown in (C). Scale bar denotes 50 nm.

Nonetheless, samples in amphipol were then flash-frozen on C-flat holey carbon grids and imaged on Titan Krios microscope equipped with Flacon 2 detector. The samples displayed moderately good particle distribution with a preference for clustering in the

proximity of the carbon grid edge (Figure A2C). Minimal aggregation has allowed for data collection on frozen-hydrated specimen samples. Subsequent data processing and 2D particle classification has resulted in poor 2D classes with no visible secondary structure elements (Figure A2D), an indication that particles could not be aligned properly due to issues with either imaging conditions, grid preparation or sample stability.

It should be noted that the excellent apparent particle homogeneity and low levels of aggregation found in EM and cryoEM analyses were no longer present if N176Y sample was used to prepare grids more than ~ 24 hours after its purification. Protein samples that were 2 – 3 days old resulted in microscopy grids with noticeably lower particle homogeneity, namely contamination with smaller particles that did not have the characteristic ‘donut’-shaped views. Our conclusion is that N176Y was unstable in both detergent and amphipol, and that hemichannels fell apart overtime, resulting in both visible sample contamination and poor 2D class averages calculated from heterogeneous, conformationally dynamic particles.

Electron microscopy of Cx26 hemichannels in nanodiscs.

In order to improve the stability of the protein, we have decided to transfer it from detergent into a more native environment than that provided by amphipol - a lipid bilayer. To this end, we have expressed and purified MSP2N2 nanodisc scaffold protein from *E. coli* (Figure A3). This particular scaffold protein allows for a formation of lipid nanodiscs ~ 150 Å in diameter, with two ~ 43 kDa scaffold proteins participating in the formation of a

single nanodisc. The choice of nanodiscs as a medium for our structural studies was largely based on several publications showing high-resolution cryoEM structures obtained in lipid bilayers [413-415].

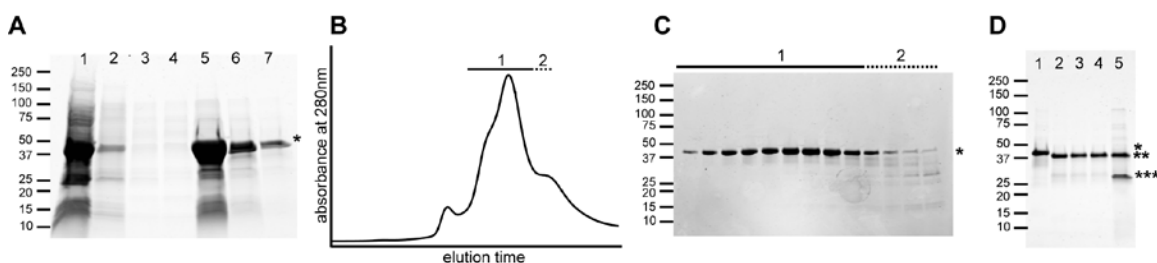


Figure A3. Purification of nanodisc scaffold protein MSP2N2. (A) IMAC purification on Ni^{2+} resin. Coomassie-stained SDS PAGE gel showing (1) flow-through, (2 – 4) washes 1 – 3, and (5 – 7) elutions 1 – 3. (B) SEC profile from the purification on Superdex 26/600 prep grade 75. The solid and dotted lines labeled (1) and (2), respectively, indicate fractions that were analyzed on an SDS PAGE gel shown in (C). (C) Coomassie-stained SDS PAGE gel. Fractions labeled with a solid line and number (1) correspond to the major peak on the chromatogram in (B) and those were pooled for further purification. (D) Coomassie-stained SDS PAGE gel showing TEV-cleavage of His-tagged MSP2N2 protein. Line (1) is a concentrated SEC-purified protein, (2) flow-through, (3) wash, (4) wash with imidazole, and (5) elution. Gel bands labeled with (*) indicate the position of His-tagged MSP2N2, (**) indicate MSP2N2, and (***) correspond to TEV protease.

Cx26 N176Y was successfully reconstituted into soybean polar lipids MSP2N2 nanodiscs, and SEC purification profile has revealed a presence of two populations of nanodiscs in our preparations – one with embedded protein and one without it (Figure A4 A and B). The fractions identified on the SDS PAGE gel as corresponding to reconstituted N176Y (Figure A4 B) were pooled and concentrated to ~ 0.4 mg/ml as assessed by absorbance reading at 280 nm. A negative stain micrograph of a purified, concentrated sample revealed minimal aggregation and largely homogenous population of nanodiscs with average diameter of 150 Å (Figure A4 C).

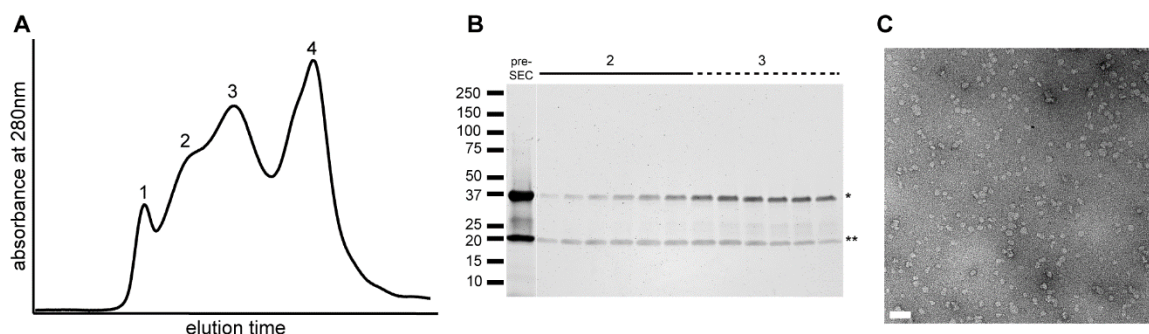


Figure A4. Reconstitution of Cx26 N176Y in nanodiscs. (A) SEC profile from the purification of MSP2N2 nanodiscs on Superdex 200 10/300 column. The labeled peaks are: (1) void, (2) nanodiscs with protein, (3) empty nanodiscs, and (4) scaffold protein. (B) Coomassie-stained SDS PAGE gel showing the contents of SEC peaks 1 and 2 showed on (A). The fractions corresponding to peak 2 were pooled and concentrated. Proteins on the gel are: (*) MSP2N2 43 kDa, and (**) Cx26 N176Y 26 kDa. (C) Electron micrograph of SEC-purified, negatively-stained Cx26 N176Y nanodiscs. Magnification = 62,000x. Scale bar denotes 50 nm.

Analysis of frozen hydrated N176Y nanodisc samples on C-flat holey carbon grids has showed uniform particle distribution and minimal aggregation (Figure A5 A). A small dataset was collected on a Titan Krios microscope with Falcon 2 detector, and calculated 2D class averages showed predicted, characteristic *en face* views of a connexin hemichannel (Figure A5 B). At this point, a lack of 2D classes unambiguously showing side views of the protein hinted at a possibility of having a preferred protein orientation on grids. The small size of the collected dataset, however, might have been partially responsible for 2D classification procedure to fail at recognizing those potentially less represented side view orientations.

Next, cryoEM grids with reconstituted N176Y were used for a larger data collection on a JEOL3200FSC microscope with K2 detector (Figure A5 C). 2D classification

of particles from this dataset has clearly proven that the protein had a preferred orientation on C-flat grids, which resulted in the majority of 2D classes representing the *en face* views of a connexin hemichannel (Figure A5 D). 2D classification has also revealed a presence of α -helical secondary structure in the best few classes which was interpreted as 1) improved hemichannel stability in nanodiscs as compared to amphipol and, 2) potential for a moderate- to high-resolution structure determination ($< 10 \text{ \AA}$ resolution).

In order to resolve the preferred particle orientation problem, we have resorted to testing multiple grid types and freezing conditions. We have tested C-flat carbon grids of different hole size, graphene-enhanced C-flat carbon grids coated in-house as well as UltrAuFoil gold grids. Additionally, we have experimented with blotting times and blot force on FEI Vitrobot and tested silica and gold nanoparticles as additives intended to increase ice thickness. Unfortunately, neither different blotting times, addition of nanoparticles nor use of varied grid types has helped alleviate the preferred orientation issue. Tests performed on graphene-enhanced grids and gold grids resulted in hardly any particles present in grid holes. We have resorted to using UltrAuFoil holey gold grids again, but this time we pegylated them in-house using a linear, thiol-bearing PEG group [411]. Images recorded on Titan Krios microscope with a Falcon 3ec camera yielded much more favorable orientational sampling which could be clearly seen on cryomicrographs (Figure A5 E). 2D class averages obtained from a sample imaged on a pegylated gold grid revealed the elusive side views which displayed traces of secondary structure elements,

in addition to more often seen *en face* views showing α -helical secondary structure (Figure A5 F).

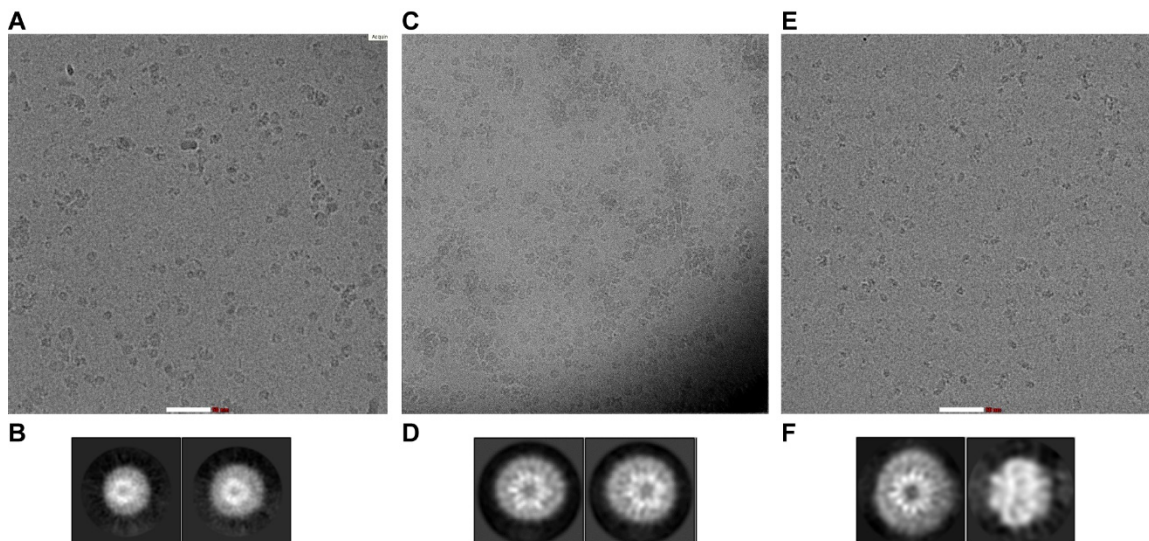


Figure A5. Electron microscopy of Cx26 N176Y hemichannel in nanodiscs. (A) Electron cryomicrograph of particles on C-flat holey carbon grids recorded on Titan Krios with a Falcon 2 detector. (B) 2D class averages obtained from particles shown in (A). (C) Electron cryomicrograph of particles on C-flat holey carbon grids recorded on JEOL3200FSC microscope with K2 detector. (D) 2D class averages obtained from particles shown in (C); α -helical secondary structure is evident in *en face* 2D class averages. (E) Electron cryomicrograph of particles on PEGylated UltrAuFoil holey gold grids recorded on Titan Krios with a Falcon 3EC detector. (F) 2D class averages obtained from particles shown in (E) show *en face* and side views displaying α -helical secondary structure. Scale bar denotes 50 nm. Image analysis performed by Ali Khan, University of Virginia.

We believe that this sample is an excellent candidate for a high-resolution reconstruction using a Titan Krios 300 kV microscope equipped with K2 direct electron detector and a Volta phase plate, which greatly improves particle contrast facilitating alignment of small protein particles [416-418].

References

1. Fukada, T. and T. Kambe, *Molecular and genetic features of zinc transporters in physiology and pathogenesis*. Metallomics, 2011. **3**(7): p. 662-74.
2. Maret, W. and Y. Li, *Coordination dynamics of zinc in proteins*. Chem Rev, 2009. **109**(10): p. 4682-707.
3. Vallee, B.L. and K.H. Falchuk, *The biochemical basis of zinc physiology*. Physiol Rev, 1993. **73**(1): p. 79-118.
4. Andreini, C., I. Bertini, and G. Cavallaro, *Minimal functional sites allow a classification of zinc sites in proteins*. PLoS One, 2011. **6**(10): p. e26325.
5. Barnett, J.P., et al., *Allosteric modulation of zinc speciation by fatty acids*. Biochim Biophys Acta, 2013. **1830**(12): p. 5456-64.
6. Reyes, J.G., *Zinc transport in mammalian cells*. Am J Physiol, 1996. **270**(2 Pt 1): p. C401-10.
7. Coyle, P., et al., *Metallothionein: the multipurpose protein*. Cell Mol Life Sci, 2002. **59**(4): p. 627-47.
8. Kambe, T., et al., *Overview of mammalian zinc transporters*. Cell Mol Life Sci, 2004. **61**(1): p. 49-68.
9. Liuzzi, J.P., et al., *Responsive transporter genes within the murine intestinal-pancreatic axis form a basis of zinc homeostasis*. Proc Natl Acad Sci U S A, 2004. **101**(40): p. 14355-60.
10. Krebs, N.F., *Overview of zinc absorption and excretion in the human gastrointestinal tract*. J Nutr, 2000. **130**(5S Suppl): p. 1374S-7S.
11. Bonaventura, P., et al., *Zinc and its role in immunity and inflammation*. Autoimmun Rev, 2015. **14**(4): p. 277-85.
12. Devirgiliis, C., et al., *Zinc fluxes and zinc transporter genes in chronic diseases*. Mutat Res, 2007. **622**(1-2): p. 84-93.
13. Hambidge, M., *Human zinc deficiency*. J Nutr, 2000. **130**(5S Suppl): p. 1344S-9S.
14. Prasad, A.S., *Discovery of human zinc deficiency and studies in an experimental human model*. Am J Clin Nutr, 1991. **53**(2): p. 403-12.
15. Uciechowski, P., et al., *TH1 and TH2 cell polarization increases with aging and is modulated by zinc supplementation*. Exp Gerontol, 2008. **43**(5): p. 493-8.
16. Prasad, A.S., *Clinical manifestations of zinc deficiency*. Annu Rev Nutr, 1985. **5**: p. 341-63.
17. Mocchegiani, E., R. Giacconi, and M. Malavolta, *Zinc signalling and subcellular distribution: emerging targets in type 2 diabetes*. Trends in Molecular Medicine, 2008. **14**(10): p. 419-28.
18. Myers, S.A., A. Nield, and M. Myers, *Zinc transporters, mechanisms of action and therapeutic utility: implications for type 2 diabetes mellitus*. J Nutr Metab, 2012. **2012**: p. 173712.
19. Penny, M.E., *Zinc supplementation in public health*. Ann Nutr Metab, 2013. **62** Suppl 1: p. 31-42.

20. Age-Related Eye Disease Study Research, G., *A randomized, placebo-controlled, clinical trial of high-dose supplementation with vitamins C and E, beta carotene, and zinc for age-related macular degeneration and vision loss: AREDS report no. 8*. Arch Ophthalmol, 2001. **119**(10): p. 1417-36.
21. Lichten, L.A. and R.J. Cousins, *Mammalian zinc transporters: nutritional and physiologic regulation*. Annual Review of Nutrition, 2009. **29**: p. 153-76.
22. Kambe, T., B.P. Weaver, and G.K. Andrews, *The genetics of essential metal homeostasis during development*. Genesis, 2008. **46**(4): p. 214-28.
23. Bin, B.H., et al., *Biochemical characterization of human ZIP13 protein: a homo-dimerized zinc transporter involved in the spondylocheiro dysplastic Ehlers-Danlos syndrome*. J Biol Chem, 2011. **286**(46): p. 40255-65.
24. Taylor, K.M., et al., *The emerging role of the LIV-1 subfamily of zinc transporters in breast cancer*. Mol Med, 2007. **13**(7-8): p. 396-406.
25. Haney, C.J., et al., *New developments in the understanding of the cation diffusion facilitator family*. J Ind Microbiol Biotechnol, 2005. **32**(6): p. 215-26.
26. Montanini, B., et al., *Phylogenetic and functional analysis of the Cation Diffusion Facilitator (CDF) family: improved signature and prediction of substrate specificity*. BMC Genomics, 2007. **8**: p. 107.
27. Ryu, M.S., et al., *Zinc transporters ZnT1 (Slc30a1), Zip8 (Slc39a8), and Zip10 (Slc39a10) in mouse red blood cells are differentially regulated during erythroid development and by dietary zinc deficiency*. J Nutr, 2008. **138**(11): p. 2076-83.
28. Kirschke, C.P. and L. Huang, *Expression of the ZNT (SLC30) family members in the epithelium of the mouse prostate during sexual maturation*. J Mol Histol, 2008. **39**(4): p. 359-70.
29. Iguchi, K., et al., *Castration- and aging-induced changes in the expression of zinc transporter and metallothionein in rat prostate*. J Androl, 2011. **32**(2): p. 144-50.
30. Henshall, S.M., et al., *Expression of the zinc transporter ZnT4 is decreased in the progression from early prostate disease to invasive prostate cancer*. Oncogene, 2003. **22**(38): p. 6005-12.
31. Smith, J.L., et al., *Altered expression of zinc transporters-4 and -6 in mild cognitive impairment, early and late Alzheimer's disease brain*. Neuroscience, 2006. **140**(3): p. 879-88.
32. Lang, C., et al., *Anti-inflammatory effects of zinc and alterations in zinc transporter mRNA in mouse models of allergic inflammation*. Am J Physiol Lung Cell Mol Physiol, 2007. **292**(2): p. L577-84.
33. Kitamura, H., et al., *Toll-like receptor-mediated regulation of zinc homeostasis influences dendritic cell function*. Nat Immunol, 2006. **7**(9): p. 971-7.
34. Dubben, S., et al., *Cellular zinc homeostasis is a regulator in monocyte differentiation of HL-60 cells by 1 alpha,25-dihydroxyvitamin D3*. J Leukoc Biol, 2010. **87**(5): p. 833-44.
35. Smidt, K., et al., *SLC30A3 responds to glucose- and zinc variations in beta-cells and is critical for insulin production and in vivo glucose-metabolism during beta-cell stress*. PLoS One, 2009. **4**(5): p. e5684.
36. Patrushev, N., B. Seidel-Rogol, and G. Salazar, *Angiotensin II requires zinc and downregulation of the zinc transporters ZnT3 and ZnT10 to induce senescence of vascular smooth muscle cells*. PLoS One, 2012. **7**(3): p. e33211.

37. Inoue, K., et al., *Osteopenia and male-specific sudden cardiac death in mice lacking a zinc transporter gene, Znt5*. Human Molecular Genetics, 2002. **11**(15): p. 1775-84.
38. Sekler, I., et al., *Mechanism and regulation of cellular zinc transport*. Molecular medicine, 2007. **13**(7-8): p. 337-343.
39. Fukunaka, A., et al., *Demonstration and characterization of the heterodimerization of ZnT5 and ZnT6 in the early secretory pathway*. J Biol Chem, 2009. **284**(45): p. 30798-806.
40. Suzuki, T., et al., *Two different zinc transport complexes of cation diffusion facilitator proteins localized in the secretory pathway operate to activate alkaline phosphatases in vertebrate cells*. The Journal of Biological Chemistry, 2005. **280**(35): p. 30956-30962.
41. Kambe, T., *Molecular architecture and function of ZnT transporters*. Curr Top Membr, 2012. **69**: p. 199-220.
42. Lu, M., J. Chai, and D. Fu, *Structural basis for autoregulation of the zinc transporter YiiP*. Nature Structural & Molecular Biology, 2009. **16**(10): p. 1063-7.
43. Lu, M. and D. Fu, *Structure of the zinc transporter YiiP*. Science, 2007. **317**(5845): p. 1746-8.
44. Ohana, E., et al., *Identification of the Zn²⁺ binding site and mode of operation of a mammalian Zn²⁺ transporter*. J Biol Chem, 2009. **284**(26): p. 17677-86.
45. Coudray, N., et al., *Inward-facing conformation of the zinc transporter YiiP revealed by cryoelectron microscopy*. PNAS, 2012. **110**(6): p. 2140-2145.
46. Palmiter, R.D. and S.D. Findley, *Cloning and functional characterization of a mammalian zinc transporter that confers resistance to zinc*. EMBO J, 1995. **14**(4): p. 639-49.
47. Cherezov, V., et al., *Insights into the mode of action of a putative zinc transporter CzrB in Thermus thermophilus*. Structure, 2008. **16**(9): p. 1378-88.
48. Higuchi, T., et al., *Crystal structure of the cytosolic domain of the cation diffusion facilitator family protein*. Proteins, 2009. **76**(3): p. 768-71.
49. Jirakulaporn, T. and A.J. Muslin, *Cation diffusion facilitator proteins modulate Raf-1 activity*. J Biol Chem, 2004. **279**(26): p. 27807-15.
50. Tanaka, N., et al., *Zinc-binding and structural properties of the histidine-rich loop of Arabidopsis thaliana vacuolar membrane zinc transporter MTP1*. FEBS Open Bio, 2013. **3**: p. 218-24.
51. Podar, D., et al., *Metal selectivity determinants in a family of transition metal transporters*. J Biol Chem, 2012. **287**(5): p. 3185-96.
52. MacDiarmid, C.W., M.A. Milanick, and D.J. Eide, *Biochemical properties of vacuolar zinc transport systems of Saccharomyces cerevisiae*. J Biol Chem, 2002. **277**(42): p. 39187-94.
53. Kawachi, M., et al., *Deletion of a histidine-rich loop of AtMTP1, a vacuolar Zn(2+)/H(+) antiporter of Arabidopsis thaliana, stimulates the transport activity*. The Journal of Biological Chemistry, 2008. **283**(13): p. 8374-83.
54. Guffanti, A.A., et al., *An antiport mechanism for a member of the cation diffusion facilitator family: divalent cations efflux in exchange for K⁺ and H⁺*. Molecular Microbiology, 2002. **45**(1): p. 145-153.
55. Lopez-Redondo, M.L., et al., *Structural basis for the alternating access mechanism of the cation diffusion facilitator YiiP*. PNAS, 2018. **115**(12): p. 3042-3047.
56. Chao, Y. and D. Fu, *Kinetic study of the antiport mechanism of an Escherichia coli zinc transporter, ZitB*. J Biol Chem, 2004. **279**(13): p. 12043-50.
57. Gati, C., et al., *The structural basis of proton driven zinc transport by ZntB*. Nat Commun, 2017. **8**(1): p. 1313.

58. Wei, Y. and D. Fu, *Binding and transport of metal ions at the dimer interface of the Escherichia coli metal transporter YiiP*. The Journal of Biological Chemistry, 2006. **281**(33): p. 23492-23502.
59. Chao, Y. and D. Fu, *Thermodynamic studies of the mechanism of metal binding to the Escherichia coli zinc transporter YiiP*. J Biol Chem, 2004. **279**(17): p. 17173-80.
60. Gupta, S., et al., *Visualizing the kinetic power stroke that drives proton-coupled zinc(II) transport*. Nature, 2014. **512**(7512): p. 101-4.
61. Kambe, T., et al., *Sequence similarity and functional relationship among eukaryotic ZIP and CDF transporters*. Genomics Proteomics Bioinformatics, 2006. **4**(1): p. 1-9.
62. Kambe, T., *An overview of a wide range of functions of ZnT and Zip zinc transporters in the secretory pathway*. Biosci Biotechnol Biochem, 2011. **75**(6): p. 1036-43.
63. Chimienti, F., et al., *In vivo expression and functional characterization of the zinc transporter ZnT8 in glucose-induced insulin secretion*. Journal of Cell Science, 2006. **119**(Pt 20): p. 4199-206.
64. Nicolson, T.J., et al., *Insulin storage and glucose homeostasis in mice null for the granule zinc transporter ZnT8 and studies of the type 2 diabetes-associated variants*. Diabetes, 2009. **58**(9): p. 2070-83.
65. Murgia, C., et al., *Diabetes-linked zinc transporter ZnT8 is a homodimeric protein expressed by distinct rodent endocrine cell types in the pancreas and other glands*. Nutrition, metabolism and cardiovascular diseases, 2009. **19**(6): p. 431-9.
66. Hoch, E., et al., *Histidine pairing at the metal transport site of mammalian ZnT transporters controls Zn²⁺ over Cd²⁺ selectivity*. PNAS, 2012. **109**(19): p. 7202-7.
67. Weijers, R.N., *Three-dimensional structure of beta-cell-specific zinc transporter, ZnT-8, predicted from the type 2 diabetes-associated gene variant SLC30A8 R325W*. Diabetology & Metabolic Syndrome, 2010. **2**(33): p. 1 - 8.
68. Kim, I., et al., *A low-risk ZnT-8 allele (W325) for post-transplantation diabetes mellitus is protective against cyclosporin A-induced impairment of insulin secretion*. Pharmacogenomics J, 2011. **11**(3): p. 191-8.
69. Fu, Y., et al., *Down-regulation of ZnT8 expression in INS-1 rat pancreatic beta cells reduces insulin content and glucose-inducible insulin secretion*. PLoS One, 2009. **4**(5): p. e5679.
70. Merriman, C., et al., *Lipid-tuned Zinc Transport Activity of Human ZnT8 Protein Correlates with Risk for Type-2 Diabetes*. J Biol Chem, 2016. **291**(53): p. 26950-26957.
71. Flannick, J., et al., *Loss-of-function mutations in SLC30A8 protect against type 2 diabetes*. Nature Genetics, 2014. **46**: p. 357-363.
72. Nica, A.C., et al., *Cell-type, allelic, and genetic signatures in the human pancreatic beta cell transcriptome*. Genome Res, 2013. **23**(9): p. 1554-62.
73. Mohanasundaram, D., et al., *Ultrastructural analysis, zinc transporters, glucose transporters and hormones expression in New world primate (Callithrix jacchus) and human pancreatic islets*. Gen Comp Endocrinol, 2011. **174**(2): p. 71-9.
74. Eizirik, D.L., et al., *The human pancreatic islet transcriptome: expression of candidate genes for type 1 diabetes and the impact of pro-inflammatory cytokines*. PLoS Genet, 2012. **8**(3): p. e1002552.
75. Pound, L.D., et al., *Characterization of the human SLC30A8 promoter and intronic enhancer*. J Mol Endocrinol, 2011. **47**(3): p. 251-9.
76. Tamaki, M., et al., *Downregulation of ZnT8 expression in pancreatic beta-cells of diabetic mice*. Islets, 2009. **1**(2): p. 124-8.

77. Pound, L.D., et al., *The pancreatic islet beta-cell-enriched transcription factor Pdx-1 regulates Slc30a8 gene transcription through an intronic enhancer*. *Biochem J*, 2011. **433**(1): p. 95-105.
78. Leung, K.W., et al., *Expression of ZnT and ZIP zinc transporters in the human RPE and their regulation by neurotrophic factors*. *Invest Ophthalmol Vis Sci*, 2008. **49**(3): p. 1221-31.
79. Deniro, M. and F.A. Al-Mohanna, *Zinc transporter 8 (ZnT8) expression is reduced by ischemic insults: a potential therapeutic target to prevent ischemic retinopathy*. *PLoS One*, 2012. **7**(11): p. e50360.
80. Smidt, K., et al., *Zinc-transporter genes in human visceral and subcutaneous adipocytes: lean versus obese*. *Mol Cell Endocrinol*, 2007. **264**(1-2): p. 68-73.
81. Overbeck, S., et al., *Intracellular zinc homeostasis in leukocyte subsets is regulated by different expression of zinc exporters ZnT-1 to ZnT-9*. *J Leukoc Biol*, 2008. **83**(2): p. 368-80.
82. Davidson, H.W., J.M. Wenzlau, and R.M. O'Brien, *Zinc transporter 8 (ZnT8) and beta cell function*. *Trends Endocrinol Metab*, 2014. **25**(8): p. 415-24.
83. Egefjord, L., et al., *Zinc transporter gene expression is regulated by pro-inflammatory cytokines: a potential role for zinc transporters in beta-cell apoptosis?* *BMC Endocr Disord*, 2009. **9**: p. 7.
84. Hales, C.N., *The role of insulin in the regulation of glucose metabolism*. *Proc Nutr Soc*, 1971. **30**(3): p. 282-8.
85. Halban, P.A., *Proinsulin processing in the regulated and the constitutive secretory pathway*. *Diabetologia*, 1994. **37 Suppl 2**: p. S65-72.
86. Zalewski, P.D., et al., *Video image analysis of labile zinc in viable pancreatic islet cells using a specific fluorescent probe for zinc*. *J Histochem Cytochem*, 1994. **42**(7): p. 877-84.
87. Dunn, M.F., *Zinc-ligand interactions modulate assembly and stability of the insulin hexamer -- a review*. *Biometals*, 2005. **18**(4): p. 295-303.
88. Dodson, G. and D. Steiner, *The role of assembly in insulin's biosynthesis*. *Curr Opin Struct Biol*, 1998. **8**(2): p. 189-94.
89. Hutton, J.C., E.J. Penn, and M. Peshavaria, *Low-molecular-weight constituents of isolated insulin-secretory granules. Bivalent cations, adenine nucleotides and inorganic phosphate*. *Biochem J*, 1983. **210**(2): p. 297-305.
90. Chimienti, F., et al., *Identification and cloning of a beta-cell-specific zinc transporter, ZnT-8, localized into insulin secretory granules*. *Diabetes*, 2004. **53**(9): p. 2330-7.
91. Gyulkhandanyan, A.V., et al., *Investigation of transport mechanisms and regulation of intracellular Zn²⁺ in pancreatic alpha-cells*. *The Journal of Biological Chemistry*, 2008. **283**(15): p. 10184-97.
92. Chimienti, F., A. Favier, and M. Seve, *ZnT-8, a pancreatic beta-cell-specific zinc transporter*. *BioMetals*, 2005. **18**(4): p. 313-7.
93. Wenzlau, J.M., J.C. Hutton, and H.W. Davidson, *New antigenic targets in type 1 diabetes*. *Current Opinion in Endocrinology, Diabetes and Obesity*, 2008. **15**(4): p. 315-320.
94. Pound, L.D., et al., *Deletion of the mouse Slc30a8 gene encoding zinc transporter-8 results in impaired insulin secretion*. *Biochem J*, 2009. **421**(3): p. 371-6.
95. Bellomo, E.A., G. Meur, and G.A. Rutter, *Glucose regulates free cytosolic Zn(2)(+) concentration, Slc39 (Zip), and metallothionein gene expression in primary pancreatic islet beta-cells*. *J Biol Chem*, 2011. **286**(29): p. 25778-89.
96. Figlewicz, D.P., et al., *65Zinc and endogenous zinc content and distribution in islets in relationship to insulin content*. *Endocrinology*, 1984. **115**(3): p. 877-81.

97. Slepchenko, K.G. and Y.V. Li, *Rising intracellular zinc by membrane depolarization and glucose in insulin-secreting clonal HIT-T15 beta cells*. *Exp Diabetes Res*, 2012. **2012**: p. 190309.
98. Zhou, H., et al., *Zinc, not insulin, regulates the rat alpha-cell response to hypoglycemia in vivo*. *Diabetes*, 2007. **56**(4): p. 1107-12.
99. Franklin, I., et al., *Beta-cell secretory products activate alpha-cell ATP-dependent potassium channels to inhibit glucagon release*. *Diabetes*, 2005. **54**(6): p. 1808-15.
100. Richards-Williams, C., et al., *Extracellular ATP and zinc are co-secreted with insulin and activate multiple P2X purinergic receptor channels expressed by islet beta-cells to potentiate insulin secretion*. *Purinergic Signal*, 2008. **4**(4): p. 393-405.
101. Huang, Q., et al., *Coupling of Insulin Secretion and Display of a Granule-resident Zinc Transporter ZnT8 on the Surface of Pancreatic Beta Cells*. *J Biol Chem*, 2017. **292**(10): p. 4034-4043.
102. Lemaire, K., et al., *Insulin crystallization depends on zinc transporter ZnT8 expression, but is not required for normal glucose homeostasis in mice*. *PNAS*, 2009. **106**(35): p. 14872-7.
103. Pound, L.D., et al., *The physiological effects of deleting the mouse SLC30A8 gene encoding zinc transporter-8 are influenced by gender and genetic background*. *PLoS One*, 2012. **7**(7): p. e40972.
104. Tamaki, M., et al., *The diabetes-susceptible gene SLC30A8/ZnT8 regulates hepatic insulin clearance*. *J Clin Invest*, 2013. **123**(10): p. 4513-24.
105. Wijesekara, N., et al., *Beta cell-specific Znt8 deletion in mice causes marked defects in insulin processing, crystallisation and secretion*. *Diabetologia*, 2010. **53**(8): p. 1656-1668.
106. Hutton, J., et al., *Proprotein processing and pancreatic islet function*. *Adv Exp Med Biol*, 2004. **552**: p. 39-65.
107. Davidson, H.W. and J.C. Hutton, *The insulin-secretory-granule carboxypeptidase H. Purification and demonstration of involvement in proinsulin processing*. *Biochem J*, 1987. **245**(2): p. 575-82.
108. Naggert, J.K., et al., *Hyperproinsulinaemia in obese fat/fat mice associated with a carboxypeptidase E mutation which reduces enzyme activity*. *Nat Genet*, 1995. **10**(2): p. 135-42.
109. Young, G.S. and J.B. Kirkland, *Rat models of caloric intake and activity: relationships to animal physiology and human health*. *Appl Physiol Nutr Metab*, 2007. **32**(2): p. 161-76.
110. Hardy, A.B., et al., *Effects of high-fat diet feeding on Znt8-null mice: differences between beta-cell and global knockout of Znt8*. *American Journal of Physiology - Endocrinology and Metabolism*, 2012. **302**(9): p. E1084–E1096.
111. Cauchi, S., et al., *The genetic susceptibility to type 2 diabetes may be modulated by obesity status: implications for association studies*. *BMC Med Genet*, 2008. **9**: p. 45.
112. Kovacs, A.D. and D.A. Pearce, *Location- and sex-specific differences in weight and motor coordination in two commonly used mouse strains*. *Sci Rep*, 2013. **3**: p. 2116.
113. Danaei, G., et al., *National, regional, and global trends in fasting plasma glucose and diabetes prevalence since 1980: systematic analysis of health examination surveys and epidemiological studies with 370 country-years and 2.7 million participants*. *Lancet*, 2011. **378**: p. 31-40.
114. Prevention, C.f.D.C.a., *National Diabetes Statistics Report, 2014*. Atlanta, GA, U.S. Department of Health and Human Services, Centers for Disease Control and Prevention, 2014.

115. Stamler, J., et al., *Diabetes, other risk factors, and 12-yr cardiovascular mortality for men screened in the Multiple Risk Factor Intervention Trial*. *Diabetes Care*, 1993. **16**(2): p. 434-44.
116. Zarich, S.W., *Antidiabetic agents and cardiovascular risk in type 2 diabetes*. *Nature Reviews Endocrinology*, 2009. **5**(9): p. 500-506.
117. Wild, S., et al., *Global prevalence of diabetes: estimates for the year 2000 and projections for 2030*. *Diabetes Care*, 2004. **27**(5): p. 1047-53.
118. Plutzky, J., *Macrovascular effects and safety issues of therapies for type 2 diabetes*. *The American Journal of Cardiology*, 2011. **108**(3 Suppl): p. 25B-32B.
119. Zeggini, E., et al., *Replication of genome-wide association signals in UK samples reveals risk loci for type 2 diabetes*. *Science*, 2007. **316**(5829): p. 1336-1341.
120. Scott, L.J., et al., *A genome-wide association study of type 2 diabetes in Finns detects multiple susceptibility variants*. *Science*, 2007. **316**(5829): p. 1341-1345.
121. Saxena, R., et al., *Genome-wide association analysis identifies loci for type 2 diabetes and triglyceride levels*. *Science*, 2007. **316**(5829): p. 1331-6.
122. Sladek, R., et al., *A genome-wide association study identifies novel risk loci for type 2 diabetes*. *Nature*, 2007. **445**(7130): p. 881-885.
123. Cauchi, S., et al., *Meta-analysis and functional effects of the SLC30A8 rs13266634 polymorphism on isolated human pancreatic islets*. *Molecular Genetics and Metabolism*, 2010. **100**(1): p. 77-82.
124. Lewis, J.P., et al., *Association analysis in african americans of European-derived type 2 diabetes single nucleotide polymorphisms from whole-genome association studies*. *Diabetes*, 2008. **57**(8): p. 2220-5.
125. Palmer, N.D., et al., *Quantitative trait analysis of type 2 diabetes susceptibility loci identified from whole genome association studies in the Insulin Resistance Atherosclerosis Family Study*. *Diabetes*, 2008. **57**(4): p. 1093-100.
126. Horikawa, Y., et al., *Replication of genome-wide association studies of type 2 diabetes susceptibility in Japan*. *J Clin Endocrinol Metab*, 2008. **93**(8): p. 3136-41.
127. Stancakova, A., et al., *Association of 18 confirmed susceptibility loci for type 2 diabetes with indices of insulin release, proinsulin conversion, and insulin sensitivity in 5,327 nondiabetic Finnish men*. *Diabetes*, 2009. **58**(9): p. 2129-36.
128. Kirchhoff, K., et al., *Polymorphisms in the TCF7L2, CDKAL1 and SLC30A8 genes are associated with impaired proinsulin conversion*. *Diabetologia*, 2008. **51**(4): p. 597-601.
129. Boesgaard, T.W., et al., *The common SLC30A8 Arg325Trp variant is associated with reduced first-phase insulin release in 846 non-diabetic offspring of type 2 diabetes patients--the EUGENE2 study*. *Diabetologia*, 2008. **51**(5): p. 816-20.
130. Wenzlau, J.M., et al., *The cation efflux transporter ZnT8 (Slc30A8) is a major autoantigen in human type 1 diabetes*. *PNAS*, 2007. **104**(43): p. 17040-17045.
131. Delli, A.J., et al., *Zinc transporter 8 autoantibodies and their association with SLC30A8 and HLA-DQ genes differ between immigrant and Swedish patients with newly diagnosed type 1 diabetes in the Better Diabetes Diagnosis study*. *Diabetes*, 2012. **61**(10): p. 2556-64.
132. Dang, M., et al., *Human type 1 diabetes is associated with T cell autoimmunity to zinc transporter 8*. *J Immunol*, 2011. **186**(10): p. 6056-63.
133. Lampasona, V., et al., *Zinc transporter 8 antibodies complement GAD and IA-2 antibodies in the identification and characterization of adult-onset autoimmune diabetes: Non Insulin Requiring Autoimmune Diabetes (NIRAD) 4*. *Diabetes Care*, 2010. **33**(1): p. 104-8.

134. Kawasaki, E., *ZnT8 and type 1 diabetes*. Endocrine Journal, 2012. **59**(7): p. 531-7.
135. Wenzlau, J.M., et al., *Mapping of conformational autoantibody epitopes in ZNT8*. Diabetes/metabolism Research and Reviews, 2011. **27**(8): p. 883-886.
136. Achenbach, P., et al., *Autoantibodies to zinc transporter 8 and SLC30A8 genotype stratify type 1 diabetes risk*. Diabetologia, 2009. **52**(9): p. 1881-8.
137. Kawasaki, E., et al., *Association between anti-ZnT8 autoantibody specificities and SLC30A8 Arg325Trp variant in Japanese patients with type 1 diabetes*. Diabetologia, 2008. **51**(12): p. 2299-302.
138. Wenzlau, J.M., et al., *A common nonsynonymous single nucleotide polymorphism in the SLC30A8 gene determines ZnT8 autoantibody specificity in type 1 diabetes*. Diabetes, 2008. **57**(10): p. 2693-7.
139. Hua, V.B., et al., *Sequence and phylogenetic analyses of 4 TMS junctional proteins of animals: connexins, innexins, claudins and occludins*. J Membr Biol, 2003. **194**(1): p. 59-76.
140. Abascal, F. and R. Zardoya, *Evolutionary analyses of gap junction protein families*. Biochim Biophys Acta, 2013. **1828**(1): p. 4-14.
141. Sosinsky, G.E. and B.J. Nicholson, *Structural organization of gap junction channels*. Biochim Biophys Acta, 2005. **1711**(2): p. 99-125.
142. Francis, D., et al., *Connexin diversity and gap junction regulation by pHi*. Dev Genet, 1999. **24**(1-2): p. 123-36.
143. Agullo-Pascual, E. and M. Delmar, *The noncanonical functions of Cx43 in the heart*. J Membr Biol, 2012. **245**(8): p. 477-82.
144. Herve, J.C., et al., *Gap junctional channels are parts of multiprotein complexes*. Biochim Biophys Acta, 2012. **1818**(8): p. 1844-65.
145. Oshima, A., et al., *Asymmetric configurations and N-terminal rearrangements in connexin26 gap junction channels*. J Mol Biol, 2011. **405**(3): p. 724-35.
146. Oshima, A., et al., *Three-dimensional structure of a human connexin26 gap junction channel reveals a plug in the vestibule*. Proc Natl Acad Sci U S A, 2007. **104**(24): p. 10034-9.
147. Unger, V.M., et al., *Three-dimensional structure of a recombinant gap junction membrane channel*. Science, 1999. **283**(5405): p. 1176-80.
148. Fleishman, S.J., et al., *A C alpha model for the transmembrane alpha helices of gap junction intercellular channels*. Mol Cell, 2004. **15**(6): p. 879-88.
149. Muller, D.J., et al., *Conformational changes in surface structures of isolated connexin 26 gap junctions*. The EMBO Journal, 2002. **21**: p. 3598-3607.
150. Hoh, J.H., et al., *Structure of the extracellular surface of the gap junction by atomic force microscopy*. Biophys J, 1993. **65**(1): p. 149-63.
151. Liu, F., et al., *Nanomechanics of hemichannel conformations: connexin flexibility underlying channel opening and closing*. J Biol Chem, 2006. **281**(32): p. 23207-17.
152. Bao, X., et al., *Functional expression in Xenopus oocytes of gap-junctional hemichannels formed by a cysteine-less connexin 43*. J Biol Chem, 2004. **279**(11): p. 9689-92.
153. Foote, C.I., et al., *The Pattern of Disulfide Linkages in the Extracellular Loop Regions of Connexin 32 Suggests a Model for the Docking Interface of Gap Junctions*. The Journal of Cell Biology, 1998. **140**(5): p. 1187-1197.
154. Nielsen, M.S., et al., *Gap junctions*. Compr Physiol, 2012. **2**(3): p. 1981-2035.

155. Mese, G., G. Richard, and T.W. White, *Gap junctions: basic structure and function*. J Invest Dermatol, 2007. **127**(11): p. 2516-24.
156. Saez, J.C., et al., *Plasma membrane channels formed by connexins: their regulation and functions*. Physiol Rev, 2003. **83**(4): p. 1359-400.
157. Simon, A.M. and D.A. Goodenough, *Diverse functions of vertebrate gap junctions*. Trends Cell Biol, 1998. **8**(12): p. 477-83.
158. Fiori, M.C., et al., *Functional analysis and regulation of purified connexin hemichannels*. Front Physiol, 2014. **5**: p. 71.
159. Nakagawa, S., S. Maeda, and T. Tsukihara, *Structural and functional studies of gap junction channels*. Curr Opin Struct Biol, 2010. **20**(4): p. 423-30.
160. Yeager, M. and A.L. Harris, *Gap junction channel structure in the early 21st century: facts and fantasies*. Curr Opin Cell Biol, 2007. **19**(5): p. 521-8.
161. Unwin, P.N. and P.D. Ennis, *Two configurations of a channel-forming membrane protein*. Nature, 1984. **307**(5952): p. 609-13.
162. Goodenough, D.A. and D.L. Paul, *Beyond the gap: functions of unpaired connexon channels*. Nat Rev Mol Cell Biol, 2003. **4**(4): p. 285-94.
163. Kumar, N.M., D.S. Friend, and N.B. Gilula, *Synthesis and assembly of human beta 1 gap junctions in BHK cells by DNA transfection with the human beta 1 cDNA*. J Cell Sci, 1995. **108 (Pt 12)**: p. 3725-34.
164. Unger, V.M., et al., *Expression, two-dimensional crystallization, and electron cryo-crystallography of recombinant gap junction membrane channels*. J Struct Biol, 1999. **128**(1): p. 98-105.
165. Anselmi, F., et al., *ATP release through connexin hemichannels and gap junction transfer of second messengers propagate Ca²⁺ signals across the inner ear*. Proc Natl Acad Sci U S A, 2008. **105**(48): p. 18770-5.
166. Beltramello, M., et al., *Impaired permeability to Ins(1,4,5)P₃ in a mutant connexin underlies recessive hereditary deafness*. Nat Cell Biol, 2005. **7**(1): p. 63-9.
167. Gossman, D.G. and H.B. Zhao, *Hemichannel-mediated inositol 1,4,5-trisphosphate (IP₃) release in the cochlea: a novel mechanism of IP₃ intercellular signaling*. Cell Commun Adhes, 2008. **15**(4): p. 305-15.
168. Kanaporis, G., et al., *Gap junction channels exhibit connexin-specific permeability to cyclic nucleotides*. J Gen Physiol, 2008. **131**(4): p. 293-305.
169. Majumder, P., et al., *ATP-mediated cell-cell signaling in the organ of Corti: the role of connexin channels*. Purinergic Signal, 2010. **6**(2): p. 167-87.
170. Kumar, N.M. and N.B. Gilula, *The gap junction communication channel*. Cell, 1996. **84**(3): p. 381-8.
171. Evans, W.H. and P.E. Martin, *Gap junctions: structure and function (Review)*. Mol Membr Biol, 2002. **19**(2): p. 121-36.
172. Harris, A.L., *Emerging issues of connexin channels: biophysics fills the gap*. Quarterly Reviews of Biophysics, 2001. **34**(03).
173. Harris, A.L., *Connexin channel permeability to cytoplasmic molecules*. Prog Biophys Mol Biol, 2007. **94**(1-2): p. 120-43.
174. Kanaporis, G., P.R. Brink, and V. Valiunas, *Gap junction permeability: selectivity for anionic and cationic probes*. Am J Physiol Cell Physiol, 2011. **300**(3): p. C600-9.
175. Martinez, A.D., et al., *Gap-junction channels dysfunction in deafness and hearing loss*. Antioxid Redox Signal, 2009. **11**(2): p. 309-22.

176. Ayad, W.A., et al., *Heteromeric, but not homomeric, connexin channels are selectively permeable to inositol phosphates*. J Biol Chem, 2006. **281**(24): p. 16727-39.
177. Bevans, C.G., et al., *Isoform composition of connexin channels determines selectivity among second messengers and uncharged molecules*. J Biol Chem, 1998. **273**(5): p. 2808-16.
178. Weber, P.A., et al., *The permeability of gap junction channels to probes of different size is dependent on connexin composition and permeant-pore affinities*. Biophys J, 2004. **87**(2): p. 958-73.
179. Laird, D.W., C.C. Naus, and P.D. Lampe, *SnapShot: Connexins and Disease*. Cell, 2017. **170**(6).
180. Bennett, M.V. and R.S. Zukin, *Electrical coupling and neuronal synchronization in the Mammalian brain*. Neuron, 2004. **41**(4): p. 495-511.
181. Lo, C.W., *The role of gap junction membrane channels in development*. J Bioenerg Biomembr, 1996. **28**(4): p. 379-85.
182. Desplantez, T., et al., *Gap junction channels and cardiac impulse propagation*. J Membr Biol, 2007. **218**(1-3): p. 13-28.
183. Johnstone, S., B. Isakson, and D. Locke, *Biological and biophysical properties of vascular connexin channels*. Int Rev Cell Mol Biol, 2009. **278**: p. 69-118.
184. Li, H., et al., *Properties and regulation of gap junctional hemichannels in the plasma membranes of cultured cells*. J Cell Biol, 1996. **134**(4): p. 1019-30.
185. Contreras, J.E., et al., *Gating and regulation of connexin 43 (Cx43) hemichannels*. Proc Natl Acad Sci U S A, 2003. **100**(20): p. 11388-93.
186. Gonzalez, D., J.M. Gomez-Hernandez, and L.C. Barrio, *Molecular basis of voltage dependence of connexin channels: an integrative appraisal*. Prog Biophys Mol Biol, 2007. **94**(1-2): p. 66-106.
187. Fasciani, I., et al., *Regulation of connexin hemichannel activity by membrane potential and the extracellular calcium in health and disease*. Neuropharmacology, 2013. **75**: p. 479-90.
188. Orellana, J.A., et al., *Hemichannels in the neurovascular unit and white matter under normal and inflamed conditions*. CNS Neurol Disord Drug Targets, 2011. **10**(3): p. 404-14.
189. Wang, N., et al., *Paracrine signaling through plasma membrane hemichannels*. Biochim Biophys Acta, 2013. **1828**(1): p. 35-50.
190. Kang, J., et al., *Connexin 43 hemichannels are permeable to ATP*. J Neurosci, 2008. **28**(18): p. 4702-11.
191. Bruzzone, S., et al., *Connexin 43 hemi channels mediate Ca²⁺-regulated transmembrane NAD⁺ fluxes in intact cells*. FASEB J, 2001. **15**(1): p. 10-12.
192. Ye, Z.C., et al., *Functional hemichannels in astrocytes: a novel mechanism of glutamate release*. J Neurosci, 2003. **23**(9): p. 3588-96.
193. Rana, S. and R. Dringen, *Gap junction hemichannel-mediated release of glutathione from cultured rat astrocytes*. Neurosci Lett, 2007. **415**(1): p. 45-8.
194. Bergoffen, J., et al., *Connexin mutations in X-linked Charcot-Marie-Tooth disease*. Science, 1993. **262**(5142): p. 2039-42.
195. Richard, G., *Connexins: a connection with the skin*. Exp Dermatol, 2000. **9**(2): p. 77-96.
196. Rabionet, R., et al., *Molecular basis of childhood deafness resulting from mutations in the GJB2 (connexin 26) gene*. Hum Genet, 2000. **106**(1): p. 40-4.
197. Chang, E.H., G. Van Camp, and R.J. Smith, *The role of connexins in human disease*. Ear Hear, 2003. **24**(4): p. 314-23.

198. White, T.W., *Unique and redundant connexin contributions to lens development*. Science, 2002. **295**(5553): p. 319-20.
199. Paznekas, W.A., et al., *Connexin 43 (GJA1) mutations cause the pleiotropic phenotype of oculodentodigital dysplasia*. Am J Hum Genet, 2003. **72**(2): p. 408-18.
200. Kelsell, D.P., J. Dunlop, and M.B. Hodgins, *Human diseases: clues to cracking the connexin code?* Trends Cell Biol, 2001. **11**(1): p. 2-6.
201. Revilla, A., M.V. Bennett, and L.C. Barrio, *Molecular determinants of membrane potential dependence in vertebrate gap junction channels*. Proc Natl Acad Sci U S A, 2000. **97**(26): p. 14760-5.
202. Bukauskas, F.F. and V.K. Verselis, *Gap junction channel gating*. Biochim Biophys Acta, 2004. **1662**(1-2): p. 42-60.
203. Trexler, E.B., et al., *The first extracellular loop domain is a major determinant of charge selectivity in connexin46 channels*. Biophys J, 2000. **79**(6): p. 3036-51.
204. Bukauskas, F.F., et al., *Coupling asymmetry of heterotypic connexin 45/connexin 43-EGFP gap junctions: properties of fast and slow gating mechanisms*. Proc Natl Acad Sci U S A, 2002. **99**(10): p. 7113-8.
205. Harris, A.L., D.C. Spray, and M.V. Bennett, *Kinetic properties of a voltage-dependent junctional conductance*. J Gen Physiol, 1981. **77**(1): p. 95-117.
206. Bukauskas, F.F., et al., *Gating Properties of Gap Junction Channels Assembled from Connexin 43 and Connexin 43 Fused with Green Fluorescent Protein*. Biophys J, 2001. **81**: p. 137-152.
207. Locke, D. and A.L. Harris, *Connexin channels and phospholipids: association and modulation*. BMC Biol, 2009. **7**: p. 52.
208. Iwatsuki, N. and O.H. Petersen, *Acetylcholine-like effects of intracellular calcium application in pancreatic acinar cells*. Nature, 1977. **268**(5616): p. 147-9.
209. Palacios-Prado, N., et al., *Molecular determinants of magnesium-dependent synaptic plasticity at electrical synapses formed by connexin36*. Nat Commun, 2014. **5**: p. 4667.
210. Sun, Z., D.Q. Zhang, and D.G. McMahon, *Zinc modulation of hemi-gap-junction channel currents in retinal horizontal cells*. Journal of neurophysiology, 2009. **101**(4): p. 1774-1780.
211. Zou, J., et al., *Gap junction regulation by calmodulin*. FEBS Lett, 2014. **588**(8): p. 1430-8.
212. Verselis, V.K., C.S. Ginter, and T.A. Bargiello, *Opposite voltage gating polarities of two closely related connexins*. Nature, 1994. **368**(6469): p. 348-51.
213. Bruzzone, R., T.W. White, and D.L. Paul, *Connections with connexins: the molecular basis of direct intercellular signaling*. Eur J Biochem, 1996. **238**(1): p. 1-27.
214. Bargiello, T.A., et al., *Voltage-dependent conformational changes in connexin channels*. Biochim Biophys Acta, 2012. **1818**(8): p. 1807-22.
215. Spray, D.C. and J.M. Burt, *Structure-activity relations of the cardiac gap junction channel*. Am J Physiol, 1990. **258**(2 Pt 1): p. C195-205.
216. Lampe, P.D., et al., *Phosphorylation of connexin43 on serine368 by protein kinase C regulates gap junctional communication*. J Cell Biol, 2000. **149**(7): p. 1503-12.
217. Gomez-Hernandez, J.M., et al., *Molecular basis of calcium regulation in connexin-32 hemichannels*. Proc Natl Acad Sci U S A, 2003. **100**(26): p. 16030-5.
218. Chen, Y., et al., *Mechanism of the defect in gap-junctional communication by expression of a connexin 26 mutant associated with dominant deafness*. FASEB J, 2005. **19**(11): p. 1516-8.

219. Bao, X., G.A. Altenberg, and L. Reuss, *Mechanism of regulation of the gap junction protein connexin 43 by protein kinase C-mediated phosphorylation*. Am J Physiol Cell Physiol, 2004. **286**(3): p. C647-54.
220. Orellana, J.A., et al., *Glial hemichannels and their involvement in aging and neurodegenerative diseases*. Rev Neurosci, 2012. **23**(2): p. 163-77.
221. Schalper, K.A., et al., *Connexin 43 hemichannels mediate the Ca²⁺ influx induced by extracellular alkalinization*. Am J Physiol Cell Physiol, 2010. **299**(6): p. C1504-15.
222. Scheckenbach, K.E., et al., *Connexin channel-dependent signaling pathways in inflammation*. J Vasc Res, 2011. **48**(2): p. 91-103.
223. Unwin, P.N. and G. Zampighi, *Structure of the junction between communicating cells*. Nature, 1980. **283**(5747): p. 545-9.
224. Unwin, P.N. and P.D. Ennis, *Calcium-mediated changes in gap junction structure: evidence from the low angle X-ray pattern*. J Cell Biol, 1983. **97**(5 Pt 1): p. 1459-66.
225. Ek-Vitorin, J.F., et al., *pH Regulation of Connexin43: Molecular Analysis of the Gating Particle*. Biophysical Journal, 1996. **71**: p. 1273-1284.
226. Trexler, E.B., et al., *Voltage gating and permeation in a gap junction hemichannel*. PNAS, 1996. **93**: p. 5836-5841.
227. Verselis, V.K., et al., *Loop gating of connexin hemichannels involves movement of pore-lining residues in the first extracellular loop domain*. J Biol Chem, 2009. **284**(7): p. 4484-93.
228. Oh, S., et al., *Stoichiometry of transjunctional voltage-gating polarity reversal by a negative charge substitution in the amino terminus of a connexin32 chimera*. J Gen Physiol, 2000. **116**(1): p. 13-31.
229. Purnick, P.E., et al., *Reversal of the Gating Polarity of Gap Junctions by Negative Charge Substitutions in the N-Terminus of Connexin 32*. Biophys J, 2000. **79**.
230. Tang, Q., et al., *Conformational changes in a pore-forming region underlie voltage-dependent "loop gating" of an unopposed connexin hemichannel*. J Gen Physiol, 2009. **133**(6): p. 555-70.
231. Bennett, B.C., et al., *An electrostatic mechanism for Ca²⁺-mediated regulation of gap junction channels*. Nat Commun, 2016. **7**: p. 8770.
232. Spray, D.C., A.L. Harris, and M.V. Bennett, *Equilibrium properties of a voltage-dependent junctional conductance*. J Gen Physiol, 1981. **77**(1): p. 77-93.
233. Ri, Y., et al., *The role of a conserved proline residue in mediating conformational changes associated with voltage gating of Cx32 gap junctions*. Biophys J, 1999. **76**(6): p. 2887-98.
234. Purnick, P.E., et al., *Structure of the amino terminus of a gap junction protein*. Arch Biochem Biophys, 2000. **381**(2): p. 181-90.
235. Bukauskas, F.F., *Inducing de novo formation of gap junction channels*. Methods Mol Biol, 2001. **154**: p. 379-93.
236. Trexler, E.B., et al., *Rapid and Direct Effects of pH on Connexins Revealed by the Connexin46 Hemichannel Preparation*. Journal of General Physiology, 1999. **113**: p. 721-742.
237. Sanchez, H.A., et al., *Altered Inhibition of Cx26 Hemichannels by pH and Zn²⁺ in the A40V Mutation Associated with Keratitis-Ichthyosis-Deafness Syndrome*. The Journal of Biological Chemistry, 2014. **289**(31): p. 21519-21532.
238. Verselis, V.K. and M. Srinivas, *Divalent cations regulate connexin hemichannels by modulating intrinsic voltage-dependent gating*. J Gen Physiol, 2008. **132**(3): p. 315-27.

239. Ebihara, L., X. Liu, and J.D. Pal, *Effect of external magnesium and calcium on human connexin46 hemichannels*. *Biophys J*, 2003. **84**(1): p. 277-86.
240. Puljung, M.C., et al., *Polyvalent cations constitute the voltage gating particle in human connexin37 hemichannels*. *J Gen Physiol*, 2004. **124**(5): p. 587-603.
241. Srinivas, M., M.G. Hopperstad, and D.C. Spray, *Quinine blocks specific gap junction channel subtypes*. *Proc Natl Acad Sci U S A*, 2001. **98**(19): p. 10942-7.
242. Oshima, A., *Structure and closure of connexin gap junction channels*. *FEBS Lett*, 2014. **588**(8): p. 1230-7.
243. Kyle, J.W., et al., *The N terminus of connexin37 contains an alpha-helix that is required for channel function*. *J Biol Chem*, 2009. **284**(30): p. 20418-27.
244. Shao, Q., et al., *Structure and functional studies of N-terminal Cx43 mutants linked to oculodentodigital dysplasia*. *Mol Biol Cell*, 2012. **23**(17): p. 3312-21.
245. Kyle, J.W., et al., *An intact connexin N-terminus is required for function but not gap junction formation*. *J Cell Sci*, 2008. **121**(Pt 16): p. 2744-50.
246. Maeda, S., et al., *Structure of the connexin 26 gap junction channel at 3.5 Å resolution*. *Nature*, 2009. **458**(7238): p. 597-602.
247. Oh, S., et al., *Molecular determinants of electrical rectification of single channel conductance in gap junctions formed by connexins 26 and 32*. *J Gen Physiol*, 1999. **114**(3): p. 339-64.
248. Oh, S., et al., *Determinants of gating polarity of a connexin 32 hemichannel*. *Biophys J*, 2004. **87**(2): p. 912-28.
249. Delmar, M., et al., *Structural bases for the chemical regulation of Connexin43 channels*. *Cardiovasc Res*, 2004. **62**(2): p. 268-75.
250. Homma, N., et al., *A particle-receptor model for the insulin-induced closure of connexin43 channels*. *Circ Res*, 1998. **83**(1): p. 27-32.
251. Liu, S., et al., *A structural basis for the unequal sensitivity of the major cardiac and liver gap junctions to intracellular acidification: the carboxyl tail length*. *Biophys J*, 1993. **64**(5): p. 1422-33.
252. Anumonwo, J.M., et al., *The carboxyl terminal domain regulates the unitary conductance and voltage dependence of connexin40 gap junction channels*. *Circ Res*, 2001. **88**(7): p. 666-73.
253. Moreno, A.P., et al., *Role of the carboxyl terminal of connexin43 in transjunctional fast voltage gating*. *Circ Res*, 2002. **90**(4): p. 450-7.
254. Morley, G.E., et al., *Structure of Connexin43 and its Regulation by pH*. *Journal of Cardiovascular Electrophysiology*, 1997. **8**(8).
255. Bukauskas, F.F. and C. Peracchia, *Two distinct gating mechanisms in gap junction channels: CO₂-sensitive and voltage-sensitive*. *Biophys J*, 1997. **72**(5): p. 2137-42.
256. Duffy, H.S., et al., *pH-dependent intramolecular binding and structure involving Cx43 cytoplasmic domains*. *J Biol Chem*, 2002. **277**(39): p. 36706-14.
257. Hirst-Jensen, B.J., et al., *Characterization of the pH-dependent interaction between the gap junction protein connexin43 carboxyl terminus and cytoplasmic loop domains*. *J Biol Chem*, 2007. **282**(8): p. 5801-13.
258. Locke, D., et al., *Mechanism for modulation of gating of connexin26-containing channels by taurine*. *J Gen Physiol*, 2011. **138**(3): p. 321-39.
259. Suchyna, T.M., et al., *Different ionic selectivities for connexins 26 and 32 produce rectifying gap junction channels*. *Biophys J*, 1999. **77**(6): p. 2968-87.

260. Forge, A. and T. Wright, *The molecular architecture of the inner ear*. Br Med Bull, 2002. **63**: p. 5-24.
261. Forge, A., et al., *Gap junctions in the inner ear: comparison of distribution patterns in different vertebrates and assesment of connexin composition in mammals*. J Comp Neurol, 2003. **467**(2): p. 207-31.
262. Gerido, D.A. and T.W. White, *Connexin disorders of the ear, skin, and lens*. Biochim Biophys Acta, 2004. **1662**(1-2): p. 159-70.
263. Zhao, H.B., et al., *Gap junctions and cochlear homeostasis*. J Membr Biol, 2006. **209**(2-3): p. 177-86.
264. Nickel, R. and A. Forge, *Gap junctions and connexins in the inner ear: their roles in homeostasis and deafness*. Curr Opin Otolaryngol Head Neck Surg, 2008. **16**(5): p. 452-7.
265. Lautermann, J., et al., *Expression of the gap-junction connexins 26 and 30 in the rat cochlea*. Cell Tissue Res, 1998. **294**(3): p. 415-20.
266. Ahmad, S., et al., *Connexins 26 and 30 are co-assembled to form gap junctions in the cochlea of mice*. Biochem Biophys Res Commun, 2003. **307**(2): p. 362-8.
267. Zhao, H.B. and N. Yu, *Distinct and gradient distributions of connexin26 and connexin30 in the cochlear sensory epithelium of guinea pigs*. J Comp Neurol, 2006. **499**(3): p. 506-18.
268. Liu, Y.P. and H.B. Zhao, *Cellular characterization of Connexin26 and Connexin30 expression in the cochlear lateral wall*. Cell Tissue Res, 2008. **333**(3): p. 395-403.
269. Kikuchi, T., et al., *Potassium ion recycling pathway via gap junction systems in the mammalian cochlea and its interruption in hereditary nonsyndromic deafness*. Med Electron Microsc, 2000. **33**(2): p. 51-6.
270. Lang, F., et al., *Functional significance of channels and transporters expressed in the inner ear and kidney*. Am J Physiol Cell Physiol, 2007. **293**(4): p. C1187-208.
271. Zdebik, A.A., P. Wangemann, and T.J. Jentsch, *Potassium ion movement in the inner ear: insights from genetic disease and mouse models*. Physiology (Bethesda), 2009. **24**: p. 307-16.
272. Adachi, N., et al., *The mechanism underlying maintenance of the endocochlear potential by the K⁺ transport system in fibrocytes of the inner ear*. J Physiol, 2013. **591**(18): p. 4459-72.
273. Matsunami, T., et al., *Gap junctions mediate glucose transport between GLUT1-positive and -negative cells in the spiral limbus of the rat cochlea*. Cell Commun Adhes, 2006. **13**(1-2): p. 93-102.
274. Chang, Q., et al., *Gap junction mediated intercellular metabolite transfer in the cochlea is compromised in connexin30 null mice*. PLoS One, 2008. **3**(12): p. e4088.
275. Wang, Y., et al., *Targeted connexin26 ablation arrests postnatal development of the organ of Corti*. Biochem Biophys Res Commun, 2009. **385**(1): p. 33-7.
276. Zhao, H.B., *Connexin26 is responsible for anionic molecule permeability in the cochlea for intercellular signalling and metabolic communications*. Eur J Neurosci, 2005. **21**(7): p. 1859-68.
277. Laird, D.W., *The gap junction proteome and its relationship to disease*. Trends Cell Biol, 2010. **20**(2): p. 92-101.
278. Apps, S.A., W.A. Rankin, and A.P. Kurmis, *Connexin 26 mutations in autosomal recessive deafness disorders: a review*. Int J Audiol, 2007. **46**(2): p. 75-81.
279. Denoyelle, F., et al., *Prelingual deafness: high prevalence of a 30delG mutation in the connexin 26 gene*. Hum Mol Genet, 1997. **6**(12): p. 2173-7.

280. Estivill, X., et al., *Connexin-26 mutations in sporadic and inherited sensorineural deafness*. Lancet, 1998. **351**(9100): p. 394-8.
281. Kelsell, D.P., et al., *Connexin 26 mutations in hereditary non-syndromic sensorineural deafness*. Nature, 1997. **387**(6628): p. 80-3.
282. Chan, D.K., I. Schrijver, and K.W. Chang, *Connexin-26-associated deafness: phenotypic variability and progression of hearing loss*. Genet Med, 2010. **12**(3): p. 174-81.
283. Duman, D. and M. Tekin, *Autosomal recessive nonsyndromic deafness genes: a review*. Front Biosci (Landmark Ed), 2012. **17**: p. 2213-36.
284. Xu, J. and B.J. Nicholson, *The role of connexins in ear and skin physiology - functional insights from disease-associated mutations*. Biochimica et biophysica acta, 2013. **1828**(1): p. 167-178.
285. Richard, G., et al., *Missense mutations in GJB2 encoding connexin-26 cause the ectodermal dysplasia keratitis-ichthyosis-deafness syndrome*. Am J Hum Genet, 2002. **70**(5): p. 1341-8.
286. Sanchez, H.A. and V.K. Verselis, *Aberrant Cx26 hemichannels and keratitis-ichthyosis-deafness syndrome: insights into syndromic hearing loss*. Frontiers in cellular neuroscience, 2014. **8**(354): p. 1 - 8.
287. Lee, J.R. and T.W. White, *Connexin-26 mutations in deafness and skin disease*. Expert Rev Mol Med, 2009. **11**: p. e35.
288. Pfahnl, A. and G. Dahl, *Localization of a voltage gate in connexin46 gap junction hemichannels*. Biophys J, 1998. **75**(5): p. 2323-31.
289. Kronengold, J., et al., *Single-channel SCAM identifies pore-lining residues in the first extracellular loop and first transmembrane domains of Cx46 hemichannels*. J Gen Physiol, 2003. **122**(4): p. 389-405.
290. Zhou, X.W., et al., *Identification of a pore lining segment in gap junction hemichannels*. Biophys J, 1997. **72**(5): p. 1946-53.
291. Sanchez, H.A., et al., *Differentially altered Ca²⁺ regulation and Ca²⁺ permeability in Cx26 hemichannels formed by the A40V and G45E mutations that cause keratitis ichthyosis deafness syndrome*. J Gen Physiol, 2010. **136**(1): p. 47-62.
292. Steel, K.P., *Perspectives: biomedicine. The benefits of recycling*. Science, 1999. **285**(5432): p. 1363-4.
293. Wangemann, P., *Supporting sensory transduction: cochlear fluid homeostasis and the endocochlear potential*. J Physiol, 2006. **576**(Pt 1): p. 11-21.
294. Johnstone, B.M., et al., *Stimulus-related potassium changes in the organ of Corti of guinea-pig*. J Physiol, 1989. **408**: p. 77-92.
295. Kudo, T., et al., *Transgenic expression of a dominant-negative connexin26 causes degeneration of the organ of Corti and non-syndromic deafness*. Hum Mol Genet, 2003. **12**(9): p. 995-1004.
296. Cohen-Salmon, M., et al., *Targeted ablation of connexin26 in the inner ear epithelial gap junction network causes hearing impairment and cell death*. Curr Biol, 2002. **12**(13): p. 1106-11.
297. Stong, B.C., et al., *A novel mechanism for connexin 26 mutation linked deafness: cell death caused by leaky gap junction hemichannels*. Laryngoscope, 2006. **116**(12): p. 2205-10.
298. Gerido, D.A., et al., *Aberrant hemichannel properties of Cx26 mutations causing skin disease and deafness*. Am J Physiol Cell Physiol, 2007. **293**: p. C337 - C345.

299. Lee, J.R., A.M. Derosa, and T.W. White, *Connexin mutations causing skin disease and deafness increase hemichannel activity and cell death when expressed in Xenopus oocytes*. J Invest Dermatol, 2009. **129**(4): p. 870-8.
300. Batir, Y., T.A. Bargiello, and T.L. Dowd, *Structural studies of N-terminal mutants of Connexin 26 and Connexin 32 using (1)H NMR spectroscopy*. Arch Biochem Biophys, 2016. **608**: p. 8-19.
301. Sanchez, H.A., et al., *Syndromic deafness mutations at Asn 14 differentially alter the open stability of Cx26 hemichannels*. J Gen Physiol, 2016. **148**(1): p. 25-42.
302. Bicego, M., et al., *Pathogenetic role of the deafness-related M34T mutation of Cx26*. Hum Mol Genet, 2006. **15**(17): p. 2569-87.
303. Houseman, M.J., et al., *Genetic analysis of the connexin-26 M34T variant: identification of genotype M34T/M34T segregating with mild-moderate non-syndromic sensorineural hearing loss*. J Med Genet, 2001. **38**(1): p. 20-5.
304. Scott, D.A., et al., *Identification of mutations in the connexin 26 gene that cause autosomal recessive nonsyndromic hearing loss*. Hum Mutat, 1998. **11**(5): p. 387-94.
305. Skerrett, I.M., et al., *Aberrant gating, but a normal expression pattern, underlies the recessive phenotype of the deafness mutant Connexin26M34T*. FASEB J, 2004. **18**(7): p. 860-2.
306. White, T.W., et al., *Connexin mutations in deafness*. Nature, 1998. **394**(6694): p. 630-1.
307. Oshima, A., et al., *Roles of Met-34, Cys-64, and Arg-75 in the assembly of human connexin 26. Implication for key amino acid residues for channel formation and function*. J Biol Chem, 2003. **278**(3): p. 1807-16.
308. Stergiopoulos, K., et al., *Hetero-Domain Interactions as a Mechanism for the Regulation of Connexin Channels*. Circulation Research, 1999. **84**(10): p. 1144-1155.
309. Iwatsuki, N. and O.H. Petersen, *Pancreatic acinar cells: the effect of carbon dioxide, ammonium chloride and acetylcholine on intercellular communication*. J Physiol, 1979. **291**: p. 317-26.
310. Turin, L. and A.E. Warner, *Intracellular pH in early Xenopus embryos: its effect on current flow between blastomeres*. J Physiol, 1980. **300**: p. 489-504.
311. Schuetze, S.M. and D.A. Goodenough, *Dye transfer between cells of the embryonic chick lens becomes less sensitive to CO₂ treatment with development*. J Cell Biol, 1982. **92**(3): p. 694-705.
312. Connors, B.W., L.S. Benardo, and D.A. Prince, *Carbon dioxide sensitivity of dye coupling among glia and neurons of the neocortex*. J Neurosci, 1984. **4**(5): p. 1324-30.
313. Noma, A. and N. Tsuboi, *Dependence of junctional conductance on proton, calcium and magnesium ions in cardiac paired cells of guinea-pig*. J Physiol, 1987. **382**: p. 193-211.
314. Reber, W.R. and R. Weingart, *Ungulate cardiac purkinje fibres: the influence of intracellular pH on the electrical cell-to-cell coupling*. J Physiol, 1982. **328**: p. 87-104.
315. Burt, J.M., *Block of intercellular communication: interaction of intracellular H⁺ and Ca²⁺*. Am J Physiol, 1987. **253**(4 Pt 1): p. C607-12.
316. Morley, G.E., S.M. Taffet, and M. Delmar, *Intramolecular interactions mediate pH regulation of connexin43 channels*. Biophys J, 1996. **70**(3): p. 1294-302.
317. Owens, L.M., et al., *Correlation of ischemia-induced extracellular and intracellular ion changes to cell-to-cell electrical uncoupling in isolated blood-perfused rabbit hearts. Experimental Working Group*. Circulation, 1996. **94**(1): p. 10-3.

318. Kleber, A.G., C.B. Riegger, and M.J. Janse, *Electrical uncoupling and increase of extracellular resistance after induction of ischemia in isolated, arterially perfused rabbit papillary muscle*. *Circ Res*, 1987. **61**(2): p. 271-9.
319. Nattel, S., *The clinical relevance of connexin gating: how to control communication in the heart*. *Heart Rhythm*, 2004. **1**(2): p. 234.
320. Yu, J., et al., *Aminosulfonate modulated pH-induced conformational changes in connexin26 hemichannels*. *J Biol Chem*, 2007. **282**(12): p. 8895-904.
321. Bevans, C.G. and A.L. Harris, *Regulation of Connexin Channels by pH*. *The Journal of Biological Chemistry*, 1999. **274**(6): p. 3711–3719.
322. Allen, M.J., et al., *Atomic force microscopy of Connexin40 gap junction hemichannels reveals calcium-dependent three-dimensional molecular topography and open-closed conformations of both the extracellular and cytoplasmic faces*. *J Biol Chem*, 2011. **286**(25): p. 22139-46.
323. Miyazawa, A., Y. Fujiyoshi, and N. Unwin, *Structure and gating mechanism of the acetylcholine receptor pore*. *Nature*, 2003. **423**(6943): p. 949-55.
324. Ebihara, L., V.M. Berthoud, and E.C. Beyer, *Distinct behavior of connexin56 and connexin46 gap junctional channels can be predicted from the behavior of their hemi-gap-junctional channels*. *Biophys J*, 1995. **68**(5): p. 1796-803.
325. Wang, X.G. and C. Peracchia, *Chemical gating of heteromeric and heterotypic gap junction channels*. *J Membr Biol*, 1998. **162**(2): p. 169-76.
326. Maeda, S. and T. Tsukihara, *Structure of the gap junction channel and its implications for its biological functions*. *Cell Mol Life Sci*, 2011. **68**(7): p. 1115-29.
327. Thimm, J., et al., *Calcium-dependent open/closed conformations and interfacial energy maps of reconstituted hemichannels*. *J Biol Chem*, 2005. **280**(11): p. 10646-54.
328. Ek Vitorin, J.F., T.K. Pontifex, and J.M. Burt, *Determinants of Cx43 Channel Gating and Permeation: The Amino Terminus*. *Biophys J*, 2016. **110**(1): p. 127-40.
329. Evans, W.H., E. De Vuyst, and L. Leybaert, *The gap junction cellular internet: connexin hemichannels enter the signalling limelight*. *Biochem J*, 2006. **397**(1): p. 1-14.
330. Ripps, H., H. Qian, and J. Zakevicius, *Properties of connexin26 hemichannels expressed in Xenopus oocytes*. *Cell Mol Neurobiol*, 2004. **24**(5): p. 647-65.
331. Lopez, W., et al., *Mechanism of gating by calcium in connexin hemichannels*. *PNAS*, 2016.
332. Bai, D. and A.H. Wang, *Extracellular domains play different roles in gap junction formation and docking compatibility*. *Biochem J*, 2014. **458**(1): p. 1-10.
333. Gong, X.Q., et al., *A mechanism of gap junction docking revealed by functional rescue of a human-disease-linked connexin mutant*. *J Cell Sci*, 2013. **126**(Pt 14): p. 3113-20.
334. Srinivas, M., et al., *Correlative studies of gating in Cx46 and Cx50 hemichannels and gap junction channels*. *Biophys J*, 2005. **88**(3): p. 1725-39.
335. Srinivas, M., et al., *Regulation of connexin hemichannels by monovalent cations*. *The Journal of general physiology*, 2006. **127**(1): p. 67-75.
336. Breitweiser, G.A., *Extracellular calcium as an integrator of tissue function*. *Int J Biochem Cell Biol*, 2008. **40**(8): p. 1467–1480.
337. Romani, A.M., *Cellular magnesium homeostasis*. *Arch Biochem Biophys*, 2011. **512**(1): p. 1-23.
338. Howson, J.M., et al., *Genetic association of zinc transporter 8 (ZnT8) autoantibodies in type 1 diabetes cases*. *Diabetologia*, 2012. **55**(7): p. 1978-84.
339. Chabosseau, P. and G.A. Rutter, *Zinc and diabetes*. *Arch Biochem Biophys*, 2016. **in press**.

340. Petersen, A.B., et al., *siRNA-mediated knock-down of ZnT3 and ZnT8 affects production and secretion of insulin and apoptosis in INS-1E cells*. *APMIS*, 2011. **119**(2): p. 93-102.
341. Kambe, T., et al., *The Physiological, Biochemical, and Molecular Roles of Zinc Transporters in Zinc Homeostasis and Metabolism*. *Physiol Rev*, 2015. **95**(3): p. 749-84.
342. Bai, J., et al., *A gene optimization strategy that enhances production of fully functional P-glycoprotein in Pichia pastoris*. *PLoS One*, 2011. **6**(8): p. e22577.
343. Lin-Cereghino, J., et al., *Condensed protocol for competent cell preparation and transformation of the methylotrophic yeast Pichia pastoris*. *Biotechniques*, 2005. **38**(1): p. 44, 46, 48.
344. Studier, F.W., *Protein production by auto-induction in high density shaking cultures*. *Protein Expr Purif*, 2005. **41**(1): p. 207-34.
345. Heuberger, E.H., et al., *Oligomeric state of membrane transport proteins analyzed with blue native electrophoresis and analytical ultracentrifugation*. *Journal of Molecular Biology*, 2002. **317**(4): p. 591-600.
346. Harlow, E. and D. Lane, *Antibodies: a laboratory manual*. 1988, Cold Spring Harbor: Cold Spring Harbor Laboratory.
347. Rasband, W.S. *ImageJ*. 1997-2015; Available from: <http://imagej.nih.gov/ij/>.
348. Bhairi, S.M., *Detergents: A guide to the properties and uses of detergents in biological systems*, Calbiochem, Editor 2007, EMD Biosciences: San Diego, CA.
349. Anatrache, *Detergent Properties Booklet*, 2014, Anatrache.
350. Alexandrov, A.I., et al., *Microscale fluorescent thermal stability assay for membrane proteins*. *Structure*, 2008. **16**(3): p. 351-359.
351. Greenfield, N.J., *Using circular dichroism spectra to estimate protein secondary structure*. *Nature Protocols*, 2006. **1**: p. 2876-2890.
352. Pace, C.N., et al., *How to measure and predict the molar absorption coefficient of a protein*. *Protein Science*, 1995. **4**: p. 2411-2423.
353. Whitmore, L. and B.A. Wallace, *DICHROWEB, an online server for protein secondary structure analyses from circular dichroism spectroscopic data*. *Nucleic Acids Res*, 2004. **32**(Web Server issue): p. W668-73.
354. Sreerama, N. and R.W. Woody, *Computation and analysis of protein circular dichroism spectra*. *Methods in Enzymology*, 2004. **383**: p. 318-351.
355. Travis, J.C., et al., *Intrinsic wavelength standard absorption bands in holmium oxide solution for UV/visible molecular absorption spectrophotometry*. *Journal of Physical and Chemical Reference Data*, 2005. **34**(1): p. 41-56.
356. Miles, A.J., et al., *Calibration and Standardisation of Synchrotron Radiation Circular Dichroism and Conventional Circular Dichroism Spectrophotometers*. *Spectroscopy*, 2003. **17**(1): p. 653-661.
357. Ohi, M., et al., *Negative Staining and Image Classification - Powerful Tools in Modern Electron Microscopy*. *Biological Procedures Online*, 2004. **6**: p. 23-34.
358. Tang, G., et al., *EMAN2: an extensible image processing suite for electron microscopy*. *Journal of Structural Biology*, 2007. **157**(1): p. 38-46.
359. Scheres, S.H., *RELION: implementation of a Bayesian approach to cryo-EM structure determination*. *J Struct Biol*, 2012. **180**(3): p. 519-30.
360. Mindell, J.A. and N. Grigorieff, *Accurate determination of local defocus and specimen tilt in electron microscopy*. *Journal of Structural Biology*, 2003. **142**(3): p. 334-347.

361. Dolan, M.A., J.W. Noah, and D. Hurt, *Comparison of common homology modeling algorithms: application of user-defined alignments*. *Methods Mol Biol*, 2012. **857**: p. 399-414.
362. Yang, Z., et al., *UCSF Chimera, MODELLER, and IMP: an integrated modeling system*. *Journal of Structural Biology*, 2012. **179**(3): p. 269-278.
363. Kozlowski, L.P. and J.M. Bujnicki, *MetaDisorder: a meta-server for the prediction of intrinsic disorder in proteins*. *BMC Bioinformatics*, 2012. **13**: p. 111.
364. Lohmeier-Vogel, E.M., D.D. McIntyre, and H.J. Vogel, *Phosphorus-31 and carbon-13 nuclear magnetic resonance studies of glucose and xylose metabolism in cell suspensions and agarose-immobilized cultures of Pichia stipitis and Saccharomyces cerevisiae*. *Appl Environ Microbiol*, 1996. **62**(8): p. 2832-8.
365. Ross, I.S., *Uptake of zinc by fungi*, in *Metal ions in fungi*, G. Winkelmann and D.R. Winge, Editors. 1994, Marcel Dekker: New York. p. 237-258.
366. Haworth, R.S. and L. Fliegel, *Intracellular pH in Schizosaccharomyces pombe - Comparison with Saccharomyces cerevisiae*. *Molecular and Cellular Biochemistry*, 1993. **124**: p. 131-140.
367. Zhao, H. and D. Eide, *The yeast ZRT1 gene encodes the zinc transporter protein of a high-affinity uptake system induced by zinc limitation*. *Proc Natl Acad Sci U S A*, 1996. **93**(6): p. 2454-8.
368. Gaither, L.A. and D.J. Eide, *Eukaryotic zinc transporters and their regulation*. *Biometals*, 2001. **14**(3-4): p. 251-70.
369. Aller, S.G., et al., *Structure of P-glycoprotein reveals a molecular basis for poly-specific drug binding*. *Science*, 2009. **323**(5922): p. 1718-1722.
370. Roberts, M.F., D.W. Taylor, and V.M. Unger, *Two modes of interaction between the membrane-embedded TARP stargazin's C-terminal domain and the bilayer visualized by electron crystallography*. *J Struct Biol*, 2011. **174**(3): p. 542-51.
371. Vergis, J.M., M.D. Purdy, and M.C. Wiener, *A high-throughput differential filtration assay to screen and select detergents for membrane proteins*. *Analytical biochemistry*, 2010. **407**(1): p. 1-11.
372. Whitmore, L. and B.A. Wallace, *Protein secondary structure analyses from circular dichroism spectroscopy: methods and reference databases*. *Biopolymers*, 2008. **89**(5): p. 392-400.
373. Kabsch, W. and C. Sander, *Dictionary of protein secondary structure: pattern recognition of hydrogen-bonded and geometrical features*. *Biopolymers*, 1983. **22**(12): p. 2577-637.
374. Reutimann, H., et al., *A conformational study of thioredoxin and its tryptic fragments*. *J Biol Chem*, 1981. **256**(13): p. 6796-803.
375. Wu, S., et al., *Fabs enable single particle cryoEM studies of small proteins*. *Structure*, 2012. **20**(4): p. 582-592.
376. Cheng, Y., *Single-Particle Cryo-EM at Crystallographic Resolution*. *Cell*, 2015. **161**(3): p. 450-457.
377. Khoshouei, M., et al., *Cryo-EM structure of haemoglobin at 3.2 Å determined with the Volta phase plate*. *Nat Commun*, 2017. **8**: p. 16099.
378. Chun, E., et al., *Fusion partner toolchest for the stabilization and crystallization of G protein-coupled receptors*. *Structure*, 2012. **20**(6): p. 967-76.
379. Alam, A., et al., *Structure of a zosuquidar and UIC2-bound human-mouse chimeric ABCB1*. *Proc Natl Acad Sci U S A*, 2018. **115**(9): p. E1973-E1982.

380. Kim, J., et al., *Subnanometre-resolution electron cryomicroscopy structure of a heterodimeric ABC exporter*. *Nature*, 2015. **517**(7534): p. 396-400.
381. Li, X., et al., *Electron counting and beam-induced motion correction enable near-atomic-resolution single-particle cryo-EM*. *Nat Methods*, 2013. **10**(6): p. 584-90.
382. Rohou, A. and N. Grigorieff, *CTFFIND4: Fast and accurate defocus estimation from electron micrographs*. *J Struct Biol*, 2015. **192**(2): p. 216-21.
383. Kimanius, D., et al., *Accelerated cryo-EM structure determination with parallelisation using GPUs in RELION-2*. *Elife*, 2016. **5**.
384. Fernandez-Leiro, R. and S.H.W. Scheres, *A pipeline approach to single-particle processing in RELION*. *Acta Crystallogr D Struct Biol*, 2017. **73**(Pt 6): p. 496-502.
385. Zhang, K., *Gctf: Real-time CTF determination and correction*. *J Struct Biol*, 2016. **193**(1): p. 1-12.
386. Scheres, S.H., *Beam-induced motion correction for sub-megadalton cryo-EM particles*. *Elife*, 2014. **3**: p. e03665.
387. Rosenthal, P.B. and R. Henderson, *Optimal determination of particle orientation, absolute hand, and contrast loss in single-particle electron cryomicroscopy*. *J Mol Biol*, 2003. **333**(4): p. 721-45.
388. Adams, P.D., et al., *PHENIX: a comprehensive Python-based system for macromolecular structure solution*. *Acta Crystallographica. Section D Biological Crystallography*, 2010. **66**(Pt 2): p. 213-221.
389. Yonekura, K. and S. Maki-Yonekura, *Refinement of cryo-EM structures using scattering factors of charged atoms*. *Journal of Applied Crystallography*, 2016. **49**(5): p. 1517-1523.
390. Emsley, P., et al., *Features and development of Coot*. *Acta Crystallogr D Biol Crystallogr*, 2010. **66**(Pt 4): p. 486-501.
391. Chen, V.B., et al., *MolProbity: all-atom structure validation for macromolecular crystallography*. *Acta Crystallographica. Section D Biological Crystallography*, 2010. **66**(Pt 1): p. 12-21.
392. Barad, B.A., et al., *EMRinger: side chain-directed model and map validation for 3D cryo-electron microscopy*. *Nat Methods*, 2015. **12**(10): p. 943-6.
393. Chalmers, M.J., et al., *Probing protein ligand interactions by automated hydrogen/deuterium exchange mass spectrometry*. *Anal Chem*, 2006. **78**(4): p. 1005-14.
394. Busby, S.A., M.J. Chalmers, and P.R. Griffin, *Improving digestion efficiency under H/D exchange conditions with activated pepsinogen coupled columns*. *International Journal of Mass Spectrometry*, 2007. **259**(1-3): p. 130-139.
395. Pascal, B.D., et al., *HDX workbench: software for the analysis of H/D exchange MS data*. *J Am Soc Mass Spectrom*, 2012. **23**(9): p. 1512-21.
396. West, G.M., et al., *Protein conformation ensembles monitored by HDX reveal a structural rationale for abscisic acid signaling protein affinities and activities*. *Structure*, 2013. **21**(2): p. 229-35.
397. Coales, S.J., et al., *Expansion of time window for mass spectrometric measurement of amide hydrogen/deuterium exchange reactions*. *Rapid Commun Mass Spectrom*, 2010. **24**(24): p. 3585-92.
398. Schmidt, C. and C.V. Robinson, *A comparative cross-linking strategy to probe conformational changes in protein complexes*. *Nat Protoc*, 2014. **9**(9): p. 2224-36.

399. Xu, H. and M.A. Freitas, *MassMatrix: a database search program for rapid characterization of proteins and peptides from tandem mass spectrometry data*. Proteomics, 2009. **9**(6): p. 1548-55.
400. Kucukelbir, A., F.J. Sigworth, and H.D. Tagare, *Quantifying the local resolution of cryo-EM density maps*. Nat Methods, 2014. **11**(1): p. 63-5.
401. Gould, T.D., et al., *Involvement of AMPA receptors in the antidepressant-like effects of lithium in the mouse tail suspension test and forced swim test*. Neuropharmacology, 2008. **54**(3): p. 577-87.
402. Shi, J.M., et al., *Bis(sulfosuccinimidyl) suberate (BS3) crosslinking analysis of the behavior of amyloid-beta peptide in solution and in phospholipid membranes*. PLoS One, 2017. **12**(3): p. e0173871.
403. Zhao, A., G. Hao, and J. Gu, *Chemical crosslinking and mass spectrometric identification of interaction sites within soluble aggregate of protein therapeutics*. J Pharm Biomed Anal, 2013. **73**: p. 99-102.
404. Armstrong, C.M. and F. Bezanilla, *Inactivation of the sodium channel. II. Gating current experiments*. J Gen Physiol, 1977. **70**(5): p. 567-90.
405. Zagotta, W.N., T. Hoshi, and R.W. Aldrich, *Restoration of inactivation in mutants of Shaker potassium channels by a peptide derived from ShB*. Science, 1990. **250**(4980): p. 568-71.
406. Zhou, M., et al., *Potassium channel receptor site for the inactivation gate and quaternary amine inhibitors*. Nature, 2001. **411**(6838): p. 657-61.
407. Yeager, M., V.M. Unger, and M.M. Falk, *Synthesis, assembly and structure of gap junction intercellular channels*. Current Opinion in Structural Biology, 1998. **8**(4): p. 517 - 524.
408. Ambrosi, C., et al., *Analysis of trafficking, stability and function of human connexin 26 gap junction channels with deafness-causing mutations in the fourth transmembrane helix*. PLoS One, 2013. **8**(8): p. e70916.
409. Abrams, C.K., et al., *Functional requirement for a highly conserved charged residue at position 75 in the gap junction protein connexin 32*. The Journal of Biological Chemistry, 2013. **288**(5): p. 3609-3619.
410. Nakagawa, S., et al., *Asparagine 175 of connexin32 is a critical residue for docking and forming functional heterotypic gap junction channels with connexin26*. J Biol Chem, 2011. **286**(22): p. 19672-81.
411. Meyerson, J.R., et al., *Self-assembled monolayers improve protein distribution on holey carbon cryo-EM supports*. Sci Rep, 2014. **4**: p. 7084.
412. Kucharska, I., et al., *Optimizing nanodiscs and bicelles for solution NMR studies of two beta-barrel membrane proteins*. J Biomol NMR, 2015. **61**(3-4): p. 261-74.
413. Gao, Y., et al., *TRPV1 structures in nanodiscs reveal mechanisms of ligand and lipid action*. Nature, 2016. **534**(7607): p. 347-51.
414. Mi, W., et al., *Structural basis of MsbA-mediated lipopolysaccharide transport*. Nature, 2017. **549**(7671): p. 233-237.
415. Taylor, N.M.I., et al., *Structure of the human multidrug transporter ABCG2*. Nature, 2017. **546**(7659): p. 504-509.
416. von Loeffelholz, O., et al., *Volta phase plate data collection facilitates image processing and cryo-EM structure determination*. J Struct Biol, 2018.
417. Danev, R., D. Tegunov, and W. Baumeister, *Using the Volta phase plate with defocus for cryo-EM single particle analysis*. ELife, 2017.

418. Danev, R. and W. Baumeister, *Cryo-EM single particle analysis with the Volta phase plate*. ELife, 2016.